Physics and Applications of Compact Optical Frequency Comb

Thesis by
Maodong Gao

In Partial Fulfillment of the Requirements for the
Degree of
Doctor of Philosophy

CALIFORNIA INSTITUTE OF TECHNOLOGY
Pasadena, California

2025
Defended June 27th, 2024

Maodong Gao
ORCID: 0000-0002-7791-0008

ACKNOWLEDGEMENTS

I would like to express my deepest gratitude to my advisor, Prof. Kerry Vahala, for his unwavering supervision and support throughout my Ph.D. journey. His guidance in navigating the academic path and his example as a dedicated researcher has been invaluable to my growth. I am also sincerely thankful to Dr. Stephanie Leifer for her crucial assistance during challenging moments in my project.

This research would not have been possible without the support of my colleagues, collaborators and friends. I am deeply grateful to each of them for their exceptional work, unique contributions, and insightful discussions, including the current lab members: Dr. Hao-Jing Chen, Dr. Zhiquan Yuan, Qing-Xin Ji, Bohan Li, Yan Yu, Peng Liu, Jin-Yu Liu, Jinhao Ge, and Kellan Colburn, as well as lab alumni: Prof. Hansuek Lee, Dr. Jiang Li, Dr. Myoung-Gyun Suh, Prof. Xu Yi, Dr. Yu-Hung Lai, Prof. Chengying Bao, Prof. Qi-Fan Yang, Dr. Boqiang Shen, Dr. Heming Wang, and Dr. Lue Wu. I am also thankful for the collaboration and support from several esteemed institutions: from the PMA division of Caltech, Prof. Charles Beichman, Dr. Nemanja Jovanovic, and Hector Rodriguez; from UCSB, Prof. John Bowers, Prof. Weiqiang Xie, Prof. Lin Chang, Prof. Chao Xiang, and Joel Guo; from EPFL, Prof. Tobias Kippenberg, Prof. Junqiu Liu, and Dr. Guanhao Huang; from NIST, Prof. Scott Papp and Dr. Su-Peng Yu; from JPL, Dr. Gautam Vasisht, Dr. Mahmood Bagheri and Dr. Wei Zhang; from Anello Photonics, Dr. Warren Jin, Dr. Avi Feshali, and Dr. Mario Paniccia; from Octave Photonics, Dr. David Carlson, Dr. Zach Newman, and Dr. Daniel Hickstein; from Aerospace Corporation, Dr. Paul Steinvurzel; from UCLA, Prof. Michael Fitzgerald and Yoo Jung Kim; from Northwestern University, Dr. Chih-Chun (Dino) Hsu; and from the W. M. Keck Observatory, Dr. Greg Doppmann, Dr. Marc Kassis, Dr. Truman Wold, Dr. Kyle Lanclos, Dr. Danny Baldwin, and Dr. Grant Hill. This list is not exhaustive and is presented in no particular order. I also wish to acknowledge the funding agencies that supported this research, each of which is recognized in the respective published papers.

I am especially grateful to my candidacy and thesis defense committee members, including Prof. Andrei Faraon (Candidacy Chair), Prof. Alireza Marandi (Thesis Chair), Prof. Kerry Vahala, Dr. Stephanie Leifer, Prof. Charles Beichman, and Prof. Paul Bellan, for their guidance and support throughout the key milestones.

Finally, I would like to thank my family for their unwavering care and support throughout this journey. Their support has been my greatest strength.

ABSTRACT

Optical frequency combs (OFC) have been vastly developing and were awarded half of the Nobel Prize in 2005. OFCs are series of optical signals with distinct and equally spaced frequencies. One reason why OFCs are essential for modern optics and photonics engineering is that OFCs serve as a bridge between optical frequencies (hundreds of THz) and frequencies within the electronic bandwidth (from MHz to GHz, which is the distance between adjacent comb teeth). In this thesis, I first introduce some physical principles of optical resonators, which are critical components for confining optical energy and generating OFCs. Then, in the main body of this thesis, I study the physics and applications of two types of compact OFCs: soliton microcombs and electro-optical frequency combs.

Microcombs are OFCs generated on integrated photonics devices. Here, I first develop a methodology to experimentally characterize two important physical properties (material absorption loss and optical nonlinearity) of integrated photonic materials. Next, I focus on a novel method to generate mode-locked soliton microcombs on ultra-low-loss Si_3N_4 material. It was considered challenging to support bright solitons due to its normal dispersion. This novel method involves two resonators that are partially coupled together, which can modify the dispersion through mode hybridization and feature symmetry breaking. Following this, I investigate two characteristics closely related to the symmetry breaking of this coupled-ring device: the observation of Kelly sidebands and multicolor bright soliton generation. Finally, I demonstrate bright soliton generation in $Al_{0.2}Ga_{0.8}As$ resonators, which feature high nonlinearity but were considered difficult to support bright solitons at room temperature due to its high material loss. Here, we mitigate the effect of material loss by pulse-pumping operation.

Electro-optical frequency combs are OFCs generated by modulating a continuous wave laser using an external radio-frequency source. Taking advantage of low-noise radio frequency and stable continuous-wave laser frequency, this OFC can serve as a frequency reference for astronomical observation. In this thesis, I first introduce the physics and operating principle of electro-optical frequency combs in Chapter 1, then discuss developing and deploying the near-infrared laser frequency comb at the W.M. Keck Observatory in Chapter 7.

In summary, the thesis discusses the physics and applications of mode-locked bright

soliton microcombs, which can generate radio frequencies by taking the beat note of this OFC. I also discuss the physics and applications of electro-optical frequency combs, which are stable OFCs used for astronomical frequency references generated by radio-frequency modulation of continuous wave lasers. The critical role of OFCs as a bridge between optical frequencies and frequencies within the electronic bandwidth (MHz to GHz) is demonstrated, and their potential to revolutionize various fields, including high-precision metrology, telecommunications, and astrophysics, is highlighted.

PUBLISHED CONTENT AND CONTRIBUTIONS

[1] Zhiquan Yuan *et al.* "Linewidth enhancement factor in a microcavity Brillouin laser," *Optica* **7**, 1150-1153 (2020). DOI: 10.1364/OPTICA.394311
M. G. designed and fabricated the devices, performed the experiment, and contributed to the writing of the manuscript.

[2] Lue Wu *et al.* "Greater than one billion Q factor for on-chip microresonators," *Opt. Lett.* **45**, 5129-5131 (2020). DOI: 10.1364/OL.394940
M. G. designed and fabricated the devices, measured the data, and contributed to the writing of the manuscript.

[3] Warren Jin *et al.* "Hertz-linewidth semiconductor lasers using CMOS-ready ultra-high-Q microresonators," *Nat. Photon.* **15**, 346–353 (2021). DOI: 10.1038/s41566-021-00761-7
M. G. performed the experiments, analyzed the data, and contributed to the writing of the manuscript.

[4] Maodong Gao *et al.*, "Probing material absorption and optical nonlinearity of integrated photonic materials," *Nat. Commun.* **13**, 3323 (2022). DOI: 10.1038/s41467-022-30966-5
M. G. participated in the conception of the project, performed the experiments, analyzed the data, and contributed to the writing of the manuscript.

[5] Zhiquan Yuan *et al.* "Correlated self-heterodyne method for ultra-low-noise laser linewidth measurements," *Opt. Express* **30**, 25147-25161 (2022). DOI: 10.1364/OE.458109
M. G. analyzed the data, wrote and maintained the open-source software, and contributed to the writing of the manuscript.

[6] Nemanja Jovanovic *et al.* "Flattening laser frequency comb spectra with a high dynamic range, broadband spectral shaper on-a-chip," *Opt. Express* **30**, 36745-36760 (2022). DOI: 10.1364/OE.470143
M. G. performed the experiments, analyzed the data, and contributed to the writing of the manuscript.

[7] Qing-Xin Ji *et al.* "Engineered zero-dispersion microcombs using CMOS-ready photonics," *Optica* **10**, 279-285 (2023). DOI: 10.1364/OPTICA.478710

M. G. participated in the conception of the project, performed the experiments, analyzed the data, and contributed to the writing of the manuscript.

[8] Lue Wu *et al.* "Hydroxyl ion absorption in on-chip high-Q resonators," *Opt. Lett.* **48**, 3511-3514 (2023). DOI: 10.1364/OL.492067
M. G. participated in the conception of the project, performed the experiments and numerical simulation, analyzed the data, and contributed to the writing of the manuscript.

[9] Zhiquan Yuan *et al.* "Soliton pulse pairs at multiple colours in normal dispersion microresonators," *Nat. Photon.* **17**, 977–983 (2023). DOI: 10.1038/s41566-023-01257-2
M. G. participated in the conception of the project, performed the experiments, analyzed the data, and contributed to the writing of the manuscript.

[10] Maodong Gao *et al.*, "Observation of interband Kelly sidebands in coupled-ring soliton microcombs," *Optica* **11**, 940-944 (2024). DOI: 10.1364/OPTICA.524074
M. G. participated in the conception of the project, performed the experiments, analyzed the data, and contributed to the writing of the manuscript.

TABLE OF CONTENTS

LIST OF ILLUSTRATIONS

LIST OF TABLES

Chapter 1

INTRODUCTION

Nonlinear systems provide exotic phenomena that significantly differ from linear systems and have been extensively studied in recent decades. In particular, nonlinear optics, which studies material optical nonlinear response to electrical fields, has emerged since the fast development of laser optics, fiber communication, and recently the optical frequency comb technology. The development of nonlinear optics opens its promising applications in optical frequency reference and radio-frequency (RF) synthesizing.

In this chapter, we first review three types of common optical nonlinearity (Photothermal, Electro-optical, and Kerr nonlinearity) in optical media. Then, we introduce the microresonator, which is an ideal platform to study nonlinear optics due to its high ability to store optical energy and accumulate to high intensity. Finally, we briefly introduce optical frequency comb, one major topic in nonlinear optics.

1.1 Optical nonlinearity

1.1.1 Introduction

The optical response of material to the electric field **E** is usually calibrated by dielectric polarization density **P**. The dependence is modelled as power series of **E**, reads

$$\mathbf{P} = \varepsilon_0 \left(\chi^{(1)}\mathbf{E} + \chi^{(2)}\mathbf{EE} + \chi^{(3)}\mathbf{EEE} + \cdots \right), \tag{1.1}$$

where ε_0 is the **vacuum permittivity**, $\chi^{(1)}$ is known as **linear susceptibility**, and $\chi^{(2)}$, $\chi^{(3)}$ are known as second, third order **nonlinear susceptibility**, respectively [1]. Here $\chi^{(n)}$ is a rank-(n+1) tensor, describing the polarization-dependent and anisotropic material response. For the studies in this thesis, it is usually sufficient to simplify these coefficients to scalar values.

The physical process that leads to second-order polarization and third-order polarization tends to be different. Second-order nonlinear interaction can only occur in materials without inversion symmetry. For example, lithium niobate ($LiNbO_3$) forms single crystal and it features strong second order nonlinearity, making it an important material for optical modulator and wavelength converter.

However, amorphous solids and many other crystals that are widely used in nonlinear optics are inversion symmetric, making $\chi^{(2)}$ coefficients for those materials strictly vanish, and thus the leading nonlinear term for these inversion symmetrical materials is the third order term associated with $\chi^{(3)}$. Typical $\chi^{(3)}$ materials involved in this thesis include amorphous silica (SiO_2) and silicon nitride (Si_3N_4).

One important phenomenon of optical nonlinearity is that the material's refractive index depends on the electric field. The refractive index describes how matter affects light propagation. For most materials with relative magnetic permittivity close to 1, the **refractive index** (or phase index) n can be calculated as

$$n \approx \left(\frac{\varepsilon}{\varepsilon_0}\right)^{1/2}, \tag{1.2}$$

where ε is the electric permittivity of the material, defined in the relation $\mathbf{P} = (\varepsilon - \varepsilon_0)\mathbf{E}$. If Eq. (1.1) only contains the linear term associated with $\chi^{(1)}$, the refractive index in Eq. (1.2) can be calculated as $n = \sqrt{1 + \chi^{(1)}}$. In this case, n is not dependent on the electric field $\mathbf{E}$. However, with the presence of nonlinear terms in Eq. (1.1), the refractive index n will involve dependence on $\mathbf{E}$, which will be further discussed in the following section.

There are many types of physical processes that can lead to optical nonlinearity, and here we briefly review three processes that are involved in this thesis.

1.1.2 Electro-optics nonlinearity

The electro-optic effect refers to the optical property of a material changes through the presence of a static or slow-changing (compared to the optical frequency) electric field. Here, we especially focus on the linear electro-optics effect, or Pockels effect, which is the proportional relation between refractive index and electric field. This effect is related to the $\chi^{(2)}$ term in Eq. (1.1), and is strong in $\chi^{(2)}$ materials such as $LiNbO_3$. By applying an electric field modulated at RF rate, the refractive index of the material can be modulated with the same RF rate. The light passing through this material will experience a modulated optical path due to refractive index modulation, causing the optical phase to be modulated. This is the operating principle of the **optical phase modulator**. This phase modulation creates optical sidebands and can further generate electro-optics frequency comb, which will be further discussed in section 1.3.4.

Here, we assume the electric field is only applied along one direction, and the susceptibilities are scalars for simplicity. Taking only the first two terms in Eq.(1.1) and the magnitude of **P** can be calculated from the magnitude of **E** by $P = \varepsilon_0(\chi^{(1)}E + \chi^{(2)}E^2)$. We can calculate the refractive index of the material from Eq. (1.2) as

$$n \approx n_0(1 + \alpha_E E), \tag{1.3}$$

where $n_0 = \sqrt{1 + \chi^{(1)}}$ is the material refractive index without external electric field, $\alpha_E = \chi^{(2)}/2n_0^2$ is the proportion coefficient in linear electro-optics effect. Higer order terms in Eq. (1.3) are neglected.

For an electro-optics based phase modulator, the electric field needed to induce a phase change of π for a light with frequency f is $E_\pi = n_0 c/\chi^{(2)} f L$, where L is the physical length of the modulator, c is the speed of light. In order to reach E_π, the voltage that is needed to be applied is defined as the **phase modulator's half-wave voltage**, or V_π. Currently, the ultra-low V_π of commercial phase modulators based on $LiNbO_3$ can be smaller than 3V. This ultra-low V_π feature is important for applications of electro-optics frequency comb, which will be discussed in Chapter 7 of this thesis.

1.1.3 Thermal-optics nonlinearity

The thermal-optics effect refers to the phenomenon that the refractive index of a material varies when the material temperature is different. Note that here we only consider homogeneous material[1]. For a material with refractive index n_0 at temperature T, its refractive index n at temperature $T + \delta T$ can be expressed as

$$n = n_0 \left(1 + \alpha_T \delta T\right), \tag{1.4}$$

where $\alpha_T = (\delta n/\delta T)/n_0$ is the thermal refractive coefficient associated with n_0.

With the presence of an electric field, the material temperature can change due to the thermal absorption of the electric field. Here, we only focus on linear absorption, where the material thermal absorption rate P_{abs} is proportional to the intensity of the electrical field I. The temperature change δT can be expressed as

$$\delta T = \left(\frac{\delta T}{P_{\text{abs}}}\right)\left(\frac{P_{\text{abs}}}{I}\right) I, \tag{1.5}$$

[1] This effect for devices with heterogeneous structure will be discussed in Section 1.2.7.4.

where $I = \frac{1}{2}cn_0\varepsilon_0|\mathbf{E}|^2$ represents the intensity of the electromagnetic wave. Combining Eq. (1.4) and (1.5), we can find that the refractive index n is dependent on $|\mathbf{E}|^2$ as mediated by thermal absorption of the optical field. The nonlinearity associated with this effect is called thermal-optics nonlinearity.

It should be noted that thermal-optics nonlinearity is mediated through thermal effect. The time scale of this effect will be determined by the thermal absorption rate of the material (typically on the order of ms [2]), and this time scale is much longer than the time scale of any coherent optical effects. As a result, this effect will not lead to any coherent nonlinear optical effects, such as sum/difference frequency generation or harmonic generation. Utilizing their different time scale can help characterize material optical absorption property P_{abs}/I in Eq. (1.5), and relevant topics will be discussed in Chapter 2 of this thesis.

1.1.4 Kerr nonlinearity

The optical Kerr effect is characterized by a change in the refractive index of a material that is directly proportional to the intensity of the incident light. This phenomenon is akin to the Kerr electro-optical effect, where the refractive index change is proportional to the square of an external electric field.

The third-order nonlinear susceptibility, $\chi^{(3)}$, is primarily responsible for this nonlinearity. As discussed in Eq. (1.1), $\chi^{(3)}$ term is the leading term in materials such as SiO_2 and Si_3N_4, and Kerr nonlinearity will be dominant for nonlinear processes in those materials. The refractive index under the influence of the Kerr effect is usually expressed by intensity $I = \frac{1}{2}cn_0\varepsilon_0|\mathbf{E}|^2$ as:

$$n = n_0 + n_2 I, \tag{1.6}$$

where n_2 is the **nonlinear refractive index** .

When two optical waves propagate together in a nonlinear medium, the Kerr effect induces refractive index changes that result in additional frequency components, a process known as four-wave mixing (FWM). FWM is a parametric process where two photons interact with the medium to generate two new photons at different frequencies, given by the relation:

$$\omega_1 + \omega_2 = \omega_3 + \omega_4, \tag{1.7}$$

where ω_1, ω_2, ω_3, and ω_4 are the angular frequencies of the interacting waves. The relation in Eq. (1.7) ensured energy conservation in FWM process. This process is phase-matched, meaning the momentum conservation law is also satisfied, given by the relation:

$$\mathbf{k}_1 + \mathbf{k}_2 = \mathbf{k}_3 + \mathbf{k}_4, \tag{1.8}$$

where $\mathbf{k}_1$, $\mathbf{k}_2$, $\mathbf{k}_3$, and $\mathbf{k}_4$ are the wave vectors of the interacting waves. This requirement is also referred to as **phase-matching condition** since wave-vector $\mathbf{k}$ describes the propagation phase of waves.

The Kerr nonlinearity and FWM play a crucial role in various applications such as optical signal processing, supercontinuum generation, and wavelength conversion. Leveraging Kerr nonlinearity in optical microresonators can develop different types of optical frequency combs with applications in precision metrology, spectroscopy, and frequency synthesizing. Those relevant topics will be discussed in the following chapters.

1.2 Optical resonator

1.2.1 Introduction

Optical resonators, also known as optical cavities, are structures that confine light within a certain volume through optical circulation. These structures are essential components in various optical systems, including lasers, optical filters, sensors, and especially in compact optical frequency comb systems. The configurations of optical resonators include Fabry-Pérot cavities, ring resonators, whispering gallery mode resonators, and photonic crystal cavities. Fabry-Pérot cavities consist of two parallel mirrors, creating a standing wave pattern between them. Ring resonators guide light in a circular path, often used in integrated photonics for their compactness and high quality. Whispering gallery mode resonators confine light via continuous total internal reflection along the optical circulation. Photonic crystal cavities use periodic dielectric structures to create bandgaps, confining light in defect regions.

Optical resonators support different types of modes, primarily categorized into transverse modes and longitudinal modes. **Transverse modes** refer to the spatial distribution of the electromagnetic field in the plane perpendicular to the direction of propagation. These modes are defined by the boundary conditions imposed by the resonator's geometry. Examples of different transverse modes include transverse electric (TE) mode and transverse magnetic (TM) mode, representing different

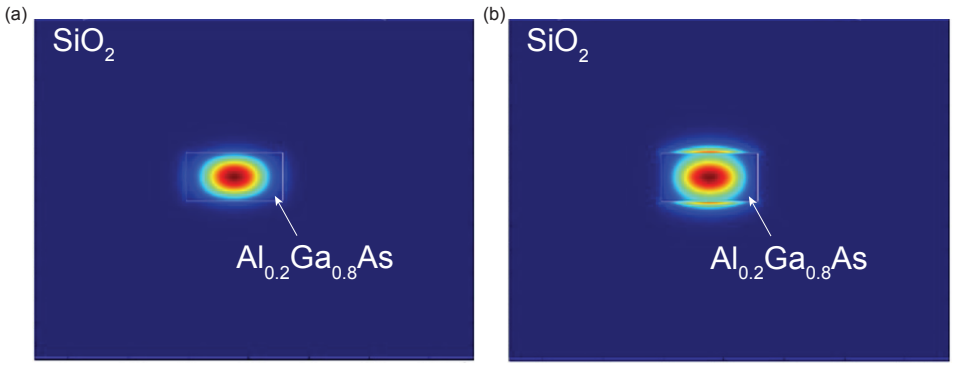

Figure 1.1: **Mode profiles of different transverse modes.** Mode profiles of $TE_{0,0}$ mode (panel a) and $TM_{0,0}$ mode (panel b) in an $Al_{0.2}Ga_{0.8}As$ integrated waveguide at 1550 nm.

directions of the electric and magnetic field components relative to the plane of propagation. Different transverse modes have different **mode profile**s along the plane perpendicular to the propagation direction. Examples of fundamental TE (or $TE_{0,0}$) mode and fundamental TM (or $TM_{0,0}$) mode profiles are shown in Fig. 1.1 [3]. Here, the two numbers in the subscript denote the number of nodes along two directions in the mode profile. When the number of nodes along one direction can only be 0, the corresponding number can sometimes be omitted (for example, TE_0, TE_1, TM_0) as long as it does not cause any confusion.

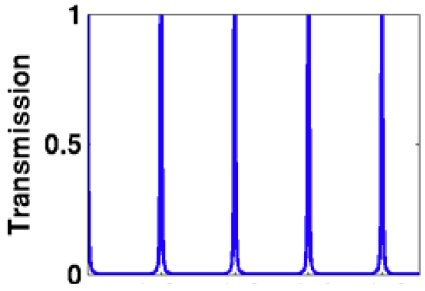

Figure 1.2: **Transmission spectrum of different longitudinal modes.** The frequency distance between two longitudinal modes is the local free-spectral-range. The modes are not strictly equal distant due to chromatic dispersion, which lead to mode dispersion and will be discussed in Section 1.2.2.

Another type of mode, **longitudinal modes**, represents the distribution of the electromagnetic field along the direction of propagation within the resonator. A series of longitudinal modes belonging to the same transverse mode is called a **(longitudinal) mode family**. Examples of the frequencies of a series of (longitudinal) mode family is shown in Fig. 1.2 Longitudinal modes arise due to the constructive interference

of light that circulates within the resonator. This interference condition is met when the round-trip phase shift of the circulating light is an integer multiple of 2π, formulated as Eq. (1.18). This integer m is called the **(absolute) mode number** of this longitudinal mode, whose angular frequency is denoted as ω_m. The frequency spacing between adjacent longitudinal modes is known as the **free spectral range (FSR** , or $D_1/2\pi$) of the resonator, with a unit of Hz. FSR is also related to the round trip time of an optical pulse, and it can be calculated using Eq. (1.20).

1.2.2 Mode dispersion

It should be noted that due to the **chromatic dispersion** (the refractive index n varies with the wavelength λ of the light) of the propagation medium, the FSR will change slightly across different wavelengths. In other words, chromatic dispersion will lead to **mode dispersion** causing ω_m can not be simply represented by $2\pi m \times \text{FSR}$.

To address this issue, ω_m is usually represented by power series around a chosen longitudial mode ω_{m_0}. Define **relative mode number** $\mu = m - m_0$ and use relative mode number as the subscript in the following discussion for convenience (for example, ω_{m_0} will be represented as ω_0), we can write,

$$\omega_\mu = \omega_0 + D_1\mu + \frac{1}{2}D_2\mu^2 + \frac{1}{6}D_3\mu^3 + \cdots, \tag{1.9}$$

where $D_1/2\pi$ is the **FSR of this (longitudinal) mode family at** ω_0, D_2 is the **second order dispersion of this mode family at** ω_0. Higher-order dispersions can be defined subsequently. It should be noted that D_1, D_2, *etc.* are local parameters and need to specify the angular frequency ω_0 when they are referenced. Those mode dispersions (D_2, D_3, *etc.*) play a critical role in nonlinear optical processes that happen in the resonator, such as frequency comb generation, parametric oscillation, harmonics generation, and soliton formation.

To clearly illustrate the mode dispersions in a resonator, we define **integrated dispersion** (sometimes also called retarded mode frequency or slow frequency) as

$$\omega_{\mu,\text{int}} = \omega_\mu - \omega_0 - D_1\mu \tag{1.10}$$

$$= \sum_{n=2}^{\infty} \frac{D_n}{n!}\mu^n, \tag{1.11}$$

and the plot between $\omega_{\mu,\text{int}}$ versus μ is called **dispersion profile** of this mode family. examples of dispersion profile is shown in Fig. 1.3 [4]. The dispersion profile of a mode family clearly illustrates the deviations from the ideal linear behavior (represented by D_1) and highlights the contributions of higher-order dispersions (D_2, D_3, *etc.*). These deviations are critical for understanding and controlling nonlinear optical processes within the resonator.

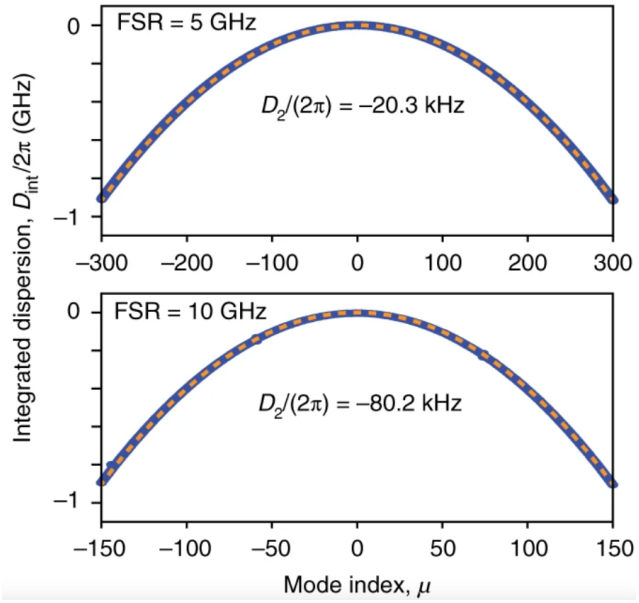

Figure 1.3: **An example of dispersion profile** (a plot between integrated dispersion and relative mode number) **for two ultra-low-loss Si_3N_4 resonators with different FSRs.** It should be noted that dispersion profile is a scattered plot where relative mode number μ can only take integer values.

Managing and engineering these dispersions enable precise control over the resonator's nonlinear dynamics and are pivotal in developing advanced photonic devices. Relevant topics will be discussed in Chapters 3 and 4 of this thesis.

1.2.2.1 Integrated (angular) frequency with respect to D_1

As an additional note, $\omega_{\mu,\text{int}}$ is the **integrated angular frequency** (or retarded angular frequency) of ω_μ with respect to D_1. For an arbitrary angular frequency ω (not limited to mode frequencies ω_μ), we can also define its integrated angular frequency ω_{int} with respect to D_1. This process is effectively mapping 1-dimensional ω axis to a 2-dimensional μ-ω_{int} plane, where ω_{int} can only take values within an interval with a range of D_1 and μ can only take integer numbers. The illustration of this mapping process is shown in Fig. 1.4.

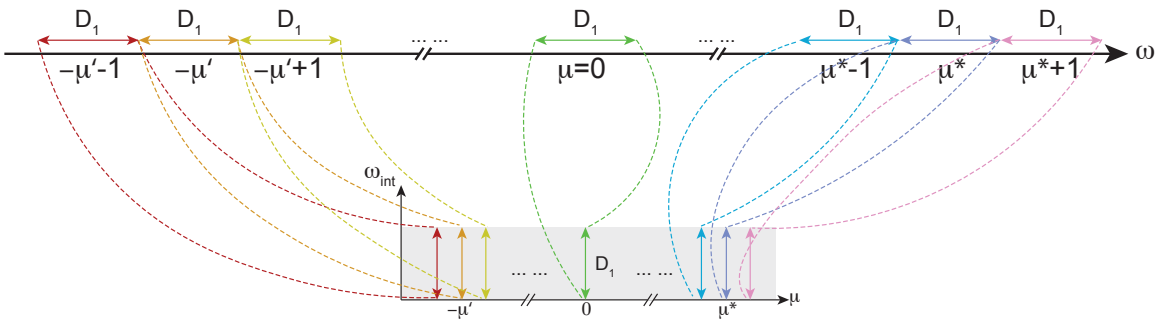

Figure 1.4: **Illustration of mapping between 1-dimensional ω axis to 2-dimensional μ-ω_{int} plane.** On μ-ω_{int} plane, μ only take integer numbers and ω_{int} only take values within an interval with a range of D_1.

The absolute value of ω_{int} is typically not important and its relative value can be represented as $\omega - \mu D_1$.

The mapping shown in Fig. 1.4 will not be one-to-one if ω_{int} takes values out of the range D_1. For example, on μ-ω_{int} plane, point (μ^*,ω^*_{int}) and ($\mu^* - 1$,$\omega^*_{\text{int}} + D_1$) represent the same absolute frequency. To avoid this effect, the values that are out of range D_1 can be "folded" within D_1, as shown in Fig.1(d) of ref. [5].

Further discussions on the physical meaning of ω_{int} when it is outside the range D_1, and its significance in indicating the occurrence of a quasi-phase-matching process in a resonator with broken symmetry, will be presented in Chapter 4 and illustrated in Fig. 4.4.

1.2.3 Relationship between mode dispersion and group-velocity dispersion

In this section, we will review some key concepts related to group-velocity dispersion in fiber optics. Understanding these concepts is crucial for studying optical resonators, as they share similar underlying principles, and have been well studied in fiber optics with well-established measured values. Clarifying their relations with microresonator parameters will be very beneficial for resonator studies. We will begin with the mode propagation constant and its dispersion properties, then examine their relationship to the group index and group-velocity dispersion, and finally discuss how these concepts apply to optical resonators.

1.2.3.1 Mode propagating constant and its dispersion

In fiber optics, the propagation of electro-magnetic waves are confined by fiber, thus the wavevectors **k** are often simplified to **mode-propogating constant** β defined by

$$\beta = n\frac{\omega}{c}, \tag{1.12}$$

where c is the speed of light. The power series of Eq. (1.12) around an angular frequency ω_0 can be written as

$$\beta(\omega) = \beta_0 + \beta_1(\omega - \omega_0) + \frac{1}{2}\beta_2(\omega - \omega_0)^2 + \cdots . \tag{1.13}$$

It should be noted that, in Eq. (1.9), the coefficients D_1, D_2, *etc.* describe the property of a resonator and can have different values for two resonators even if they are made from the same material. The β_0, β_1, *etc.* values in Eq. (1.13) describe the property of a material because they are solely dependent on the chromatic dispersion $n(\omega)$ in Eq. (1.12). The values of β_0, β_1, *etc.* are often available in Scientific Handbooks for many commonly used photonic materials. Additionally, β_0, β_1, *etc.* are also local parameters and need to specify the angular frequency ω_0 when they are referenced.

1.2.3.2 β_1 parameter and group index n_g

In Eq. (1.13), mode-propogating constant at ω_0 is $\beta_0 = n\omega_0/c$, and

$$\beta_1 = \left(\frac{\mathrm{d}\beta}{\mathrm{d}\omega}\right)_{\omega=\omega_0} = \frac{1}{v_g} = \frac{n_g}{c}, \tag{1.14}$$

where v_g is the **group velocity**, n_g is the **group index**. With Eq. (1.12) and the definition of n_g in Eq. (1.14), we can see that in principle, n_g can be negative (leading to $v_g < 0$) [6]. For the materials we commonly work with, we do not have negative group velocities. Thus in the following discussion, we only consider cases when $n_g > 0$.

Group index n_g is also a useful parameter to characterize the refractive index change over different frequencies. Here, we further derive some useful equations related to n_g. With Eqs. (1.12) and (1.14), we have

$$\beta_1 = \left(\frac{\mathrm{d}\beta}{\mathrm{d}\omega}\right)_{\omega=\omega_0} = \frac{1}{c}\left(\frac{\mathrm{d}(n\omega)}{\mathrm{d}\omega}\right)_{\omega=\omega_0} = \frac{1}{c}\left(\frac{\omega\mathrm{d}n + n\mathrm{d}\omega}{\mathrm{d}\omega}\right)_{\omega=\omega_0} = \frac{n_g}{c}.$$

Therefore by fully expanding the above equation, we can get the relationship between n_g and the refractive index change $\mathrm{d}n$ when the angular frequency changes $\mathrm{d}\omega$ by [2]

$$\frac{\mathrm{d}n}{n_g - n} = \frac{\mathrm{d}\omega}{\omega} = -\frac{\mathrm{d}\lambda_{\mathrm{vac}}}{\lambda_{\mathrm{vac}}} = -\frac{n}{n_g}\frac{\mathrm{d}\lambda_{\mathrm{med}}}{\lambda_{\mathrm{med}}}, \tag{1.15}$$

where λ_{vac} is the corresponding light's wavelength in vacuum, $\lambda_{\mathrm{med}} = \lambda_{\mathrm{vac}}/n$ is the wavelength in medium.

1.2.3.3 Group velocity dispersion parameter β_2

Additionally, for β_2 in Eq. (1.13), we have

$$\beta_2 = \left(\frac{\mathrm{d}^2\beta}{\mathrm{d}\omega^2}\right)_{\omega=\omega_0} = \left(\frac{\mathrm{d}\beta_1}{\mathrm{d}\omega}\right)_{\omega=\omega_0}, \tag{1.16}$$

and this term represents the variation of the group velocity with respect to frequency.

Physically speaking, the envelope of an optical pulse travels at the group velocity v_g, with the parameter β_2 representing the dispersion of this group velocity, leading to pulse broadening. This effect is known as **group-velocity dispersion (GVD)**, and β_2 is the **GVD parameter**, with unit of $\mathrm{ps}^2/\mathrm{km}$.

In practice, another dispersion parameter d_2 in unit of ps/(km·nm), representing two closely aligned wavepackets with wavelength difference $\mathrm{d}\lambda$ (in unit of nm) walks off in time (in unit of ps) after propagating 1 kilo-meter due to their different propagation speed. Formalized as

$$d_2 = \lim_{\mathrm{d}\lambda\to 0}\frac{\beta_1(\lambda+\mathrm{d}\lambda) - \beta_1(\lambda)}{\mathrm{d}\lambda} = \frac{\mathrm{d}\beta_1}{\mathrm{d}\omega}\frac{\mathrm{d}\omega}{\mathrm{d}\lambda} = -\frac{2\pi c}{\lambda^2}\beta_2. \tag{1.17}$$

1.2.3.4 Relationship to mode dispersion

In optical resonator, the propagating constant β of mode with absolute mode number m should satisfy

$$\beta L = 2\pi m \tag{1.18}$$

[2]Note that the second equality in Eq. (1.15) can be derived by taking derivation to both sides of $\ln(\omega) = \ln(2\pi c/\lambda_{\mathrm{vac}})$, which gives $\mathrm{d}(\ln\omega) = \mathrm{d}\omega/\omega = -\mathrm{d}(\ln\lambda_{\mathrm{vac}}) = -\mathrm{d}\lambda_{\mathrm{vac}}/\lambda_{\mathrm{vac}}$, as a pure mathematical trick without physical meaning. Similarly, the third equality in Eq. (1.15) can be verified by taking the total derivation of $\ln(\lambda_{\mathrm{med}}) = \ln(\lambda_{\mathrm{vac}}/n)$, which gives $\mathrm{d}\lambda_{\mathrm{med}}/\lambda_{\mathrm{med}} = \mathrm{d}\lambda_{\mathrm{vac}}/\lambda_{\mathrm{vac}} - \mathrm{d}n/n$ (also a pure mathematical trick without physical meaning).

to meet the resonant condition.

Sometimes, the parameters β_1 (or n_g) and β_2 of the propagating medium within the optical resonator can be found in reference handbooks. Then the FSR (or $D_1/2\pi$) and mode dispersion parameter D_2 can be calculated from β_1 and β_2. Take ω in Eq. (1.13) as the frequency of a longitudinal mode with relative mode number μ, and bring the expression of ω_μ in Eq. (1.9) into Eq. (1.13), we have

$$\begin{aligned}\beta(\omega_\mu) - \beta_0 &= \frac{2\pi\mu}{L} \\ &= \beta_1\left(D_1\mu + \frac{1}{2}D_2\mu^2 + \cdots\right) + \frac{1}{2}\beta_2\left(D_1\mu + \frac{1}{2}D_2\mu^2 + \cdots\right)^2 + \cdots\end{aligned} \tag{1.19}$$

where the $2\pi\mu/L$ is calculated from Eq. (1.18).

Comparing the coefficients before μ and μ^2 in Eq. (1.19), we have: (used definition of n_g in Eq. (1.14), also note FSR=$D_1/2\pi$)

$$D_1 = \frac{2\pi}{\beta_1 L} = \frac{2\pi c}{n_g L}, \tag{1.20}$$

with a unit of rad·s^{-1}. And

$$D_2 = -\frac{\beta_2 D_1^2}{\beta_1} = -c\frac{\beta_2 D_1^2}{n_g}. \tag{1.21}$$

Alternatively, Eq. (1.13) (can be interpreted as $\mathbf{k}(\omega)$) is related to the inverse series of Eq. (1.9) (related to $\omega(\mathbf{k})$, where $\mathbf{k}$ solely depend on m by Eq. (1.18)), thus the relations in Eqs. (1.20) and (1.21) can also be derived by calculating series reversion coefficients[3]. Higher-order dispersion parameters (D_3, D_4, *etc.*) can be calculated similarly.

It should be noted that the index appeared in Eqs. (1.20) and (1.21) are group index n_g instead of the phase index n. This fact is especially important when dealing with materials like $Al_xGa_{1-x}As$, whose n_g and n differ by 2.5% at vacuum wavelength $1.55\mu m$ when x = 0.21 [7].

[3]Conveniently, this can be calculated with `InverseSeries` function in Wolfram Mathematica.

1.2.4 Momentum conservation of FWM in optical resonator

Similar to fibers, the propagation direction of electro-magnetic waves in optical resonator is also confined. Thus it makes sense to use mode-propogating constant β defined in Eq. (1.12) (or equivalently use mode number m in Eq. (1.18)) to represent wave vector $\mathbf{k}$. Then the momentum conservation requirement in Eq. (1.8) can be written as

$$\begin{aligned} \beta_{0,m_1} + \beta_{0,m_2} &= \beta_{0,m_3} + \beta_{0,m_4}, && \text{or} \\ n_{m_1}\omega_{m_1} + n_{m_2}\omega_{m_2} &= n_{m_3}\omega_{m_3} + n_{m_4}\omega_{m_4}, && \text{or} \\ m_1 + m_2 &= m_3 + m_4, && (1.22) \end{aligned}$$

where m_1, m_2, m_3 and m_4 are the absolute mode numbers of the interacting waves. Here, we do not consider the case when the interacting waves are counter-propogating in the resonator against each other. This equation posed requirements to achieve an efficient FWM process. Under different situations, one form of expression in Eq. (1.22) will be adapted to represent the momentum conservation (phase matching) condition.

The momentum conservation requirement for other nonlinear processes such as harmonic generation and parametric oscillation can be written similarly.

Note that for degenerated FWM in optical resonator, where $m_3 = m_4 = m$, $\omega_3 = \omega_4 = \omega$, the condition in Eq. (1.7) and (1.22) expressed in terms of relative mode number μ by

$$\begin{aligned} 2\omega &= \omega_1 + \omega_2, && \text{and} \\ 2\mu &= \mu_1 + \mu_2, && (1.23) \end{aligned}$$

where ω, ω_1, ω_2 are the angular frequencies of interacting waves. The requirement in Eq. (1.23) can be easily represented in terms of integrated angular frequency plot (as illustrated in the lower panel of Fig. 1.4) by identifying the point $(\mu, \omega - \mu D_1)$ is the mid-point between $(\mu_1, \omega_1 - \mu_1 D_1)$ and $(\mu_2, \omega_2 - \mu_2 D_1)$.

1.2.5 Normal dispersion and anomalous dispersion

Dispersion refers to the frequency dependence of various properties. Common examples include refractive index dispersion, which causes prisms to separate white

light into its constituent colors, and focal length dispersion in lenses, leading to chromatic aberration.

Normal and anomalous dispersion describes the frequency dependence of the group index n_g (not the phase index n). Dispersion is termed normal if n_g increases with angular frequency and anomalous if n_g decreases with angular frequency. The transition points between these regimes are the zero-dispersion points. For instance, the normal and anomalous dispersion regimes for fused silica are illustrated in Fig. 1.5 [1].

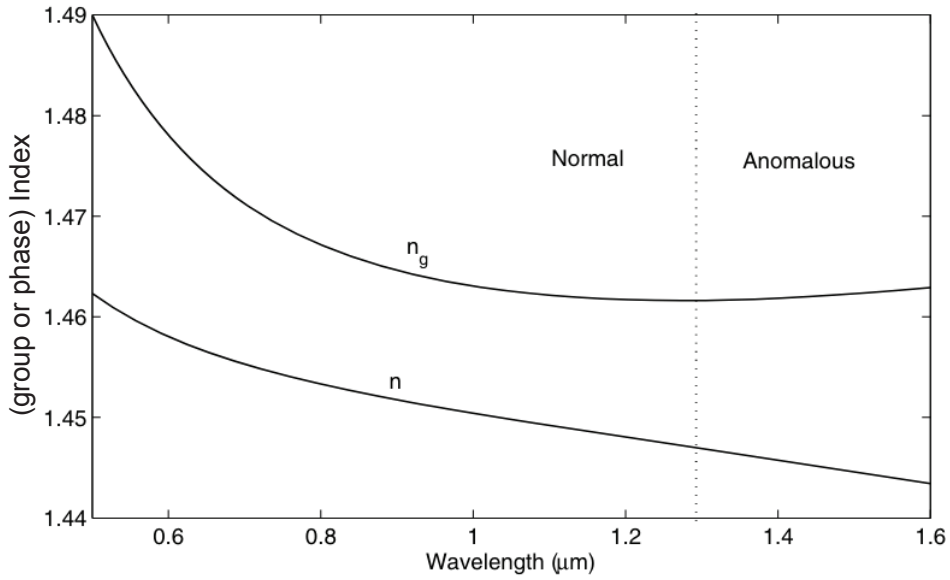

Figure 1.5: **Dependence of the refractive index (n) and group index (n_g) on vacuum wavelength for fused silica.** It should be noted that the dispersion is normal or anomalous is determined by whether n_g is decreasing or increasing over wavelength, not phase index n.

When the dispersion is normal, $\frac{\mathrm{d}n_g}{\mathrm{d}\omega} > 0$. According to Eqs. (1.14), (1.16), and (1.21), this implies $\beta_2 > 0$ and $D_2 < 0$. Note that D_2 is also related to the curvature of the dispersion profile ($\omega_{\mu,\mathrm{int}}$ versus μ plot) as defined in Eq. (1.11). Table 1.1 summarizes the relationships between these parameters for normal and anomalous dispersion, highlighting how to identify the dispersion properties of optical resonators. For example, both dispersion profiles shown in Fig. 1.3 has negative curvature (concave down) at $\mu = 0$, therefore both resonators in Fig. 1.3 feature normal dispersion at $\mu = 0$.

Identifying dispersion parameters is crucial for the design and optimization of optical systems. The nonlinear behavior of light in optical resonators is significantly

Table 1.1: Summary of values for normal and anomalous dispersion (when $n_g > 0$). Examples of normal dispersion are shown in Figs. 1.3 and D.4(b). Examples of anomalous dispersion are shown in Figs. D.1(b) and Fig. D.2(b).

Dispersion Type	$\frac{\mathrm{d}n_g}{\mathrm{d}\omega}$	β_2	D_2	Dispersion Profile Curvature
Normal Dispersion	$\frac{\mathrm{d}n_g}{\mathrm{d}\omega} > 0$	$\beta_2 > 0$	$D_2 < 0$	Negative (Concave Down)
Anomalous Dispersion	$\frac{\mathrm{d}n_g}{\mathrm{d}\omega} < 0$	$\beta_2 < 0$	$D_2 > 0$	Positive (Concave Up)

influenced by the type of dispersion present. Normal and anomalous dispersion affect pulse propagation and the process of optical soliton generation. The technique of manipulating the dispersion profile in optical resonators to generate optical bright soliton will be discussed in Chapter 3 of this thesis.

1.2.6 Quality of the resonator

1.2.6.1 Resonator-environment interaction

In the following sections, we focus on the behavior of a single resonator mode rather than discussing the properties of a mode family. As discussed earlier, the absolute angular frequency ω_0 of a mode can be determined by Eqs. (1.12) and (1.18). However, in practical scenarios, the resonator interacts with the environment, causing the mode to resonate within a bandwidth around ω_0 rather than at a single frequency. A high-quality resonator exhibits minimal interaction with the environment, and this interaction extent is critical in describing the resonator's quality.

Another way to interpret this excitation bandwidth is through mode coupling. The coupling between the resonator mode and the environmental heat bath creates new eigenmodes, which comprise components from both the environment and the resonator. These new eigenmodes form a spectrum around the original angular frequency ω_0. For angular frequencies near but not exactly at ω_0, if the mode coupling is strong, the eigenmodes will have a higher composition from the resonator, making it easier to excite the resonator at these frequencies. Conversely, if the mode coupling is weak, the resonator's contribution to the eigenmodes is low, making it harder to excite the resonator at angular frequencies away from ω_0. Phenomenally, stronger (weaker) resonator-environment interaction, or lower (higher) resonator quality, results in a larger (smaller) excitation bandwidth. This excitation bandwidth can be characterized by the **linewidth of a mode**, as shown in Fig.1.6(a)[8].

This resonator-environment interaction is also usually[4] simplified to a **total dissipation rate** (or **total coupling rate**), κ, which is a real positive constant ($\kappa \in \mathbb{R}_+$) in unit of rad $\cdot$ s^{-1}, representing the fraction of intracavity energy lost to the environment per unit time. Using this definition, the dynamic of intracavity energy can be represented as

$$\frac{\mathrm{d}|a|^2}{|a|^2} = -\kappa \mathrm{d}t, \tag{1.24}$$

where $|a|^2$ is the intracavity energy of the resonator in unit of J, t represents time in unit of Second (s). Definition of a will be introduced in Eq. (1.33). Furthermore, κ is the excitation bandwidth (or **linewidth of a mode**) we discussed before, which will also be introduced in Section 1.2.8.2, Eq. (1.62).

Using the relation in Eq. (1.24), κ can be measured with a "ring-down" experiment, as shown in Fig. 1.6(b) [8], where the intracavity energy in unit of Joule (J) is measured as a function of time. Other ways to measure κ will also be introduced in Section 1.2.8.2.

In practice, people also model the loss as propagation loss σ, in unit of dB$\cdot$ m^{-1}. The fraction of energy remaining after the wave packet propagates a distance z is given [5] by $\mathrm{e}^{-\frac{z}{c/n_g}\kappa}$. Therefore, σ is related to κ by

$$\sigma = \frac{1}{z} 10 \cdot \log_{10}\left(\frac{1}{\mathrm{e}^{-\frac{z}{c/n_g}\kappa}}\right) = \frac{10}{\ln(10)} \cdot \frac{n_g \kappa}{c} \approx 4.343 \frac{n_g}{c}\kappa, \tag{1.25}$$

where ln represents $\log_\mathrm{e}$.

1.2.6.2 Intrinsic and external coupling

Additionally, different types of resonator-environment interactions contribute to κ. To probe the resonator, we deliberately interact with it. This part of the interaction,

[4] This simplification is particularly useful when we study ring resonator and whispering gallery mode resonator, where the commonly used concept of transmission and reflection in Fabry-Pérot cavity is not suitable. Resonators that are suitable for this simplification have a Lorentzian resonance lineshape, which will be further discussed in Section 1.2.8.2. Resonators that are not suitable for this simplification (for example, Fabry-Pérot cavity) may have other lineshapes.

[5] The time that wavepacket with power P_in travels through distance dz is $\frac{\mathrm{d}z}{c/n_g}$, therefore the fraction of power that are lost after wavepacket travels through distance dz is $\frac{\mathrm{d}z}{c/n_g}\kappa$. By solving differential equation $\frac{\mathrm{d}P}{P} = -\frac{\mathrm{d}z}{c/ng}\kappa$, we can get $P/P_\mathrm{in} = \mathrm{e}^{-\frac{z}{c/n_g}\kappa}$. The amount of loss after travelling distance of z (expressed in dB number) is $10 \cdot \log_{10}(P_\mathrm{in}/P)$, leading to the result in Eq. (1.25).

which does not describe the resonator's intrinsic quality, is separated from κ and defined as the **external dissipation rate** (or **external coupling rate**), κ_e. The remaining part is the **intrinsic dissipation rate** (or **intrinsic coupling rate**), κ_0, which accounts for the resonator's inherent interaction with the environment. This intrinsic dissipation rate is crucial for calibrating the resonator's quality. Mathematically,

$$\kappa = \kappa_0 + \kappa_e \tag{1.26}$$

satisfies. κ, κ_0 and κ_e all positive real constants ($\in \mathbb{R}_+$).

Among the intrinsic resonator-environment interactions, several types of interactions are involved. Scattering loss can be mitigated by improving surface roughness and fabrication techniques, while absorption loss, which transfers optical energy to heat, poses a fundamental limit to the material's performance. By leveraging thermo-optic nonlinearity, it is possible to isolate absorption loss from other intrinsic losses, which will be discussed in Chapter 2.

1.2.6.3 Quality (Q) factor

The quality of a resonator is often quantified by unitless Q-factor (quality factor), which is related to the fraction of energy loss per optical oscillaton cycle [6]. Mathematically, the Q-factors are defined as:

$$Q_0 = \frac{\omega_0}{\kappa_0}, \tag{1.27}$$

$$Q_e = \frac{\omega_0}{\kappa_e}, \tag{1.28}$$

$$Q = \frac{\omega_0}{\kappa}, \tag{1.29}$$

where Q is the **total quality factor** (or **loaded quality factor**), Q_0 is the **intrinsic quality factor**, and Q_e is the **external quality factor**.

Rewriting the relation in Eq. (1.26) in terms of Q-factors, we have:

$$\frac{1}{Q} = \frac{1}{Q_0} + \frac{1}{Q_e}. \tag{1.30}$$

[6] Generally, Q-factor is defined as $Q = 2\pi \frac{\text{stored energy}}{\text{energy loss per oscillation cycle}}$. This can be further derived to Eq. (1.29) by $Q = 2\pi \frac{1}{\kappa \cdot (1/f)}$, where $f = \omega/2\pi$.

The intrinsic Q_0 reflects the resonator's inherent losses, while the external Q_e represents losses due to external coupling that is deliberately applied to probe the resonator. High Q-factor is equivalent to low dissipation rate (κ) and narrow resonance bandwidth, which is favored in many applications.

1.2.6.4 Finesse

Another unitless number $\mathscr{F}$, or **finesse**, is also used to quantify the quality of the resonator. Adapting a similar idea as Q-factor, which relates to energy loss per optical oscillation cycle, $\mathscr{F}$ relates to energy loss per resonator round trip. $\mathscr{F}$ is defined using the full-width at half-maximum (FWHM) $\delta\nu_{\mathrm{FWHM}}$ of the resonance[7], thus may have different mathematical forms for resonators with different lineshape[8]. For the resonators that are suitable for the simplification in Eq. (1.24) (with Lorentzian resonance lineshape), we have

$$\mathscr{F} = \frac{\mathrm{FSR}}{\kappa/2\pi}. \tag{1.31}$$

Intrinsic and external finesse can be defined similarly as Eqs. (1.27) and (1.28).

1.2.7 Characteristics of mode and its resonance angular frequency

In this section[9], we will study the mode profile of transverse modes in optical resonator, when the resonator is consisted of heterogeneous structures with spatially varying refractive index $n(r, \theta, z)$. Here (r, θ, z) is the cylindrical coordinate[10] with the value of $r \in [0, +\infty)$, $\theta \in [0, 2\pi)$ and $z \in \mathbb{R}$. Then study its resonant angular frequency ω_0 and how ω_0 is changed when spatially-varying refractive index has a pertubation Δn. Finally we will define mode volume of the transverse mode, which is important in nonlinear optics to calculate energy density.

1.2.7.1 Helmholtz equation

We start with the Helmholtz equation for a single-mode within the resonator,

$$-\nabla \times \nabla \times \tilde{\mathbf{E}}(\mathbf{r}, \omega_0) + \frac{n^2\omega_0^2}{c^2}\tilde{\mathbf{E}}(\mathbf{r}, \omega_0) = 0, \tag{1.32}$$

[7] Generally, finesse is defined as $\mathscr{F} = \mathrm{FSR}/\delta\nu_{\mathrm{FWHM}}$.

[8] For example, $\mathscr{F}$ for Fabry-Pérot cavities has a different form than Eq. (1.31).

[9] The contents in Section 1.2.7 are mainly adapted from the Supplementary Information of ref. [2]. The main text contents of ref. [2] will be discussed in Chapter 2 of this thesis.

[10] We focus on ring resonators or whisper-gallery resonators with azimuthal symmetry in this section.

where $\tilde{\mathbf{E}}$ is the (real) modal electric field, c is the vacuum speed of light, and ω_0 is the resonance angular frequency. For convenience, $\tilde{\mathbf{E}}$ can be expressed as a phasor,

$$\tilde{\mathbf{E}} = \frac{1}{2}\mathbf{E} + \text{c.c.}, \quad \mathbf{E} = a\mathbf{F}(r, \theta, z)e^{-i\omega_0 t}, \tag{1.33}$$

where a is the complex mode amplitude and $\mathbf{F}$ is the field distribution. For $|a|^2 = a \cdot a^*$ (defined in Eq. (1.24)) to represent the optical energy stored in the mode, the normalization for $\mathbf{F}$ reads [11]

$$\frac{\varepsilon_0}{2}\int n^2|\mathbf{F}|^2 \mathrm{d}V = 1, \tag{1.34}$$

where $|\mathbf{F}|^2 \equiv \mathbf{F} \cdot \mathbf{F}^*$ and the volume integral goes over the entire resonator. Here we assume that the modal field is sufficiently localized so convergence problems associated with quasimodes can be neglected.

The field distribution $\mathbf{F}$ can be further represented as

$$\mathbf{F}(r, \theta, z) = \mathbf{f}(r, z)\mathrm{e}^{im\theta}, \tag{1.35}$$

where $\mathbf{f}(r, z)$ represents the transverse mode profile shown in Fig. 1.1, $\mathrm{e}^{im\theta}$ represents the longitudinal mode order shown in Fig. 1.2. Any additional constant phases in Eq. (1.33) can be absorbed in a.

1.2.7.2 Resonance angular frequency and its variation

For the Helmholtz equation Eq. (1.32), ω_0^2 can be expressed in its variational form:

$$\omega_0^2 = c^2 \frac{\int |\nabla \times \mathbf{F}|^2 \mathrm{d}V}{\int n^2|\mathbf{F}|^2 \mathrm{d}V}. \tag{1.36}$$

For a slight change in refractive index Δn that is applied externally, the perturbed eigenfrequency can be written similarly as:

$$(\omega_0 + \Delta\omega_0)^2 = c^2 \frac{\int |\nabla \times \mathbf{F}|^2 \mathrm{d}V}{\int (n' + \Delta n)^2 |\mathbf{F}|^2 \mathrm{d}V}, \tag{1.37}$$

where the field $\mathbf{F}$ can be regarded as not changing up to first order of Δn, and n' is the refractive index at the new eigenfrequency $\omega_0 + \Delta\omega_0$ to take account of the chromatic dispersion of the material. Using Eq. (1.15), n' can be expanded as

$$n' \approx n + \frac{\partial n}{\partial \omega}\Delta\omega_0 = n + (n_g - n)\frac{\Delta\omega_0}{\omega_0}. \tag{1.38}$$

[11] Eq. (1.34) is derived by calculating volume integration of energy density $\frac{1}{2}\varepsilon|\mathbf{E}|^2$, where ε is replaced by Eq. (1.2).

By expanding Eq. (1.37) up to first order in Δn, and use the expression of ω_0 in Eq. (1.36), we can obtain

$$\begin{aligned}\frac{1}{(\omega_0+\Delta\omega_0)^2} &\approx \frac{\int n^2|\mathbf{F}|^2\mathrm{d}V}{c^2\int|\nabla\times\mathbf{F}|^2\mathrm{d}V}+\frac{2\int\left[n(n_g-n)\Delta\omega_0/\omega_0\right]|\mathbf{F}|^2\mathrm{d}V}{c^2\int|\nabla\times\mathbf{F}|^2\mathrm{d}V}+\frac{2\int n\Delta n|\mathbf{F}|^2\mathrm{d}V}{c^2\int|\nabla\times\mathbf{F}|^2\mathrm{d}V}\\ &= \frac{1}{\omega_0^2}-\frac{2}{\omega_0^2}\frac{\Delta\omega_0}{\omega_0}+2\frac{\Delta\omega_0}{\omega_0}\frac{\int nn_g|\mathbf{F}|^2\mathrm{d}V}{c^2\int|\nabla\times\mathbf{F}|^2\mathrm{d}V}+\frac{2\int n\Delta n|\mathbf{F}|^2\mathrm{d}V}{c^2\int|\nabla\times\mathbf{F}|^2\mathrm{d}V}\\ &\approx \frac{1}{(\omega_0+\Delta\omega_0)^2}+\frac{2}{c^2\int|\nabla\times\mathbf{F}|^2\mathrm{d}V}\left(\frac{\Delta\omega_0}{\omega_0}\int nn_g|\mathbf{F}|^2\mathrm{d}V+\int n\Delta n|\mathbf{F}|^2\mathrm{d}V\right).\end{aligned} \tag{1.39}$$

Therefore the $\Delta\omega_0$ can be solved as,

$$\frac{\Delta\omega_0}{\omega_0}=-\frac{\int n\Delta n|\mathbf{F}|^2\mathrm{d}V}{\int nn_g|\mathbf{F}|^2\mathrm{d}V}. \tag{1.40}$$

1.2.7.3 Kerr nonlinearity perturbation and effective mode volume

Here we consider a special case when Δn in Eq. (1.40) is contributed by Kerr nonlinearity discussed in Section 1.1.4. In this case, the local refractive change induced by the Kerr nonlinearity for an isotropic material has the form

$$\Delta n=n_2 I=n_2\frac{\varepsilon_o cn}{2}|\mathbf{E}|^2, \tag{1.41}$$

where n_2 is the nonlinear index associated with n. Note here the resonator we discuss has spatially varying structure, including refractive index $n(r,\theta,z)$ and Kerr coefficient $n_2(r,\theta,z)$. Substituting Δn into Eq. (1.40), we have

$$\frac{\Delta\omega_0}{\omega_0}=-\frac{\varepsilon_o c}{2}|a|^2\frac{\int n^2n_2|\mathbf{F}|^4\mathrm{d}V}{\int nn_g|\mathbf{F}|^2\mathrm{d}V}. \tag{1.42}$$

To gain insight to the expression in Eq. (1.42), we separate it into three terms (normalization relation in Eq. (1.34) is used) [12]. We define the weighted nonlinear

[12]The explicit formalism of this separation to Eq. (1.42) is

$$\frac{\Delta\omega_0}{\omega_0}=-c|a|^2\left(\frac{\int n^2n_2|\mathbf{F}|^4\mathrm{d}V}{\int n^2|\mathbf{F}|^4\mathrm{d}V}\right)\left(\frac{\int n^2|\mathbf{F}|^4\mathrm{d}V}{\underbrace{\left(\int n^2|\mathbf{F}|^2\mathrm{d}V\right)}_{=\frac{2}{\varepsilon_0}}\left(\int|\mathbf{F}|^2\mathrm{d}V\right)}\right)\left(\frac{\int|\mathbf{F}|^2\mathrm{d}V}{\int nn_g|\mathbf{F}|^2\mathrm{d}V}\right).$$

index,

$$\overline{n_2} = \frac{\int n^2 n_2 |\mathbf{F}|^4 \mathrm{d}V}{\int n^2 |\mathbf{F}|^4 \mathrm{d}V}, \tag{1.43}$$

the effective mode volume,

$$V_{\text{eff}} = \frac{\int n^2 |\mathbf{F}|^2 \mathrm{d}V \int |\mathbf{F}|^2 \mathrm{d}V}{\int n^2 |\mathbf{F}|^4 \mathrm{d}V}, \tag{1.44}$$

and the weighted index product,

$$\overline{nn_g} = \frac{\int n n_g |\mathbf{F}|^2 \mathrm{d}V}{\int |\mathbf{F}|^2 \mathrm{d}V}. \tag{1.45}$$

Using these relations, the eigenfrequency shift in Eq. (1.42) can be expressed as

$$\Delta\omega_0 = -\frac{\omega_0 c \overline{n_2}}{\overline{nn_g} V_{\text{eff}}} |a|^2 = -\frac{\omega_0 c \overline{n_2}}{\overline{nn_g}} \rho = -g\rho, \tag{1.46}$$

where $\rho = |a|^2 / V_{\text{eff}}$ is the intracavity energy density, g is the **Kerr nonlinear coefficient**[13], which takes the simple form

$$g = \frac{\omega_0 c \overline{n_2}}{\overline{nn_g}}. \tag{1.47}$$

We note that, for resonators made with a single material, the averages in the expression drop out, and we recover the conventional result $g = \omega_0 c n_2 / (n n_g)$.

The fact that there is one appearance of phase index n and one appearance of group index n_g in Eq. (1.47) is particularly important[14] when we deal with materials (for example, $\mathrm{Al_xGa_{1-x}As}$) whose n_g and n can be different by 2.5% [7].

1.2.7.4 Thermal-optics nonlinearity perturbation

Here we consider another special case when Δn in Eq. (1.40) is contributed by Thermal-optics nonlinearity discussed in Section 1.1.3. In this case, the local refractive change induced by temperature change reads

$$\Delta n = n \alpha_T \Delta T, \tag{1.48}$$

[13] In some papers, g may be defined as $-\Delta\omega_0 / |a|^2$, which is equivalent to $g' = g / V_{\text{eff}}$ in our definition. In other papers, g may also have an additional factor of $\hbar\omega_0$ if $|a|^2$ is normalized to photon number instead of energy. $\hbar$ is the reduced Planck constant.

[14] A common mistake is over-simplify Eq. (1.47) to $g = \omega_0 c n_2 / n^2$. This simplification may work under many circumstances. However, it becomes critical when we try to characterize material properties, which will be discussed in Chapter 2 of this thesis.

where $\alpha_T(r,\theta,z)$ and temperature change $\Delta T(r,\theta,z)$ are also spatially varying[15]. Substituting Δn into Eq. (1.40), we have

$$\frac{\Delta\omega_0}{\omega_0} = -\frac{\int n^2\alpha_T\Delta T|\mathbf{F}|^2\mathrm{d}V}{\int nn_g|\mathbf{F}|^2\mathrm{d}V}. \tag{1.49}$$

For later convenience, we define a temperature average with respect to the optical field,

$$\overline{\Delta T} = \frac{\int n^2\alpha_T\Delta T|\mathbf{F}|^2\mathrm{d}V}{\int n^2\alpha_T|\mathbf{F}|^2\mathrm{d}V} \tag{1.50}$$

such that different temperature distributions with equal $\overline{T}$ will induce the same frequency shift:

$$\frac{\Delta\omega_0}{\omega_0} = -\overline{\Delta T}\frac{\int n^2\alpha_T|\mathbf{F}|^2\mathrm{d}V}{\int nn_g|\mathbf{F}|^2\mathrm{d}V}. \tag{1.51}$$

Similar to Eq. (1.5), we calculate the rate of total power loss inducing the temperature change equals

$$P_{\mathrm{abs}} = \frac{1}{2}\varepsilon_o|a|^2\int\kappa_a n^2|\mathbf{F}|^2\mathrm{d}V \tag{1.52}$$

where $\kappa_a(r,\theta,z)$ is the thermal absorption rate. Eq. (1.52) can be written as $P_{\mathrm{abs}} = \overline{\kappa_{\mathrm{a}}}|a|^2$, where the averaged absorption rate reads (Normalization relation in Eq. (1.34) is used)

$$\overline{\kappa_{\mathrm{a}}} = \frac{P_{\mathrm{abs}}}{|a|^2} = \frac{\int\kappa_{\mathrm{a}}n^2|\mathbf{F}|^2\mathrm{d}V}{\int n^2|\mathbf{F}|^2\mathrm{d}V}. \tag{1.53}$$

Now the absorption can be related to cavity resonance shift by [16]

$$\Delta\omega_0 = \left(\frac{\Delta\omega_0}{\overline{\Delta T}}\right)\left(\frac{\overline{\Delta T}}{P_{\mathrm{abs}}}\right)P_{\mathrm{abs}} = \left(\frac{\Delta\omega_0}{\overline{\Delta T}}\right)\left(\frac{\overline{\Delta T}}{P_{\mathrm{abs}}}\right)\overline{\kappa_{\mathrm{a}}}|a|^2 = -\alpha\rho, \tag{1.54}$$

In Eq. (1.54), the first coefficient can be measured from experiment, and the second coefficient can be calculated from thermal simulation. By measuring the

[15]The distribution of $\Delta T(r,\theta,z)$ can be simulated by taking the simulated electrical field distribution $\mathbf{F}$ as the heat source of the thermal diffusion equation:

$$\rho_{\mathrm{m}}C\frac{\partial T}{\partial t} - k\nabla^2 T = \frac{1}{2}\varepsilon_o n^2|a|^2\kappa_a|\mathbf{F}|^2,$$

where ρ_{m} is the mass density in unit of ($\mathrm{kg\cdot m^{-3}}$), k is the Thermal conductivity in unit of ($\mathrm{W\cdot m^{-1}\cdot K^{-1}}$), C is the Heat capacity in unit of ($\mathrm{J\cdot kg^{-1}\cdot K^{-1}}$). The right hand side represents the power density absorbed and κ_a is the absorption rate.

[16]Here the negative sign in front of α is because for most of the materials we work with, the value of $\Delta\omega_0/\overline{\Delta T}$ is negative.

resonance shift $\Delta\omega_0$ under different intracavity power $|a|^2$, we can measure the material absorption rate $\overline{\kappa_\mathrm{a}}$ from Eq. (1.54). Details of this experiment will be discussed in Chapter 2.

Using $\rho \equiv |a|^2/V_\mathrm{eff}$, the **photothermal nonlinear coefficient** α can be calculated as

$$\alpha = -\overline{\kappa_\mathrm{a}}\left(\frac{\Delta\omega_0}{\overline{\Delta T}}\right)\left(\frac{\overline{\Delta T}}{P_\mathrm{abs}}\right)V_\mathrm{eff}. \tag{1.55}$$

1.2.8 Dynamics in an optical resonator

In this section, we give the time-dynamics of complex mode amplitude of the resonator.

1.2.8.1 Linear dynamics of mode amplitude

In this section we give the time dynamics of mode amplitude when the resonator is pumped by an external laser with angular frequency ω_P.

We define slow varying amplitude with optical oscillation angular frequency ω_P as

$$A = a\mathrm{e}^{-i(\delta\omega)t}, \tag{1.56}$$

where the **pump detuning** of the mode is defined as

$$\delta\omega = \omega_0 - \omega_\mathrm{P}. \tag{1.57}$$

Then, the dynamic equation of A reads

$$\frac{\mathrm{d}A}{\mathrm{d}t} = -\left(\frac{\kappa}{2} + i\delta\omega\right)A + \sqrt{\kappa_\mathrm{e}}a_\mathrm{in}, \tag{1.58}$$

where $|a_\mathrm{in}|^2$ is the power input to the external coupling:

$$|a_\mathrm{in}|^2 = P_\mathrm{in}, \tag{1.59}$$

with a unit of Watt (W). Further details of Eq. (1.58) derivation process can be found in Chapter 1.2 of ref. [9] [17].

[17] The A we use is normalized to make sure $|A|^2$ has unit of J and represents optical energy stored in the mode. In Chapter 1.2 of ref. [9], a is normalized to make sure $a^\dagger a$ is photon number operator of the mode. a operator in Chapter 1.2 of ref. [9] is equivalent to $A/\sqrt{\hbar\omega_0}$ in our definition, where $\hbar$ is the reduced Planck constant.

As an additional note, $\delta\omega < 0$ indicates that the pump frequency is higher than the mode frequency, which is known as **blue detuned**. Conversely $\delta\omega > 0$ indicates that pump frequency is lower than the mode frequency and is known as **red detuned**.

1.2.8.2 Lineshape and Q-factor measurement

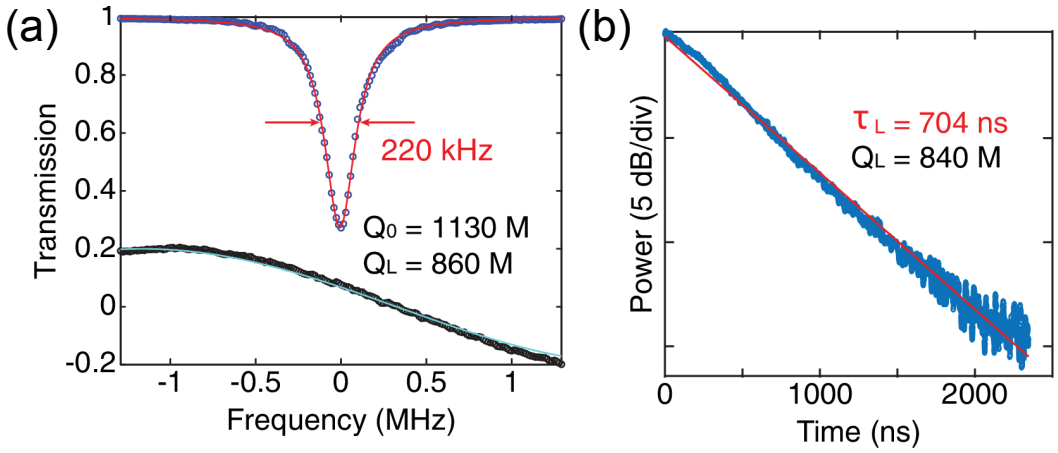

Figure 1.6: **Lorentzian lineshape of a resonance in SiO_2 microresonator, and the respective ring down measurement.** **(a)** Resonance linewidth measurement of a 10 GHz FSR device at 1585 nm. The upper trace is resonance transmission (blue dots) with Lorentzian lineshape fitting (red curve). The linewidth of this mode (as discussed in Section 1.2.6.1) is 220 kHz. The Q-factors are extracted using the methods introduced in Section 1.2.8.2 Eq.(1.61), with a value of intrinsic Q_0=1130 million and loaded (total) Q=860 million. (Note the relation between Q and κ was discussed in Eq.(1.29), M: million). The lower trace is a frequency calibration (black dots) from a Mach–Zehnder interferometer (FSR is 5.979 MHz) with sinusoidal fitting (cyan curve). **(b)** Ring-down measurement (blue) of the mode measured in the left panel. An exponential decay (Eq.(1.24)) fitting is shown in red. Photon lifetime is 704 ns, corresponding to loaded (total) $Q \approx 840$ million.

Measuring the Q-factor, or equivalently measuring dissipation rates κ (as discussed in Section 1.2.6.3), is an important task for resonator quality calibration. We can measure κ by adibatically changing $\delta\omega$ so that $\frac{dA}{dt} \approx 0$, then calculate κ from the lineshape we measured.

Now, we want to know the field amplitude that bypass the resonator after some power is coupled into the resonator. This output field amplitude a_{out} can be calculated with input-output equation[18]

[18] $|a_{\text{out}}|^2$ is also normalized to power, with a unit of Watt (W).

$$a_{\text{out}} = -\sqrt{\kappa_{\text{e}}}A + a_{\text{in}}. \tag{1.60}$$

Therefore under quasi-static frequency tuning condition ($\frac{\mathrm{d}A}{\mathrm{d}t} \approx 0$), the output power $|a_{\text{out}}|^2$ can be solved as

$$\frac{|a_{\text{out}}|^2}{|a_{\text{in}}|^2} = \left| 1 - \frac{\kappa_{\text{e}}}{\frac{\kappa}{2} + i\delta\omega} \right|^2, \tag{1.61}$$

which features a **Lorentzian lineshape**, as shown in Fig. 1.6(a) [8]. The relative value of $\delta\omega$ can be calibrated by a Mach-Zehnder interferometer (MZI). To measure κ and κ_{e}, we can fit the lineshape to Eq. (1.61). However, only two information that are in the lineshape is important, the first one is resonator excitation bandwidth (or FWHM)

$$\delta\omega_{\text{FWHM}} = \kappa, \tag{1.62}$$

and the second one is resonance depth (which is achieved when $\delta\omega = 0$)

$$\left(\frac{|a_{\text{out}}|^2}{|a_{\text{in}}|^2} \right)_{\text{min}} = \left(\frac{\kappa_0 - \kappa_{\text{e}}}{\kappa_0 + \kappa_{\text{e}}} \right)^2 = (1 - 2\eta)^2, \tag{1.63}$$

where $\eta = \kappa_{\text{e}}/\kappa$ is the **coupling efficiency**. Other than fitting the resonance lineshape in Eq. (1.61), we can also solve κ and κ_{e} from Eqs. (1.62) and (1.63).

A critical condition $\min(|a_{\text{out}}/a_{\text{in}}|^2) = 0$ is satisfied when $\kappa_0 = \kappa_{\text{e}} = \kappa/2$. This coupling condition is called **critical coupling**. When $\kappa_0 > \kappa_{\text{e}}$ ($\kappa_0 < \kappa_{\text{e}}$), the coupling condition is called **under (over) coupling**.

It should also be noted that if $(\kappa, \kappa_{\text{e}})=(\kappa', \kappa'_{\text{e}})$ is a solution to Eqs. (1.62) and (1.63), then $(\kappa, \kappa_{\text{e}})=(\kappa', \kappa' - \kappa'_{\text{e}})$ will also be a solution. Thus the lineshape measurement itself cannot distinguish whether the resonator is under-coupled or over-coupled. To further identify the coupling condition, we can apply modulation to a_{in} and measure the demodulated error signal, which has been discussed in ref. [10].

1.2.8.3 Effect of Kerr and thermal-optics nonlinearity on optical resonator

As discussed in Section 1.2.7.3 and 1.2.7.4, the resonance angular frequency ω_0 in Eq. (1.57) will be perturbed by Eqs. (1.46) and (1.54). Therefore, the dynamic equation of Eq. (1.58) will change to

$$\frac{\mathrm{d}A}{\mathrm{d}t} = -\left(\frac{\kappa}{2} + i\left(\delta\omega - (\alpha + g)\rho\right) \right) A + \sqrt{\kappa_{\text{e}}}a_{\text{in}}, \tag{1.64}$$

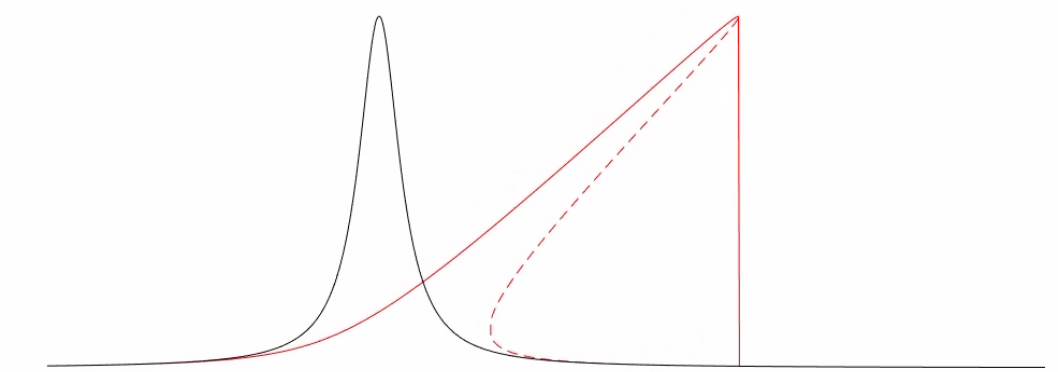

Figure 1.7: **The hysteresis behavior of Lorentzian lineshape with Kerr and thermal-optics nonlinearity.** Kerr and thermal-optics nonlinearity effectively shifts the cold resonance frequency (black line) and creates hysteresis lineshape (red shape).

where $\rho = |A|^2/V_{\text{eff}}$. An important feature of quasi-static solution to Eq. (1.64) is that it has multiple solutions to a at some detuning $\delta\omega$, since Eq. (1.64) is cubic to a. This will lead to a hysteresis behavior of the lineshape, which is represented in Fig. 1.7.

In terms of time scales, Kerr nonlinearity happens almost instantaneously and will appear in the dynamic equation no matter what time scale we study. However, at a time scale much faster than the thermal bandwidth (typically on the order of ms), the thermal-optic nonlinearity does not have any dynamic effect because the nonlinearity mediated by thermal absorption vanishes. This is also the main reason why thermal-optics nonlinearity typically will not lead to any coherent optical effects, as discussed in Section 1.1.3. Here we define a **thermal response function** $\widetilde{r}(\Omega)$ as

$$\widetilde{r}(\Omega) = \frac{\widetilde{T}(\Omega)}{\widetilde{|a|^2}(\Omega)} \Big/ \frac{\widetilde{T}(\Omega = 0)}{\widetilde{|a|^2}(\Omega = 0)}, \tag{1.65}$$

where T is the temperature of the resonator, Ω is the modulation angular frequency of energy stored in the cavity. The AC component of z's Fourier transform is denoted as $\widetilde{z}$. By definition of Eq. (1.65), $\widetilde{r}(\Omega = 0) = 1$. The **thermal bandwidth** of the resonator is defined as the $\Omega/2\pi$ where $\widetilde{r}(\Omega) = 0.5$. Typical thermal bandwidth for integrated on-chip microresonator without suspended structure[19] is between 10^3 to 10^4 Hz [20] as shown in Figs. D.1, D.3, D.2, and D.4 (c), depending on the size of

[19] An example of suspended on-chip resonator is SiO_2 wedge resonator reported in ref. [8, 11]. Those resonators have smaller thermal bandwidth because they are not well thermal conducted.

[20] This value is for resonators with FSR around 20 GHz.

the resonator [21]. Further details of the finite element simulation process of $\widetilde{r}$ can be found in the published available data of ref. [2].

With the definition of $\widetilde{r}$, the Fourier transform of Eq. (1.64) can be written as

$$i\Omega\widetilde{A} = -\left(\frac{\kappa}{2} + i\left(\delta\omega - \frac{\alpha\widetilde{r} + g}{V_{\text{eff}}}\widetilde{|A|^2}\right)\right)\widetilde{A} + \sqrt{\kappa_{\text{e}}}\widetilde{a_{\text{in}}}. \tag{1.66}$$

And the solution of Eq. (1.66) can be approximated as quasi-static if the tuning speed of $\delta\omega$ is much slower than the thermal bandwidth of the resonator.

Furthermore, since thermal-optic nonlinearity typically does not lead to any coherent optical effect, Eq. (1.64) are often simplified to

$$\frac{\mathrm{d}A}{\mathrm{d}t} = -\left(\frac{\kappa}{2} + i\left(\delta\omega - g'|A|^2\right)\right)A + \sqrt{\kappa_{\text{e}}}a_{\text{in}}, \tag{1.67}$$

when we study coherent nonlinear optic processes in the resonator. For future convenience, we denote

$$g' = \frac{g}{V_{\text{eff}}} = \frac{\omega_0 c\overline{n_2}}{V_{\text{eff}}\overline{n}n_g}. \tag{1.68}$$

1.2.8.4 Effect of mode dispersion on optical resonator and Lugiato-Lefever equation

In this section, we do not consider nonlinearities other than Kerr nonlinearity.

First of all, mode dispersion, as introduced in Section 1.2.2, involves a series of longitudinal mode within one mode family. Each longitudinal mode has their own angular frequency ω_μ in the phase factor $\mathrm{e}^{-i\omega_\mu t}$ of Eq. (1.33). To study how mode dispersion is going to affect the dynamics of the resonator, we need to define A operator for each longitudinal mode within this mode family.

It is worth to note that the dynamic equation for multiple coupled modes are fundamentally different from single mode due to the Kerr nonlinearity.

a. Find overall complex mode amplitude ψ when multiple longitudinal modes exist

The A operator can be defined similarly to the definition in Eq. (1.56), reads

$$A_\mu = a_\mu \mathrm{e}^{-i(\omega_\mu - \omega_{\text{P}} - D_1\mu)t}, \tag{1.69}$$

[21] The thermal bandwidth is generally larger for smaller resonator, which is easier to reach thermal equilibrium.

where A_μ (slow varying amplitude of mode μ with optical oscillation angular frequency $\omega_P + D_1\mu$) is the A operator for the longitudinal mode with relative mode number μ. $D_1/2\pi$ is the FSR at ω_0. The coupled mode equations of A_μ reads

$$\frac{\mathrm{d}A_\mu}{\mathrm{d}t} = -\left(\frac{\kappa_\mu}{2} + i\left(\delta\omega_\mu\right)\right)A_\mu + \sqrt{\kappa_{e,\mu}}a_{in}\delta_{0,\mu} + ig'\sum_{\mu_1,\mu_2} A_{\mu_1}A_{\mu_2}A^*_{\mu_1+\mu_2-\mu}, \tag{1.70}$$

where $\delta_{0,\mu}$ is the Kronecker delta function, κ_μ, $\kappa_{e,\mu}$ are the total and external dissipation rate for the longitudinal mode with relative mode number μ. $\delta\omega_\mu$ is similar to Eq. (1.57), reads

$$\begin{aligned}\delta\omega_\mu &= \omega_\mu - \omega_P - D_1\mu &(1.71)\\ &= \omega_0 + D_1\mu + \omega_{\mu,int} - \omega_P - D_1\mu &(1.72)\\ &= \delta\omega_0 + \omega_{\mu,int}, &(1.73)\end{aligned}$$

where Eq. (1.72) used the definition of integrated dispersion $\omega_{\mu,int}$ in Eq. (1.11); $\delta\omega_0$ in Eq. (1.73) is defined in Eq. (1.71) when $\mu = 0$. The terms associated with g' in Eq. (1.70) are the Kerr nonlinear terms that satisfy phase-matching condition in Eq. (1.22). Furthermore, since in Eq. (1.69), the optical oscillation angular frequency of A_μ is $\omega_P + D_1\mu$, the phase matching between A_{μ_1}, A_{μ_2}, A_μ and $A_{\mu_1+\mu_2-\mu}$ automatically ensured their energy conservation requirement in Eq. (1.7). Additionally, the coupled mode dynamic equation in Eq. (1.70) is recovered to single mode dynamic equation in Eq. (1.67) when: "$A_\mu \neq 0$ only if $\mu = 0$."

The electric field phasor in the resonator mode with mode number μ, as defined in Eq. (1.33), can be expressed in terms of A operators by substituting Eq. (1.69) to Eq. (1.33), resulting in [22]

$$\begin{aligned}\mathbf{E}_\mu &= a_\mu\mathbf{F}_\mu(r,\theta,z)e^{-i\omega_\mu t}\\ &= A_\mu e^{i(\omega_\mu-\omega_P-D_1\mu)t}\mathbf{F}_\mu(r,\theta,z)e^{-i\omega_\mu t}\\ &= A_\mu e^{-i(D_1\mu)t}\mathbf{F}_\mu(r,\theta,z)e^{-i\omega_P t}\\ &= A_\mu e^{-i(D_1\mu)t}\mathbf{e}^{i\mu\theta}\mathbf{f}(r,z)e^{i(m_0\theta-\omega_P t)}, &(1.74)\end{aligned}$$

[22] Note that the definition of θ here is consistent with Eq. (1.33), which represents the θ component of the cylindrical coordinate system (r,θ,z) with a value of $\theta \in [0, 2\pi)$.

where m_0 is the absolute mode number associated with the mode with relative mode number $\mu = 0$. $\mathbf{f}(r, z)$ in Eq. (1.74) was defined in Eq. (1.35). In Eq. (1.74), the term $\mathbf{f}(r, z)$, which represents the transverse mode profile, will be assumed to be identical within the range of μ we are interested in.

Finally, express the total electrical field phasor $\mathbf{E}$ as the superposition of all phasors $\mathbf{E}_\mu$ calculated in Eq. (1.74), we get

$$\begin{aligned}\mathbf{E} = \sum_\mu \mathbf{E}_\mu &= \left(\sum_\mu A_\mu \mathrm{e}^{i\mu(\theta - D_1 t)}\right)\mathbf{f}(r, z)\mathrm{e}^{i(m_0\theta - \omega_\mathrm{P} t)} \\ &= \left(\sum_\mu A_\mu \mathrm{e}^{i\mu\phi}\right)\mathbf{f}(r, z)\mathrm{e}^{i(m_0\theta - \omega_\mathrm{P} t)} \\ &= \psi(\phi, t)\mathbf{f}(r, z)\mathrm{e}^{i(m_0\theta - \omega_\mathrm{P} t)}, \end{aligned} \tag{1.75}$$

where overall complex mode amplitude ψ is defined as

$$\psi(\phi, t) = \sum_\mu A_\mu \mathrm{e}^{i\mu\phi}, \tag{1.76}$$

and the **co-moving coordinate** (or **co-moving frame**) ϕ is defined as

$$\phi = \theta - D_1 t. \tag{1.77}$$

Note that we did not add any relative phase between different $\mathbf{E}_\mu$ in Eq. (1.75) because any additional constant phase can be absorbed in A_μ.

b. Revisit mode expansion of electric field phasor

Next we revisit the mode expansion of electric field phasor in Eq. (1.75), especially what this means in time domain.

Eq. (1.75) can be re-written as

$$\mathbf{E} = \left(\sum_\mu A_\mu \mathrm{e}^{i\mu\theta}\mathrm{e}^{-i(D_1\mu)t}\right)\mathrm{e}^{-i(\omega_\mathrm{P})t} \cdot \mathrm{e}^{im_0\theta}\mathbf{f}(r, z). \tag{1.78}$$

In (angular) frequency domain, Eq. (1.78) represents series of discrete signals around ω_P, with equal spacing D_1. This is called a **Optical Frequency Comb**,

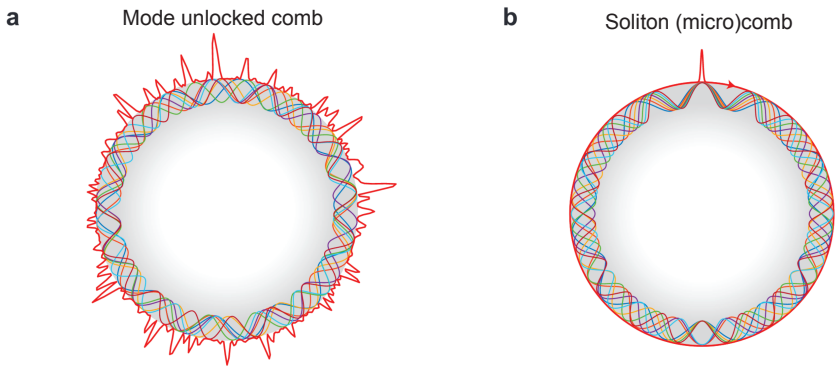

Figure 1.8: **Mode unlocked comb and soliton (micro)comb in resonator fast time domain. Red line indicates the overall mode amplitude of the comb at $t = 0$.** Note that this figure contains no information on time domain. The oscillations within the gray circle only tell which mode propagation constant β (or relative mode number μ) it is representing. In this figure, the optical oscillation angular frequency for the sinusoidal wave with relative mode number μ is $\omega_0 + D_1\mu$, instead of ω_μ.

which is very useful in modern optics and photonics engineering. Optical Frequency Comb will be a main topic we will discuss in the rest of this thesis.

Fig. 1.8 illustrated series of $A_\mu e^{i\mu\theta}$ by many sinusoidal functions of θ within the gray circle with multiple colors. And the value of $\sum A_\mu e^{i\mu\theta}$ as a function of θ is illustrated by the red line circulating outside the gray circle.

If every complex mode amplitude A_μ has the same phase, then every term in $\sum A_\mu e^{i\mu\theta}$ can constructively interfere with each other, as shown in Fig. 1.8(b), creating a comb with the same phase, whose time domain features optical pulses. Fig. 1.8(b) is a demonstration of soliton microcomb, which will be discussed in Section 1.3.5.

c. Understand co-moving coordinate ϕ

As illustrated in Fig. 1.9, mode amplitude represented by ϕ eliminated the group velocity of the wavepacket. Using this coordinate helps us to eliminate propagation and allows us to focus on the pulse shape evolution. Periodic boundary condition $\psi(\phi, t) = \psi(\phi + 2\pi, t)$ is satisfied.

In Fig. 1.9, the time interval t between right and left panel is assumed to be very small so the pulse shape is assumed to be unchanged. However, as the propagation time increases, generally the pulse will not maintain its shape because waves with different mode number have different phase velocity. This effect in the resonator was described as mode dispersion, which has been discussed in Section 1.2.2. The

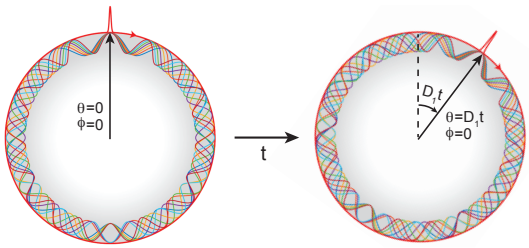

Figure 1.9: **Illustration of the relationship between cylindrical coordinate θ and comoving coordinate ϕ.** Cylindrical coordinate $\theta \in [0, 2\pi)$ represents spatial position. Comoving coordinate $\phi \in \mathbb{R}$ is moving together with the wave packet. Overall mode amplitude $\mathrm{Re}(\psi)$ is represented by the red line. In this figure, we assume t is very small, so the pulse GVD is not illustrated.

differential equation that includes this effect is Lugiato-Lefever equation (LLE) which will be discussed later.

d. Calculate energy and its spectrum from complex mode amplitude ψ

The total energy stored in the optical resonator $\mathcal{E}$ in unit of J can be expressed as

$$\begin{aligned}\mathcal{E}(t) &= \frac{1}{2\pi}\int_0^{2\pi} \mathrm{d}\phi |\psi(\phi,t)|^2 \\ &= \frac{1}{2\pi}\sum_{\mu_1,\mu_2} A_{\mu_1}A^*_{\mu_2}\int_0^{2\pi}\mathrm{d}\phi \mathrm{e}^{i\phi(\mu_1-\mu_2)} \\ &= \sum_{\mu}|A_\mu|^2. \end{aligned} \tag{1.79}$$

And as discussed in Section 1.2.8.4.b, its spectrum features equally spaced discrete frequency comb, and the energy of its μ-th comb line $\widetilde{\mathcal{E}}_{(\omega_\mathrm{P}+D_1\mu)}$ can be calculated as

$$\widetilde{\mathcal{E}}_{(\omega_\mathrm{P}+D_1\mu)}(t) = |A_\mu|^2 = \left|\frac{1}{2\pi}\int_0^{2\pi}\mathrm{d}\phi\psi(\phi,t)\mathrm{e}^{-i\mu\phi}\right|^2. \tag{1.80}$$

e. Lugiato-Lefever equation (LLE)

Lugiato-Lefever equation is the partial differential equation describing the dynamic of $\psi(\phi,t)$. ($\psi(\phi,t)$ is defined in Eq. (1.76).) $\psi(\phi,t)$ is important in the study of the total electric field of the optical resonator because it is the only dynamic part we are interested in Eq. (1.75).

$$\frac{\partial\psi(\phi,t)}{\partial t} = \frac{\partial}{\partial t}\sum_{\mu} A_\mu e^{i\mu\phi} = \sum_{\mu} e^{i\mu\phi}\frac{dA_\mu}{dt}$$

$$= \sum_{\mu} e^{i\mu\phi}\left(-\left(\frac{\kappa_\mu}{2} + i\left(\delta\omega_\mu\right)\right)A_\mu + \sqrt{\kappa_{e,\mu}}a_{in}\delta_{0,\mu} + ig'\sum_{\mu_1,\mu_2} A_{\mu_1}A_{\mu_2}A^*_{\mu_1+\mu_2-\mu}\right) \tag{1.81}$$

$$= -\sum_{\mu}\left(\frac{\kappa_\mu}{2} + i\left(\delta\omega_0\right)\right)A_\mu e^{i\mu\phi} + \sqrt{\kappa_{e,0}}a_{in} - i\sum_{\mu} e^{i\mu\phi}\omega_{\mu,int}A_\mu$$
$$+ ig'\sum_{\mu}\sum_{\mu_1,\mu_2}\left(A_{\mu_1}e^{i\mu_1\phi}\right)\cdot\left(A_{\mu_2}e^{i\mu_2\phi}\right)\cdot\left(A^*_{\mu_1+\mu_2-\mu}e^{-i(\mu_1+\mu_2-\mu)\phi}\right), \tag{1.82}$$

where Eq. (1.81) is get by replacing dA_μ/dt with Eq. (1.70), Eq. (1.82) is get by replacing $\delta\omega_\mu$ with Eq. (1.73). Next we assume the total dissipation rate κ_μ are identical for every μ Eq. (1.82) can be further simplified to

$$\frac{\partial\psi(\phi,t)}{\partial t} = -\left(\frac{\kappa}{2} + i\left(\delta\omega_0\right)\right)\psi + \sqrt{\kappa_{e,0}}a_{in} - i\sum_{\mu}\left(\sum_{n=2}^{\infty}\frac{1}{n!}D_n\mu^n\right)A_\mu e^{i\mu\phi}$$
$$+ ig'\sum_{\mu_1+\mu_2-\mu}\sum_{\mu_1,\mu_2}\left(A_{\mu_1}e^{i\mu_1\phi}\right)\cdot\left(A_{\mu_2}e^{i\mu_2\phi}\right)\cdot\left(A^*_{\mu_1+\mu_2-\mu}e^{-i(\mu_1+\mu_2-\mu)\phi}\right), \tag{1.83}$$

where we change the independent summation subscript in the last term from (μ, μ_1, μ_2) to ($\mu_1+\mu_2-\mu$, μ_1, μ_2). Note that

$$\frac{\partial^n}{\partial\phi^n}\psi(\phi,t) = \sum_{\mu} A_\mu\frac{\partial^n}{\partial\phi^n}e^{i\mu\phi} = i^n\sum_{\mu}\mu^n A_\mu e^{i\mu\phi},$$

which can be substituted to the dispersion term in Eq. (1.83).

Finally, the **Lugiato-Lefever Equation (LLE)** which is the partial differential equation describing the time dynamic of field amplitude within an optical resonator in co-moving frame, can be summarized as

$$\frac{\partial\psi(\phi,t)}{\partial t} = -\left(\frac{\kappa}{2} + i\left(\delta\omega_0\right)\right)\psi + \sqrt{\kappa_{e,0}}a_{in} - \frac{1}{i^{n-1}}\sum_{n=2}^{\infty}\frac{1}{n!}D_n\frac{\partial^n\psi}{\partial\phi^n} + ig'|\psi|^2\psi. \tag{1.84}$$

This is in the same form as the equation proposed in ref. [12].

1.2.9 Parametric oscillation and its threshold

Here we consider the following case: when the resonator mode with relative mode number $\mu = 0$, whose angular frequency is ω_0, is pumped by external laser with angular frequency ω_{P}, what will happen to the other two modes with relative mode number $\pm\mu$. Under this condition, we have

$$\delta\omega_{\pm\mu} = \omega_0 - \omega_{\mathrm{P}} + \omega_{\pm\mu,\mathrm{int}} = \delta\omega_0 + \frac{1}{2}D_2\mu^2 \tag{1.85}$$

using the definition in Eq. (1.72). Here, we only preserve the leading term D_2 of $\omega_{\pm\mu,\mathrm{int}}$, which is defined in Eq. (1.11).

The reason we consider two modes with A operator $A_{\pm\mu}$ is because: $A_{\pm\mu}$ (defined in Eq. (1.69), with optical oscillating angular frequency $\omega_0 \pm D_1\mu$) automatically satisfied degenerate FWM energy and momentum matching condition (summarized in Eq. (1.23)) with A_0 (A_0 has an optical oscillating frequency of ω_0).

In this context, we assume $|A_0|$ is quasi-static ($\frac{\mathrm{d}A_0}{\mathrm{d}t} \approx 0$) and $|A_0| \gg |A_{\pm\mu}|$, and the mode numbers under consideration include μ, 0 and $-\mu$. The dynamic equation of $A_{\pm\mu}$ can be derived from Eq. (1.70). In Eq. (1.70), there are total of six terms associated with $\sum_{\mu_1,\mu_2} A_{\mu_1}A_{\mu_2}A^*_{\mu_1+\mu_2-\mu}$, which are listed in Table 1.2.

Table 1.2: Nonlinear Term Representation for $\sum_{\mu_1,\mu_2} A_{\mu_1}A_{\mu_2}A^*_{\mu_1+\mu_2-\mu}$ in Eq. (1.70).

$\mu_1\backslash\mu_2$	$+\mu$	0	$-\mu$
$+\mu$	$A_{+\mu}A_{+\mu}A^*_{+\mu}$	$A_{+\mu}A_0A^*_0$	$A_{+\mu}A_{-\mu}A^*_{-\mu}$
0	$A_0A_{+\mu}A^*_0$	$A_0A_0A^*_{-\mu}$	
$-\mu$	$A_{-\mu}A_{+\mu}A^*_{-\mu}$		

We preserve terms up to the first order of $|A_{\pm\mu}|$, then dynamic equation for A_μ and $A^*_{-\mu}$ in Eq. (1.70) reads

$$\frac{\mathrm{d}}{\mathrm{d}t}\begin{pmatrix} A_\mu \\ A^*_{-\mu}\end{pmatrix} = \begin{pmatrix} -\frac{\kappa_\mu}{2} - i\delta\omega_\mu + 2ig'|A_0|^2 & ig'A_0^2 \\ -ig'(A_0^*)^2 & -\frac{\kappa_{-\mu}}{2} + i\delta\omega_{-\mu} - 2ig'|A_0|^2\end{pmatrix}\begin{pmatrix} A_\mu \\ A^*_{-\mu}\end{pmatrix}. \tag{1.86}$$

Let us denote the matrix in Eq. (1.86) as $\mathbf{M}$:

$$\mathbf{M} = \begin{pmatrix} -\frac{\kappa_\mu}{2} - i\delta\omega_\mu + 2ig'|A_0|^2 & ig'A_0^2 \\ -ig'(A_0^*)^2 & -\frac{\kappa_{-\mu}}{2} + i\delta\omega_{-\mu} - 2ig'|A_0|^2\end{pmatrix}. \tag{1.87}$$

The field amplitude A_μ and $A_{-\mu}$ can not be accumulated if $|A_0|$ is not high enough and the real part of two eigenvalues of $\mathbf{M}$ are all smaller than zero. At the critical point of modulation instability, the real part of (at least) one eigenvalue is zero. Denote this eigenvalue as λi ($\lambda \in \mathbb{R}$), we have

$$\left(-\frac{\kappa}{2} - i\delta\omega_\mu + 2ig'|A_0|^2 - \lambda i\right) \cdot \left(-\frac{\kappa}{2} + i\delta\omega_{-\mu} - 2ig'|A_0|^2 - \lambda i\right) - (g')^2|A_0|^4 = 0, \tag{1.88}$$

where we assumed $\kappa_\mu = \kappa_{-\mu} = \kappa$.

The imaginary part of Eq. (1.88) is

$$\begin{aligned} &-\frac{\kappa}{2}(+\delta\omega_{-\mu} - 2g'|A_0|^2 - \lambda - \delta\omega_\mu + 2g'|A_0|^2 - \lambda) \\ =&-\frac{\kappa}{2}(\delta\omega_{-\mu} - \delta\omega_\mu - 2\lambda) = 0. \end{aligned} \tag{1.89}$$

Substitute Eq. (1.89) into Eq. (1.88), we get the real part of Eq. (1.88) as

$$\left(2g'|A_0|^2 - \frac{\delta\omega_{-\mu} + \delta\omega_\mu}{2}\right)^2 = (g')^2|A_0|^4 - \left(\frac{\kappa}{2}\right)^2. \tag{1.90}$$

Importantly, in the following discussion, we study necessary but NOT sufficient conditions to get parametric oscillations (solution to Eqs. (1.89) and (1.90)).

The left-hand side of Eq. (1.90) is non-negative, thus the minimum $|A_0|^2$ when Eq. (1.90) has solution to $|A_0|^2$ is

$$\mathcal{E}_{\text{th}} = |A_0|^2_{\text{th}} = \frac{\kappa}{2g'}. \tag{1.91}$$

where $\mathcal{E}_{\text{th}}$ is the threshold energy required in mode ω_0 to generate modulation instability at mode $\pm\mu_{\text{th}}$ who satisfies

$$\frac{\delta\omega_{-\mu_{\text{th}}} + \delta\omega_{\mu_{\text{th}}}}{2} = \kappa. \tag{1.92}$$

Eq. (1.91) is get by setting right-hand side of Eq. (1.90) to 0. Eq. (1.92) is get by bringing Eq. (1.91) into Eq. (1.90).

Next, we calculate the minimum input power $|a_{\text{in}}|^2$, in unit of W, to achieve the threshold energy $\mathcal{E}_{\text{th}}$ in Eq. (1.91). Using the quasi-static solution of Eq. (1.67), we have

$$P_{\mathrm{in,th}}(\delta\omega_0) = |a_{\mathrm{in}}|^2_{\mathrm{th}} = \frac{1}{\kappa_{\mathrm{e}}}\left|\frac{\kappa}{2} + i(\delta\omega_0 - g'|A_0|^2_{\mathrm{th}})\right|^2 \cdot |A_0|^2_{\mathrm{th}},$$

which is minimized to **modulation instability** (or **parametric oscillation) threshold power**

$$P_{\mathrm{in,th}} = \frac{1}{\kappa_e}\left|\frac{\kappa}{2}\right|^2 \cdot |A_0|^2_{\mathrm{th}} = \frac{\kappa^3}{8g'\kappa_{\mathrm{e}}} \tag{1.93}$$

when

$$\delta\omega_0 = g'|A_0|^2_{\mathrm{th}} = \frac{\kappa}{2}. \tag{1.94}$$

And the threshold mode number μ_{th} can be solved from Eqs. (1.85), (1.92), and (1.94) as

$$\mu_{\mathrm{th}} = \sqrt{\frac{\kappa}{D_2}}. \tag{1.95}$$

One reason the above parametric oscillation threshold conditions are **only necessary but not sufficient** is that Eq. (1.95) may not result in an integer mode number. The actual physical process of modulation instability is more complicated, and more discussions can be found in ref. [13].

In summary, at the (ideal) parametric oscillation threshold described above, resonator mode with angular frequency ω_0, relative mode number $\mu = 0$ is pumped by an external laser with power $\kappa^3/8g'\kappa_{\mathrm{e}}$ (Eq. (1.93)) and angular frequency $\omega_{\mathrm{P}} = \omega_0 - \kappa/2$ (Eq. (1.94)). Then, two other longitudinal modes with relative mode number $\pm\sqrt{\kappa/D_2}$ (Eq. (1.92)) start to **parametric oscillate**, rising power from the quantum noise in these modes. This effect is called **modulation instability**, which is usually considered as the starting point (sometimes referred to as **primary comb**) of optical frequency comb generation using an optical resonator [14]. Cascaded modulation instability may generate chaotic comb, which can be used in parallel ranging [15].

The above physical process can only happen when D_2 in Eq. (1.95) is positive. This requirement is usually summarized as the mode dispersion (defined in Section 1.2.5) has to be anomalous in order to get modulation instability.

However, if we do not make the assumption that $\omega_{\pm\mu,\mathrm{int}} = D_2\mu^2/2$ in Eq. (1.85), then μ_{th} need to be solved from Eqs. (1.10), (1.73), (1.92), and (1.94). In this case,

although the resonator may have an overall normal dispersion, a perturbation to the angular frequency of pump mode ω_0 (by **selective mode splitting**) may also enable parametric oscillation [16].

As an additional note, the parametric oscillation threshold (in Eq. (1.93)) is NOT minimized when the resonator is critically coupled ($\eta = 1/2$, where η was defined in Eq. (1.63)). Instead, the $P_{\text{in,th}}$ in Eq. (1.93) is minimized when

$$\kappa_e = \frac{1}{2}\kappa_0, \quad \eta = \frac{1}{3}, \quad \left(\frac{|a_{\text{out}}|^2}{|a_{\text{in}}|^2}\right)_{\text{min}} = \frac{1}{9}. \tag{1.96}$$

1.3 Optical frequency combs

We gave a bottom-up introduction to the optical frequency comb generated in the optical resonator in Sections 1.2.8.4.b and 1.2.9. In this section, we will introduce optical frequency comb in a top-down way. We will also include discussions on the engineering and applications of optical frequency combs.

In this section, we no longer study the modal distribution of electric field **E**. Therefore, electric field **E** will be simplified to E in Section 1.3.

1.3.1 Introduction

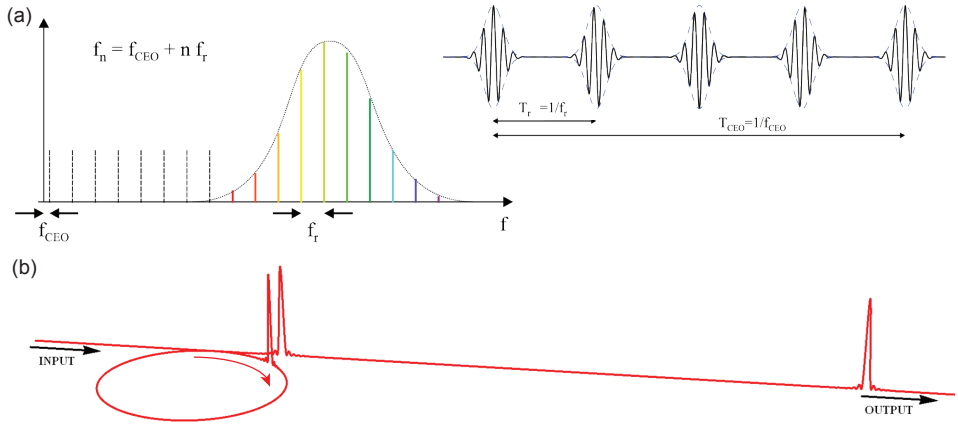

Figure 1.10: **Conceptual illustration of Optical Frequency Comb and its time domain. (a)** Illustration of the spectrum of a mode-locked optical frequency comb and its electrical field in time domain. Here T_r is the repetition time, T_{CEO} is the carrier-envelop phase match period. **(b)** The pulses coupled from optical resonator forms a periodic pulse train in time domain, which is an optical frequency comb in frequency domain.

Optical frequency comb in frequency domain contains a series of discrete comb lines, with a equal distance of f_r, as shown in Fig. 1.10(a). The frequency of the

n-th order comb line can be represented as

$$f_{\mathrm{n}} = n f_{\mathrm{r}} + f_{\mathrm{CEO}}, \tag{1.97}$$

where f_{CEO} is the **baseband offset frequency** (or **carrier-envelope offset frequency**), which is the same for all comb lines. In time domain, the electric field of optical frequency comb is a collection of series of frequency components, which has been illustrated in Fig. 1.8, with a repetition rate f_{r}, as shown in Fig. 1.10(a) inset.

Mode-locked pulses (Fig. 1.8(b)) coupled from optical resonator forms a periodic pulse train and becomes optical frequency comb in frequency domain. A conceptual illustration is shown in Fig. 1.10(b).

Optical frequency comb is one of the most critical components for modern photonics because it acts as a bridge between optical frequency (THz) and the frequency within electronic bandwidth (f_{r} range from MHz $\sim$ GHz), which has been well discussed in ref. [17]. Some concepts in ref. [17] used in this thesis include:

1. From a single frequency continuous wave (CW) laser, we can modulate it with RF signal generated by electronics, and the modulated CW laser becomes a comb in optical frequency domain.

2. From a optical frequency comb, its radio-frequncy beat note at frequency $D_1/2\pi$ has a phasor of $\sum_\mu A_\mu A^*_{\mu+1}$, which can constructively interfere and become a single tone RF signal if every A_μ has the same phase (Fig. 1.8(b)).

Therefore, with the help of optical frequency comb, the technologies to stabilize optical frequency (radio frequency) can be utilized to transfer this stability into radio frequency (optical frequency). Some examples used in this thesis include:

1. From RF to optics: Using optical frequency comb as a calibration source for Astronomical observation. This will be discussed in Chapter 7 of this thesis.

2. From optics to RF: Using mode-locked optical frequency comb to generate RF signal which can be further stabilized using optical frequency division. The generation of a mode-locked comb will be discussed in Chapter 3 of this thesis.

In summary, optical frequency combs have a wide range of applications in science and technology, including time keeping, optical frequency synthesis, spectroscopy, ranging, astronomical calibration, microwave generation, *etc.*.

1.3.2 Comb in frequency domain and repeated pulse in time domain

Next, we explain the relation between "comb in frequency domain" and "repeated pulse in time domain" from the concept of the Fourier transform of sampling function.

We start from focusing on a single pulse in Fig. 1.10(a) inset. We denote the electric field of this single pulse as $E(t)$, and its Fourier transform in frequency domain as $\widetilde{E}(f)$. We have

$$\widetilde{E}(f) = \mathcal{F}\left[E(t)\right], \tag{1.98}$$

where $\mathcal{F}[\cdot]$ ($\mathcal{F}^{-1}[\cdot]$) represents (inverse) Fourier transform operator. Note that the intensity spectrum of $\widetilde{E}(f)$ is a continuous function, represented by the dashed envelope of Fig. 1.10(a). The spectrum of optical frequency comb $\widetilde{E}_{\mathrm{comb}}(f)$ is the sampling of $\widetilde{E}(f)$, which can be written as

$$\widetilde{E}_{\mathrm{comb}}(f) \propto \widetilde{E}(f) \cdot \text{Ш}\left(\frac{f - f_{\mathrm{CEO}}}{f_{\mathrm{r}}}\right). \tag{1.99}$$

Here $\text{Ш}(x)$ is the unit sampling distribution (or unit Sha-distribution) defined as

$$\text{Ш}(x) = \sum_{n\in\mathbb{Z}} \delta(x - n). \tag{1.100}$$

This distribution, also known as the (unit) **Dirac comb**, is a valuable tool with applications in Fourier analysis [18], signal processing [19], and various other scientific fields [20]. Further discussions on the properties of the Dirac comb are provided in the respective references.

In Appendix A.1, we will show that the Fourier transform of unit sampling function is itself [21], reads

$$\mathcal{F}\left[\text{Ш}(x)\right] = \text{Ш}(x). \tag{1.101}$$

Take the Fourier transform of Eq. (1.99), we can calculate the time domain of optical frequency comb $E_{\mathrm{comb}}(t)$ reads [23]

[23] Here we used the property of Fourier transform $\mathcal{F}^{-1}\left[h(\frac{f-a}{b})\right] = b\mathrm{e}^{i2\pi ta}\mathcal{F}^{-1}\left[h\right](bt)$.

$$
\begin{aligned}
E_{\mathrm{comb}}(t) = \mathcal{F}^{-1}\left[\widetilde{E}_{\mathrm{comb}}(f)\right] &\propto \mathcal{F}^{-1}\left[\widetilde{E}(f)\cdot \text{Ш}\left(\frac{f-f_{\mathrm{CEO}}}{f_{\mathrm{r}}}\right)\right] \\
&= \mathcal{F}^{-1}\left[\widetilde{E}(f)\right] \otimes \mathcal{F}^{-1}\left[\text{Ш}\left(\frac{f-f_{\mathrm{CEO}}}{f_{\mathrm{r}}}\right)\right] \\
&\propto E(t)\otimes\left(\mathrm{e}^{i2\pi t f_{\mathrm{CEO}}}\text{Ш}(f_{\mathrm{r}}t)\right) \\
&= \int_{-\infty}^{\infty} E(t-\tau)\mathrm{e}^{i2\pi\tau f_{\mathrm{CEO}}}\text{Ш}(f_{\mathrm{r}}\tau)\mathrm{d}\tau \\
&\propto \sum_{n\in\mathbb{Z}} E\left(t-\frac{n}{f_{\mathrm{r}}}\right)\mathrm{e}^{i2\pi\frac{nf_{\mathrm{CEO}}}{f_{\mathrm{r}}}}, \qquad (1.102)
\end{aligned}
$$

where "$g(x)\otimes h(x)$" means the convolution between $g(x)$ and $h(x)$.

Eq. (1.102) shows that: frequency sampling a continuous signal spectrum every f_{r} results in repeating the signal every $1/f_{\mathrm{r}}$ in time domain, with an additional phase $2\pi n f_{\mathrm{CEO}}/f_{\mathrm{r}}$ to each repetition. This additional phase result in the phase of the pulse within each repetition is different from each other, as shown in Fig. 1.10(a) inset.

In practice, the proportion coefficient in Eq. (1.102) which we did not consider should be determined by energy conservation within sampling bandwidth.

1.3.3 Stability of optical frequency comb

In order to fully stabilize the comb in optical domain, both f_{r} and f_{CEO} needs to be stabilized. Stabilizing f_{r} prevents the frequency comb from "accordion" like instability. Some techniques to stabilize f_{r} include quiet-point operation and optical frequency division. Stabilizing f_{CEO} prevents the instability of the comb's absolute frequency. An important technique to stabilize f_{CEO} is self-referencing (or referencing to a self-referenced comb). Additionally, locking to atom transitions can also offer reference to the absolute frequency of an optical frequency comb.

The stability of f_{r} are often measured by its **single-side-band (SSB) phase noise** spectra in unit of dBc/Hz. Further discussion of this concept can be found in ref. [22].

In astronomical calibration, an important stability measure is the **Allan deviation** σ_f of the optical frequency. The allan deviation measures what is the relative standard deviation $\delta f/f$ of the frequency of a comb line over a measurement period t. The reason why this is important will be discussed in Chapter 7 Eq. (7.2) and Section 7.3.2 of this thesis.

1.3.4 Electro-optics frequency comb

The physical configuration of electro-optics frequency comb can be found in Fig.8.2 of ref. [23]. In this section, we summarize the operating principle of electro-optics frequency comb from a mathematical perspective.

An electro-optics frequency comb is generated from phase modulating a single-frequency continuous wave (CW) laser, whose phasor is represented as $E_0 e^{-i2\pi f_0 t}$. Here the phase modulation is achieved by utilizing electro-optics nonlinearity discussed in Section 1.1.2. The CW laser pass through a phase modulator (PM), whose refractive index along the optical path is modulated by an external electric field with frequency f_r. The amplitude of this external electrical field is denoted as $E_{\text{ext,PM}}$. The principle of this refractive index modulation has been discussed in Eq. (1.3).

The electric field phasor of the CW laser after being phase-modulated reads

$$E_0 e^{-i2\pi f_0 t} \cdot e^{i\beta_P \sin(2\pi f_r t)},$$

where $\beta_P = \pi E_{\text{ext,PM}}/E_{\pi,\text{PM}}$ is the depth of phase modulation (E_π was defined in Section 1.1.2). Any additional constant phase can be absorbed into E_0.

After phase modulation, a second stage intensity modulator (IM) is added to spectrally flatten the modulated comb. The intensity modulation is achieved by a Mach-Zehnder interferometer, which first split the light with 50/50 splitter, then apply electric field $E_{\text{ext,IM}}$ to phase modulate one path, and finally recombine the two paths with 50/50 combiner. The resulted electric field phasor reads

$$E = E_0 e^{-i2\pi f_0 t} \cdot e^{i\beta_P \sin(2\pi f_r t)} \cdot \left(\frac{1}{\sqrt{2}} \left(e^{i\phi_{\text{DC}}} + e^{i\beta_I \sin(2\pi f_r t + \phi_I)} \right) \right), \tag{1.103}$$

where $\beta_I = \pi E_{\text{ext,IM}}/E_{\pi,\text{IM}}$ is the depth of intensity modulation, ϕ_I is the relative phase between intensity modulation and phase modulation, ϕ_{DC} is the offset bias of intensity modulator (operation position of Mach-Zehnder interferometer).

Next, we investigate what the parameters are when EO comb is under optimized operation point. In order to get in-phase intensity modulation, we first set

$$\phi_I = 0, \tag{1.104}$$

then we have

$$E = \frac{1}{\sqrt{2}} E_0 \mathrm{e}^{-i2\pi f_0 t} \cdot \left(\mathrm{e}^{i\phi_{\mathrm{DC}}} \mathrm{e}^{i\beta_P \sin(2\pi f_{\mathrm{r}} t)} + \mathrm{e}^{i(\beta_P+\beta_I)\sin(2\pi f_{\mathrm{r}} t)} \right)$$

$$= \frac{1}{\sqrt{2}} E_0 \mathrm{e}^{-i2\pi f_0 t} \cdot \sum_{n\in\mathbb{Z}} \mathrm{e}^{i2\pi f_{\mathrm{r}} t \cdot n} \left(\mathrm{e}^{i\phi_{\mathrm{DC}}} \mathrm{J}_n(\beta_P) + \mathrm{J}_n(\beta_P + \beta_I) \right) \tag{1.105}$$

$$\approx \frac{1}{\sqrt{2}} E_0 \mathrm{e}^{-i2\pi f_0 t} \cdot \sum_{n\in\mathbb{Z}} \mathrm{e}^{i2\pi f_{\mathrm{r}} t \cdot n} \sqrt{\frac{2}{\pi\beta_P}} \left(\mathrm{e}^{i\phi_{\mathrm{DC}}} \cos\left(\beta_P - \frac{n\pi}{2} - \frac{\pi}{4}\right) + \cos\left(\beta_P + \beta_I - \frac{n\pi}{2} - \frac{\pi}{4}\right) \right), \tag{1.106}$$

where $\mathrm{J}_n(z)$ represents n-th order Bessel functions of the first kind. Eq. (1.105) used Jacobi–Anger expansion $\exp(iz\sin(\theta)) = \sum_{n\in\mathbb{Z}} \mathrm{J}_n(z)\exp(in\theta)$. Eq. (1.106) used asymptotic expansion of $\mathrm{J}_n(z) \approx \sqrt{\frac{2}{\pi z}}\cos(z - \frac{n\pi}{2} - \frac{\pi}{4})$ when $\beta_P \gg 1$ [24] and $\beta_P \gg \beta_I$. We assumed β_P is a large number because β_P is the main driving source of the electro-optic comb, and usually this driving source has a much higher power (typically $\sim$ 30 dBm) than the signal that drives the intensity modulator. From Eq. (1.105), we can also identify that β_P is roughly half of the number of comb lines, because the function[25] $h_x(n) = |\mathrm{J}_n(x)|$ is approximately maximized when $n \approx x$ and decays very fast when $n > x$.

In Eq. (1.106), we can see that under the condition

$$\phi_{\mathrm{DC}} = \frac{\pi}{2}, \quad \beta_I = \frac{\pi}{2}, \tag{1.107}$$

the final modulated electric field reads a simple form

$$E \approx \frac{i}{\sqrt{\pi\beta_P}} E_0 \mathrm{e}^{-i2\pi f_0 t} \cdot \sum_{n\in\mathbb{Z}} \mathrm{e}^{i2\pi f_{\mathrm{r}} t \cdot n} \cdot \mathrm{e}^{i\left(\beta_P - \frac{n\pi}{2} - \frac{\pi}{4}\right)}, \tag{1.108}$$

which means the intensity of comb lines at every order n are the same. Note that the equation in Eq. (1.108) is valid only when the asymptotic expansion from Eq. (1.105) to Eq. (1.106) are valid (when $|n| \ll \sqrt{\beta_P}$). Therefore, the conditions in Eqs. (1.104) and (1.107) can only guarantee comb line intensity are the same when $|n| \ll \sqrt{\beta_P}$. Actually, when $|n| \sim \beta_P$, the intensity of comb lines becomes stronger and presents the well-known "two-sided wing" behavior of electro-optics comb, as shown in Fig. 7.3.

[24] Strictly speaking, this should be $\beta_P \gg \left|n^2 - \frac{1}{4}\right|$. The approximation used in Eq. (1.106) works for the comb order n much smaller than $\sqrt{\beta_P}$.

[25] Note $h_x(n)$ is a function of n, and is defined on $\mathbb{Z}$. x is the parameter, not the argument of $h_x(n)$.

Finally, the conditions in Eqs. (1.104) and (1.107) constitute the optimal operation point of EO comb. If we have multiple stages of phase modulation, then we need to add another optimal operation condition, which is the relative modulation phase between different phase modulators ϕ_P needs to be the same.

Experimentally, the process of tuning EO comb to its optimal operation point can be summarized as following:

1. Attenuate the RF signal send into IM to near zero ($\beta_I \approx 0$), tune the DC bias applied to IM (ϕ_{DC}) until the transmission output power is approximately half of maximum output power (tuned $\phi_{\mathrm{DC}} = \pi/2$).

2. Tune the RF phase shifter of the IM driving signal (change ϕ_I), until the output spectrum looks symmetric ($\phi_I = 0$). Because if $\phi_I \neq 0$, there will be terms asymmetrical to n in Eq. (1.105).

3. Tune the RF phase shifter to different PM (if the comb is driven by multiple stages of PM), until the bandwidth of the comb is maximized (ϕ_P are the same for every PM).

4. Tune the variable RF attenuator to drive the IM until the comb is flat around the spectrum center. ($\beta_I = \pi/2$).

5. Iterate steps 1 to 4 to optimize the comb.

If we consider the higher order terms in the asymptotic expansion from Eq. (1.105) to Eq. (1.106), we can calculate the phase dispersion of electro-optics comb. Experimentally, the dispersion of EO comb can be well compensated by second-order dispersion. After dispersion compensation, we can generate an optical pulse in the time domain.

1.3.5 Soliton (micro)comb

Soliton microcomb is a kind of mode-locked frequency comb generated in microresonators. It is a special solution of $\psi(\phi, t)$ in Eq. (1.84) which does not depend on t. This t independent feature indicates that this solution does not evolve over time. Physically speaking, this solution of $\psi(\theta - D_1 t, t)$ can propagate around the resonator and sustain itself. The solution has analytical form in absence of the pump term $\sqrt{\kappa_{\mathrm{e},0}} a_{\mathrm{in}}$, loss term κ and high-order ($n \geq 3$) dispersion terms of Eq. (1.84), reads

$$\frac{\partial \psi(\phi,t)}{\partial t} = -i\left(\delta\omega_0\right)\psi + i\frac{1}{2}D_2\frac{\partial^2\psi}{\partial\phi^2} + ig'|\psi|^2\psi. \tag{1.109}$$

And this t independent solution to $\psi(\phi,t)$ is

$$\psi(\phi,t) = \sqrt{\frac{2\delta\omega_0}{g'}}\operatorname{sech}\left(\sqrt{\frac{2\delta\omega_0}{D_2}}\phi\right). \tag{1.110}$$

1.4 Chapter overview

Chapter 2 explores the critical role of high-quality factor (Q) optical microresonators in integrated photonic devices, focusing on the measurement of material-limited Q factors and Kerr nonlinearities in SiO_2, Si_3N_4, $Al_{0.2}Ga_{0.8}As$, and Ta_2O_5. Through cavity-enhanced photothermal spectroscopy, we quantify the ultimate Q determined by material absorption and evaluate the Kerr nonlinearity in each platform. The findings provide insights into the interplay between material nonlinearity and Q factor, informing the design and development of next-generation photonic integrated systems by establishing performance limits and guiding microresonator material improvements.

Chapter 3 introduces a novel microcomb that achieves mode-locking through the formation of pulse pairs in normal-dispersion coupled-ring resonators. Unlike traditional microcombs, these pulse pairs must phase lock together to create a bright soliton comb, and they form at recurring spectral windows with distinct optical spectra. We also demonstrated 3-ring systems where three pulses achieve mode locking through alternating pairwise coupling. The results are facilitated by a new CMOS-foundry platform, previously incapable of bright soliton generation due to its inherent normal dispersion. This capability to generate multi-color pulse pairs across multiple rings holds significant potential for all-optical soliton buffers, memories, and advances in quantum combs and topological photonics.

Chapter 4 explores the generation of Kelly sidebands (KS) in coupled-ring soliton microcombs. Kelly sidebands, a type of dispersive wave typically observed in mode-locked systems, are produced here through continuous-wave (CW) excitation in a partially-coupled racetrack-resonator microcomb. This configuration supports two optical bands, allowing the soliton and Kelly sideband to reside in distinct bands. This interband excitation lowers power requirements and facilitates CW sideband excitation. The chapter also investigates the tuning of sideband spectral positions under pulsed excitation. Both numerical simulations and experiments

show that symmetry breaking in the partially-coupled two-ring system is crucial for KS formation. The findings highlight the potential of multi-band systems to engineer Kelly sidebands for microcomb spectral broadening.

Chapter 5 presents the generation of multi-color co-propagating and counter-propagating solitons using a coupled-ring microresonator in the ultra-low-loss Si_3N_4 platform. The soliton spectra and beatnotes are measured, and potential applications are discussed. The study demonstrates how multi-color pulse pairs can form in distinct spectral windows driven by two continuous-wave pumps, highlighting the capability of multi-pump methods to extend microcomb bandwidth.

Chapter 6 discusses the generation of mode-locked soliton microcombs in $Al_{0.2}Ga_{0.8}As$ microresonators using pulse pumping at room temperature. $Al_{0.2}Ga_{0.8}As$ offers advantageous nonlinearity and compatibility with active gain, making it suitable for high-efficiency frequency combs. However, challenges such as strong absorption complicate soliton generation. This study demonstrates how pulse pumping can mitigate thermal effects, enabling robust soliton formation and stabilization. The results suggest potential applications in integrated photonics and provide insights into soliton dynamics in $Al_{0.2}Ga_{0.8}As$ microresonators.

Chapter 7 presents the development and commissioning of a near-infrared (NIR) Laser Frequency Comb (LFC) for the NIRSPEC instrument on the Keck observatory. The LFC operates over wavelengths from 1.2 to 2.1 μm, with future extension to 2.5 μm, and has an intrinsic mode spacing of 16 GHz. By referencing a Rubidium standard, the LFC achieves long-term stability of less than 10 cm s^{-1}. This development enhances the capabilities of high-precision radial velocity (PRV) measurements, which are crucial for exoplanet detection and characterization. The chapter details the LFC signal chain, stability analysis, and on-sky observations, demonstrating the LFC's potential for improving the precision of exoplanet searches.

References

[1] Boyd, R. W. *Nonlinear Optics* (Elsevier, 2008).

[2] Gao, M. *et al.* Probing material absorption and optical nonlinearity of integrated photonic materials. *Nat Commun* **13**, 3323 (2022).

[3] Xie, W. *et al.* Ultra-high-Q AlGaAs-on-insulator microresonators for integrated nonlinear photonics. *Opt. Express* **28**, 32894–32906 (2020).

[4] Jin, W. *et al.* Hertz-linewidth semiconductor lasers using CMOS-ready ultra-high-Q microresonators. *Nat. Photonics* **15**, 346–353 (2021).

[5] Anderson, M. H. *et al.* Dissipative solitons and switching waves in dispersion-modulated Kerr cavities. *Phys. Rev. X* **13**, 011040 (2023).

[6] Feigenbaum, E., Kaminski, N. & Orenstein, M. Negative group velocity: Is it a backward wave or fast light? (2008). ArXiv:0807.4915.

[7] Papatryfonos, K. *et al.* Refractive indices of MBE-grown AlxGa(1-x)As ternary alloys in the transparent wavelength region. *AIP Advances* **11**, 025327 (2021).

[8] Wu, L. *et al.* Greater than one billion Q factor for on-chip microresonators. *Opt. Lett.* **45**, 5129–5131 (2020).

[9] Wang, H. *Kerr solitons and Brillouin lasers in optical microresonators*. Doctoral dissertation, California Institute of Technology (2021).

[10] Chow, J. H. *et al.* Critical coupling control of a microresonator by laser amplitude modulation. *Opt. Express* **20**, 12622 (2012).

[11] Lee, H. *et al.* Chemically etched ultrahigh-Q wedge-resonator on a silicon chip. *Nat. Photonics* **6**, 369–373 (2012).

[12] Lugiato, L. A. & Lefever, R. Spatial dissipative structures in passive optical systems. *Phys. Rev. Lett.* **58**, 2209–2211 (1987).

[13] Godey, C., Balakireva, I. V., Coillet, A. & Chembo, Y. K. Stability analysis of the spatiotemporal Lugiato-Lefever model for Kerr optical frequency combs in the anomalous and normal dispersion regimes. *Phys. Rev. A* **89**, 063814 (2014).

[14] Kippenberg, T. J., Spillane, S. M. & Vahala, K. J. Kerr nonlinearity optical parametric oscillation in an ultrahigh-Q toroid microcavity. *Phys. Rev. Lett.* **93**, 083904 (2004).

[15] Lukashchuk, A., Riemensberger, J., Tusnin, A., Liu, J. & Kippenberg, T. J. Chaotic microcomb-based parallel ranging. *Nat. Photonics* **17**, 814–821 (2023).

[16] Lucas, E., Yu, S.-P., Briles, T. C., Carlson, D. R. & Papp, S. B. Tailoring microcombs with inverse-designed, meta-dispersion microresonators. *Nat. Photon.* **17**, 943–950 (2023).

[17] Diddams, S. A., Vahala, K. & Udem, T. Optical frequency combs: Coherently uniting the electromagnetic spectrum. *Science* **369**, eaay3676 (2020).

[18] Osgood, B. Lecture notes for EE 261: The Fourier transform and its applications. (2002).

[19] Tenoudji, F. C. *Analog and digital signal analysis: From basics to applications* (Springer, 2018).

[20] Kirby, J. *Spectral methods for the estimation of the effective elastic thickness of the lithosphere* (Springer, 2022).

[21] Bracewell, R. *The Fourier transform & its aplications* (McGraw-Hill, 1999).

[22] Riley, W. & Howe, D. A. *Handbook of frequency stability analysis* (NIST, 2008).

[23] Yi, X. *Physics and applications of microresonator solitons and electro-optic frequency combs*. Doctoral dissertation, California Institute of Technology (2017).

Chapter 2

MATERIAL ABSORPTION AND OPTICAL NONLINEARITY CHARACTERIZATION OF INTEGRATED PHOTONIC MATERIALS

This chapter is based on the following published paper:
Gao, M., Yang, Q.-F., Ji, Q.-X. *et. al.* Probing material absorption and optical nonlinearity of integrated photonic materials. *Nat Commun* **13**, 3323 (2022).
https://doi.org/10.1038/s41467-022-30966-5

Optical microresonators with high quality (Q) factors are essential to a wide range of integrated photonic devices. Steady efforts have been directed towards increasing microresonator Q factors across a variety of platforms. With success in reducing microfabrication process-related optical loss as a limitation of Q, the ultimate attainable Q, as determined solely by the constituent microresonator material absorption, has come into focus. Here, we report measurements of the material-limited Q factors in several photonic material platforms. High-Q microresonators are fabricated from thin films of SiO_2, Si_3N_4, $Al_{0.2}Ga_{0.8}As$ and Ta_2O_5. By using cavity-enhanced photothermal spectroscopy, the material-limited Q is determined. The method simultaneously measures the Kerr nonlinearity in each material and reveals how material nonlinearity and ultimate Q vary in a complementary fashion across photonic materials. Besides guiding microresonator design and material development in four material platforms, the results help establish performance limits in future photonic integrated systems.

2.1 Introduction

Performance characteristics of microresonator-based devices improve dramatically with increasing Q factor [1]. Nonlinear optical oscillators, for example, have turn-on threshold powers that scale inverse quadratically with Q factor [2–4]. The fundamental linewidth of these and conventional lasers also vary in this way [5–7]. In other areas including cavity quantum electrodynamics [8], integrated quantum optics [9–12], cavity optomechanics [13] and sensing [14], a higher Q factor provides at least a linear performance boost. In recent years, applications that rely upon these microresonator-based phenomena, including microwave generation [15], frequency microcomb systems [16], high-coherence lasers [7, 17, 18] and chip-based optical

gyroscopes [19–21], have accelerated the development of high-Q photonic-chip systems [18, 22–31].

Q factor is determined by material losses, cavity loading (i.e., external waveguide coupling), and scattering losses (see Fig. 2.1(a)). To increase Q factor, there have been considerable efforts focused on new microfabrication methods and design techniques that reduce scattering loss associated with interface roughness [22, 32, 33] and coupling non-ideality[34, 35]. Impressive progress has resulted in demonstrations of high-Q microresonator systems with integrated functionality [36, 37], as well as resonators that are microfabricated entirely within a CMOS foundry [18]. With these advancements, attention has turned towards Q limits imposed by the constituent photonic material themselves. For example, the presence of water, hydrogen, trace metal ions [33, 38–41] and other pathways [42, 43] are known to increase absorption. In this work, cavity-enhanced photothermal spectroscopy [39, 41, 44–47] is used to determine the absorption-limited Q factor (Q_{abs}) and optical nonlinearity of state-of-the-art high-Q optical microresonators fabricated from four different photonic materials on silicon wafer.

2.2 Logic of measurement

Images of the microresonators characterized in this study are shown in Fig. 2.1(b), where the microresonators are SiO_2 [4, 48] microdisks and Si_3N_4 [47], $Al_{0.2}Ga_{0.8}As$ [26, 27] and Ta_2O_5 [49] microrings. Details of the device fabrication processes are given in the Methods. Typical microresonator transmission spectra showing optical resonances are presented in Fig. 2.1(b). The transmission spectra feature Lorentzian lineshapes, but in some cases are distorted by etalon effects resulting from reflection at the facets of the coupling waveguide. With such etalon effects accounted for (see Appendix B.1), the intrinsic (Q_0) and external (coupling) (Q_e) Q factors can be determined. The measured intrinsic Q_0 factors are 418 million, 30.5 million, 2.01 million, and 2.69 million, for SiO_2, Si_3N_4, $Al_{0.2}Ga_{0.8}As$, and Ta_2O_5 devices, respectively.

The microresonator intrinsic Q_0 is determined by scattering and absorption losses. In order to isolate the absorption loss contribution, cavity-enhanced photothermal spectroscopy is used. The principle is based on that the resonant frequencies of dielectric microresonators are shifted by the Kerr effect and the photothermal effect, both of which result from the refractive index change that depends on the intracavity optical intensity. Because these two effects occur on very distinct time-scales

Table 1 | Properties of materials in current integrated high-Q microresonators at 1550 nm

Material	Growth method	Structure	n_o	Reported n_2 (10^{-20} m^2 W^{-1})	n_2 (10^{-20} m^2 W^{-1})	Q_{abs} (M)	σ_{abs} (dB m^{-1})
SiO_2	Wet oxidation	Amorphous	1.44	2.2	-	3900 ± 200	0.0065 ± 0.0003
Si_3N_4	LPCVD	Amorphous	2.00	24	22 ± 1	290 ± 50	0.12 ± 0.02
$Al_{0.2}Ga_{0.8}As$	MBE	Crystal	3.28	2600	1700 ± 100	2.0 ± 0.2	28 ± 2
Ta_2O_5	IBS	Amorphous	2.06	62	27 ± 3	2.4 ± 0.3	15 ± 2

Table 2.1: Summary of material loss and nonlinearity. LPCVD: low-pressure chemical vapour deposition; MBE: molecular beam epitaxy; IBS: ion-beam sputtering. Propagation loss σ_{abs} induced by absorption is calculated as $\sigma_{\text{Mat}} = (10/\ln 10)\omega_0 n_g/(Q_{\text{abs}}c)$. Error indicates standard deviation. These numbers should be viewed as state-of-the-art values rather than fundamental limits. Possible systematic errors of measurement values are discussed in Section 2.8.6. The Q_{abs} for Ta_2O_5 is further discussed in Appendix D.4.

(Kerr effect being ultra-fast and optical absorption occurring at a relatively slow thermal time scale from milliseconds to microseconds), it is possible to distinguish their respective contributions to resonant frequency shift and infer their nonlinear coefficients [45]. Two distinct measurements are performed to determine the absorption-limited Q_{abs}. Here, they are referred to as the "sum measurement" and "ratio measurement." In the sum measurement, resonant frequency shift is measured to obtain the sum of Kerr and photothermal effects. In the ratio measurement, the photothermal frequency response is measured to distinguish its contribution from the Kerr effect.

2.3 Sum measurement

In the sum measurement, the microresonator is probed by a tunable laser whose frequency is slowly swept across a resonance from the higher frequency side of a resonance (i.e., blue-detuned side). The input light polarization is aligned to the fundamental TE (Si_3N_4, $Al_{0.2}Ga_{0.8}As$, and Ta_2O_5) or TM (SiO_2) mode of the microresonator. In the case of SiO_2, because of the presence of multiple transverse modes, a fundamental mode well separated from other resonances was used so as to reduce the influence of mode interactions. The experimental setup is depicted in Fig. 2.2(a). The frequency scan is calibrated by a radio-frequency calibrated Mach-Zehnder interferometer (MZI) [50]. The probe laser frequency scan is sufficiently slow (i.e., quasi-static scan, see Fig. D.1, Fig. D.2, Fig. D.3, and Fig. D.4 for details) to ensure that scan speed does not impact the observed lineshape through transient thermal processes within the microresonator. The transmission spectra exhibit a triangular shape [51] as shown in Fig. 2.2(b). Theoretical fittings of the

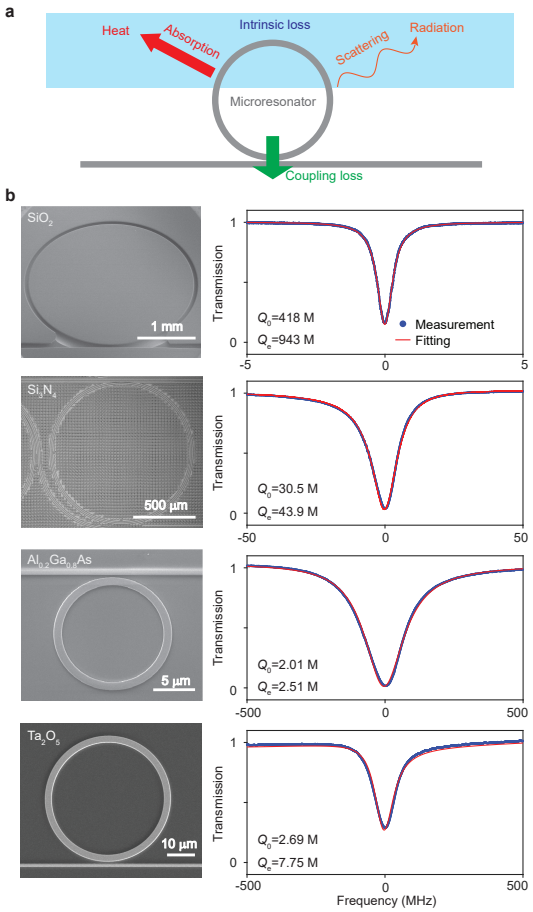

Figure 2.1: **High-Q optical microresonators characterized in this work. (a)** Schematic showing optical loss channels for high-Q integrated optical microresonators. The loss channels include surface (and bulk) scattering loss and material absorption loss. The intrinsic loss rate is characterized by the intrinsic Q factor (Q_0). Bus waveguide coupling also introduces loss that is characterized by the external (coupling) Q factor (Q_e). **(b)** Left column: images of typical microresonators used in this study. Right column: corresponding low input-power spectral scans (blue points) with fitting (red). The intrinsic and external Q factors are indicated. M: million.

transmission spectra are shown in red and discussed in Methods. Also, the cold resonance spectra (i.e., with very low waveguide power) measured under the same coupling conditions are plotted for comparison (dashed curve).

By changing the input pump laser power with a voltage-controlled optical attenuator (VOA), the quasi-static resonance shift $\delta\omega_0$ of the resonant frequency ω_0 versus the intracavity circulating optical energy density ρ (units of J·m^{-3}) is determined and summarized in Fig. 2.2(c). The observed linear dependence contains contributions

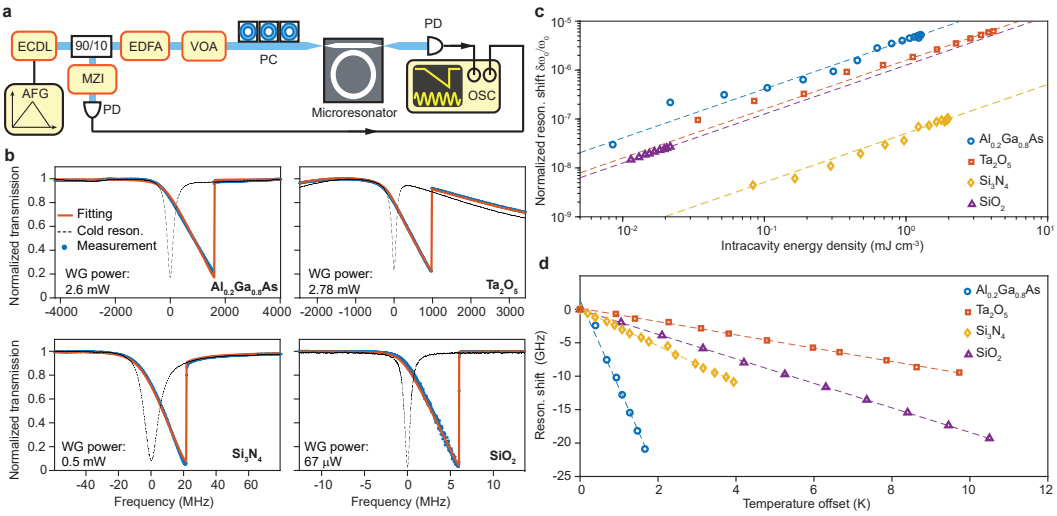

Figure 2.2: **The sum measurement.** This experiment measures the sum of Kerr and photothermal nonlinear coefficients $(g + \alpha)$. **(a)** Experimental setup. ECDL: external-cavity diode laser; EDFA: erbium-doped fiber amplifier; VOA: voltage-controlled optical attenuator; PC: polarization controller; PD: photodetector; MZI: Mach-Zehnder interferometer; AFG: arbitrary function generator; OSC: oscilloscope. For SiO_2 experiment, ECDL is replaced by a narrow-linewidth fiber laser to achieve a slower frequency tuning speed. As an aside due to narower tuning range of fiber laser, this experiment is only performed at 1550nm for SiO_2. **(b)** Typical transmission spectra of microresonators with photothermal and Kerr self-phase modulation, where the input power in the bus waveguide is indicated. Theoretical fittings are plotted in red and discussed in Methods. The cold transmission spectra measured at low pump power are also plotted with dashed lines for comparison. WG power: optical power in the bus waveguide. **(c)** Measured resonant frequency shift versus intracavity power for microresonators based on different materials. Dashed lines are linear fittings of the measured data. The four traces have the same slope, which is a result of the proportional relation shown in Eq. (2.1). **(d)** Measured resonant frequency shift versus microresonator chip temperature for the four materials, with linear fittings. The fitted shift for $Al_{0.2}Ga_{0.8}As$, Si_3N_4, SiO_2 and Ta_2O_5 are -13.1, -2.84, -1.83 and -0.996, in units of GHz·K^{-1}, respectively.

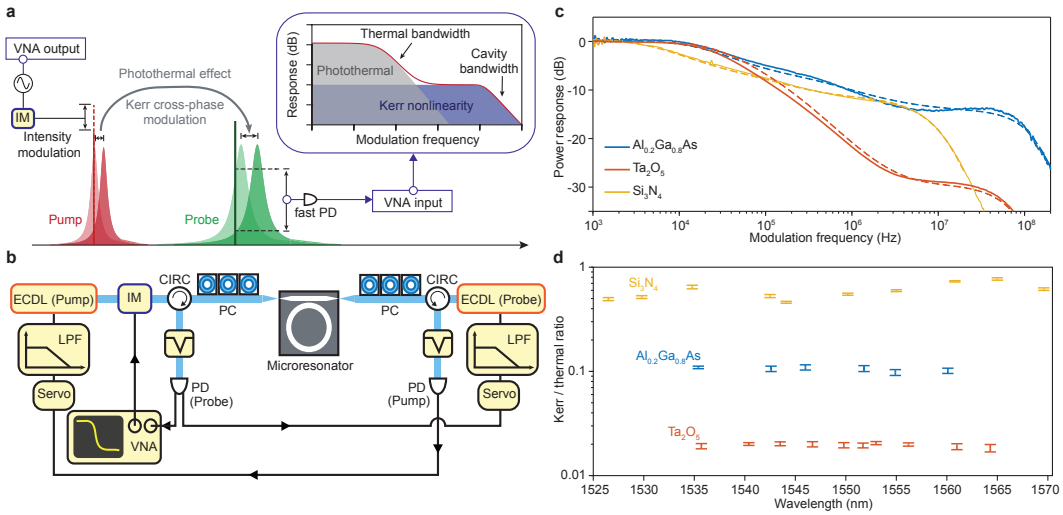

Figure 2.3: **The ratio measurement.** This experiment measures the ratio of Kerr and photothermal nonlinear coefficients g/α. **(a)** Illustration of the ratio measurement. A pump laser is stabilized to a resonance and modulated by an intensity modulator. The intracavity power is thus modulated. As a result of photothermal effect and Kerr cross-phase modulation, the frequency of a nearby resonance is also modulated. Another probe laser is stabilized near this resonance, and its transmission is monitored by a vector network analyzer (VNA). Inset: the modulation response allows distinguishing the photothermal and Kerr effects. **(b)** Experimental setup. IM: intensity modulator; CIRC: optical circulator; LPF: low-pass filter; VNA: vector network analyzer. **(c)** Typical measured response functions of the probe laser transmission $\tilde{\mathcal{R}}$ as a function of modulation frequency Ω. Numerical fittings are outlined as dashed curves. For modulation frequencies below 1 kHz, the probe response is suppressed by the servo feedback locking loop. Some artifacts appear around 1 kHz as a result of the servo control. Here the experimental trace is smoothed over 5 points. **(d)** Measured wavelength dependence of the ratios between the Kerr nonlinearity and photothermal effect for three materials. Vertical error bars give 95% confidence intervals.

from the Kerr self-phase modulation and photothermal effects as,

$$\frac{\delta\omega_0}{\omega_0} = -\frac{1}{\omega_0}(\alpha + g)\rho, \tag{2.1}$$

where α and g denote the photothermal coefficient and the Kerr coefficient given by:

$$\begin{aligned} \alpha &= \overline{\kappa_a}\frac{\overline{\delta T}}{P_{\text{abs}}}\left(-\frac{\delta\omega_0}{\overline{\delta T}}\right)V_{\text{eff}}, \\ g &= \frac{\overline{n_2}}{\overline{n}\,\overline{n_g}}\omega_0 c. \end{aligned} \tag{2.2}$$

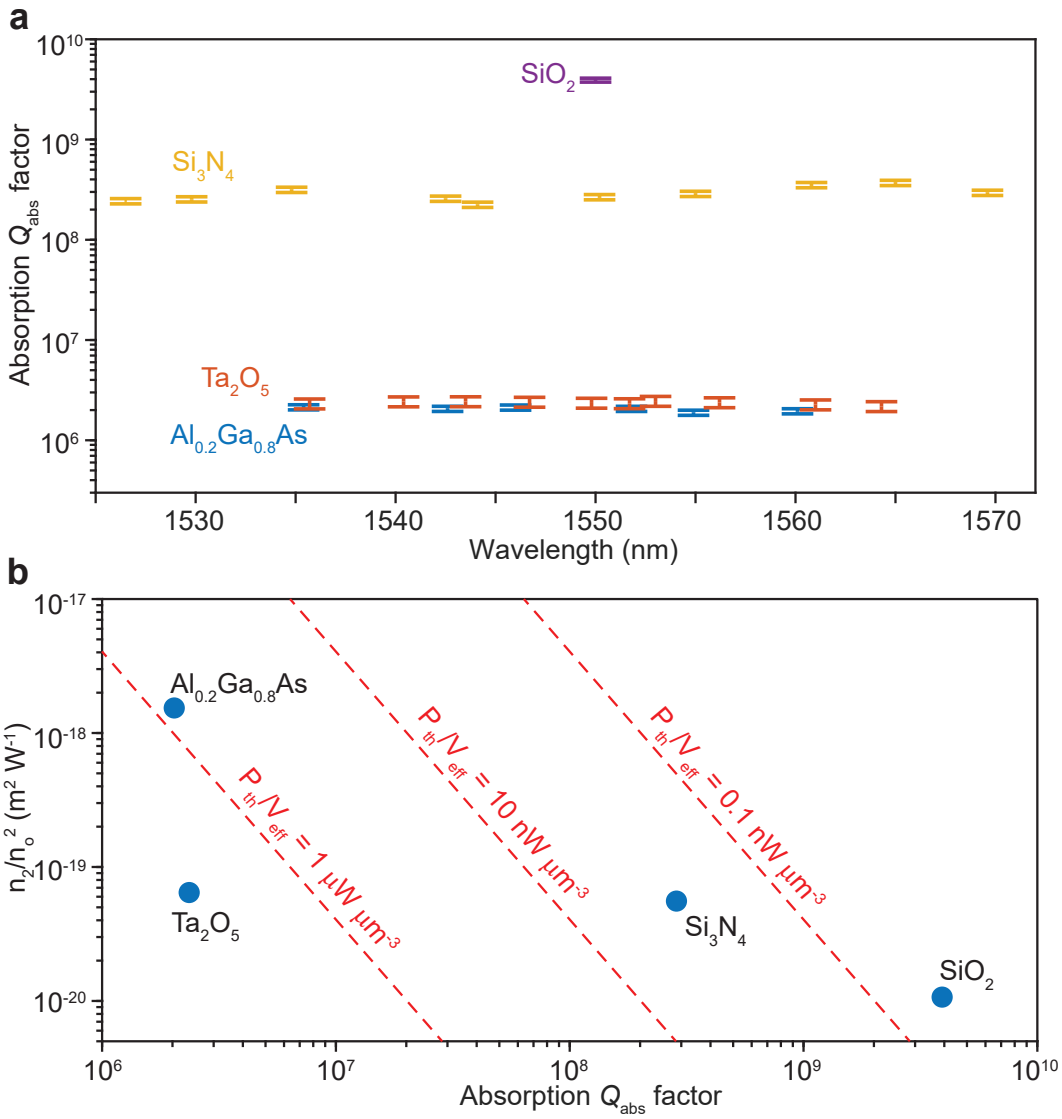

Figure 2.4: **Absorption Q_{abs}, nonlinear coefficients and parametric oscillation threshold.** **(a)** Measured absorption Q_{abs} factors at different wavelengths in the telecommmunication C-band for the four materials. Vertical error bars give standard deviations of measurements. **(b)** Comparison of absorption Q_{abs} factors and normalized nonlinear index (n_2/n^2) for the four materials. Measured n_2 values are listed in Table 2.1. The n_2 of SiO_2 was not measured here and a reported value of 2.2×10^{-20} m^2 W^{-1} is used. Parametric oscillation threshold for a single material normalized by mode volume ($P_{\text{th}}/V_{\text{eff}}$) is indicated by the red dashed lines, assuming $\lambda = 1550$ nm, intrinsic Q_0 equals material absorption Q, and $Q_e = Q_0$ (i.e., critical coupling condition).

Here, κ_a is the energy **loss rate (or dissipation rate) due to optical absorption**, n_2 is the material Kerr nonlinear refractive index, n is the material refractive index, n_g is the material chromatic group refractive index, c is the speed of light in vacuum, P_{abs} is the absorbed optical power by the microresonator and T is the temperature of the microresonator. The bar (e.g., $\overline{n_2}$) denotes the average value of the underneath variable weighted by the field distribution of the optical mode. The exact definition of each average is provided in Eqs. (1.43), (1.44), and (1.45).

The energy loss rate κ_a is related to the material **absorption-limited Q_{abs} factor** by

$$Q_{\text{abs}} = \frac{\omega_0}{\kappa_a}. \tag{2.3}$$

To determine κ_a and hence Q_{abs} from α, it is necessary to determine V_{eff}, $\overline{\delta T}/P_{\text{abs}}$ and $\delta\omega_0/\delta T$. The effective mode volume V_{eff} is calculated using the optical mode obtained in finite-element modeling, and $\overline{\delta T}/P_{\text{abs}}$ is further calculated using the finite-element modeling with a heat source spatially distributed as the optical mode. The resonance tuning coefficient $\delta\omega_0/\delta T$ is directly measured by varying the temperature of the microresonator chip using a thermoelectric cooler (TEC), and the results are shown in Fig. 2.2(d). Since the TEC heats the entire chip, the thermo-elastic effect of the silicon substrate contributes to the frequency shift and combines with the photothermal effect. However, this thermo-elastic contribution does not appear in the sum measurement, where the heating originates only from the optical mode. Thus, the thermal-elastic contribution of the silicon substrate must be deducted from the TEC measured results (see Section 2.8.5). Other effects that may lead to frequency shift or linewidth broadening (discussed in Section 2.8.6), such as harmonic generation or multi-photon absorption, are not significant in the samples, as confirmed by observing the coupling efficiency with respect to power (see Fig. D.1(d), Fig. D.2(d), Fig. D.3(d), and Fig. D.4(d)).

2.4 Ratio experiment

The measurement associated with Eq. (2.1) wherein the sum contributions of Kerr and photothermal effects are measured is supplemented by a measurement that provides the ratio of these quantities. This second measurement takes advantage of the very different relaxation time scales of Kerr and photothermal effects. The experimental concept and setup are depicted in Figs. 2.3a and 2.3b. Pump and probe lasers are launched from opposite directions into the microresonator. The pump laser is stabilized to one resonance by monitoring the transmission signal and locking close to the center of the resonance. Pump power is modulated over a range

of frequencies using a commercial lithium niobate electro-optic modulator driven by a vector network analyzer (VNA). Similarly, the probe laser is locked to another nearby resonance, and is slightly detuned from the center resonant frequency. Both probe and pump modes are fundamental spatial modes, but not necessarily in the same polarization state. For $Al_{0.2}Ga_{0.8}As$ and Ta_2O_5, both pump and probe modes belong to the fundamental TE mode, while for Si_3N_4, pump and probe modes belong to the fundamental TE and TM modes, respectively (see Appendix D.2). It is also noted that this measurement was challenging to perform in the suspended SiO_2 microdisks on account of a very slow thermal diffusion process (see Appendix D.1). Instead, a published value of n_2 for SiO_2 (2.2×10^{-20} $m^2 \cdot W^{-1}$) was used [52].

With this arrangement, pump power modulation in the first resonance induces modulation of the output probe power in the second resonance, through the effect of Kerr- and photothermal-induced refractive index modulations. As illustrated in the inset of Fig. 2.3(a), photothermal modulation determines the low frequency response in this measurement, while the Kerr effect determines the intermediate frequency response, and the highest corner frequency is set by the cavity dissipation rate (see Methods). The probe frequency response measured for three different microresonators is presented in Fig. 2.3c. The response at very low frequencies is normalized to 0 dB. Both pump and probe laser powers are sufficiently low to minimize the thermal locking effect [51]. The plateau in the frequency response at low frequency gives the combined quasi-static contributions of photothermal and Kerr effects in the sum measurement (inset of Fig. 2.3(a)), while the high frequency response constitutes only the Kerr contribution. In addition, the Kerr effect here is the cross-phase modulation contribution (from the pump to the probe), while, as noted above, the Kerr self-phase modulation contribution appears in Eq. (2.1). These two effects are related by a cross-phase modulation factor γ determined by the mode combinations used (see Methods). By numerically fitting the response curves (see Appendix C.1), the ratio between Kerr and photothermal effects is extracted over a range of wavelengths and plotted in Fig. 2.3d.

2.5 Measurement result of absorption limited Q-factor

Combining results from the above sum and ratio measurements, the photothermal and Kerr coefficients are obtained individually. The inferred absorption-limited Q_{abs} values measured over the telecommunication C-band for each material are summarized in Fig. 2.4(a). It is worth mentioning that the SiO_2 microdisk measurement requires a narrow-linewidth, highly-stable fiber laser on account of the microres-

onator's ultra-high Q factor. The use of the fiber laser limits the measurement range to near 1550 nm. A combined plot of the measured n_2 values (normalized by n^2) versus the absorption Q_{abs} is given in Fig. 2.4(b) (the n_2 of SiO_2 is taken from the literature [52]). Also, in the cases of critical coupling ($Q_e = Q_0$) and absorption-limited intrinsic Q factors ($Q_0 = Q_{\text{abs}}$), the parametric oscillation threshold (derived in Eq.(1.93)) per unit mode volume [3, 53, 54] for a single material is shown by dashed red iso-contours:

$$\frac{P_{\text{th}}}{V_{\text{eff}}} = \frac{n^2\,\omega_o}{n_2 Q_{\text{abs}}^2 c}, \tag{2.4}$$

where V_{eff} is the effective mode volume. It should be noted that actual thresholds may be different if the optical field is not tightly confined in the core of the microresonator heterostructure.

The results described above are further summarized in Table 2.1, where, for SiO_2 and Si_3N_4, the measured material absorption losses are much lower than the present microresonator intrinsic losses. Therefore, improvement in microfabication of SiO_2 and Si_3N_4 to reduce surface roughness, hence to reduce scattering losses, will benefit photonic integrated circuits using these materials. For $Al_{0.2}Ga_{0.8}As$ and Ta_2O_5, the material losses are close to their respective intrinsic losses, which suggests that both material and scattering loss contributions should be addressed.

2.6 Additional discussion for each materials

Overall, the absorption Q_{abs} values reported here should be viewed as state-of-the-art values that are not believed to be at fundamental limits. For example, silica glass in optical fiber exhibits loss (typically 0.2 dB·km^{-1}) [55] that is over one order of magnitude lower than that reported in Fig. 2.4(b).

Likewise, Ta_2O_5 is the premier material for optical coatings employed, for example, in the highest performance optical clocks and gravitational-wave interferometers. However, Ta_2O_5 exhibits fascinating stoichiometry and crystallization effects, which require careful mitigation in deposition and processing. The material-limited Q of Ta_2O_5 and TiO_2:Ta_2O_5 has been measured to be 5 million and 25 million, respectively [56]. Hence, the nanofabricated devices and precision-measurement technique reported here highlight the promise to optimize material-limited performance in the Ta_2O_5 platform. It is also noted that in $Al_{0.2}Ga_{0.8}As$, a compound semiconductors material, surface defects may generate mid-gap states [42] which cause extra material absorption loss. This loss mechanism will depend upon process conditions and

intrinsic Q factors as high as 3.52 M for $Al_{0.2}Ga_{0.8}As$ have been reported elsewhere [27]. Finally, some of the material parameters used in modeling are impacted by factors such as the film deposition method. For example, thermal conductivity of Ta_2O_5 can depend upon the deposition method as is reflected by a wide range of values available in the literature (see Appendix D.4). Such effects could also impact other materials used in this study, but we have nonetheless relied upon bulk values and simplifications in modeling (see Table 2.3). Certain details in the simulation, e.g., heat dissipation rate into the air (see Table 2.4), are also possible contributing factors. Domain size in the finite element simulation have been optimized and not considered as an error source.

The current method also provides *in-situ* measurement of n_2 for integrated photonic microresonators. We compare the n_2 values measured here with other reported values in Table 2.1. Reported n_2 values are taken from ref. [52] (SiO_2), ref. [57] (Si_3N_4), ref. [58] ($Al_{0.2}Ga_{0.8}As$) and ref. [49] (Ta_2O_5).

To give a fashion of how the nonlinearity varies between the four materials, third-order nonlinear susceptibility $\chi_{(3)}$ is calculated from the measured n_2 and compared with the linear susceptibility $\chi_{(1)}$. The Miller's rule [59, 60] $\chi_{(3)} \propto \chi_{(1)}^4$ relating the scaling of these two quantities is observed (see Section 2.7).

In summary, the absorption loss and Kerr nonlinear coefficients of four leading integrated photonic materials have been measured using cavity-enhanced photothermal spectroscopy. The material absorption sets a practical limit of these materials in microcavity applications. The Kerr nonlinear coefficients have also been characterized, and the results are consistent with a general trend relating to nonlinearity and optical loss. Overall, the results suggest specific directions where there can be improvement in these systems as well as providing a way to predict future device performance.

2.7 Observation of Miller's rule

The Miller's rule gives a phenomenological prediction of the material nonlinear coefficients based on its linear susceptibility [59, 60]. Specifically, the third-order nonlinear susceptibility $\chi_{(3)}$ is predicted to be proportional to the linear susceptibility $\chi_{(1)}^4$, where

$$\chi_{(3)} = \frac{4\varepsilon_0 c n^2}{3} n_2, \tag{2.5}$$

$$\chi_{(1)} = n^2 - 1. \tag{2.6}$$

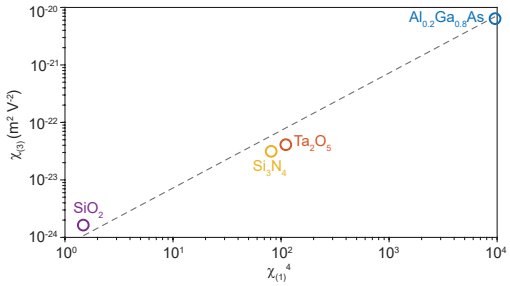

Figure 2.5: **Observation of Miller's rule of nonlinear susceptibility.**

The measured $\chi_{(3)}$ (as calculated from n_2) is plotted in Fig. 2.5, along with a fourth-power fitting (dashed). Despite a difference of 4 orders of magnitude in $\chi_{(3)}$ between different materials, the fourth-power scaling is evident as shown in the figure.

2.8 Methods and supplementary information

2.8.1 Fabrication of optical microresonators

The SiO_2 microresonator is fabricated by thermally growing 8-μm thick thermal wet oxide on a 4 inch float-zone silicon wafer, followed by i-line stepper photolithography, buffered oxide etch, XeF_2 silicon isotropic dry etch and thermal annealing [4, 48]. The Si_3N_4 microresonator is fabricated with the photonic Damascene process, including using deep-ultraviolet stepper lithography, preform etching, low-pressure chemical vapour deposition, planarization, cladding and annealing [47]. The $Al_{0.2}Ga_{0.8}As$ microresonator is fabricated with an epitaxial $Al_{0.2}Ga_{0.8}As$ layer bonded onto a silicon wafer with a 3-μm thermal SiO_2 layer, followed by GaAs substrate removal, deep ultraviolet patterning, inductively coupled plasma etching, passivation with Al_2O_3 and SiO_2 cladding [26, 27]. The Ta_2O_5 microresonator is fabricated by ion-beam sputtering Ta_2O_5 deposition followed by annealing, electron-beam lithography, Ta_2O_5 etching, ultraviolet lithography and dicing [49].

2.8.2 Experimental details

In the sum measurement, the scanning speed of the laser frequency is decreased until the mode's broadening as induced by the thermo-optic shift becomes stable (i.e., not influenced by the scan rate). Also, the waveguide input power is minimized such that it is well below the threshold of parametric oscillation. The power is calibrated using the photodetector voltage.

In the ratio measurement, the optical frequencies of the pump and probe lasers are

locked to their respective cavity modes using a servo feedback with 1 kHz bandwidth. The pump laser is locked near the mode resonant frequency, while the probe laser is locked to the side of the resonance to increase transduction of refractive index modulation into transmitted probe power. The intensity modulator is calibrated in a separate measurement under the same driving power.

2.8.3 Fitting of spectra in the sum measurement

For Si_3N_4 and Ta_2O_5 devices, the transmission spectrum is the interference of a Lorentzian-lineshaped mode resonance with a background field contributed by facet reflections of the waveguide. The transmission function of a cavity resonance is given by

$$T_{\mathrm{res}} = 1 - \frac{\kappa_e}{\kappa/2 + i[\Delta - (\alpha + g)\rho]}, \tag{2.7}$$

where Δ is the cold-cavity laser-cavity detuning, α and g are the absorption and Kerr nonlinear coefficients, respectively, and ρ is the intracavity energy density as defined in the main text. The reflection at the two waveguide facets forms a low-finesse Fabry–Pérot resonator. Combining this waveguide reflection with the cavity resonance, the overall amplitude transmission is given by (see Appendix B.1)

$$T \propto \left| \frac{T_{\mathrm{res}}}{1 - rT_{\mathrm{res}}^2 \exp[i(-\Delta/\omega_{\mathrm{FP}} + \phi)]} \right|^2, \tag{2.8}$$

where r is the reflectivity at the waveguide facet, ω_{FP} is the free spectral range of the facet-induced Fabry–Pérot cavity (in rad/s units), and ϕ is a constant phase offset.

In the experiment, the above quantities are fitted in three steps. First, ω_{FP} and r are obtained by measuring the transmission away from mode resonances. Next, loss rates κ and κ_e can be determined by measuring the transmission of the mode at a low probe power. Finally, launching higher power into the microresonator allows the mode broadening to be observed and the transmission is fitted with Eq. (2.8), where $(\alpha + g)$ is the fitting variable and other parameters are obtained from the previous steps. For $Al_{0.2}Ga_{0.8}As$ and SiO_2 devices which have no Fabry–Pérot background, r can be set to zero and the first step in the above fitting procedure can be omitted. The fitting results are presented in Fig. 2.2(b).

2.8.4 Fitting of response in the ratio measurement

The response of the probe mode resonant frequency $\tilde{\delta}_\mathrm{b}$ as a result of pump power modulation $\tilde{P}_\mathrm{in}$ can be described by (see Appendix C.1),

$$\frac{\tilde{\delta}_\mathrm{b}(\Omega)}{\tilde{P}_\mathrm{in}(\Omega)} = -\frac{\alpha\tilde{r}(\Omega)+\gamma g}{V_\mathrm{eff}}\frac{2\eta_\mathrm{p}}{i\Omega+\kappa_\mathrm{p}/2}. \tag{2.9}$$

where Ω is the pump power modulation frequency (in rad/s units), $\tilde{P}_\mathrm{in}$ is the modulation amplitude of the pump power, κ_p is the total loss rate of the pump mode, $\eta_\mathrm{p} = \kappa_{e,\mathrm{p}}/\kappa_\mathrm{p}$ is the coupling efficiency for pump mode, α is the absorption coefficient as mentioned in the previous section, $\tilde{r}$ is the frequency response of modal temperature modulation as a result of thermal diffusion, and the factor γ accounts for cross-phase modulation of the probe mode by the pump mode. The denominator in Eq. (2.9) creates a corner frequency for the response that is illustrated in the inset of Fig. 2.3(a) and that appears in the data and fitting in Fig. 2.3(c).

The frequency response of the transmitted probe mode with respect to its resonance shift $\tilde{\delta}_\mathrm{b}(\Omega)$ is derived in Appendix C.1 and has the following form:

$$\frac{\tilde{T}_\mathrm{b}(\Omega)}{\tilde{\delta}_\mathrm{b}(\Omega)} = -\frac{2\kappa_{e,\mathrm{b}}\Delta_\mathrm{b}^{(0)}}{\kappa_\mathrm{b}^2/4+\left(\Delta_\mathrm{b}^{(0)}\right)^2}\frac{\kappa_\mathrm{b}-\kappa_{e,\mathrm{b}}+i\Omega}{(\kappa_\mathrm{b}/2+i\Omega)^2+\left(\Delta_\mathrm{b}^{(0)}\right)^2}|a_{\mathrm{in,b}}|^2, \tag{2.10}$$

where $\Delta_\mathrm{b}^{(0)}$ is the steady-state detuning of the probe mode when no modulation is present, and κ_b and $\kappa_{e,\mathrm{b}}$ refer to the total loss rate and external coupling rate for the probe mode.

The response curve in Fig. 2.3(c) is modeled by

$$\tilde{\mathcal{R}}(\Omega) = \frac{\tilde{T}_\mathrm{b}(\Omega)}{\tilde{P}_\mathrm{in}(\Omega)} = \frac{\tilde{T}_\mathrm{b}(\Omega)}{\tilde{\delta}_\mathrm{b}(\Omega)}\frac{\tilde{\delta}_\mathrm{b}(\Omega)}{\tilde{P}_\mathrm{in}(\Omega)}, \tag{2.11}$$

and is fitted according to Eqs. (2.9) and (2.10). In the fitting, κ and κ_e have been measured separately, $\tilde{r}$ is determined from finite element method simulations, and the probe mode Δ_0 and ratio α/g are parameters to be fitted.

2.8.5 Calibration of resonance thermal shift

In the sum experiment, resonance shift originates from localized material absorption. This increases the resonator temperature locally, and shifts the resonance primarily through the thermo-optical effect (factor α_n is defined in Eq. (1.48)). However, when the resonance shift is calibrated using a thermoelectric cooler (TEC) (see Fig. 2.2(d)), the entire chip is heated, and the resonance shift therefore includes a

contribution from the thermo-elastic expansion created by the silicon substrate. To remove this extra contribution, the coefficient of linear thermal expansion $\alpha_{l,\mathrm{sub}}$ of the silicon substrate is subtracted. As a check of this approach, Table 2.2 compiles measured values for $\alpha_n + \alpha_{l,\mathrm{sub}}$ using the TEC as described in the main text along with values for α_n and α_l (coefficient of linear thermal expansion) reported in the literature for the relevant materials. The TEC measured values are close compared to the reported α_n with the silicon (substrate material) α_l added. The discrepancy between α_n reported for $Al_{0.2}Ga_{0.8}As$ makes the same comparison difficult, but the result for this case falls reasonably close to the measured value.

	α_n, reported	α_l, reported	$\alpha_n + \alpha_{l,\mathrm{sub}}$, measured (TEC)
SiO_2	0.752 (ref. [61])	0.055 (ref. [62])	0.95
Si_3N_4	1.25 (ref. [63])	0.33 (ref. [64])	1.47
$Al_{0.2}Ga_{0.8}As$	6.970 (ref. [26]) 6.054 (ref. [66])	0.562 (ref. [65])	6.798
Ta_2O_5	0.29 (ref. [67])	0.24 (ref. [68])	0.52
Si (Substrate)	–	0.26 (ref. [69])	–

Table 2.2: Thermo-optic and thermo-elastic coefficients reported in the literature compared with the measured combined effect determined by heating of the resonator chip.

2.8.6 Sources of systematic errors in Q_{abs} and n_2

Material	Density ρ_{m} ($\mathrm{kg{\cdot}m^{-3}}$)	Thermal conductivity k ($\mathrm{W{\cdot}m^{-1}{\cdot}K^{-1}}$)	Heat capacity C ($\mathrm{J{\cdot}kg^{-1}{\cdot}K^{-1}}$)
Si (ref. [70])	2.33×10^3	130	700
SiO_2 (ref. [70])	2.2×10^3	1.4	740
Si_3N_4 (ref. [70, 71])	3.17×10^3	30	800
$Al_xGa_{1-x}As$ (ref. [65])	$(5.32 - 1.56x) \times 10^3$	$55 - 212x + 248x^2$	$320 + 132x$
Ta_2O_5	6.85×10^3 (ref. [72])	0.4 (ref. [73])	306 (ref. [74])

Table 2.3: Thermal constants of resonator materials used in finite-element method simulations. The thermal conductivity of Ta_2O_5 is further discussed in Appendix D.4.

The Q_{abs} and n_2 are calculated from measured α and g factors, respectively, utilizing Eq. (2.2). The calculation uses material constants from handbooks, where a measurement of these parameters is beyond the scope of this study.

- Thermal properties of the materials are taken from references as summarized in Tables (2.3) and (2.2). The values not only depend upon the specific

bulk material, but also on layer deposition and growth processes. In turn, a variation in these parameters will directly impact the inferred Q_{abs}. Using a larger thermal conductivity (or heat capacity) reduces the inferred $\overline{\delta T}$ for the same absorbed power (as in Eq. (1.55)), and leads to a lower calculated Q_{abs}. As an example, the reported thermal conductivity for Ta_2O_5 has variations and its impact is further discussed in Appendix D.4.

- Similarly, the optical refractive index n_o and group index n_g refer to bulk materials. These parameters appear in Eq. (1.47) and affect the calculated n_2. Also, refractive indices determine the modal field distribution for averaging (as in Eqs. (1.43), (1.45), and (1.53)), which also affect the calculated material properties.

- In the experiment the air surrounding the sample is static, and the convective heat flux coefficient $h = 10\ \text{W}\cdot\text{m}^{-2}\cdot\text{K}^{-1}$ (ref. [75]) is used in all simulations. A larger convective heat flux coefficient will lead to lower temperature increase per unit absorbed power ($\overline{\delta T}/P_{\text{abs}}$), and to a lower calculated Q_{abs}. However, numerical simulations indicate that this effect is minor (see below).

$\overline{\delta T}/P_{\text{abs}}$ ($\text{K}\cdot\text{W}^{-1}$)	SiO_2	Si_3N_4	$Al_{0.2}Ga_{0.8}As$	Ta_2O_5
$h = 2\ \text{W}\cdot\text{m}^{-2}\cdot\text{K}^{-1}$	558	95.3	90.7	1085.1
$h = 10\ \text{W}\cdot\text{m}^{-2}\cdot\text{K}^{-1}$	552	95.3	90.7	1085.1
$h = 25\ \text{W}\cdot\text{m}^{-2}\cdot\text{K}^{-1}$	542	95.3	90.7	1085.1

Table 2.4: $\overline{\delta T}/P_{\text{abs}}$ values with different heat dissipation rate.

Furthermore, there are physical processes neglected in the modelling that may lead to systematic errors.

- Surface and interface effects between different layers in the heterogeneous structure may alter the theoretical model. For example, contact thermal resistance is present at the interfaces between different materials, and this could not be evaluated here. However, for micron-scale cross-section structures in our study, the induced thermal resistance is negligible. As an example, for the interface between silicon and silica, numerical studies [76] and measurements [77] estimate the interface thermal resistance per unit area as 0.9×10^{-9} $\text{m}^2\cdot\text{K}\cdot\text{W}^{-1}$ and 2.3×10^{-9} $\text{m}^2\cdot\text{K}\cdot\text{W}^{-1}$, respectively. Meanwhile, with parameters in Table. 2.3, the thermal resistance of a 1-micron-thick silica film is

evaluated to be 7.1×10^{-7} $m^2 \cdot K \cdot W^{-1}$, more than 10^2 larger than the interface contribution. Apart from contact thermal resistance, surface absorption may also be prominent for semiconductors ($Al_{0.2}Ga_{0.8}As$) and is discussed in Appendix D.4.

- There are absorption pathways where a portion of the absorbed energy does not end up as heat (e.g., Raman and Brillouin scattering). Including such effects requires more absorbed power for the same $\overline{\delta T}$, and leads to a lower calculated Q_{abs}. We do not believe these processes are significant since the phase-matching condition is not favorable in measured devices.

- Harmonics generation, multi-photon absorption and other nonlinear optical effects may also lead to frequency shift or linewidth broadening. However, because these will induce a power-dependent loss on the pump mode, coupling efficiency of the pump mode will decrease when these effects are prominent, and this is not observed in the transmission traces (see Figs. D.1d, D.2d, D.3d, and D.4d). As a result, these effects are also neglected in the model.

It should be noted that error bars in the main text represent measurement errors only (including instrumental error and data fitting error), while systematic errors discussed above are not included. To ensure accuracy, the mode used for testing should minimize all of the above nonlinear optical effects.

References

[1] Vahala, K. J. Optical microcavities. *Nature* **424**, 839 (2003).

[2] Spillane, S., Kippenberg, T. & Vahala, K. Ultralow-threshold raman laser using a spherical dielectric microcavity. *Nature* **415**, 621–623 (2002).

[3] Kippenberg, T. J., Spillane, S. M. & Vahala, K. Kerr-nonlinearity optical parametric oscillation in an ultrahigh-Q toroid microcavity. *Phys. Rev. Lett.* **93**, 083904 (2004).

[4] Lee, H. *et al.* Chemically etched ultrahigh-Q wedge-resonator on a silicon chip. *Nat. Photon.* **6**, 369–373 (2012).

[5] Schawlow, A. L. & Townes, C. H. Infrared and optical masers. *Phys. Rev.* **112**, 1940 (1958).

[6] Vahala, K. J. Back-action limit of linewidth in an optomechanical oscillator. *Phys. Rev. A* **78**, 023832 (2008).

[7] Li, J., Lee, H., Chen, T. & Vahala, K. J. Characterization of a high coherence, Brillouin microcavity laser on silicon. *Opt. Express* **20**, 20170–20180 (2012).

[8] Aoki, T. *et al.* Observation of strong coupling between one atom and a monolithic microresonator. *Nature* **443**, 671–674 (2006).

[9] Lu, X. *et al.* Chip-integrated visible–telecom entangled photon pair source for quantum communication. *Nat. Phys.* **15**, 373–381 (2019).

[10] Lu, X. *et al.* Efficient telecom-to-visible spectral translation through ultralow power nonlinear nanophotonics. *Nat. Photon.* **13**, 593–601 (2019).

[11] Lukin, D. M. *et al.* 4H-silicon-carbide-on-insulator for integrated quantum and nonlinear photonics. *Nat. Photon.* **14**, 330–334 (2020).

[12] Ma, Z. *et al.* Ultrabright quantum photon sources on chip. *Phys. Rev. Lett.* **125**, 263602 (2020).

[13] Kippenberg, T. J. & Vahala, K. J. Cavity optomechanics: Back-action at the mesoscale. *Science* **321**, 1172–1176 (2008).

[14] Vollmer, F. & Yang, L. Label-free detection with high-Q microcavities: A review of biosensing mechanisms for integrated devices. *Nanophotonics* **1**, 267–291 (2012).

[15] Li, J., Lee, H. & Vahala, K. J. Microwave synthesizer using an on-chip Brillouin oscillator. *Nat. Commun.* **4**, 1–7 (2013).

[16] Kippenberg, T. J., Gaeta, A. L., Lipson, M. & Gorodetsky, M. L. Dissipative Kerr solitons in optical microresonators. *Science* **361** (2018).

[17] Gundavarapu, S. *et al.* Sub-hertz fundamental linewidth photonic integrated Brillouin laser. *Nat. Photon.* **13**, 60–67 (2019).

[18] Jin, W. *et al.* Hertz-linewidth semiconductor lasers using cmos-ready ultra-high-q microresonators. *Nat. Photon.* **14**, 346–352 (2021).

[19] Li, J., Suh, M. G. & Vahala, K. J. Microresonator Brillouin gyroscope. *Optica* **4**, 346–348 (2017).

[20] Liang, W. *et al.* Resonant microphotonic gyroscope. *Optica* **4**, 114–117 (2017).

[21] Lai, Y.-H. *et al.* Earth rotation measured by a chip-scale ring laser gyroscope. *Nat. Photon.* **14**, 345–349 (2020).

[22] Ji, X. *et al.* Ultra-low-loss on-chip resonators with sub-milliwatt parametric oscillation threshold. *Optica* **4**, 619–624 (2017).

[23] Zhang, M., Wang, C., Cheng, R., Shams-Ansari, A. & Lončar, M. Monolithic ultra-high-Q lithium niobate microring resonator. *Optica* **4**, 1536–1537 (2017).

[24] Yang, K. Y. *et al.* Bridging ultrahigh-Q devices and photonic circuits. *Nat. Photon.* **12**, 297 (2018).

[25] Wilson, D. J. *et al.* Integrated gallium phosphide nonlinear photonics. *Nat. Photon.* **14**, 57–62 (2020).

[26] Chang, L. *et al.* Ultra-efficient frequency comb generation in algaas-on-insulator microresonators. *Nat. Commun.* **11**, 1–8 (2020).

[27] Xie, W. *et al.* Ultrahigh-Q AlGaAs-on-insulator microresonators for integrated nonlinear photonics. *Opt. Express* **28**, 32894–32906 (2020).

[28] Liu, J. *et al.* Photonic microwave generation in the X- and K-band using integrated soliton microcombs. *Nat. Photon.* **14**, 486–491 (2020).

[29] Liu, X. *et al.* Aluminum nitride nanophotonics for beyond-octave soliton microcomb generation and self-referencing. *Nat. Commun.* **12**, 5428 (2021).

[30] Gao, R. *et al.* Broadband highly efficient nonlinear optical processes in on-chip integrated lithium niobate microdisk resonators of Q-factor above 10^8. *arXiv:2102.00399* (2021).

[31] Biberman, A., Shaw, M. J., Timurdogan, E., Wright, J. B. & Watts, M. R. Ultralow-loss silicon ring resonators. *Opt. Lett.* **37**, 4236–4238 (2012).

[32] Vernooy, D. W., Ilchenko, V. S., Mabuchi, H., Streed, E. W. & Kimble, H. J. High-Q measurements of fused-silica microspheres in the near infrared. *Opt. Lett.* **23**, 247–249 (1998).

[33] Pfeiffer, M. H. *et al.* Ultra-smooth silicon nitride waveguides based on the damascene reflow process: Fabrication and loss origins. *Optica* **5**, 884–892 (2018).

[34] Pfeiffer, M. H., Liu, J., Geiselmann, M. & Kippenberg, T. J. Coupling ideality of integrated planar high-Q microresonators. *Phys. Rev. Appl.* **7**, 024026 (2017).

[35] Spencer, D. T., Bauters, J. F., Heck, M. J. & Bowers, J. E. Integrated waveguide coupled Si_3N_4 resonators in the ultrahigh-Q regime. *Optica* **1**, 153–157 (2014).

[36] Liu, J. *et al.* Monolithic piezoelectric control of soliton microcombs. *Nature* **583**, 385–390 (2020).

[37] Xiang, C. *et al.* Laser soliton microcombs heterogeneously integrated on silicon. *Science* **373**, 99–103 (2021).

[38] Gorodetsky, M. L., Savchenkov, A. A. & Ilchenko, V. S. Ultimate Q of optical microsphere resonators. *Opt. Lett.* **21**, 453–455 (1996).

[39] Rokhsari, H., Spillane, S. & Vahala, K. Loss characterization in microcavities using the thermal bistability effect. *Appl. Phys. Lett.* **85**, 3029–3031 (2004).

[40] Liu, J. *et al.* Ultralow-power chip-based soliton microcombs for photonic integration. *Optica* **5**, 1347–1353 (2018).

[41] Puckett, M. W. *et al.* 422 million intrinsic quality factor planar integrated all-waveguide resonator with sub-MHz linewidth. *Nat. Commun.* **12**, 1–8 (2021).

[42] Parrain, D. *et al.* Origin of optical losses in gallium arsenide disk whispering gallery resonators. *Opt. Express* **23**, 19656–19672 (2015).

[43] Guha, B. *et al.* Surface-enhanced gallium arsenide photonic resonator with quality factor of 6×10^6. *Optica* **4**, 218–221 (2017).

[44] An, K., Sones, B. A., Fang-Yen, C., Dasari, R. R. & Feld, M. S. Optical bistability induced by mirror absorption: Measurement of absorption coefficients at the sub-ppm level. *Opt. Lett.* **22**, 1433–1435 (1997).

[45] Rokhsari, H. & Vahala, K. J. Observation of Kerr nonlinearity in microcavities at room temperature. *Opt. Lett.* **30**, 427–429 (2005).

[46] Wang, T. *et al.* Rapid and high precision measurement of opto-thermal relaxation with pump-probe method. *Sci. Bull.* **63**, 287–292 (2018).

[47] Liu, J. *et al.* High-yield, wafer-scale fabrication of ultralow-loss, dispersion-engineered silicon nitride photonic circuits. *Nat. Commun.* **12**, 2236 (2021).

[48] Wu, L. *et al.* Greater than one billion Q factor for on-chip microresonators. *Opt. Lett.* **45**, 5129–5131 (2020).

[49] Jung, H. *et al.* Tantala Kerr nonlinear integrated photonics. *Optica* **8**, 811–817 (2021).

[50] Li, J., Lee, H., Yang, K. Y. & Vahala, K. J. Sideband spectroscopy and dispersion measurement in microcavities. *Opt. Express* **20**, 26337–26344 (2012).

[51] Carmon, T., Yang, L. & Vahala, K. Dynamical thermal behavior and thermal self-stability of microcavities. *Opt. Express* **12**, 4742–4750 (2004).

[52] Agrawal, G. P. *Nonlinear fiber optics* (Academic Press, 2007).

[53] Li, J., Lee, H., Chen, T. & Vahala, K. J. Low-pump-power, low-phase-noise, and microwave to millimeter-wave repetition rate operation in microcombs. *Phys. Rev. Lett.* **109**, 233901 (2012).

[54] Yi, X., Yang, Q.-F., Yang, K. Y., Suh, M.-G. & Vahala, K. Soliton frequency comb at microwave rates in a high-q silica microresonator. *Optica* **2**, 1078–1085 (2015).

[55] Miya, T., Terunuma, Y., Hosaka, T. & Miyashita, T. Ultimate low-loss single-mode fibre at 1.55 μm. *Electron. Lett.* **15**, 106–108 (1979).

[56] Pinard, L. *et al.* Toward a new generation of low-loss mirrors for the advanced gravitational waves interferometers. *Opt. Lett.* **36**, 1407–1409 (2011).

[57] Ikeda, K., Saperstein, R. E., Alic, N. & Fainman, Y. Thermal and Kerr nonlinear properties of plasma-deposited silicon nitride/silicon dioxide waveguides. *Opt. Express* **16**, 12987–12994 (2008).

[58] Pu, M., Ottaviano, L., Semenova, E. & Yvind, K. Efficient frequency comb generation in algaas-on-insulator. *Optica* **3**, 823–826 (2016).

[59] Miller, R. C. Optical second harmonic generation in piezoelectric crystals. *Appl. Phys. Lett.* **5**, 17–19 (1964).

[60] Ettoumi, W., Petit, Y., Kasparian, J. & Wolf, J.-P. Generalized Miller formulæ. *Opt. Express* **18**, 6613–6620 (2010).

[61] Gao, H. *et al.* Investigation on the thermo-optic coefficient of silica fiber within a wide temperature range. *J. Light. Technol.* **36**, 5881–5886 (2018).

[62] Matsko, A. B., Savchenkov, A. A., Yu, N. & Maleki, L. Whispering-gallery-mode resonators as frequency references. I. Fundamental limitations. *J. Opt. Soc. Am. B* **24**, 1324–1335 (2007).

[63] Elshaari, A. W., Zadeh, I. E., Jöns, K. D. & Zwiller, V. Thermo-optic characterization of silicon nitride resonators for cryogenic photonic circuits. *IEEE Photon. J.* **8**, 10 (2016).

[64] Tien, C.-L. & Lin, T.-W. Thermal expansion coefficient and thermomechanical properties of SiN_x thin films prepared by plasma-enhanced chemical vapor deposition. *Appl. Opt.* **51**, 7229–7235 (2012).

[65] Shur, M. S. *Handbook Series on Semiconductor Parameters - Volume 2: Ternary and Quaternary III-V Compounds*, 1–36 (World Scientific Publishing Company, Singapore, 1999).

[66] Kim, J. P. & Sarangan, A. M. Temperature-dependent Sellmeier equation for the refractive index of $Al_xGa_{1-x}As$. *Opt. Lett.* **32**, 536–538 (2007).

[67] Wu, C.-L. *et al.* Tantalum pentoxide (Ta_2O_5) based athermal micro-ring resonator. *OSA Continuum* **2**, 1198–1206 (2019).

[68] Tien, C.-L., Lee, C.-C., Chuang, K.-P. & Jaing, C.-C. Simultaneous determination of the thermal expansion coefficient and the elastic modulus of Ta_2O_5 thin film using phase shifting interferometry. *J. Mod. Opt.* (2009).

[69] Okada, Y. & Tokumaru, Y. Precise determination of lattice parameter and thermal expansion coefficient of silicon between 300 and 1500 K. *J. Appl. Phys.* **56**, 314–320 (1984).

[70] Haynes, W. M. (ed.) *CRC Handbook of Chemistry and Physics* (CRC Press, 2016), 97th edn.

[71] Huang, G. *et al.* Thermorefractive noise in silicon-nitride microresonators. *Phys. Rev. A* **99**, 061801 (2019).

[72] Martin, P. *et al.* Mechanical and optical properties of the films of tantalum oxide deposited by ion-assisted deposition. *Mater. Res. Soc. Symp. Proc.* **308**, 583 (1993).

[73] Farsi, A., Siciliani de Cumis, M., Marino, F. & Marin, F. Photothermal and thermo-refractive effects in high reflectivity mirrors at room and cryogenic temperature. *J. Appl. Phys.* **111**, 043101 (2012).

[74] Samsonov, G. V. *The Oxide Handbook*, 145. IFI Data Base Library (Springer US, 1973).

[75] Çengel, Y. A. *Heat Transfer: A Practical Approach* (McGraw-Hill, 2003).

[76] Chen, J., Zhang, G. & Li, B. Thermal contact resistance across nanoscale silicon dioxide and silicon interface. *J. of Appl. Phys.* **112**, 064319 (2012).

[77] Hurley, D. H., Khafizov, M. & Shinde, S. Measurement of the Kapitza resistance across a bicrystal interface. *J. of Appl. Phys.* **109**, 083504 (2011).

Chapter 3

SOLITON PULSE PAIRS AT MULTIPLE COLOURS IN NORMAL DISPERSION MICRORESONATORS

This chapter is based on the following published paper:
Yuan, Z., **Gao, M.**, Yu, Y. *et. al.* Soliton pulse pairs at multiple colours in normal dispersion microresonators. *Nat. Photon.* **17**, 977–983 (2023).
https://doi.org/10.1038/s41566-023-01257-2

Soliton microcombs [1] are helping to advance the miniaturization of a range of comb systems [2]. These combs mode lock through the formation of short temporal pulses in anomalous dispersion resonators. Here, a new microcomb is demonstrated that mode locks through the formation of pulse pairs in normal-dispersion coupled-ring resonators. Unlike conventional microcombs, pulses in this system cannot exist alone, and instead must phase lock in pairs to form a bright soliton comb. Also, the pulses can form at recurring spectral windows and the pulses in each pair feature different optical spectra. This pairwise mode-locking modality extends to higher dimensions and we demonstrate 3-ring systems in which 3 pulses mode lock through alternating pairwise pulse coupling. The results are demonstrated using the new CMOS-foundry platform that has not previously produced bright solitons on account of its inherent normal dispersion [3]. The ability to generate multi-color pulse pairs over multiple rings is an important new feature for microcombs. It can extend the concept of all-optical soliton buffers and memories [4, 5] to multiple storage rings that multiplex pulses with respect to soliton color and that are spatially addressable. The results also suggest a new platform for the study of quantum combs [6–8] and topological photonics [9–11].

3.1 Introduction

Microresonator solitons exist through a balance of optical nonlinearity and dispersion, which must be anomalous for bright soliton generation. Moreover, microresonators must feature high optical Q factors for low pump power operation of the resulting microcomb. While these challenges have been addressed at telecommunications wavelengths using a range of material systems [1], CMOS-foundry resonators do not yet support bright solitons as their waveguides feature normal dispersion [3]. Furthermore, all resonators are dominated by normal dispersion at

shorter wavelengths. For these reasons, there has been keen interest in developing methods to induce anomalous dispersion for bright soliton generation in systems that otherwise feature normal dispersion. Such methods have in common the engineering of dispersion through coupling of resonator mode families, including those associated with concentric resonator modes [12, 13], polarization [14] or transverse modes [15].

Here, we engineer anomalous dispersion in CMOS-foundry resonators by partially-coupling resonators as illustrated in Fig. 3.1(a). This geometry introduces unusual new features to bright soliton generation. For example, spectra resembling single pulse microcombs form instead from pulse pairs as illustrated in Fig. 3.1(a). The pulse pairs circulate in a mirror-image fashion in the coupled rings to form coherent comb spectra (Fig. 3.1(b)) with highly stable microwave beat notes (Fig. 3.1(c)). The interaction of the pulses in the coupling section between the rings is shown to induce anomalous dispersion that compensates for the overall normal dispersion of each ring. This pairwise compensation spectrally recurs thereby opening multiple anomalous dispersion windows for the formation of multi-color soliton pairs. These windows can be engineered during resonator design. Furthermore, the spectral composition of each pulse in a pair is different. Fig. 3.1(b), for example, shows through-port and drop-port spectra that reflect the distinct spectral compositions of pulses in cavity A and cavity B of Fig. 3.1(a). This peculiar effect is also associated with Dirac solitons [16] and it is shown that the 2-ring pulse pair represents a new embodiment of a Dirac soliton as the underlying dynamical equation (see Section 3.6.3) resembles the nonlinear Dirac equation in 1 + 1 dimensions. Pulse pairing is also extendable to higher-dimensional designs with additional normal dispersion rings. For example, in Fig. 3.1(d,e,f) 3 pulses in 3 coupled rings alternately pair to compensate for the normal dispersion of each ring.

In what follows, we first study the dispersion of this system and compare it to previous mode coupling methods. Experimental results including dispersion measurement and comb formation are then presented. Pairwise pulse formation is then studied in the time domain. Finally, because multi-pulse spectra in these systems resemble conventional single-pulse soliton spectra, it is convenient to resolve this ambiguity by denoting 2 and 3 ring systems as bipartite and tripartite soliton microcombs, respectively. The need for this nomenclature becomes clear by the demonstration of multiple pulse-pair states, including a 2 ring microcomb state containing 4 pulses that behaves as a 2-pulse soliton crystal, and a 3 ring state with 12 pulses that behaves

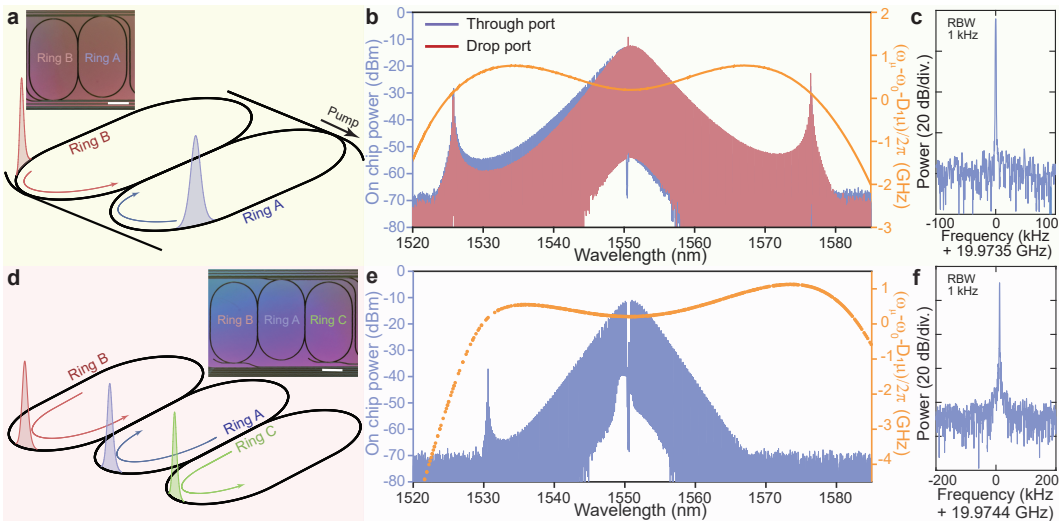

Figure 3.1: **Soliton pulse pair generation in two- and three-coupled-ring microresonators. (a)** Schematic showing coherent pulse pairs that form a composite excitation. Inset: Photomicrograph of the two-coupled-ring resonator used in the experiments. Rings A and B are indicated. The scale bar is 1 mm. **(b)** Simultaneous measurement of optical spectra collected from the through port (pumping port) and drop port in the coupled-ring resonator of panel **a**. The measured mode dispersion is also plotted (orange). Two dispersive waves are observed at spectral locations corresponding to the phase matching condition as indicated by the dispersion curve. **(c)** Radio-frequency spectrum of microcomb beatnote (RBW: resolution bandwidth). **(d)** Illustration of 3 pulse generation in a three-coupled-ring microresonator wherein pulses alternately pair. Inset: Photomicrograph of the three-coupled-ring microresonator used in the experiments. The scale bar is 1 mm. **(e)** Measurement of optical spectrum of the three pulse microcomb. The measured mode dispersion is also plotted (orange). **(f)** Radio frequency spectrum of the microcomb beatnote.

as a 4-pulse soliton crystal.

3.2 Recurring spectral windows

Before addressing pulse pair propagation in the 2-ring and 3-ring systems, the conventional mode-family coupling approach is considered [12–14]. As a representative example, the case of a concentric resonator system is chosen as illustrated in the left panel of Fig. 3.2(a). The characteristics of this system are identical to other methods. First, a phase matching condition must be satisfied by a mode in each resonator such that the absolute mode number in each ring must be equal at the same optical frequency. This mode number determines the wavelength where soliton formation is possible. Second, the free-spectral-range values, FSR_A and FSR_B, of the uncoupled mode families of ring A and ring B must be close in value compared

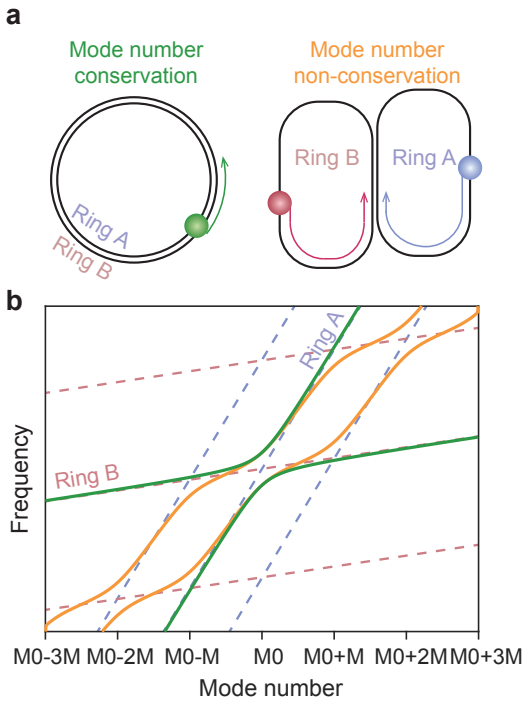

Figure 3.2: **Illustration of inter-ring coupling with (without) mode number conservation. (a)** The top panel shows two different coupling schemes between two ring resonators with different FSRs. The left configuration possesses a continuous rotational symmetry that allows coupling only between modes with the same absolute mode (azimuthal) number (i.e., mode number is conserved). In this case, the coupling opens a gap at the mode crossing and creates two hybrid mode branches (green curves in the lower panel). Here the center blue and red dashed lines represent the resonance frequency of individual rings, and their intersection point corresponds to phase matching. In this work (top right panel), inter-ring mode coupling depends on the matching of resonance frequency instead of mode number (i.e., mode number is not conserved), so that the dispersion is strongly altered at all frequency degeneracies. **(b)** In the lower panel, frequency degeneracies are marked by crossings between the blue and red dashed lines, which still represent the dispersion of individual rings, but with the abscissa shifted by integer numbers as a result of spectral folding allowed by non-conservation of mode number. Compared to the first configuration, the dispersion curve of the coupled rings repeats itself every $2M$ modes, with $M = 1/(2\epsilon)$ set by the length contrast of the rings.

to their average FSR = $(\mathrm{FSR}_A + \mathrm{FSR}_B)/2$ so that phase matching occurs over a large number of modes. With these conditions satisfied, the resulting dispersion will be as illustrated schematically in the Fig. 3.2(b) (green curves). Comparison to the uncoupled dispersion curves (center dashed blue and red lines) shows that anomalous dispersion is possible for the upper mode family branch in the spectral vicinity of the phase matching mode number M_0.

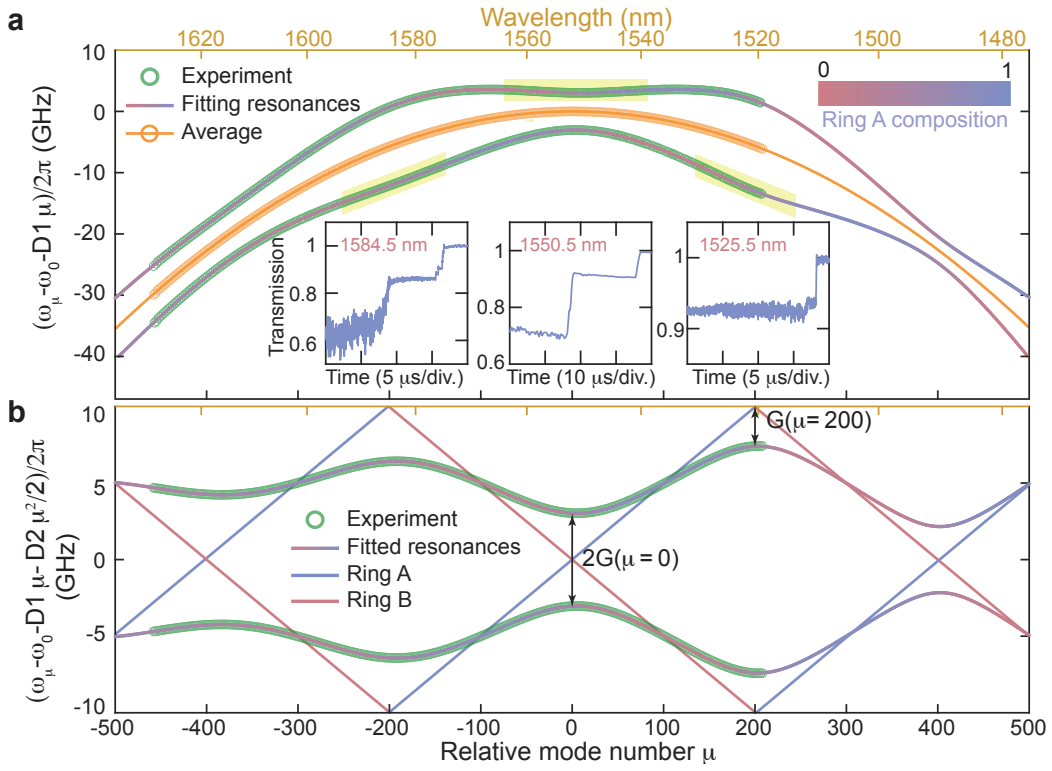

Figure 3.3: **Mode number non-conservation coupling and recurring bright soliton windows.** **(a)** Measured frequency dispersion of the coupled resonator (green circles) versus relative mode number μ. Here $D_1/(2\pi) = 19.9766$ GHz, and ω_0 is chosen so that $\mu = 0$ is at the crossing center (1552.3 nm). Multiple anomalous dispersion windows appear around $\mu = 0$ and 400 for the upper branch and $\mu = -200$ and 200 for the lower branch. The anomalous dispersion window near $\mu = -200$, 0 and 200 have been highlighted. Solid curves are fittings and the color refers to the energy contribution from ring A (obtained from theoretical calculations). The average of the upper and lower branch mode frequencies is plotted as orange circles and fitted by a second-order dispersion model (orange curve). Inset: transmission observed when scanning a laser over resonances in the anomalous dispersion windows. Soliton steps are observed around $\mu = -200$, 0 and 200. **(b)** Measured relative frequency dispersion of the coupled resonator (green circles) versus relative mode number μ. Here $D_2/(2\pi) = -283.0$ kHz, and other parameters are the same as panel (b). Solid curves are the theoretical fittings described by Eq. (3.2). Fitted mode frequency dispersion diagrams of the single rings without coupling are shown as red and blue lines.

Next, consider the case where two rings are placed side-by-side and coupled together as illustrated in the right panel of Fig. 3.2(a). The two ring cavities differ only in length, with ring B slightly longer than ring A so that $\mathrm{FSR}_A > \mathrm{FSR}_B$. Considering the straight coupling section from a coupled-mode perspective, modes of

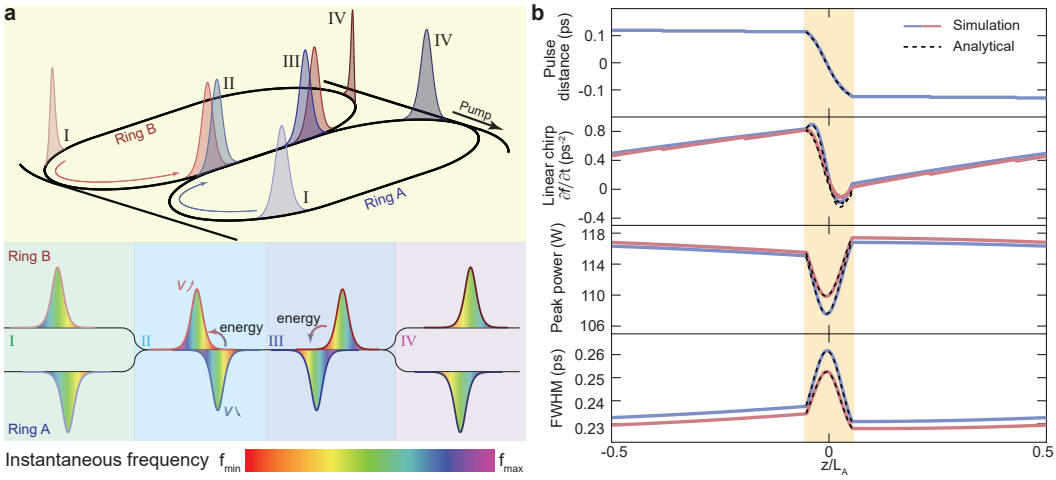

Figure 3.4: **Temporal evolution of the soliton pulse pair in the two-ring coupled resonator. (a)** Upper panel: Illustration of the time evolution of the soliton pair inside the two rings during one round trip time. Lower panel: Snapshots of the pulses at different positions. In the non-coupled regions (I and IV), pulses accumulate positive chirp due to nonlinearity and normal dispersion of the waveguide. Pulse in ring A is leading in time at I due to shorter ring circumference. When the pulses enter the coupling region (II), the pulses exchange energy, which leads to relative position shifts as well as chirp compensation (III). The pulses exit the coupled region (IV) with position shifts and chirping compensated. **(b)** Simulated pulse pair properties are plotted versus pulse position in each ring during one round trip. The two rings are aligned at the coupling region center, and the surplus length in ring B is omitted in the figure. The yellow shaded area represents the coupling region. The quantities are, from top to bottom: pulse timing difference (pulse center-to-center), linear chirp, peak power, and full width at half maximum. The blue (red) lines represent simulation results for the pulse in ring A (B). The dashed lines are analytical results from a linear coupling model (see Methods), and are consistent with simulation results.

the two rings will strongly couple if they have matching wavevectors (or equivalently, resonance frequencies), while there are no requirements on mode number matching of the rings (i.e., mode number is not conserved). In comparison to the concentric ring configuration, this dramatically modifies the dispersion relation as illustrated in Fig 3.2b, where the orange curves give the resulting dispersion. Due to the loss of mode number conservation, inter-ring coupling pushes the resonance frequencies away from that of the individual rings (blue and red dashed lines) at all frequency degeneracies, so that recurring anomalous dispersion windows now appear in the spectrum. These result from spectral folding that occurs between the cavity resonances. As an aside, because mode number is not conserved, modeling

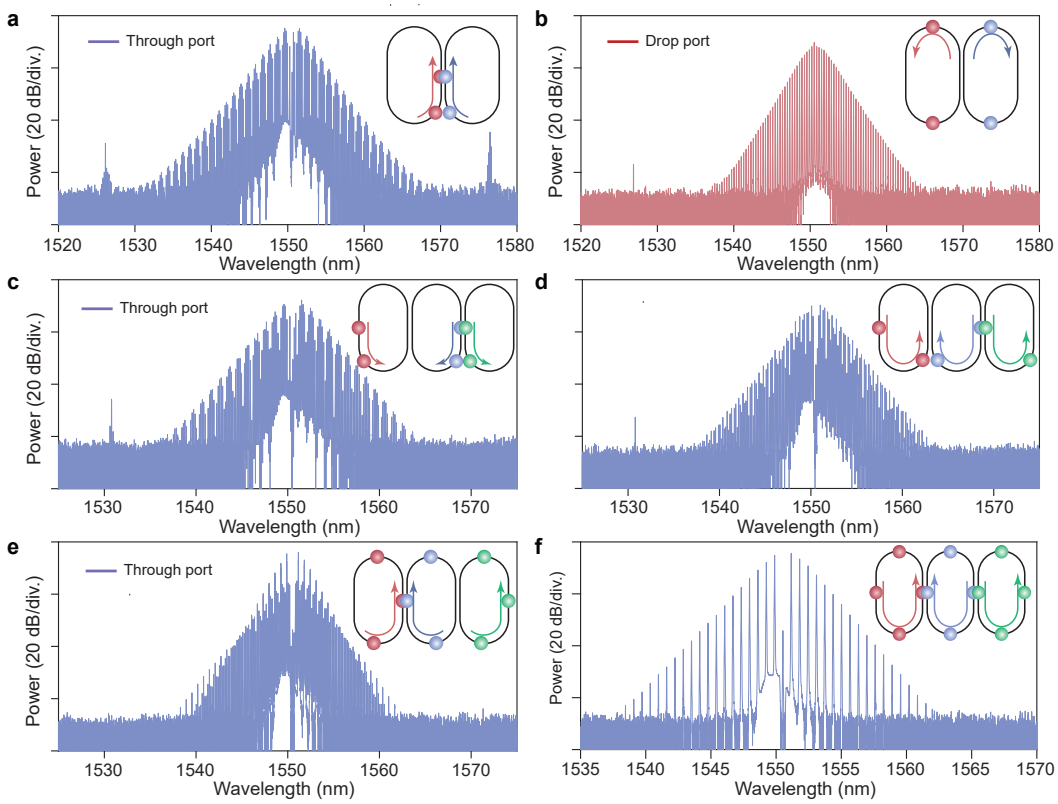

Figure 3.5: **Observation of bipartite and tripartite multi soliton states in two- and three-coupled-ring microresonators. (a, b)** Optical spectra of bipartite two-soliton states with different relative soliton positions. The state in panel (b) is a two-soliton crystal state. Insets: relative position of the two solitons inside each microresonator. **(c, d)** Through port optical spectra of tripartite two-soliton states with different relative positions. Inset: relative position of the two solitons inside each microresonator. **(e)** Through port optical spectrum of a tripartite three-soliton state. Inset: relative position of the three solitons inside each microresonator. **(f)** Through port optical spectrum of a tripartite four-soliton crystal. Inset: relative position of the four solitons inside each microresonator.

of this dispersion proceeds differently relative to the standard coupled-mode family approach (see Appendix F.1 and F.2).

3.3 Dispersion measurements and soliton pulse pair generation

The coupled resonators in both 2-ring and 3-ring geometries consist of thin Si_3N_4 single-mode racetrack waveguide resonators with the same cross sections. Bus waveguides are provided for external coupling. Optical images of 2-ring and 3-ring coupled resonators are provided in Fig. 3.1(a) and 3.1(d) insets. For the coupled 2-ring device, the round trip length of ring A is 9.5 mm, which corresponds to

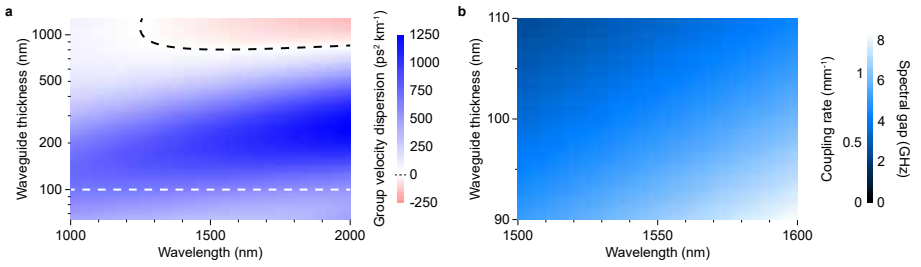

Figure 3.6: **Dispersion and coupling characteristics of the ring waveguide. (a)** Finite element simulation results for dispersions of straight Si_3N_4 waveguides with fixed width (2.8 μm) as a function of wavelength and waveguide thickness. The zero-dispersion boundary is marked as the black dashed curve. Nominal waveguide thickness (100 nm) for the current process is marked as the white dashed line. **(b)** Numerical simulations of the waveguide coupling rate g_{co} and the corresponding spectral gap ($2G = g_{co}L_{co}D_1/\pi$, with $L_{co} = 1.0$ mm and $D_1 = 2\pi \times 20$ GHz) are plotted as a function of wavelength and waveguide thickness. The gap between waveguides is 2.4 μm.

a free spectral range (FSR) of ~20 GHz, and ring B is 0.5% longer than ring A. For the 3-ring device, the rightmost ring has a circumference of 9.5 mm, and each other ring is 0.3% longer than its right neighbor. The rings feature high intrinsic Q factors exceeding 75 million, but individually each ring does not support bright soliton formation around 1550 nm due to the strong normal dispersion associated with the low confinement waveguide structure (see Fig. 3.6). Prior studies on similar single-ring structures have generated only dark pulse comb spectra [3].

The measured resonance frequency dispersion (green points) for the 2-ring system with comparison to theory (solid lines) is shown in Fig. 3.3(a). The dispersion of the 3-ring resonator is discussed in Section F.2. The measurement is performed using a radio-frequency calibrated interferometer in combination with a wavelength-tunable laser [17]. The coupled resonators produce the two bands measured in Fig. 3.3(a) where three anomalous dispersion windows are highlighted. At each window, soliton steps are observed when scanning the laser frequency over a cavity resonance (see insets in Fig. 3.3(a)). Operation at the longest and shortest wavelength windows (1584.5 nm and 1525.5 nm) was challenging due to low laboratory laser power and as a result, the time duration of the soliton steps for these wavelengths is relatively shorter.

Analysis shows that the average frequency of the two bands (i.e., $\omega_\mu \equiv (\omega_{\mu,+} + \omega_{\mu,-})/2$) is given by the mode frequency for a length-averaged resonator at the same

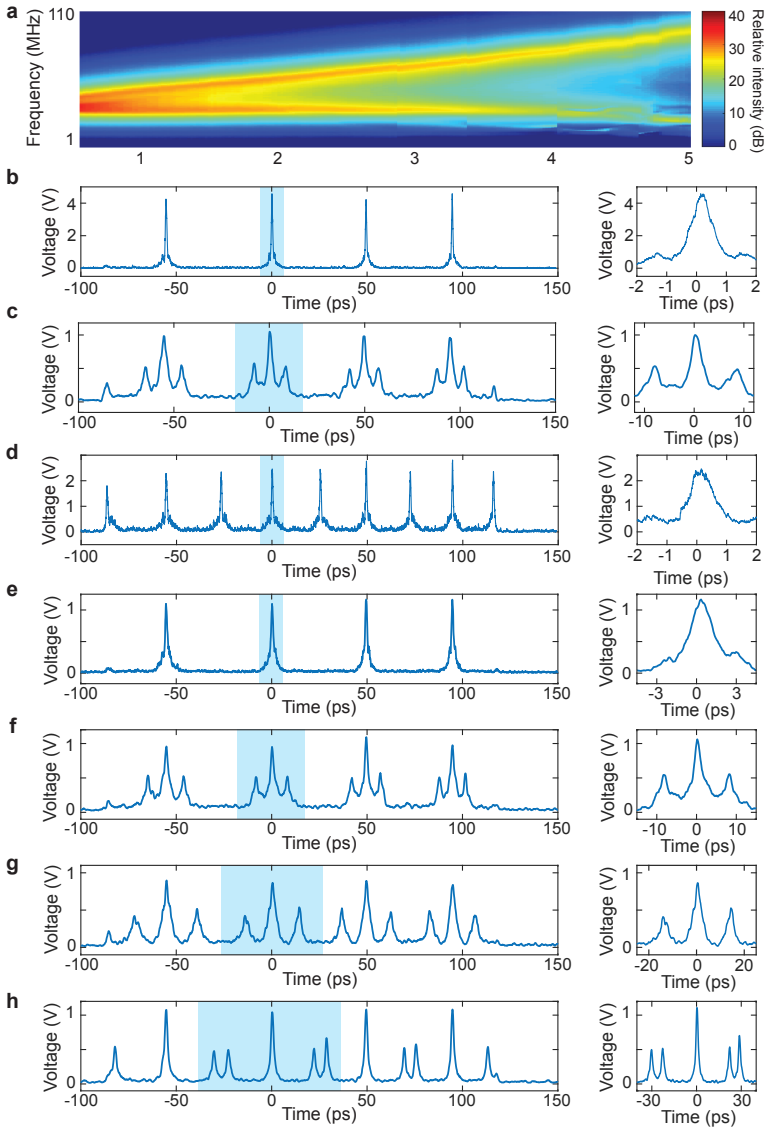

Figure 3.7: C **and** $\mathcal{S}$ **resonances and autocorrelation measurements of solitons in the coupled-ring resonator.** **(a)** The relative frequency of the C and $\mathcal{S}$ resonances are measured using a vector network analyzer and plotted versus tuning voltage in the two-ring resonator. **(b,c,d,e,f,g,h)** Experimental autocorrelation measurements of: **(b)** single soliton state in a two-ring resonator (state in Fig. 3.1(b)); **(c)** two soliton state in a two-ring resonator (state in Fig. 3.5(a)); **(d)** two soliton crystal state in a two-ring resonator (state in Fig. 3.5(b)); **(e)** single soliton state in a three-ring resonator (state in Fig. 3.1(e)); **(f)** two soliton state in a three-ring resonator (state in Fig. 3.5(c)); **(g)** two soliton state in a three-ring resonator (state in Fig. 3.5(d)); **(h)** three soliton state in a three-ring resonator (state in Fig. 3.5(e)). The resolution of the autocorrelation setup is 100 fs. The zoom-in of each autocorrelation measurements are shown in corresponding right panel.

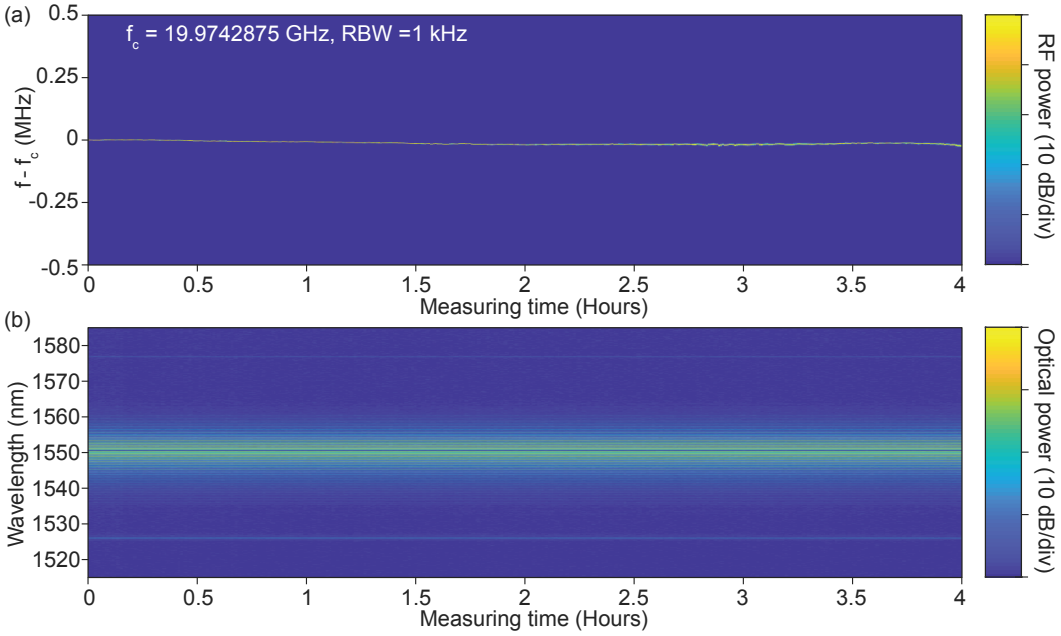

Figure 3.8: **Stable soliton operation in the two-ring resonator measured over 4 hours. (a)** Continuous measurement of the RF beat note of a pulse pair soliton microcomb over 4 hours. The RF beatnote peak drift over 4 hours is within 25.7 kHz (1.29 PPM). f: RF frequency, f_c: center RF frequency, RBW: resolution bandwidth. **(b)** Simultaneous measurement of the optical spectrum of the pulse pair soliton microcomb in panel **a** over 4 hours.

mode number (see Appendix F.1). We note that averaging the frequencies of the two bands removes the effect of the coupling entirely, and the resulting average dispersion shown in Fig. 3.3(a) (orange points) closely matches a parabolic-shaped dispersion curve (orange curve). Accordingly, this average frequency can be described by a second-order dispersion model:

$$\omega_\mu \approx \omega_0 + D_1\mu + \frac{1}{2}D_2\mu^2 \tag{3.1}$$

where ω_0 is the mode frequency at $\mu = 0$ and μ is a relative mode number referenced to the frequency degeneracy at 1552.3 nm. D_1 is the length-averaged FSR for the resonator at $\mu = 0$, $D_2 = -cD_1^2\beta_2/n_\mathrm{g}$ is the second-order dispersion parameter at $\mu = 0$ with group velocity dispersion β_2 and waveguide group index n_g.

On the other hand, the effect of the coupling is made clearer by plotting the mode frequencies relative to the averaged frequency (i.e., relative mode frequency $\omega_{\mu,\pm} - \omega_\mu$) as shown in Fig. 3.3(b). Without inter-ring coupling, the relative mode frequencies of the single rings appear as straight lines on the mode spectrum plot. These lines are related to the straight dashed lines for the uncoupled resonators in

Fig. 3.2(a). Their positive and negative slopes in Fig. 3.3(b) result from removing a linear component of dispersion in this plot given by the average FSR, D_1. Mode number walk-off also causes the lines to vertically wrap around at $\pm D_1/2$. For the rings used here, the length of ring B is 0.5% longer than ring A, and frequency degeneracy of the rings occurs every 200 ring A modes (or every 201 ring B modes). The introduction of coupling opens gaps at all frequency degeneracies, regardless of whether the absolute mode number is matched.

More detailed analysis shows that each of the gap widths equals $2G \equiv g_{\mathrm{co}} L_{\mathrm{co}} D_1/\pi$, where g_{co} is the coupling strength per unit length and L_{co} is the effective coupler length. The full dispersion relation is found to be (see Appendix F.1):

$$\omega_{\mu,\pm} = \omega_\mu \pm \frac{D_1}{2\pi} \arccos\left[\cos(g_{\mathrm{co}} L_{\mathrm{co}}) \cos\left(2\pi\epsilon\mu\right)\right] \tag{3.2}$$

where $\epsilon = (L_{\mathrm{B}} - L_{\mathrm{A}})/(L_{\mathrm{B}} + L_{\mathrm{A}})$ is the length contrast of the rings, and L_{A} (L_{B}) is the length of ring A (B). For the current design $\epsilon = 1/401$, and the gap is modulated with respect to mode number with period $\epsilon^{-1} = 401$ (corresponding to 8 THz in the spectrum). The small length contrast ϵ guarantees the wide spectral range of the anomalous dispersion window. Overall, there is very good agreement between the model and the measured data in Fig. 3.3(a) and Fig. 3.3(b), and the fitting allows determination of key resonator parameters (see figure caption). As an aside, the spectral gap is smaller at larger mode numbers, which can be attributed to the wavelength dependence of g_{co}, as shorter wavelength results in stronger mode confinement, and hence smaller coupling with the adjacent waveguide. When combined with the original normal dispersion of each ring, the net dispersion for coupled system remains anomalous around $\mu = 0$ and 400 for the upper branch and around $\mu = -200$ and 200 for the lower branch.

Besides the observation of soliton steps (Fig. 3.3(a)), microcomb spectra measured around 1550 nm for through port (ring A) and drop port (ring B) are presented in Fig. 3.1(b). The microcomb was stabilized by measuring comb power from the through port and feeding back to the pump laser frequency, which controls the pump-cavity offset frequency [18]. The comb exhibits excellent stability and measurements of comb spectra and repetition rate over 4 hours of operation are provided in the Fig. 3.8. The theoretical pulse width of the comb spectra in the figure is estimated to be $\sim$ 250 fs. Comb coherence and soliton pulse behavior were confirmed in several ways. The radio-frequency spectrum of the soliton beatnote is presented in Fig. 3.1(c). Also, the soliton $\mathcal{S}$-resonance and $\mathcal{C}$-resonance [19, 20] were measured

using a vector network analyzer. Plots of their relative frequencies versus laser-cavity detuning are given in Fig. 3.7. Finally, time domain autocorrelation measurements are also given in the Fig. 3.7. Multiple pulse pair comb states are discussed in the next section and autocorrelation measurements for these comb states are also included in Fig. 3.7.

Through port and drop port spectra correspond to pulses in ring A and ring B, and show these pulses are both different from each other and deviate from the conventional sech^2 shape of Kerr solitons. The through port spectrum is stronger (weaker) than the drop port at shorter (longer) wavelengths. This is a result of this system representing a new version of the Dirac soliton [16] as discussed in the Methods section.

In Fig. 3.1(b), two strong dispersive waves (DWs) are observed near 1526 nm and 1577 nm. These correspond to spectral locations where modes of the coupled resonator phase-match to the soliton comb line. For comparison, the dispersion in the vicinity of the comb spectrum has been overlaid in the figure. The DWs broaden the soliton spectrum and provide higher power comb lines (1.5 μW on-chip power at shorter wavelength and 5.4 μW at longer wavelength), which is advantageous for application to optical frequency division [2]. To further confirm coherence, the radio frequency spectrum of the soliton beatnote is presented (Fig. 3.1(c)). Finally, the soliton $\mathcal{S}$-resonance and C-resonance [19] were measured using a vector network analyzer. Plots of their relative frequencies versus laser-cavity detuning are given in Fig. 3.7.

Comb generation in the 3-ring system was also demonstrated (see Fig. 3.1(d)). Here, the coupling on both sides of the middle ring creates local anomalous dispersion windows (Appendix F.2). Fig. 3.1(e) shows the spectrum of three pulses as measured from the center ring. The measured dispersion is also included in the figure. The pump laser wavelength is several nanometers away from the anomalous dispersion center frequency, and, as a result, the spectrum features only one dispersive wave at the shorter wavelength side. The radio frequency spectrum of the soliton beatnote is presented in Fig. 3.1(f), indicating good coherence.

3.4 Pulse pairs and multi-partite states

This section describes a time domain picture of the coupled-ring system. Besides providing a complementary physical picture (to the dispersion analysis above), simulations of mode locking show microcombs form as phase-locked pulse pairs where

the pulses have opposite phases. The pair viewpoint provides a powerful framework for visualization of mode locking that readily explains observable multi pulse-pair states and higher dimensional systems comprising multiple coupled cavities.

Simulations of pulse propagation in the 2-ring system are presented in Fig. 3.4(a). Here, the ring FSRs and couplings are those of the experimental system studied in Fig. 3.3 and excitation occurs for the mode $\mu = 0$. As shown in Fig. 3.4(b), each pulse undergoes shape, chirp, and pulse width variations that repeat upon each round trip. Before entering the coupling region (point I in Fig. 3.4(a)), the chirp of both pulses has increased due to uncompensated Kerr nonlinearity from propagation in normal dispersion waveguides of each ring. Pulse chirp is indicated in the lower panel of Fig. 3.4(a), where the color represents instantaneous frequency. The pulse in ring B (red) also lags behind its counterpart in ring A (blue) due to the difference in ring lengths. However, upon entering the coupling region (point II), the ring B (A) pulse accelerates (decelerates) and becomes the leading (lagging) pulse when exiting the coupling region (point III). In the meantime, the chirp of both pulses decreases through the coupling region. Upon exiting the coupling region, the pulses propagate in their respective waveguides (point IV) where chirp increases as the pulses circle back through point I. Detailed numerical simulations are used to further explore and confirm the pulse pair evolution (Fig. 3.4(b)).

This picture of pairwise round trip compensation of normal dispersion enables understanding of how compensation works for multi-pair systems as well as for higher dimensions with additional ring cavities. Specifically, it constrains the ways these states are allowed to form. For example, consider the coupled-ring states in Fig. 3.5(a,b) wherein 2 pulse pairs circulate in a mirror-image like fashion to form the observed spectra. Here, to reduce confusion with corresponding multi-pulse soliton systems, we adopt the nomenclature that a single pulse pair in a 2 ring system is a bipartite single soliton (see Fig. 3.1(a,b)), while multi-pair states in the same are bipartite multi soliton systems. Specfically, the states in Fig. 3.5(a,b) are bipartite 2 soliton states. The state in Fig. 3.5(b) is moreover a bipartite 2-soliton crystal. Notice that the requirements imposed on pulse pairing allow a one-to-one correspondence between conventional multi-soliton states and bipartite states, since the pulse configurations in each ring resonator must mirror image its neighboring ring.

The same is true for higher dimensional systems. For example, three pulses compensate normal dispersion by alternating their pairwise coupling as illustrated in Fig.

3.1(d). Here, the outer ring pulses experience compensation once per cycle, but the inner ring pulse experiences compensation twice per cycle. Moreover, the pairwise compensation works when additional pulses are added to each cavity. For example, measurement of tripartite 2 soliton, 3 soliton and a 4 soliton crystal state (containing respectively 6, 9, and 12 pulses) are presented in Fig. 3.5(c,d,e,f). Notice that the measured comb line spacing (79.93 GHz) for the crystal state is four times the FSR of a single ring as is consistent with a conventional 4 soliton crystal state.

3.5 Discussion

In summary, we have observed a new type of microcavity soliton that mode locks as pulse pairs distributed spatially over multiple ring resonators. The requirement to compensate overall normal dispersion of the rings requires that the pulses in each ring arrange themselves as a mirror image of the pulses in neighboring rings. Partial coupling of the resonators creates a situation in which ring resonator mode number is not conserved and this enables recurring spectral windows where the pairs can be formed. The presented bright soliton results use the CMOS-ready process that has previously been restricted to only dark pulse generation. The ability to distribute coherent pulses over multiple rings with individual taps and with simultaneous pulse formation at multiple wavelengths presents new opportunities for soliton science and microcomb applications.

3.6 Methods and supplementary information

3.6.1 Resonator design

The rings consist of Si_3N_4 waveguides (2800 nm width and 100 nm thickness) embedded in silica and formed into a racetrack shape. The waveguide cross-section only supports one polarization mode. Detailed information on fabrication steps can be found elsewhere [3]. For the two-ring device, ring A has a circumference of 9.5 mm, and ring B is 0.5% longer. For the three-ring device, the rightmost ring has a circumference of 9.5 mm, and each other ring is 0.3% longer than its right neighbor. The adiabatic waveguide bend has the shape of a fifth-degree spline such that the curvature is continuous along the curve and transition loss is minimized. The gap between the inner edges of the two waveguides in the coupling region is 2400 nm, and the effective coupling length is 1.0 mm including contributions from the adiabatic bend (which is 10.5% of the shortest ring circumference).

The simulated dispersion of straight Si_3N_4 waveguides with 2.8 μm width are shown in Extended Data Fig. 3.6(a). For these calculations, the effective index

of the fundamental TE mode was calculated and the group velocity dispersion determined through $\beta_2 = \lambda^3/(2\pi c^2)\partial^2 n_{\mathrm{wg}}/\partial\lambda^2$, where λ is the vacuum wavelength. For waveguides with thickness under 780 nm, the fundamental TE mode always features normal dispersion in the C-band. To maintain high optical Q factors, the waveguide thickness is about 100 nm for the current process, which places the waveguide deep into the normal dispersion region.

Simulations of the waveguide coupling rate g_{co} with 2.4 μm coupling gap are presented in Extended Data Fig. 3.6(b). The effective index of the two supermodes at the coupling region is calculated, and the coupling rate g_{co} is related to the index difference of the supermodes Δn_{wg} by $g_{\mathrm{co}} = \Delta n_{\mathrm{wg}}\pi/\lambda$. With a thinner waveguide or a longer wavelength, the optical confinement is weaker, leading to a larger coupling strength and larger spectral gap width.

3.6.2 Dispersion measurement and fitting

The dispersion is measured by sweeping a mode-hop-free laser while pumping the resonator, recording the mode positions from the transmission signal, and comparing it against a calibrated Mach-Zehnder interferometer [17]. The averaged mode frequencies are fitted by a second-order dispersion model given by Eq. (3.1) with $D_1 = 2\pi \times 19.9766$ GHz and $D_2 = 2\pi \times (-283.0)$ kHz. The relative frequencies are fitted with Eq. (3.2), where we assume that the coupling is exponentially decaying with respect to mode number:

$$g_{\mathrm{co}} = g_{\mathrm{co},0} \exp(-\mu/\mu_g) \tag{3.3}$$

where μ_g gives a decay scale. The fitting uses $g_{\mathrm{co},0}$, μ_g and the crossing center position as fitting parameters, while D_1 and D_2 are derived from the mode frequency average fitting and $\epsilon = 1/401$ is taken from design values. Fitting gives $g_{\mathrm{co},0}L_{\mathrm{co}} = 0.954$ and $\mu_g = 1196$. The coupling is equivalent to a 33% : 67% coupler near $\mu = 0$, and the coupling rate increases by 5.4% for every 10 nm increased near 1550 nm. The coupling rate and decaying scale are close to simulation results ($g_{\mathrm{co},0}L_{\mathrm{co}} = 0.782$, 5.5% increase per 10 nm; see Extended Data Fig. 3.6(b)). Differences between measured and simulated values may result from refractive index and layer thickness variations.

3.6.3 Dynamics of the soliton pulse pair

The optical fields in the two rings are governed by the coupled nonlinear wave equations:

$$\begin{aligned}\frac{\partial E_{\mathrm{A}}}{\partial t} =& -\left(\frac{\kappa}{2}+i\delta\omega_{\mathrm{A}}\right)E_{\mathrm{A}} - v_{\mathrm{g}}\frac{\partial E_{\mathrm{A}}}{\partial z} - i\frac{\beta_2 v_{\mathrm{g}}^3}{2}\frac{\partial^2 E_{\mathrm{A}}}{\partial z^2} \\ &+ ig_{\mathrm{co}}v_{\mathrm{g}}\chi_{\mathrm{co}}(z)E_{\mathrm{B}} + ig_{\mathrm{NL}}|E_{\mathrm{A}}|^2E_{\mathrm{A}} + F \qquad (3.4)\\ \frac{\partial E_{\mathrm{B}}}{\partial t} =& -\left(\frac{\kappa}{2}+i\delta\omega_{\mathrm{B}}\right)E_{\mathrm{B}} - v_{\mathrm{g}}\frac{\partial E_{\mathrm{B}}}{\partial z} - i\frac{\beta_2 v_{\mathrm{g}}^3}{2}\frac{\partial^2 E_{\mathrm{B}}}{\partial z^2} \\ &+ ig_{\mathrm{co}}v_{\mathrm{g}}\chi_{\mathrm{co}}(z)E_{\mathrm{A}} + ig_{\mathrm{NL}}|E_{\mathrm{B}}|^2E_{\mathrm{B}} \qquad (3.5)\end{aligned}$$

accompanied by periodic boundary conditions in the z direction, where $E_{\mathrm{A,B}}$ denotes the optical field in the two rings normalized to photon numbers in the corresponding length-averaged ring, $\kappa = \kappa_{\mathrm{in}} + \kappa_{\mathrm{ex}}$ is the loss rate (sum of intrinsic and external loss) for the individual rings (assumed to be identical for ring A and B), which can be linked to the quality factors via $\kappa = \omega_0/Q$, $\kappa_{\mathrm{in}} = \omega_0/Q_{\mathrm{in}}$, and $\kappa_{\mathrm{ex}} = \omega_0/Q_{\mathrm{ex}}$. Also, $\delta\omega_{\mathrm{A,B}} = \omega_{0\mathrm{A,B}} - \omega_{\mathrm{p}}$ is the pump laser detuning, $v_{\mathrm{g}} = c/n_{\mathrm{g}}$ is the group velocity of the waveguide, $z \in [0, L_{\mathrm{A,B}})$ is the resonator coordinate with $L_{\mathrm{A,B}}$ the ring length, β_2 is the waveguide group velocity dispersion, g_{co} is the coupling strength between the two waveguides in the coupling region, $\chi_{\mathrm{co}}(z)$ is the indicator function with value 1 in the coupling region and 0 elsewhere, $g_{\mathrm{NL}} = \hbar\omega_0^2 D_1 n_2/(2\pi n_{\mathrm{g}} A_{\mathrm{eff}})$ is the nonlinear coefficient with A_{eff} being the effective mode area, and $F = \sqrt{\kappa_{\mathrm{ex}} P_{\mathrm{in}}/\hbar\omega_0}$ is the pump term where P_{in} is the on-chip pump power. For simplicity, the pump and loss terms are averaged over the entire resonator without considering the detailed coupling geometry between the rings and the bus waveguides.

To demonstrate that the resulting soliton resembles the optical Dirac soliton [16], we will convert the above equations into a form that is analogous to the Dirac equation in quantum field theory. We start by defining a common roundtrip variable θ for both resonators, with $\theta = 2\pi z/L_{\mathrm{A}}$ for ring A and $\theta = 2\pi z/L_{\mathrm{B}}$ for ring B. With this change, the LLE reads

$$\begin{aligned}\frac{\partial E_{\mathrm{A}}}{\partial t} =& -\left(\frac{\kappa}{2}+i\delta\omega_{\mathrm{A}}\right)E_{\mathrm{A}} \\ &- \frac{D_1}{1-\epsilon}\frac{\partial E_{\mathrm{A}}}{\partial\theta} + i\frac{D_2}{2(1-\epsilon)^2}\frac{\partial^2 E_{\mathrm{A}}}{\partial\theta^2} \\ &+ ig_{\mathrm{co}}v_{\mathrm{g}}\chi_{\mathrm{co}}(\theta)E_{\mathrm{B}} + ig_{\mathrm{NL}}|E_{\mathrm{A}}|^2E_{\mathrm{A}} + F \qquad (3.6)\end{aligned}$$

and similarly for E_{B} with ϵ replaced by $-\epsilon$ and pump term dropped. The unified roundtrip variable breaks the correspondence of waveguide sections in the coupling

region, but these have been neglected as the pulse width is much larger compared to the ring length difference (Fig. 3.3(b)). Switching to the co-moving frame of the pulse [$\psi_{\mathrm{A,B}}(\theta,t) \equiv E_{\mathrm{A,B}}(\theta + D_1 t, t)$] leads to

$$\begin{aligned}\frac{\partial \psi_{\mathrm{A}}}{\partial t} \approx &-\left(\frac{\kappa}{2} + i\delta\omega_{\mathrm{A}}\right)\psi_{\mathrm{A}} - \epsilon D_1 \frac{\partial \psi_{\mathrm{A}}}{\partial \theta} + i\frac{D_2}{2}\frac{\partial^2 \psi_{\mathrm{A}}}{\partial \theta^2} \\ &+ iG\psi_{\mathrm{B}} + ig_{\mathrm{NL}}|\psi_{\mathrm{A}}|^2\psi_{\mathrm{A}} + F \end{aligned} \tag{3.7}$$

and similarly for E_{B}, where we retain the lowest order of ϵ and further assume that the pulse varies slowly within one round trip such that the effect of coupling is averaged over the resonator length (i.e., uniform coupling which conserves the mode number). Finally, shifting the wavevector and frequency reference ($\tilde{\psi}_{\mathrm{A,B}} \equiv \psi_{\mathrm{A,B}} \exp(ik_0\theta - i\omega_0 t)$) gives

$$\begin{aligned}\frac{\partial \tilde{\psi}_{\mathrm{A}}}{\partial t} \approx &-i\left(\delta\omega_{\mathrm{A}} - \epsilon D_1 k_0 + \omega_0\right)\tilde{\psi}_{\mathrm{A}} - \epsilon D_1 \frac{\partial \tilde{\psi}_{\mathrm{A}}}{\partial \theta} + iG\tilde{\psi}_{\mathrm{B}} \\ &+ ig_{\mathrm{NL}}|\tilde{\psi}_{\mathrm{A}}|^2\tilde{\psi}_{\mathrm{A}} \\ &- \frac{\kappa}{2}\tilde{\psi}_{\mathrm{A}} + i\frac{D_2}{2}\frac{\partial^2 \tilde{\psi}_{\mathrm{A}}}{\partial \theta^2} + F\exp(ik_0\theta - i\omega_0 t) \end{aligned} \tag{3.8}$$

$$\begin{aligned}\frac{\partial \tilde{\psi}_{\mathrm{B}}}{\partial t} \approx &-i\left(\delta\omega_{\mathrm{B}} + \epsilon D_1 k_0 + \omega_0\right)\tilde{\psi}_{\mathrm{B}} + \epsilon D_1 \frac{\partial \tilde{\psi}_{\mathrm{B}}}{\partial \theta} + iG\tilde{\psi}_{\mathrm{A}} \\ &+ ig_{\mathrm{NL}}|\tilde{\psi}_{\mathrm{B}}|^2\tilde{\psi}_{\mathrm{B}} \\ &- \frac{\kappa}{2}\tilde{\psi}_{\mathrm{B}} + i\frac{D_2}{2}\frac{\partial^2 \tilde{\psi}_{\mathrm{B}}}{\partial \theta^2} \end{aligned} \tag{3.9}$$

where we assume that we are pumping near the crossing center such that $\epsilon D_1 \ll D_2 k_0$ and high-order terms in k_0 could be neglected. Choosing $k_0 = (\delta\omega_{\mathrm{A}} - \delta\omega_{\mathrm{B}})/(2\epsilon D_1)$ and $\omega_0 = -(\delta\omega_{\mathrm{A}} + \delta\omega_{\mathrm{B}})/2$ removes the effective detuning terms from the two equations.

This can now be compared to the massive Dirac equation in $1+1$ dimension written in a chiral basis [21]:

$$\partial_t \psi_{\mathrm{L}} = -c\partial_x \psi_{\mathrm{L}} + i\frac{Mc^2}{\hbar}\psi_{\mathrm{R}} \tag{3.10}$$

$$\partial_t \psi_{\mathrm{R}} = +c\partial_x \psi_{\mathrm{R}} + i\frac{Mc^2}{\hbar}\psi_{\mathrm{L}} \tag{3.11}$$

where M is interpreted as the mass, and corresponds to the coupling term (the massless Dirac equation with $M = 0$ would correspond to an uncoupled system with frequency gap closed). The momentum term corresponds to the FSR difference. The nonlinear term converts the equation into a nonlinear Dirac equation, although there

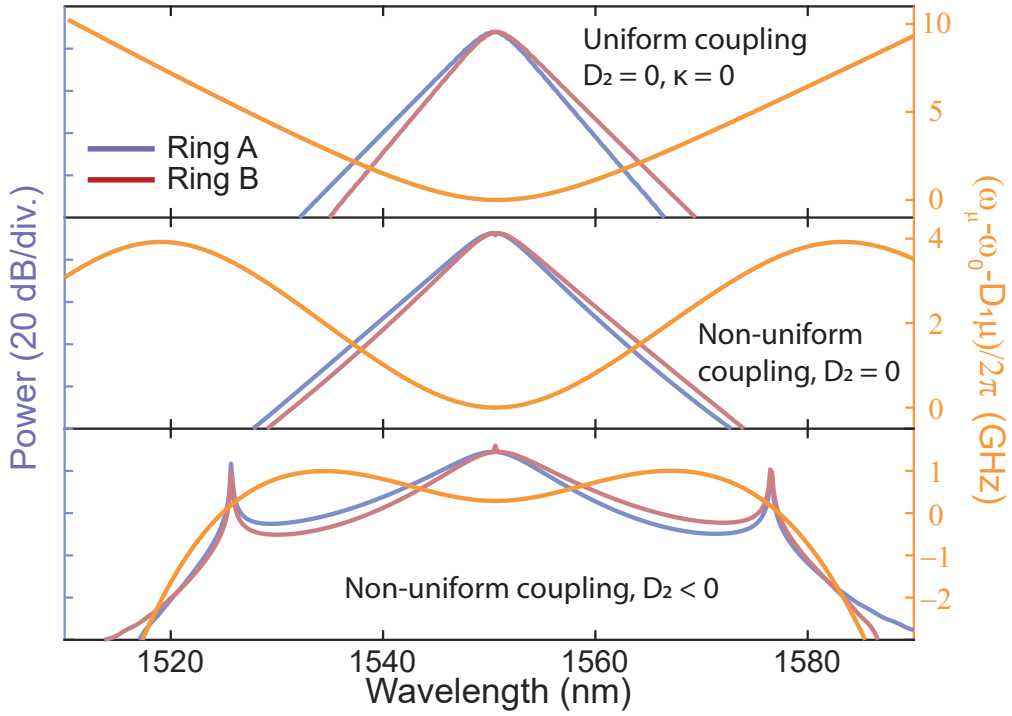

Figure 3.9: **Simulated optical spectra and dispersion relation for Dirac solitons assuming different levels of approximations in the model.** Top panel: Uniform coupling between two rings (mode number conservation), without pump and loss, and with zero second-order dispersion. Middle panel: Non-uniform coupling between two rings (mode number non-conservation), with pump and loss included, and with zero second-order dispersion. Recurring dispersion relations can be observed but the spectrum is free of strong dispersive waves. Bottom panel: Non-uniform coupling between two rings (mode number non-conservation), with pump and loss, and with negative second-order dispersion [i.e., full Eqs. (3.4) and (3.5)].

is no exact analogue of the self-phase modulation in quantum field theory as this contradicts the Pauli exclusion principle. Loss, pump and second-order dispersion terms do not have analogues in the nonlinear Dirac equation, and could be treated as perturbations for the soliton dynamics. For example, D_2 is no longer the dominant contribution to dispersion near the mode crossing center. We note that these terms do not change the qualitative features of the generated soliton, therefore establishing the link between the current soliton and the optical Dirac soliton previously studied [16]. A comparison of the simulated soliton spectral profile using different levels of approximation can be found in Fig. 3.9.

3.6.4 Simulations of soliton pulse pair formation

Numerical simulations have been performed based on the nonlinear wave equations [Eqs. (3.4) and (3.5)] and the results are used for plotting Fig. 3.3(b). For simplicity, the coupling is assumed to be wavelength independent ($g_{\mathrm{co}} = g_{\mathrm{co},0}$), which makes understanding the dispersion compensation in the coupling region more transparent. Parameters used for numerical simulations are: $\omega_0 = 2\pi \times 193.34$ THz, $Q_{\mathrm{in}} = 75$ M, $Q_{\mathrm{ex}} = 45$ M, $\delta\omega_{\mathrm{A}} = \delta\omega_{\mathrm{B}} = 12.5\kappa - G$ where G is the half gap created by the coupling (pump is red-detuned with respect to the upper branch resonance by 12.5κ), $D_1 = 2\pi \times 19.9766$ GHz, $D_2 = -2\pi \times 283.0$ kHz, $n_{\mathrm{g}} = 1.575$, $P_{\mathrm{in}} = 300$ mW, $g_{\mathrm{NL}} = 0.0277\ \mathrm{s}^{-1}$, and $g_{\mathrm{co},0} = 0.954\ \mathrm{mm}^{-1}$.

3.6.5 Soliton dynamics in the coupling region

In the coupling region where linear interaction is dominant in the soliton dynamics, the coupled LLE can be reduced to:

$$\frac{\partial E_{\mathrm{A}}}{\partial z} + \frac{1}{v_{\mathrm{g}}}\frac{\partial E_{\mathrm{A}}}{\partial t} = i g_{\mathrm{co}} E_{\mathrm{B}} \tag{3.12}$$

$$\frac{\partial E_{\mathrm{B}}}{\partial z} + \frac{1}{v_{\mathrm{g}}}\frac{\partial E_{\mathrm{B}}}{\partial t} = i g_{\mathrm{co}} E_{\mathrm{A}} \tag{3.13}$$

where $z = 0$ denotes the beginning of the coupling region. Note that g_{co} here is assumed to be wavelength independent for simplicity. The optical fields at z can be related to the incident fields ($z = 0$) as

$$E_{\mathrm{A}}(z,t) = \cos(g_{\mathrm{co}} z) E_{\mathrm{A}}(0,t') + i \sin(g_{\mathrm{co}} z) E_{\mathrm{B}}(0,t') \tag{3.14}$$

$$E_{\mathrm{B}}(z,t) = \cos(g_{\mathrm{co}} z) E_{\mathrm{B}}(0,t') + i \sin(g_{\mathrm{co}} z) E_{\mathrm{A}}(0,t') \tag{3.15}$$

where $t' = t - z/v_{\mathrm{g}}$ is the retarded time. The evolution of soliton properties with propagation distance plotted in Fig. 3.3(b) is obtained from Eqs. (3.14) and (3.15), with initial conditions $E_{\mathrm{A,B}}(0,t')$ taken from simulations, and shows good agreement with the simulation results using Eqs. (3.4) and (3.5).

References

[1] Kippenberg, T. J., Gaeta, A. L., Lipson, M. & Gorodetsky, M. L. Dissipative Kerr solitons in optical microresonators. *Science* **361**, eaan8083 (2018).

[2] Diddams, S. A., Vahala, K. & Udem, T. Optical frequency combs: Coherently uniting the electromagnetic spectrum. *Science* **369** (2020).

[3] Jin, W. *et al.* Hertz-linewidth semiconductor lasers using CMOS-ready ultra-high-Q microresonators. *Nat. Photon.* **15**, 346–353 (2021).

[4] Wabnitz, S. Suppression of interactions in a phase-locked soliton optical memory. *Opt. Lett.* **18**, 601–603 (1993).

[5] Leo, F. *et al.* Temporal cavity solitons in one-dimensional Kerr media as bits in an all-optical buffer. *Nat. Photon.* **4**, 471–476 (2010).

[6] Reimer, C. *et al.* Generation of multiphoton entangled quantum states by means of integrated frequency combs. *Science* **351**, 1176–1180 (2016).

[7] Kues, M. *et al.* On-chip generation of high-dimensional entangled quantum states and their coherent control. *Nature* **546**, 622–626 (2017).

[8] Kues, M. *et al.* Quantum optical microcombs. *Nat. Photon.* **13**, 170–179 (2019).

[9] Lu, L., Joannopoulos, J. & Soljačić, M. Topological photonics. *Nat. Photon.* **8**, 821–829 (2014).

[10] Ozawa, T. *et al.* Topological photonics. *Rev. Mod. Phys.* **91**, 015006 (2019).

[11] Tikan, A. *et al.* Protected generation of dissipative Kerr solitons in supermodes of coupled optical microresonators. *Sci. Adv.* **8**, eabm6982 (2022).

[12] Soltani, M., Matsko, A. & Maleki, L. Enabling arbitrary wavelength frequency combs on chip. *Laser Photonics Rev.* **10**, 158–162 (2016).

[13] Kim, S. *et al.* Dispersion engineering and frequency comb generation in thin silicon nitride concentric microresonators. *Nat. Commun.* **8**, 1–8 (2017).

[14] Lee, S. H. *et al.* Towards visible soliton microcomb generation. *Nat. Commun.* **8**, 1–8 (2017).

[15] Karpov, M., Pfeiffer, M., Liu, J. & et. al. Photonic chip-based soliton frequency combs covering the biological imaging window. *Nat. Commun.* **9** (2018).

[16] Wang, H. *et al.* Dirac solitons in optical microresonators. *Light sci. appl.* **9**, 1–15 (2020).

[17] Yi, X., Yang, Q.-F., Yang, K. Y., Suh, M.-G. & Vahala, K. Soliton frequency comb at microwave rates in a high-Q silica microresonator. *Optica* **2**, 1078–1085 (2015).

[18] Yi, X., Yang, Q.-F., Yang, K. Y. & Vahala, K. Active capture and stabilization of temporal solitons in microresonators. *Opt. Lett.* **41**, 2037–2040 (2016).

[19] Guo, H. *et al.* Universal dynamics and deterministic switching of dissipative Kerr solitons in optical microresonators. *Nat. Phys.* **13**, 94–102 (2017).

[20] Lucas, E., Karpov, M., Guo, H., Gorodetsky, M. & Kippenberg, T. J. Breathing dissipative solitons in optical microresonators. *Nat. Commun.* **8**, 1–11 (2017).

[21] de Wit, B. & Smith, J. *Field theory in particle physics* (1986).

Chapter 4

OBSERVATION OF INTERBAND KELLY SIDEBANDS IN COUPLED-RING SOLITON MICROCOMBS

This chapter is based on the following published paper:
Gao M., Yuan Z. Yan Y. *et. al.*, Observation of interband Kelly sidebands in coupled-ring soliton microcombs, *Optica* **11**, 940-944, (2024).
https://doi.org/10.1364/OPTICA.524074

Kelly sidebands are a special type of dispersive wave that appear in mode locked systems and they have recently been observed by pulsed excitation in integrated microcombs. Here, Kelly sidebands are generated by continuous-wave excitation in a partially-coupled racetrack-resonator microcomb. The coupled-racetrack system supports two optical bands so that, in contrast to earlier studies, the soliton and Kelly sideband reside in distinct bands. The resulting interband excitation of the Kelly sidebands relaxes power requirements and continuous-wave sideband excitation is demonstrated. Tuning of sideband spectral position under pulsed excitation is also studied. Numerical simulation and the experiment show that the sidebands rely upon symmetry breaking caused by partial coupling of the two-ring system. More generally, multi-band systems provide a new way to engineer Kelly sidebands for spectral broadening of microcombs.

4.1 Introduction

Kelly sidebands (KSs) [1] have been intensively studied in soliton mode-locked fiber lasers [2–7]. They resemble dispersive waves (DWs) [8–11] but their phase relative to the mode-locked optical pulse changes by integer multiples of 2π (instead of 0) every cavity round trip. This roundtrip phase mismatch prevents coupling of the soliton and KS unless a symmetry is broken in the system. Like DWs, KSs extend the spectral reach of the pulse. However, generating KSs is challenging in integrated photonic resonators on account of their smaller round trip path lengths compared to table-top mode locked systems. Nonetheless, KSs have recently been observed in pulsed-pumped soliton microcombs featuring broken symmetry [12].

Here, interband KSs are observed in soliton microcombs formed using dual-racetrack Si_3N_4 microresonators [13] (Fig. 4.1(a)). The Si_3N_4 waveguides used to fabricate

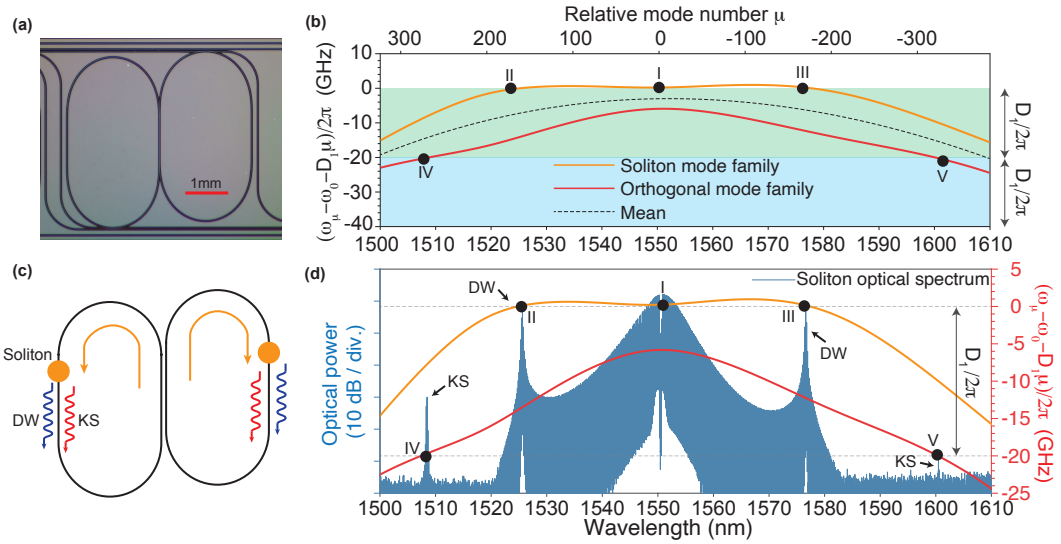

Figure 4.1: **Illustration of KS generation.** **(a)** Optical image of the partially coupled racetrack resonator. **(b)** Measured integrated dispersion of the two hybrid mode families (orange and red) is plotted versus wavelength and relative mode number. When pumped near point I (anomalous dispersion center of the upper band), soliton pulse pairs form as illustrated in panel (c). Also, DWs (interband KSs) appear at points II & III (IV & V). The appearance of KSs at points IV and V is discussed in Section 4.5.1. ω_μ: frequency of mode μ, ω_0: center mode frequency, $D_1/2\pi$: free-spectral-range (FSR) of the resonator, μ: relative mode number such that μ=0 corresponds to the pump mode. **(c)** Schematic showing soliton pulse pair propagation in the coupled racetracks. DW and KS waves are indicated as oscillatory backgrounds. **(d)** Measured optical spectrum of soliton pulse pair from continuous-wave laser pumping. DWs and interband KSs are observed at the predicted location in panel (b). Dispersion curves are overlaid onto the soliton spectrum for reference.

the racetracks feature normal dispersion, however, partial coupling of racetracks having slightly different free-spectral-ranges (FSRs) creates two optical frequency bands associated with the hybridization of the individual racetrack modes. The measured integrated dispersion of these bands is plotted in Fig. 4.1(b), and shows that the frequency bands feature spectral windows with anomalous dispersion. For example, the upper band (soliton mode band in Fig. 4.1(b)) features anomalous dispersion in the vicinity of point I, and pumping near this point has been shown to form bright soliton pulse pairs that circulate in a mirror-image fashion as shown in Fig. 4.1(c) [13]. In this work, the impact of this multi frequency band structure on KS formation is studied. Specifically, interband KSs are shown to form in the orthogonal band in Fig. 4.1(b). Also, as discussed in the Section 4.5.1, partial coupling of the racetracks creates symmetry breaking that allows the soliton to cou-

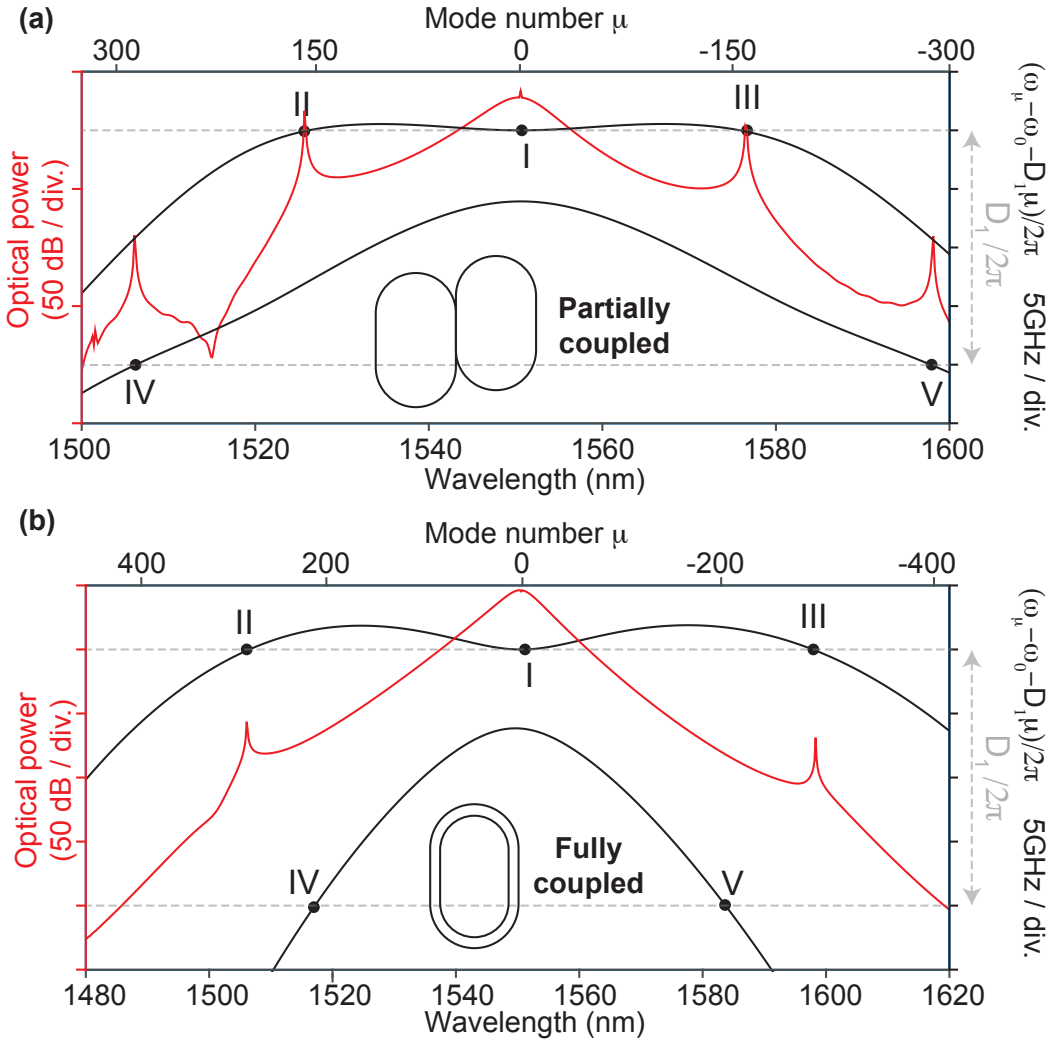

Figure 4.2: **Comparison of numerical simulation results for sideband generation in partially coupled and fully coupled resonators.** **(a)** Simulated soliton spectrum and dispersion profile of the partially coupled racetrack. The soliton, when pumped at point I, generates two dispersive waves (point II and III) and two interband Kelly sidebands (point IV and V). **(b)** Simulated soliton spectrum and dispersion profile of the fully coupled racetrack. In this case, the Kelly sidebands at point IV and V do not appear, because of phase mismatch. **Panel (a,b) Insets:** illustration of partially coupled and fully coupled racetrack configuration.

ple to these KSs. The spectral shift provided by interband excitation of the KSs relaxes otherwise challenging KS excitation requirements on comb bandwidth in micocombs, and continuous-wave excitation is demonstrated. In addition pulsed pumping is studied as a way to tune the KSs spectral locations.

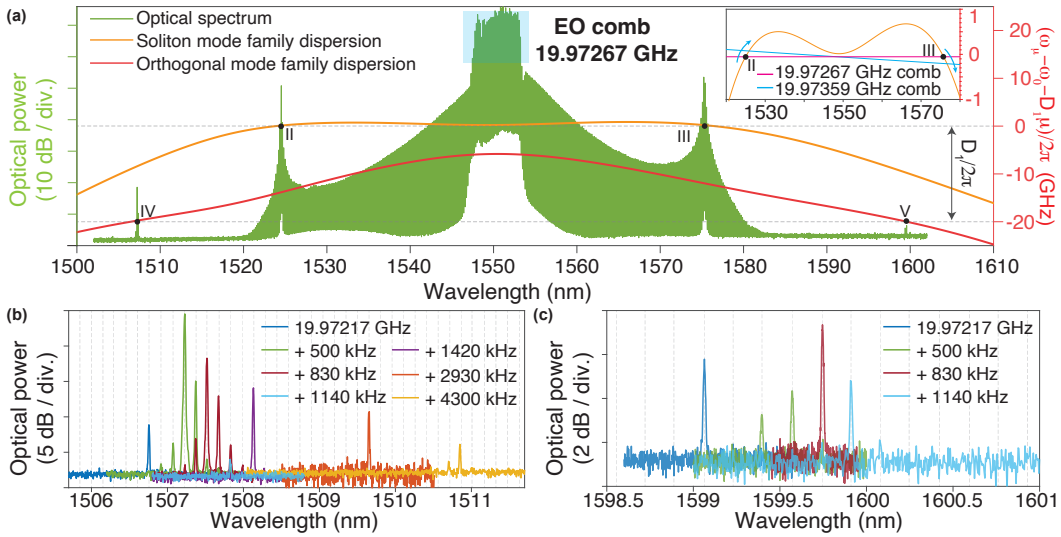

Figure 4.3: **Active control of KS wavelengths on blue and red sides through pulse pumping.** **(a)** Optical spectrum of soliton pulse pair generated from pulse pumping. The measured mode frequency dispersion for the two bands is also plotted. **Inset:** zoom in of the dispersion curve of the pumped mode family and its comparison with 19.97267 GHz comb frequency line (horizontal magenta line) and 19.97359 GHz comb frequency (tilted blue line). The right vertical axis of the inset is a magnified version of the right vertical axis of the main panel. **(b, c)** Zoom-in optical spectra of the two KSs at shorter wavelengths (panel **b**) and longer wavelengths (panel **c**) for different input pump-pulse repetition rates. Legend gives the repetition rate of the input pump pulse relative to 19.97217 GHz. Vertical dashed grid lines indicate multiples of the comb repetition rate of 19.97267 GHz.

4.2 Obsrvation of Kelly sideband

The coupled-ring devices are fabricated using the CMOS-compatible process described in reference [14]. Continuous-wave laser pumping around the anomalous dispersion window near point I produces the optical spectrum shown in Fig. 4.1(d). This spectrum corresponds to soliton pulse pair mode locking as illustrated in Fig. 4.1(c) [13]. For comparison, portions of the dispersion spectra for the two frequency bands in Fig. 4.1(b) are overlaid with the pulse-pair spectrum.

The spectrum in Fig. 4.1(d) features two DWs at points II and III. These DWs correspond to modes that phase match with soliton comb frequencies. Meanwhile, two further sidebands are observed at points IV and V, which are identified as KSs. These sidebands are notable because they form on the other frequency band (interband KS) relative to the frequency band used to generate the soliton pulse pair. As indicated, the values of their integrated dispersion differ by one FSR ($D_1/2\pi$ in the figure) compared to point I, and as such the sideband phases are mismatched by

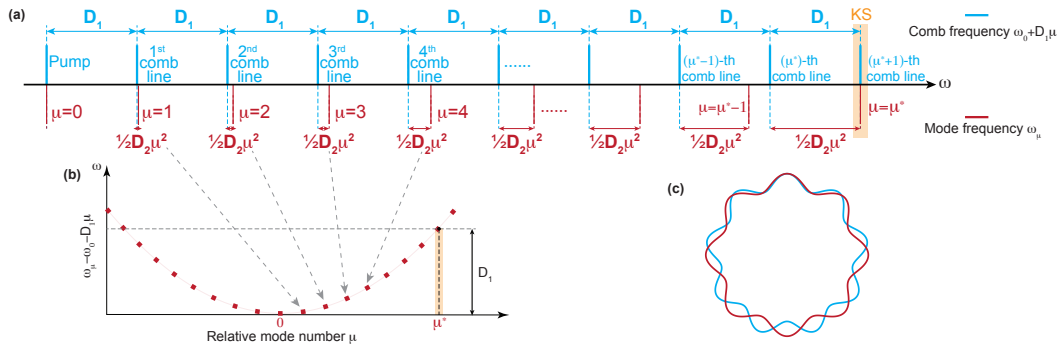

Figure 4.4: **Explanation of Kelly sideband (KS) formation. (a)** Comb frequencies (blue) walk-off from resonator mode frequencies (red) by $D_2\mu^2/2$ as a result of anomalous dispersion. Comb line at $\mu = 0$ is also the pump. The comb and mode frequency become aligned (orange highlight) when this walk-off is equal to an integer multiple of D_1 (FSR). This frequency is approximately the frequency of the KSs. μ: relative mode number. ω_μ: frequency of each mode. $D_1/2\pi$: FSR of the resonator. D_2: second-order dispersion of the resonator. **(b)** Dispersion profile of the mode family shown in panel a. The first few corresponding modes in panel (a) are indicated by dashed arrows. When a mode frequency is an integer times $D_1/2\pi$ relative to the pumped mode at μ=0, it becomes possible to generate a KS at this frequency, provided a second condition is satisfied as described in panel (c). **(c)** Illustration of the propagation phase of the comb and the mode at μ^*. Their relative phase changes by a multiple 2π every round trip, leading to phase mismatch of the waves and preventing KS generation when the resonators are fully coupled.

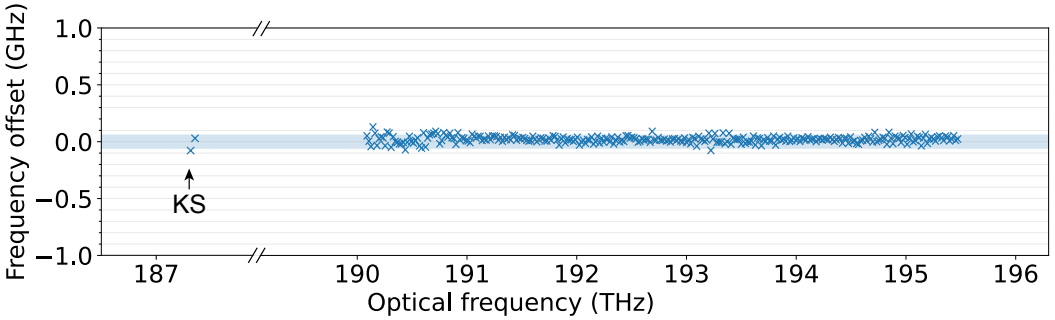

Figure 4.5: **Analysis of the comb and KS frequency offset using frequencies measured with a high-resolution OSA** (resolution of 125 MHz, blue shaded area). The comb spectral lines (from around 190 THz to 195 THz) and the Kelly sidebands (KS) on the red side (two data points around 187 THz) exhibit approximately the same offset frequency, within the precision limits of the spectrometer. Data at higher frequencies were not collected due to spectrometer limitations. Further details are provided in the text.

2π relative to the pumped mode every round trip (See Fig. 4.4). It is important to note that this mismatch is primarily accumulated because the soliton and KS waves

reside in distinct frequency bands (separated by a frequency shift comparable to the cavity FSR). As shown in the Section 4.5.1, the accumulation of this shift would normally require a larger number of mode shifts and hence greater comb bandwidth and power. While other types of interband sideband generation in coupled-ring solitons have been studied before [15], the KSs in our study are fundamentally different from conventional phase-matched sidebands that do not require symmetry breaking.

4.3 Numerical simulation

Numerical simulation is performed to compare the difference of KS generation in the partially coupled and fully coupled devices. The result is shown in Fig. 4.2. The simulation for the partially coupled case is based on the coupled mode Lugiato-Lefever equation (LLE) with a position-dependent coupling term in the lab coordinate, formalized as [13],

$$\begin{aligned}\frac{\partial E_{\mathrm{R}}}{\partial t} =& -\left(\frac{\kappa}{2}+i\delta\omega_{\mathrm{R}}\right)E_{\mathrm{R}} - v_{\mathrm{g}}\frac{\partial E_{\mathrm{R}}}{\partial z} - i\frac{\beta_2 v_{\mathrm{g}}^3}{2}\frac{\partial^2 E_{\mathrm{R}}}{\partial z^2} \\ &+ ig_{\mathrm{K}}|E_{\mathrm{R}}|^2 E_{\mathrm{R}} + ig_{\mathrm{c}}v_{\mathrm{g}}\chi_{\mathrm{c}}(z)E_{\mathrm{L}} + f_{\mathrm{p}},\end{aligned} \tag{4.1}$$

and

$$\begin{aligned}\frac{\partial E_{\mathrm{L}}}{\partial t} =& -\left(\frac{\kappa}{2}+i\delta\omega_{\mathrm{L}}\right)E_{\mathrm{L}} - v_{\mathrm{g}}\frac{\partial E_{\mathrm{L}}}{\partial z} - i\frac{\beta_2 v_{\mathrm{g}}^3}{2}\frac{\partial^2 E_{\mathrm{L}}}{\partial z^2} \\ &+ ig_{\mathrm{K}}|E_{\mathrm{L}}|^2 E_{\mathrm{L}} + ig_{\mathrm{c}}v_{\mathrm{g}}\chi_{\mathrm{c}}(z)E_{\mathrm{R}},\end{aligned} \tag{4.2}$$

where $E_{\mathrm{L,R}}$ denotes the normalized optical field in the left and the right racetrack, $\kappa = \kappa_{\mathrm{in}} + \kappa_{\mathrm{ex}}$ is the sum of intrinsic and external loss rate for each racetrack, $\delta\omega_{\mathrm{L,R}}$ is the pump laser detuning, v_{g} is the group velocity and β_2 is the group velocity dispersion of the waveguide, z is the coordinate of each resonator, g_{c} is the coupling strength per unit length, g_{K} is the Kerr nonlinear coefficient and f_{p} is the continuous-wave pumping term. The function $\chi_{\mathrm{c}}(z)$ is an indicator function with a value of 1 where the two racetracks are coupled and a value of 0 where two rings are not coupled. For the simulation in Fig. 4.2(a), the two racetracks are partially coupled together, and this indicator function is

$$\chi_{\mathrm{c}}(z) = \begin{cases} 1 & z \in [0, L_{\mathrm{c}}), \\ 0 & \text{elsewhere}, \end{cases} \tag{4.3}$$

where L_{c} is the effective length of the section where two racetracks are coupled together. For the simulation in Fig. 4.2(b), the two racetracks are fully coupled

together (i.e., χ_c is unity at all positions) so that the coupled LLE in the rotating frame [16] is used to study soliton dynamics. Parameters used in this simulation are listed in Section 4.5.2.

In Fig. 4.2, the simulated results of the soliton spectrum are plotted as the red curves, together with the dispersion as the black curves. The spectrum in Fig. 4.2(a) of partial coupling (i.e., symmetry broken case) shows a similar structure to our observation in Fig. 4.1(d). Specifically, the spectrum contains two DWs at points II and III, and two interband KSs around points IV and V. For comparison, the simulated soliton spectrum in the fully coupled ring is shown in Fig. 4.2(b). Here, the KSs are absent and only two DW sidebands appear at points II and III. In this fully coupled case (i.e., symmetrical case), the frequency-matched interband modes at points IV and V cannot generate KSs because of phase mismatch. As an aside, in comparing the simulated spectrum in Fig. 4.2(a) with the measurement in Fig. 4.1(d), the measured KSs exhibit an asymmetry in power. This happens for several reasons. First, the optical field of the modes at point IV (V) is mainly distributed in the right (left) ring, while the measured output is coupled from the right ring [13]. Accordingly, the KS appears to be stronger at point IV (blue side) than point V (red side). Second, the pumping laser is slightly blue-detuned relative to the anomalous dispersion window center and this contributes to such a difference in measured KS power.

Increasing comb bandwidth would tend to strengthen the KS. And comb bandwidth can be increased through control of the integrated dispersion profile. As discussed in ref. [13] this can be tuned by controlling g_c and the round trip length ratio between the rings. A stronger KS is potentially useful for optical frequency division [17–19]. We also note that the KS strength may be limited by the strength of DWs, which tend to destabilize the soliton as the detuning or pump power is further increased [20].

4.4 Active control of Kelly sideband position by pulsed pumping

To further study the tuning properties of the KSs, an optical pumping pulse is generated by forming an electro-optic comb and then applying pulse compression methods [21]. This method of pumping enables higher peak pumping powers and also allows exploration of variation of pumping repetition rate on sideband formation. The resulting microcomb spectrum is shown in Fig. 4.3(a), and the electro-optic comb pump spectral lines are visible near the spectral center of the

comb. Similar to the continuous-wave pump case, two DWs form around points II & III and the two KSs appear around points IV & V in the spectrum. In contrast to the continuous-wave pump case, the repetition rate of the soliton spectrum is determined by the electro-optic pump pulse [22, 23]. The impact of varying this rate on DW spectral location is illustrated in the Fig. 4.3(a) inset, which overlays the dispersion of the upper frequency band with the equally-spaced comb frequencies as given by a line. The intersection of the dispersion curve with the soliton line gives the condition for phase matching of the soliton with the dispersive wave. Tuning of the soliton repetition rate causes a shift in the frequencies of the DWs as illustrated.

A similar phase matching condition will also apply for the KSs, but with respect to the second frequency band shifted by $D_1/2\pi$. Here, as the repetition rate increases, the wavelength of the strongest blue and red KSs would be expected to both increase. This is confirmed experimentally in Fig. 4.3(b) and Fig. 4.3(c), where tuning by about 1.14 MHz of the repetition rate causes the interband KS to jump by 7 modes (blue side), and by 5 modes (red side). For a larger repetition rate, the KS on the red side becomes indistinguishable from the instrumental noise floor.

4.5 Supplementary information

4.5.1 Principle of conventional KS generation

To illustrate the principle of conventional KS generation [1], consider the spectrum of a frequency comb as illustrated in Fig. 4.4(a). The comb lines (blue) are equally spaced by a separation approximately equal to the resonator FSR (or $D_1/2\pi$). The comb line at relative mode number μ=0 is also the optical pump. The frequencies of the resonator modes are illustrated as red lines. Due to the dispersion of the resonator, these frequencies are not equally spaced. Assuming anomalous second-order dispersion (D_2), as required for soliton formation, the frequencies of the resonator modes and comb lines walk off by $D_2\mu^2/2$ versus μ. The integrated dispersion plot of this mode family in Fig. 4.4(b) shows that, as a result of this walk-off, the relative mode number μ^* is aligned to the $(\mu^* + 1)$-th comb line when the walk-off $D_2\mu^{*2}/2 = D_1$. This mode is orange highlighted in both Fig. 4.4(a) and (b). This alignment is a necessary condition for generation of the KS at this frequency, and the large FSR of microcombs makes excitation of this KS mode more challenging. In the case of interband excitation, modes from the orthogonal band align with the comb at a smaller walk-off than the soliton band due to the spectral gap between the bands, thus relaxing the power requirements for KSs.

A second condition must also be satisfied for KS excitation. The accumulated round trip phase of the KS wave in Fig. 4.4(a) is offset by 2π from the original comb every round trip. This is illustrated in Fig. 4.4(c), and the integrated roundtrip coupling of soliton to the KS wave is zero as a result of phase interference (i.e., phase mismatch). Generation of the KS wave is thereby prevented in cases where the resonators are fully coupled together, as shown in Fig. 4.2(b). However, if the additional condition of partial racetrack coupling is added (as formalized in Eq. (4.3)), then the partial roundtrip integral is non-zero and KS generation occurs. In effect, the fully coupled racetrack system features a reflection symmetry that is lifted by partial coupling, thereby allowing the soliton and KS wave to couple when the eigenmode frequency aligns with the comb frequency (for example, points IV and V in Fig. 4.1(b)). This effect is also discussed in Fig. 4.2 of the main text. In addition to KSs in mode-locked soliton combs, similar parametric sidebands can also be generated in resonators with broken symmetry [24].

4.5.2 Parameters in coupled mode LLE

In Eqs. (4.1) and (4.2), the parameter definitions are the same as those used in ref. [13]. The optical field $E_{\mathrm{L,R}}$ is normalized to photon numbers in the length-averaged ring. $\kappa_{\mathrm{in,ex}}$ is related to the resonator Q-factor by $\kappa_{\mathrm{in,ex}} = \omega_0/Q_{\mathrm{in,ex}}$. The laser frequency detuning $\delta\omega_{\mathrm{L}} = \delta\omega_{\mathrm{R}} = 12.5\kappa - G$, where $\kappa = \kappa_{\mathrm{in}} + \kappa_{\mathrm{ex}}$, $G = g_c L_{\mathrm{c}} D_1/2\pi$. G is the half frequency gap created by coupling. $v_{\mathrm{g}} = c/n_{\mathrm{g}}$ is the group velocity, where c is the speed of light. and n_{g} is the waveguide group index. $g_{\mathrm{K}} = \hbar\omega_0^2 D_1 n_2/(2\pi n_{\mathrm{g}} A_{\mathrm{eff}})$ is the nonlinear coefficient with A_{eff} effective mode area and n_2 is the nonlinear coefficient of the waveguide. The group velocity dispersion is related to D_1 and D_2 by $\beta_2 = -n_{\mathrm{g}} D_2/(cD_1^2)$. $f_{\mathrm{p}} = \sqrt{\kappa_{\mathrm{ex}} P_{\mathrm{in}}/(\hbar\omega_0)}$ is the pump term, where P_{in} is the on-chip pump power. The argument z is limited to $[0, L_{\mathrm{L,R}})$, where $L_{\mathrm{L.R}}$ is the respective resonator round trip length.

The numerical values of the relevant parameters are $Q_{\mathrm{in}} = 75\times10^6$; $Q_{\mathrm{ex}} = 45\times10^6$; $\omega_0 = 2\pi \times 193.34$ THz; $L_{\mathrm{R}} = 9.5$ mm; $L_{\mathrm{L}} = 1.005 \times L_{\mathrm{R}}$ ($D_{1,\mathrm{R}} = 1.005 \times D_{1,\mathrm{L}}$); $L_{\mathrm{c}} = 1$ mm; $n_{\mathrm{g}} = 1.575$; $g_{\mathrm{K}} = 0.0277$ s^{-1}; $g_{\mathrm{c}} = 0.954$ mm^{-1}; $P_{\mathrm{in}} = 300$ mW, $D_1 = 2\pi \times 19.97$ GHz; $D_2 = -2\pi \times 283.0$ kHz.

To investigate how L_{c} can affect the KS strength, we also perform multiple simulations with different coupling lengths L_{c} while keeping $g_{\mathrm{c}} L_{\mathrm{c}}$ fixed so that the dispersion profile remains unchanged. The results suggest that from $L_{\mathrm{c}}/L_{\mathrm{R}} = 0.105$ to 0.667, the KS power decreases slightly with increasing coupling length under the

same dispersion profile and pumping conditions. This is because as L_c increases, the coupling strength between modes of the two individual rings with relative mode numbers offset by 1 decreases slightly.

In the fully coupled case, Q-factors, waveguide dispersion, FSRs, nonlinear coefficient, pump frequency, power, and detuning are unchanged. The coupling between two rings is averaged over the entire ring, keeping G (half bandgap opened by the coupling) the same as the partially coupled case.

4.5.3 Alignment of interband KSs with the main comb grid

To further verify that the KS frequencies align with the main comb and share the same carrier-envelope offset frequency, the frequency of the comb and the KS (on the red side) are measured using a high-precision spectrometer with an accuracy of 1 pm (125 MHz). This data is then used to construct the plot in Fig. 4.5 wherein $\nu_\mu - \mu f_{\text{rep}}$ is plotted versus ν, where ν_μ is the frequency of comb line (or KS line) with relative order μ and f_{rep} is the comb repetition rate. The plot confirms the alignment of the KS with the main comb within the resolution of the spectrometer. Notably, the KS on the blue side does not appear in the plot because its frequency is beyond the range of the spectrometer.

4.6 Summary

In summary, interband Kelly sidebands have been produced using both continuous-wave and pulsed pumping. The sidebands reside in a frequency band that is distinct from the soliton pulse in a coupled-racetrack resonator microcomb. Their interband nature relaxes excitation requirements. The wavelengths of the Kelly sidebands agree with predictions based on mode dispersion measurements. Pulsed-pump operation allowed exploration of the sideband tuning properties.

References

[1] Kelly, S. M. J. Characteristic sideband instability of periodically amplified average soliton. *Electron. Lett.* **28**, 806–807 (1992).

[2] Smith, N., Blow, K. & Andonovic, I. Sideband generation through perturbations to the average soliton model. *J. Light. Technol.* **10**, 1329–1333 (1992).

[3] Pandit, N., Noske, D. U., Kelly, S. M. J. & Taylor, J. R. Characteristic instability of fibre loop soliton lasers. *Electron. Lett.* **28**, 455–457 (1992).

[4] Dennis, M. & Duling, I. Experimental study of sideband generation in femtosecond fiber lasers. *IEEE J. Quantum Electron.* **30**, 1469–1477 (1994).

[5] Jang, J. K., Erkintalo, M., Murdoch, S. G. & Coen, S. Observation of dispersive wave emission by temporal cavity solitons. *Opt. Lett.* **39**, 5503–5506 (2014).

[6] Bao, C. & Yang, C. Stretched cavity soliton in dispersion-managed Kerr resonators. *Phys. Rev. A* **92**, 023802 (2015).

[7] Ceoldo, D. *et al.* Multiple four-wave mixing and Kerr combs in a bichromatically pumped nonlinear fiber ring cavity. *Opt. Lett.* **41**, 5462–5465 (2016).

[8] Wai, P. K. A., Menyuk, C. R., Lee, Y. C. & Chen, H. H. Nonlinear pulse propagation in the neighborhood of the zero-dispersion wavelength of monomode optical fibers. *Opt. Lett.* **11**, 464–466 (1986).

[9] Brasch, V. *et al.* Photonic chip based optical frequency comb using soliton cherenkov radiation. *Science* **351**, 357–360 (2016).

[10] Yang, Q.-F., Yi, X., Yang, K. Y. & Vahala, K. Spatial-mode-interaction-induced dispersive waves and their active tuning in microresonators. *Optica* **3**, 1132–1135 (2016).

[11] Yi, X. *et al.* Single-mode dispersive waves and soliton microcomb dynamics. *Nat. Commun.* **8**, 1–9 (2017).

[12] Anderson, M. H. *et al.* Dissipative solitons and switching waves in dispersion-modulated Kerr cavities. *Phys. Rev. X* **13**, 011040 (2023).

[13] Yuan, Z. *et al.* Soliton pulse pairs at multiple colors in normal dispersion microresonators. *Nat. Photon.* **610**, 977–983 (2023).

[14] Jin, W. *et al.* Hertz-linewidth semiconductor lasers using CMOS-ready ultra-high-q microresonators. *Nat. Photon.* **15**, 346–353 (2021).

[15] Tikan, A. *et al.* Emergent nonlinear phenomena in a driven dissipative photonic dimer. *Nat. Phys.* **17**, 604–610 (2021).

[16] Wang, H. *et al.* Dirac solitons in optical microresonators. *Light sci. appl.* **9**, 1–15 (2020).

[17] Ji, Q.-X. *et al.* Dispersive-wave-agile optical frequency division. *arXiv:2403.00973* (2024).

[18] Li, J., Yi, X., Lee, H., Diddams, S. A. & Vahala, K. J. Electro-optical frequency division and stable microwave synthesis. *Science* **345**, 309–313 (2014).

[19] Diddams, S. A., Vahala, K. & Udem, T. Optical frequency combs: Coherently uniting the electromagnetic spectrum. *Science* **369**, eaay3676 (2020).

[20] Herr, T. *et al.* Mode spectrum and temporal soliton formation in optical microresonators. *Phys. Rev. Lett.* **113**, 123901 (2014).

[21] Torres-Company, V. & Weiner, A. M. Optical frequency comb technology for ultra-broadband radio-frequency photonics. *Laser Photonics Rev.* **8**, 368–393 (2014).

[22] Obrzud, E., Lecomte, S. & Herr, T. Temporal solitons in microresonators driven by optical pulses. *Nat. Photon.* **11**, 600–607 (2017).

[23] Li, J. *et al.* Efficiency of pulse pumped soliton microcombs. *Optica* **9**, 231–239 (2022).

[24] Huang, S.-W. *et al.* Quasi-phase-matched multispectral Kerr frequency comb. *Opt. Lett.* **42**, 2110–2113 (2017).

Chapter 5

SIMUTANEOUS GENERATION OF MULTI-COLOR SOLITONS IN COUPLED-RING MICRORESONATORS

This chapter is based on the following published conference abstract:
Gao M., Ge J., Yuan Z., *et. al.*, Multi-color solitons in coupled-ring microresonators, in CLEO 2024, Technical Digest Series (*Optica Publishing Group*), paper SM3G.1.
https://opg.optica.org/abstract.cfm?uri=CLEO_SI-2024-SM3G.1

Multi-color co-propagating and counter-propagating solitons are generated using a coupled-ring microresonator in the ultra-low-loss Si_3N_4 platform. Soliton spectra and beatnotes are measured and potential applications are discussed.

5.1 Multicolor operation

Soliton microcombs have found diverse applications across various material platforms[1]. In a recent development, microcombs formed as coherent pulse pairs have been demonstrated in the ultra-low-loss Si_3N_4 on silicon platform [2]. This pulse pair mode locking modality overcomes the inherent normal dispersion of this system, leading to bright soliton microcombs. In this study, we showcase another feature of the pulse pair system, which is multi-color operation. Driven by two continuous-wave pumps, as illustrated in Fig. 5.1(a), two pulse pairs form in distinct spectral windows. The multi-color pairs can be pumped so as to co-propagate or counter-propagate.

The device consists of two coupled racetrack resonators with slightly different free-spectral ranges (FSRs). The uncoupled resonators feature normal dispersion, which is characteristic of the ultra-low-loss Si_3N_4 platform. However, their coupling gives rise to the formation of two hybridized mode families, whose dispersion characteristics are illustrated in Fig. 5.1(b). Significant to the current study is that the coupling of the resonators covers only a fraction of their circumference, meaning that mode hybridization does not require mode-number matching. As a result, hybridization has a spectral recurrence set by the offset in the resonator FSRs, leading to multiple anomalous dispersion windows where pulse pair formation is possible. Two such windows are indicated in Fig. 5.1(b) wherein strong hybridization causes

anomalous dispersion characterized by a positive curvature in the dispersion plot. By pumping in the vicinity of these anomalous dispersion windows, bright soliton pulse pairs form and circulate in a mirror-image fashion around the two resonators [2]. In the measurement, pulse pairs are stabilized by detection of their comb power followed by servo control of the corresponding pump laser frequency. The experimental setup is shown in Fig. 5.1c and is similar to that used for stabilization of conventional soliton microcombs [3].

5.2 Freqeuncy multiplexed soliton spectrum

The measured comb spectra resulting from the simultaneous generation of two-color pulse pairs are shown in Fig. 5.1(d). Each individual soliton spectrum exhibits an approximately sech^2 envelope shape. Furthermore, dispersive waves [4] and Kelly sidebands [5] emerge at points where mode and comb frequencies coincide, leading

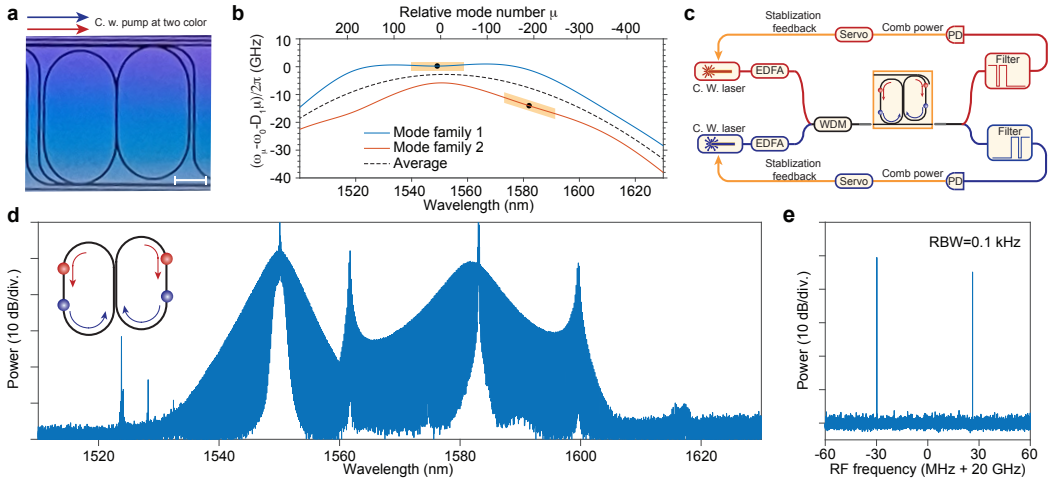

Figure 5.1: **Co-propagation:** **(a)** Optical image of the coupled-ring microresonator. Scale bar, 1mm. **(b)** Dispersion characteristics of hybrid mode families versus wavelength. Two regions exhibiting anomalous dispersion are highlighted in orange. The black dots indicate the frequencies of two continuous-wave pump lasers. The frequencies of the dashed line are the average of the two hybrid mode families and feature normal dispersion. ω_μ: frequency of each mode; ω_0: center mode frequency; D_1: FSR of the mode family 1 at μ=0 where $D_1/2\pi \approx 19.97$ GHz. **(c)** Experimental setup for co-propagating multi-color pulse pair generation. C.W.: continuous-wave; EDFA: erbium-doped fiber amplifier; WDM: wavelength division multiplexer; PD: photodetector. **(d)** Experimental spectra for co-propagating multi-color pulse-pairs. A schematic depicting the co-propagating two-color pulse pairs is shown in the inset. **(e)** Measured radio-frequency (RF) beatnotes of multi-color pulse pairs. RBW: resolution bandwidth.

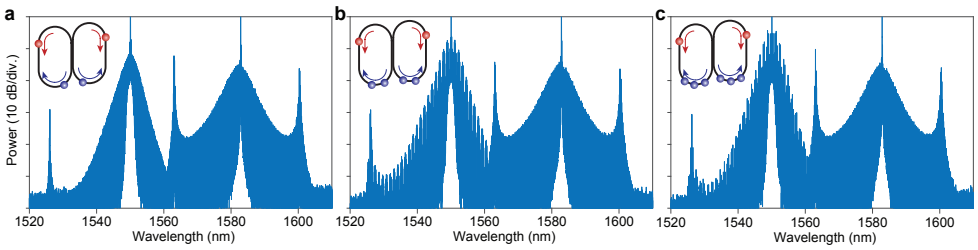

Figure 5.2: **Counter-propagation: experimental spectra for simultaneous generation of a single 1582 nm pulse pair in the presence of varying numbers of counter-propagating 1550 nm pulse pairs. (a)** One 1582 nm pulse pair with one 1550 nm pulse pair. **(b)** One 1582 nm pulse pair with two 1550 nm pulse pairs. **(c)** One 1582 nm pulse pair with three 1550 nm pulse pairs. The insets are schematic representations of the counter-propagating multi-color pulse pairs for each case.

to resonant power enhancement. Additionally, weak spectral features appear that are attributed to parasitic four-wave mixing (FWM) effects between a given pulse pair and the pump for the other pulse pair. The broader bandwidth of the 1582 nm soliton as well as the presence of more pronounced dispersive waves is attributed to the reduced curvature (i.e., second-order dispersion) in the corresponding dispersion profile. This reduced curvature is predicted from dispersion modeling due to larger waveguide coupling strength between the two resonators at longer wavelengths, which opens a larger gap in frequency for the hybrid modes [2].

The radio-frequency beatnote of the two-color pulse-pair spectrum is shown in Fig. 5.1(e). Frequencies corresponding to the pulse pairs at 1550 nm and 1582 nm are 19.970 GHz and 20.026 GHz, respectively. This difference reflects slight differences in FSR values at the two spectral windows in Fig. 5.1(b). In the current resonator design, the local FSR difference at the two pump wavelengths is 56.6 MHz, which is in reasonable agreement with the experimentally measured 56.0 MHz difference in pulse-pair repetition rates.

5.3 Co-propagation and counter-propagation multicolor soliton

In addition to co-propagating two-color pulse pairs, we also demonstrated counter-propagating two-color pulse pairs as shown in Fig. 5.2. In contrast to the co-propagating scenario, interactions between counter-propagating solitons are weaker[6], and FWM features are not observed. By actively selecting different stabilization parameters[3], it is also possible to controllably select the number of pulse pairs circulating at a given color as shown in Fig. 5.2(b) and 5.2(c). The RF beat notes of these spectra exhibit two distinct peaks, similar to that observed in Fig. 5.1(e).

5.4 Summary

In summary, we have demonstrated the generation of both co-propagating and counter-propagating two-color soliton pulse pairs in ultra-low-loss Si_3N_4 coupled-ring microresonators. This results suggest the potential to extend the microcomb bandwidth through multi-pump methods[7, 8]. Furthermore, by carefully designing the dispersion profile, the spectral overlap between the two pulse pairs could be harnessed for applications such as dual-comb spectroscopy. The difference in repetition rates between two soliton pulse pairs can be designed, and is potentially useful for application to ranging [9].

References

[1] Kippenberg, T. J., Gaeta, A. L., Lipson, M. & Gorodetsky, M. L. Dissipative Kerr solitons in optical microresonators. *Science* **361**, eaan8083 (2018).

[2] Yuan, Z. *et al.* Soliton pulse pairs at multiple colours in normal dispersion microresonators. *Nat. Photon.* **17**, 977–983 (2023).

[3] Yi, X., Yang, Q.-F., Yang, K. Y., Suh, M.-G. & Vahala, K. Soliton frequency comb at microwave rates in a high-Q silica microresonator. *Optica* **2**, 1078–1085 (2015).

[4] Yang, Q.-F., Yi, X., Yang, K. Y. & Vahala, K. Spatial-mode-interaction-induced dispersive waves and their active tuning in microresonators. *Optica* **3**, 1132–1135 (2016).

[5] Gao, M. *et al.* Observation of interband kelly sidebands in coupled-ring soliton microcombs. *Optica* **11**, 940–944 (2024).

[6] Bao, C. *et al.* Quantum diffusion of microcavity solitons. *Nat. Phys.* **17**, 462–466 (2021).

[7] Moille, G. *et al.* Ultra-broadband Kerr microcomb through soliton spectral translation. *Nat. Commun.* **12**, 7275 (2021).

[8] Zhang, S., Silver, J. M., Bi, T. & Del'Haye, P. Spectral extension and synchronization of microcombs in a single microresonator. *Nat. Commun.* **11**, 6384 (2020).

[9] Na, Y. *et al.* Ultrafast, sub-nanometre-precision and multifunctional time-of-flight detection. *Nat. Photon.* **14**, 355–360 (2020).

Chapter 6

PULSE-PUMPED GENERATION OF BRIGHT SOLITON IN $AL_{0.2}GA_{0.8}AS$ RESONATOR UNDER ROOM TEMPERATURE

6.1 Introduction

Mode locked soliton microcombs [1] have been demonstrated as a miniaturized solution for precision measurements [2–5] and multi-channel systems, which have been demonstrated in a variety of microresonators [6–15]. $Al_{0.2}Ga_{0.8}As$, a material with advantageous nonlinearity coefficient [16] and compatibility of active gain, has been demonstrated to drive silicon photonics modules for multi-functions [17]. Combined with the small mode area enabled by its high refractive index, as well as reduced scattering losses [18, 19], ultra-efficient frequency combs are feasible under tens of μW pumping [16].

However, $Al_{0.2}Ga_{0.8}As$ (also other similar III/VI materials) preserves difficulty in generating soliton frequency combs due to its strong absorption at the optical C band [20] (attributed to its smaller bandgap [21, 22]) and large thermo-opto coefficient [11] (an order of magnitude higher than silica and SiN) , especially at CMOS-capable repetition rates. The absorption converted to heat shifts the cavity resonance dramatically upon soliton formation, which makes it challenging for soliton stabilization [23]. Indeed, a stabilized soliton microcomb has only be obtained at cryogenic temperatures for $Al_{0.2}Ga_{0.8}As$ [11], while a soliton 'step' at room temperature has only been observed with a scanning laser [16]. AlN, another III/VI material has reported stabilized soliton microcombs with self-referencing using a rapid laser tuning system to overcome the thermal shift [13, 24], which involves extra electronics. As an aside, non-bright solitons have been demonstrated in $Al_{0.2}Ga_{0.8}As$ resonators where the intracavity power changing is relatively small [25], however, with limited number (tens) of comb lines and beyond CMOS compatible rates.

Synchronized pumping with a picosecond pulse for soliton generation launches less averaged power into a resonator, which reduces the influence of thermal heating [26]. It has also been reported to increase soliton conversion efficiency, regulate the soliton behaviour and lay insights on soliton trapping physics. The scheme also merits capability of integration with active modules by electrically pulse driving a gain-switched semiconductor laser [27]. Here, we generate soliton microcombs in

CMOS-ready $Al_{0.2}Ga_{0.8}As$ resonators using pulse pumping at room temperatures.

6.2 Results

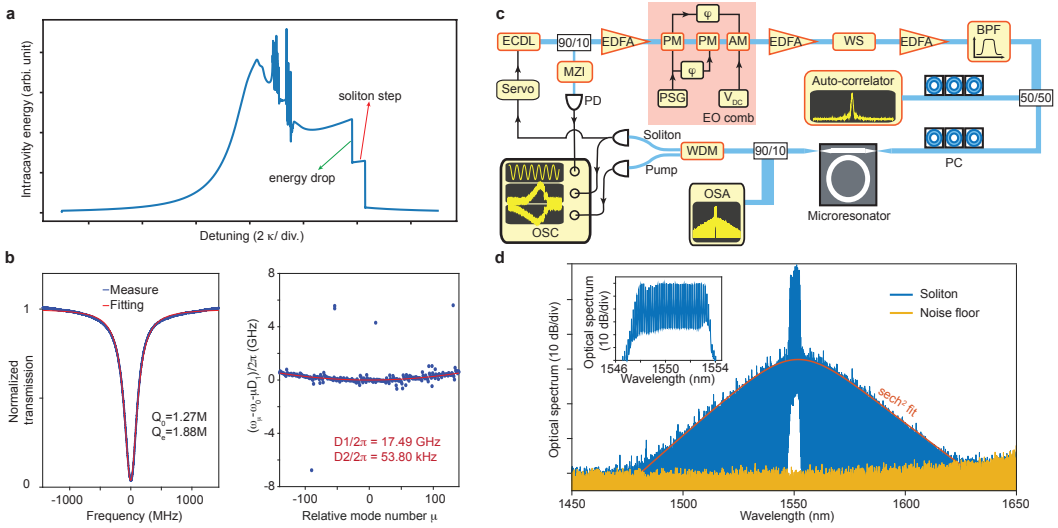

Figure 6.1: **Demonstration of microwave rate soliton in $Al_{0.2}Ga_{0.8}As$ microresonator at room temperature. (a)** Simulation result showing the process of soliton formation. Soliton can be generated when the input laser is scanned from blue to red, indicated by the soliton step. However, the generation of soliton will introduce a intracavity power drop, which will destabilize the resonator due to thermal-optics nonlinearity. **(b)** Characterization of the resonator used to generate the soliton. The resonator has a intrinsic Q-factor of 1.27 Million, and second order dispersion $D_2 \approx 17.49$GHz. **(c)** The experimental setup to generate the soliton in $Al_{0.2}Ga_{0.8}As$ resonator using electro-optical modulated optical pulse. ECDL: external-cavity diode laser; EDFA: erbium-doped fiber amplifier; PM: phase modulator; AM: intensity modulator; PSG: RF signal generator; φ: RF phase shifter; WS: waveshaper; BPF: Bandpass filter; PC: polarization controller; PD: photodetector; MZI: Mach-Zehnder interferometer; OSC: oscilloscope; OSA: optical spectrum analyzer. **(d)** The optical spectrum of generated optical soliton. The envelope of the soliton features sech^2 function. The soliton spectrum has 422 comb lines in 10dB bandwidth and 705 comb lines in 20dB bandwidth.

Schematic illustration and simulation of thermal effects under conventional cw pumping and pulse pumping is shown in Fig. 6.1(a). Generally speaking, solitons are generated by pumping a cavity resonance with a laser scanned from blue to red detuned. Solitons are thus generated after experiencing a high intra-cavity power chaotic regime, associated with a sudden power drop inside the cavity. A portion of the circulating power inside the resonator is converted into heat (especially for $Al_{0.2}Ga_{0.8}As$ whose absorption is strong [20]), which shifts the cavity resonant wavelength through the thermo-opto effect. And this sudden power drop shifts

the resonant wavelength significantly, pushing the laser-cavity detuning out of the possible soliton existence range. This effect is illustrated in Fig. 6.1(a). Numerical simulation based on the Lugiato-Lefever model cooperating thermal effect [28] is plotted in the same figure, where a soliton step [6, 7] cannot be observed. Here, FEM simulations give a thermal dissipation bandwidth of 10 kHz using the method in ref. [20], and the material absorption loss rate is $\sigma_{\mathrm{MAT}} = 28$ dB m^{-1}. For pulse pumping a microresonator (μs round trip time) with a pico-second pulse, as result of the reduced averaged pump power [26], the thermal shift upon soliton formation is smaller, which retrieved the soliton step for further caption and stabilization [23].

In experiment, an $Al_{0.2}Ga_{0.8}As$ micreresonator is adapter for soliton generation under a pico-second pulse pump. The resonator features a quality factor higher than 10^6 (Fig. 6.1(b), upper left), with anomalous dispersion (Fig. 6.1(b), upper right) fitted to feature $D_1/2\pi = 17.49$ GHz and $D_2/2\pi = 53.80$ kHz. The fitting residual is plotted in Fig. 6.1(b) lower right with scattered mode distribution, which is a result of fabrication non-perfections. The pico-second pulse is generated by electro-opto modulating an amplified tunable laser (ECDL) and dispersion compensation with a wave shaper. Amplified spontaneous emission from the Erbium amplifier is filtered out by a bandpass filter, and the pump pulse is coupled onto the $Al_{0.2}Ga_{0.8}As$ chip via a lensed fiber. The generated soliton comb is filtered out by a wavelength division multiplexer (WDM), detected by a photo detector and sent to a servo for stabilization of the soliton by applying feedback to the pumping laser frequency. Representative optical spectrum of the generated soliton comb at the throughout waveguide is plotted in Fig. 6.1(d) in blue with the sech^2 envelope fitting (fitted pulse width 46 fs), where the optical spectral analyzer (OSA) noise floor is plotted in yellow. Optical spectrum of the pumping pulse is plotted in the inset of Fig. 6.1(d) (2 ps pulse width as measured by an autocorrelator).

6.3 Summary

In conclusion, we demonstrated dissipative Kerr solitons inside an integrated $Al_{0.2}Ga_{0.8}As$ resonator at room temperature with a pico-second pulsed pump. The pulse pumping also enables robust generation of single soliton state with high fidelity; This work provides a method for generating solitons microcombs in integrated III/IV microresonators, and lay sights on soliton dynamics inside $Al_{0.2}Ga_{0.8}As$ microresonators.

References

[1] Kippenberg, T. J., Gaeta, A. L., Lipson, M. & Gorodetsky, M. L. Dissipative Kerr solitons in optical microresonators. *Science* **361** (2018).

[2] Suh, M.-G., Yang, Q.-F., Yang, K. Y., Yi, X. & Vahala, K. J. Microresonator soliton dual-comb spectroscopy. *Science* **354**, 600–603 (2016).

[3] Suh, M.-G. & Vahala, K. J. Soliton microcomb range measurement. *Science* **359**, 884–887 (2018).

[4] Trocha, P. *et al.* Ultrafast optical ranging using microresonator soliton frequency combs. *Science* **359**, 887–891 (2018).

[5] Yang, Q.-F. *et al.* Vernier spectrometer using counterpropagating soliton microcombs. *Science* **363**, 965–968 (2019).

[6] Herr, T. *et al.* Temporal solitons in optical microresonators. *Nat. Photon.* **8**, 145–152 (2014).

[7] Yi, X., Yang, Q.-F., Yang, K. Y., Suh, M.-G. & Vahala, K. Soliton frequency comb at microwave rates in a high-Q silica microresonator. *Optica* **2**, 1078–1085 (2015).

[8] Brasch, V. *et al.* Photonic chip–based optical frequency comb using soliton Cherenkov radiation. *Science* **351**, 357–360 (2016).

[9] Yang, K. Y. *et al.* Bridging ultrahigh-Q devices and photonic circuits. *Nat. Photon.* **12**, 297 (2018).

[10] He, Y. *et al.* Self-starting bi-chromatic $LiNbO_3$ soliton microcomb. *Optica* **6**, 1138–1144 (2019).

[11] Moille, G. *et al.* Dissipative Kerr solitons in a III-V microresonator. *Laser Photonics Rev.* **14**, 2000022 (2020).

[12] Jung, H. *et al.* Tantala Kerr nonlinear integrated photonics. *Optica* **8**, 811–817 (2021).

[13] Liu, X. *et al.* Aluminum nitride nanophotonics for beyond-octave soliton microcomb generation and self-referencing. *Nat. Commun.* **12**, 1–7 (2021).

[14] Guidry, M. A., Lukin, D. M., Yang, K. Y., Trivedi, R. & Vučković, J. Quantum optics of soliton microcombs. *Nat. Photon.* **16**, 52–58 (2022).

[15] Cai, L., Li, J., Wang, R. & Li, Q. Octave-spanning microcomb generation in 4H-silicon-carbide-on-insulator photonics platform. *Photon. Res.* **10**, 870–876 (2022).

[16] Chang, L. *et al.* Ultra-efficient frequency comb generation in AlGaAs-on-insulator microresonators. *Nat. Commun.* **11**, 1–8 (2020).

[17] Shu, H. *et al.* Bridging microcombs and silicon photonic engines for optoelectronics systems. *arXiv:2110.12856* (2021).

[18] Chang, L. *et al.* Low loss (al) gaas on an insulator waveguide platform. *Opt. Lett.* **44**, 4075–4078 (2019).

[19] Xie, W. *et al.* Ultrahigh-Q AlGaAs-on-insulator microresonators for integrated nonlinear photonics. *Opt. Express* **28**, 32894–32906 (2020).

[20] Gao, M. *et al.* Probing material absorption and optical nonlinearity of integrated photonic materials. *Nat. Commun.* **13**, 3323 (2022).

[21] Parrain, D. *et al.* Origin of optical losses in gallium arsenide disk whispering gallery resonators. *Opt. Express* **23**, 19656–19672 (2015).

[22] Guha, B. *et al.* Surface-enhanced gallium arsenide photonic resonator with quality factor of 6×10^6. *Optica* **4**, 218–221 (2017).

[23] Yi, X., Yang, Q.-F., Yang, K. Y. & Vahala, K. Active capture and stabilization of temporal solitons in microresonators. *Opt. Lett.* **41**, 2037–2040 (2016).

[24] Gong, Z. *et al.* High-fidelity cavity soliton generation in crystalline AlN micro-ring resonators. *Opt. Lett.* **43**, 4366–4369 (2018).

[25] Shu, H. *et al.* Sub-milliwatt, widely-tunable coherent microcomb generation with feedback-free operation. *arXiv:2112.08904* (2021).

[26] Obrzud, E., Lecomte, S. & Herr, T. Temporal solitons in microresonators driven by optical pulses. *Nat. Photon.* **11**, 600 (2017).

[27] Weng, W. *et al.* Gain-switched semiconductor laser driven soliton microcombs. *Nat. Commun.* **12**, 1–9 (2021).

[28] Li, Q. *et al.* Stably accessing octave-spanning microresonator frequency combs in the soliton regime. *Optica* **4**, 193–203 (2017).

Chapter 7

EXOPLANET SEARCHING USING ELECTRO-OPTIC FREQUENCY COMB AS NEAR-INFRARED FREQUENCY REFERENCE

The discovery and characterization of exoplanets using the Precision Radial Velocity (PRV) and transit spectroscopy techniques relies on high spectral resolution spectrometers with extremely stable and long-term wavelength solutions. The development of Laser Frequency Combs (LFC) plays a key role in advancing the observational capabilities of existing and future spectrometers. We report the development and commissioning of a near-infrared (NIR) LFC for the NIRSPEC instrument on the 10-m Keck-2 telescope of the Keck Observatory on Maunakea. The Electro-Optical Modulation LFC operates over wavelengths from 1.2 to 2.1 μm with future extension to 2.5 μm. The LFC has an intrinsic mode spacing of 16 GHZ with a long term stability < 10 cm s^{-1} by reference to a Rubidium standard.

7.1 Introduction to exoplanet searching and Precision Radial Velocity (PRV) technique

The search for exoplanets, planets orbiting stars outside our solar system, has become one of the most exciting fields in modern astronomy. The discovery of these distant worlds not only enhances our understanding of planetary systems but also fuels the quest to find potentially habitable environments beyond Earth. Various techniques are employed to detect and characterize exoplanets, including transit photometry, radial velocity, direct imaging, microlensing, and astrometry. According to the Open Exoplanet Catalogue database [1], as of June 25, 2024, a total of 5,414 exoplanets have been confirmed, and 1,075 of them are confirmed using the PRV method. A statistical plot of discovery methods is shown in Fig. 7.1. Among these methods, the **Precision Radial Velocity (PRV) method** is one of the most successful and widely used.

The PRV technique involves measuring the effective two-body motion of the star caused by the gravitational pull of an orbiting planet. As a planet orbits a star, it induces a periodic shift in the star's velocity along the line of sight to the observer. This shift can be detected as changes in the star's spectral lines due to the Doppler effect. By precisely measuring these changes in the star's spectrum over time,

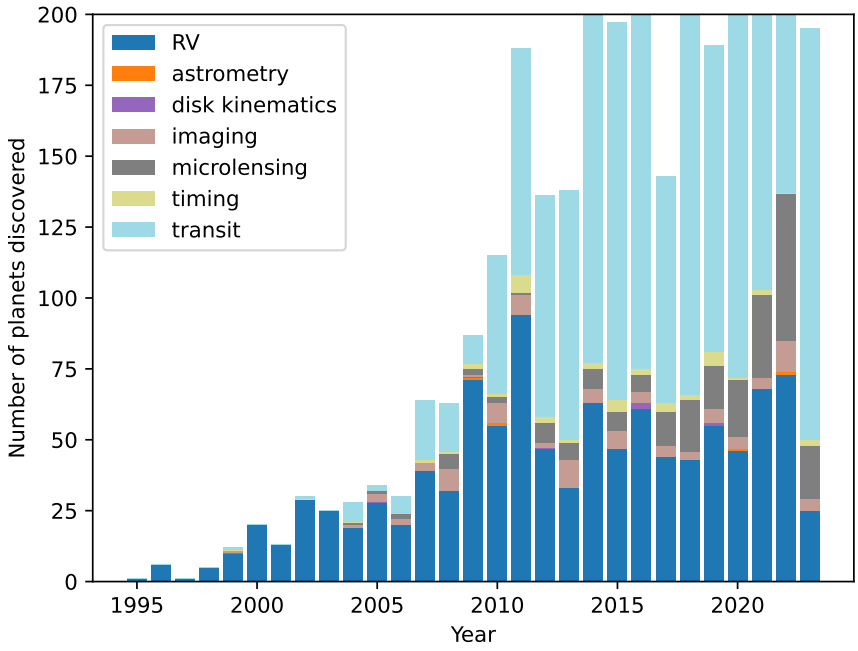

Figure 7.1: **Number of exoplanets discovered by various methods over time.** The methods include Radial Velocity (RV), transit photometry, disk kinematics, direct imaging, timing, microlensing, and astrometry. The PRV method has been particularly successful, contributing significantly to the total number of confirmed exoplanets. The data used to plot this figure is from Open Exoplanet Catalogue database. This figure is up-to-date as of June 24, 2024. Python code to plot the most up-to-date version of this figure is attached in Appendix G.1.

astronomers can infer the presence of an exoplanet, estimate its mass, and determine its orbital parameters. It is also worth to note that among all the methods listed in Fig. 7.1, only PRV and astrometry are able to characterize the mass of the exoplanets. However, while astrometry can not be performed from the ground, PRV can.

The frequency of the observed spectral line f_{obs} when the star emits a frequency f_{emit}, affected by the **optical Doppler effect**, is given by:

$$f_{\text{obs}} = f_{\text{emit}} \sqrt{\frac{c+v}{c-v}}, \tag{7.1}$$

where v is the velocity of the star along the line of sight (negative when the star is moving away from the observer and positive when moving towards the observer). Taking the derivative of Eq. (7.1), we have

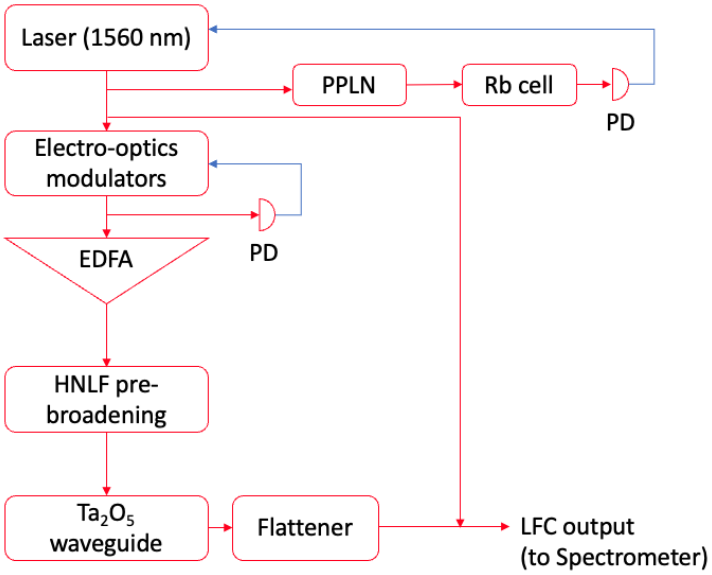

Figure 7.2: **Schematic of the Laser Frequency Comb (LFC) signal chain.** The system starts with a laser at 1560 nm, which is modulated by electro-optic modulators. The signal is amplified using an Erbium-Doped Fiber Amplifier (EDFA) and pre-broadened through a Highly Nonlinear Fiber (HNLF). The broadened signal then passes through a Ta_2O_5 waveguide and a flattener before being directed to the spectrometer as the LFC output. Part of the signal is also directed through periodically poled lithium niobate (PPLN) and a Rubidium cell for stabilization and locking, monitored by photodetectors (PD). Both PDs are used for stabilization and locking of the LFC.

$$\frac{\delta f_{\text{obs}}}{f_{\text{obs}}} = \frac{\delta v}{c}, \tag{7.2}$$

where δf_{obs} is the uncertainty of the observed frequency, δv is the uncertainty of the star velocity.

By achieving smaller uncertainties in the star's velocity, astronomers can detect lower-mass planets, which produce smaller velocity shifts in their host stars. Although detecting Earth-like planets orbiting sun-like stars remains extremely challenging due to the minute RV signals (around 9 cm/s) and other contributing factors such as stellar noise (e.g., spots, granulation, and faculae), this level of precision is significant. Additionally, because this comb/spectrograph works well into the near-infrared (NIR), it can effectively characterize planets orbiting smaller, cooler stars, such as M-dwarfs, providing crucial data for the search for potentially habitable exoplanets. Current astronomical spectrometers can achieve an observed frequency

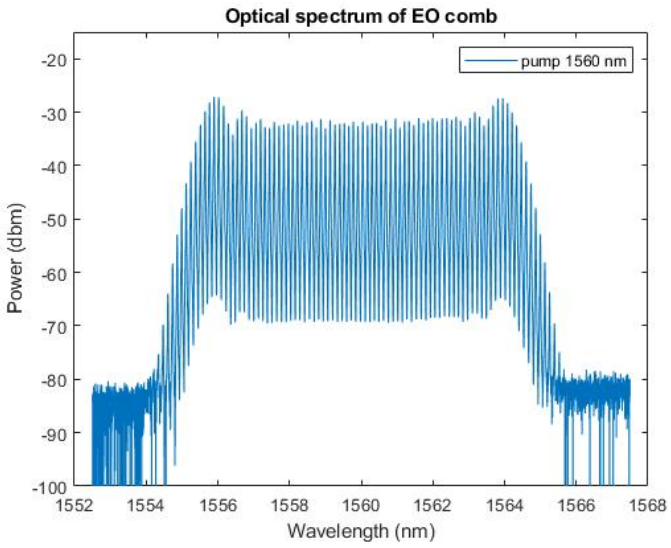

Figure 7.3: **Optical spectrum of the electro-optic (EO) comb generated by the 1560 nm laser.** The comb has a bandwidth of approximately 12 nm. After dispersion compensation, this comb can achieve a full width at half maximum (FWHM) in the time domain around 800 fs.

uncertainty corresponding to a radial velocity precision of around 0.3 m s^{-1} or better, according to ref. [2].

To achieve such high precision, advanced calibration techniques and stable wavelength references, such as Laser Frequency Combs (LFCs), are employed.

Achieving high precision in stellar velocity measurements requires advanced calibration techniques and stable wavelength references, such as Laser Frequency Combs (LFCs). These technologies ensure the spectrograph's stability and accuracy, enabling precise measurements of stellar velocities over long periods. This chapter discusses the development and implementation of an Electro-Optical Modulation LFC for the NIRSPEC instrument, enhancing its capability to perform high-precision PRV measurements in the near-infrared spectrum.

7.2 LFC signal chain

The Laser Frequency Comb (LFC) signal chain is a compact system designed to provide precise and stable wavelength references for high-precision radial velocity measurements. The signal chain, as depicted in Figure 7.2, involves several key components and processes that ensure the stability and accuracy of the LFC output.

The process begins with a laser operating at 1560 nm. The linewidth of the initial

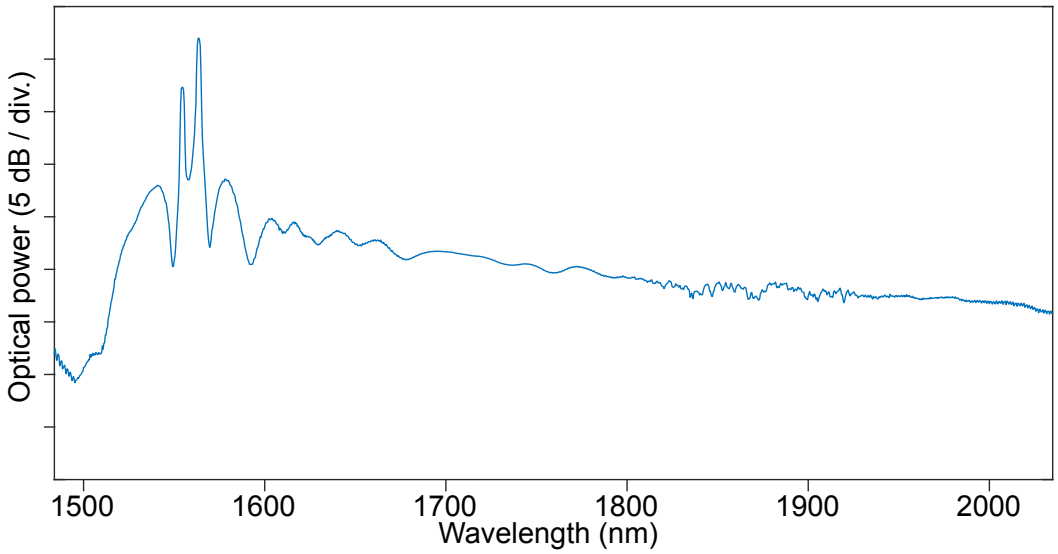

Figure 7.4: **Optical spectrum of the fully broadened comb after Ta_2O_5 waveguide.** This spectrum shows the broadened comb spans from 1400nm to 2100nm. The peak around 1560nm is the amplified EO comb pump.

laser source is critical as it serves as the basis for subsequent frequency modulation and broadening. The laser's frequency is doubled through a periodically poled lithium niobate (PPLN) crystal and then referenced to a Rubidium (Rb) cell to lock its absolute frequency.

The laser signal is then directed through three electro-optic modulators in series and an intensity modulator, creating the electro-modulated seed signal. The spectrum of the electro-modulated comb is shown in Figure 7.3. The dispersion of this comb is then compensated with a waveshaper, forming the mode-locked electro-optic comb. The DC bias of the intensity modulator is locked to keep the operating point at $\phi_{\mathrm{DC}} = \pi/2$.

Following modulation, the signal is amplified using an Erbium-Doped Fiber Amplifier (EDFA) and then undergoes pre-broadening through a section of Highly Nonlinear Fiber (HNLF). The HNLF compresses the mode-locked pulse in the time domain, which is critical for the subsequent waveguide to function effectively. The spectrum bandwidth of the pre-broadened comb is approximately 200 nm. The lengths of the HNLF and the subsequent dispersion compensation PM1550 fiber need to be carefully optimized.

After pre-broadening, the signal is passed through a Ta_2O_5 waveguide. This waveguide handles pulses with energies greater than 160 pJ and durations shorter than

120 fs, broadening these pulses in the spectral domain. Under optimal operation, the waveguide can achieve spectral broadening to cover one octave. The spectrum after waveguide broadening is shown in Fig. 7.4.

Finally, the comb spectrum is flattened using a commercial spectral flattener. The flattened spectrum is then directed to the spectrometer as the LFC output. This output serves as a highly precise wavelength reference, enabling the spectrometer to perform accurate and stable measurements over long periods.

In addition to the primary signal path, part of the laser signal is re-injected into the comb as a center indicator. This auxiliary pump indicator creates a single strong comb line to indicate which line corresponds to half of the Rb transition frequency.

It is critical to emphasize that every component within this system must be polarization-maintained. Without maintaining polarization, the generated comb will not meet the required stability. A photo of the full setup is shown in Fig. 7.5.

Figure 7.5: **Photo of the full setup of LFC.** The setup contains one equipment rack on the right, together with two bread boards covered by the black enclosure on the optical table.

7.3 Stability

The stability of the Laser Frequency Comb (LFC) is crucial for ensuring precise and consistent wavelength references over time. In this section, we discuss two important aspects of LFC stability: power stability and frequency stability, as characterized by Allan deviation.

7.3.1 Power stability

The stability of pulse energy injected into the waveguide is important, as fluctuations in pulse energy may result in variations in the final full comb bandwidth. Here,

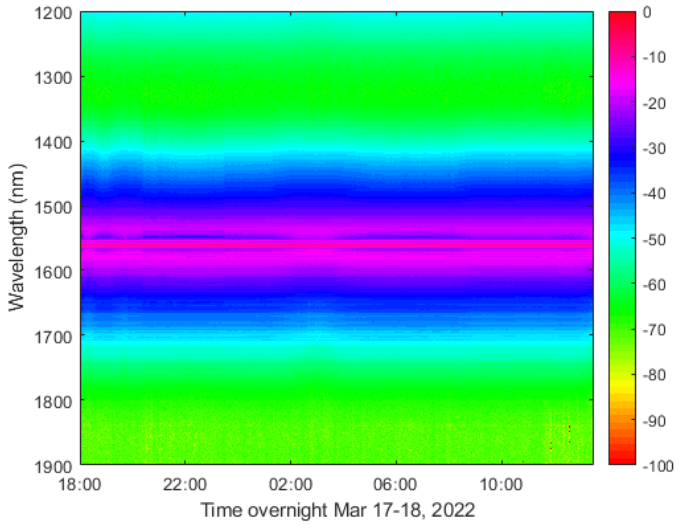

Figure 7.6: **Power stability of the LFC over time** The data was collected from the evening of March 17, 2022, to the morning of March 18, 2022. The color scale represents the power (dBm) at different wavelengths (nm).

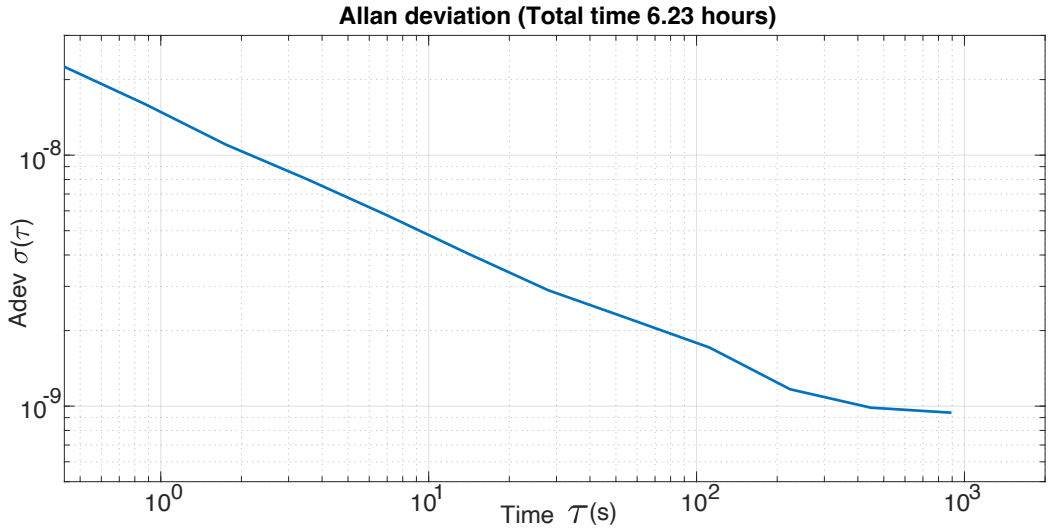

Figure 7.7: **Allan deviation of LFC optical frequency.** This data is collected by beating LFC against a commercialized HCN-referenced laser with an Allan deviation of 10^{-9} at 10^{2} seconds offset time.

we characterized the stability of the comb spectrum power after the HNLF pre-broadening stage overnight. The result is shown in Figure 7.6.

The results show that the comb power does not exhibit strong fluctuations. This data was collected while the amplifiers were operating under a constant power output mode, which minimized noise transfer from any power fluctuations in the source

laser.

7.3.2 Allan deviation

The stability of the LFC optical frequency is crucial because it determines the uncertainty of the observed star light frequency, $\delta f_{\rm obs}$. As shown in Eq. (7.2), the relative uncertainty of optical frequency, $\delta f_{\rm obs}/f_{\rm obs}$, directly affects the uncertainty of the star's radial velocity, δv. Here, $\delta f_{\rm obs}/f_{\rm obs}$ is characterized by the Allan deviation of the optical frequency. This measurement was performed by monitoring the beat-note between the pump laser and a wavelength-reference laser. The wavelength-reference laser is a commercial laser with its frequency locked to HCN. The frequency Allan deviation of this commercial reference laser is 10^{-9} at 10^2 seconds.

From Eq. (7.2), we can see that an Allan deviation of 10^{-9} corresponds to $\delta v = 10^{-9}c = 10$ cm s^{-1}. Compared to the wavelength calibration of spectrographs, this precision is improved by four orders of magnitude.

7.4 On sky observation

First we demonstrated the LFC exposure on NIRSPEC spectrograph. The result is shown in Fig. 7.8.

After KPIC is installed in February 2024, LFC and star light will be able to simultaneously inject into the NIRSPEC. One simultaneous exposure is shown in Fig. 7.9. This data is collected on April 26, 2024.

Acknowledgement

The project discussed in this chapter is supported by Heising-Simons Foundation.

References

[1] Rein, H. A proposal for community driven and decentralized astronomical databases and the open exoplanet catalogue. *arXiv.1211.7121* (2012).

[2] KPF Home Page. URL `https://www2.keck.hawaii.edu/inst/kpf/`.

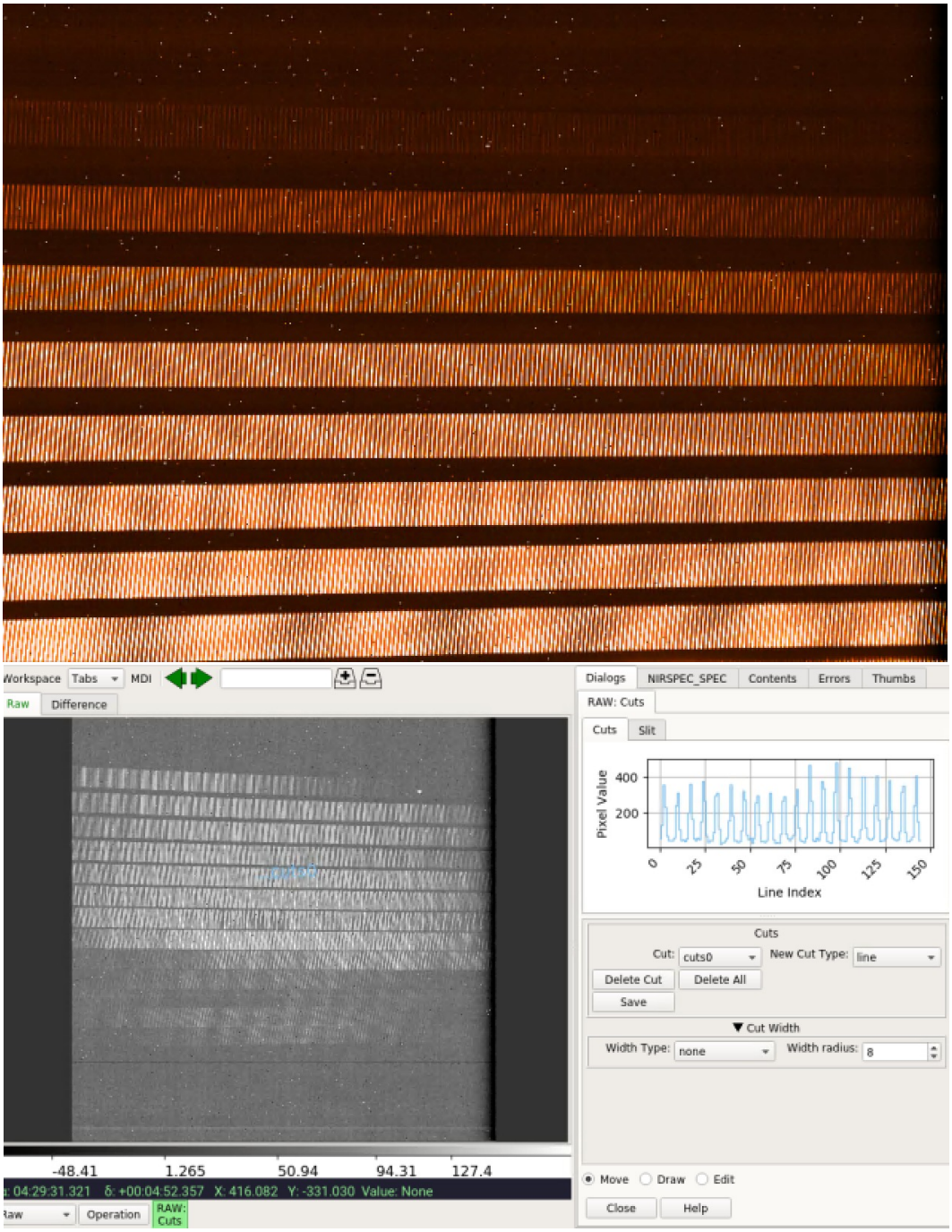

Figure 7.8: **LFC signal collected by NIRSPEC spectrograph.**

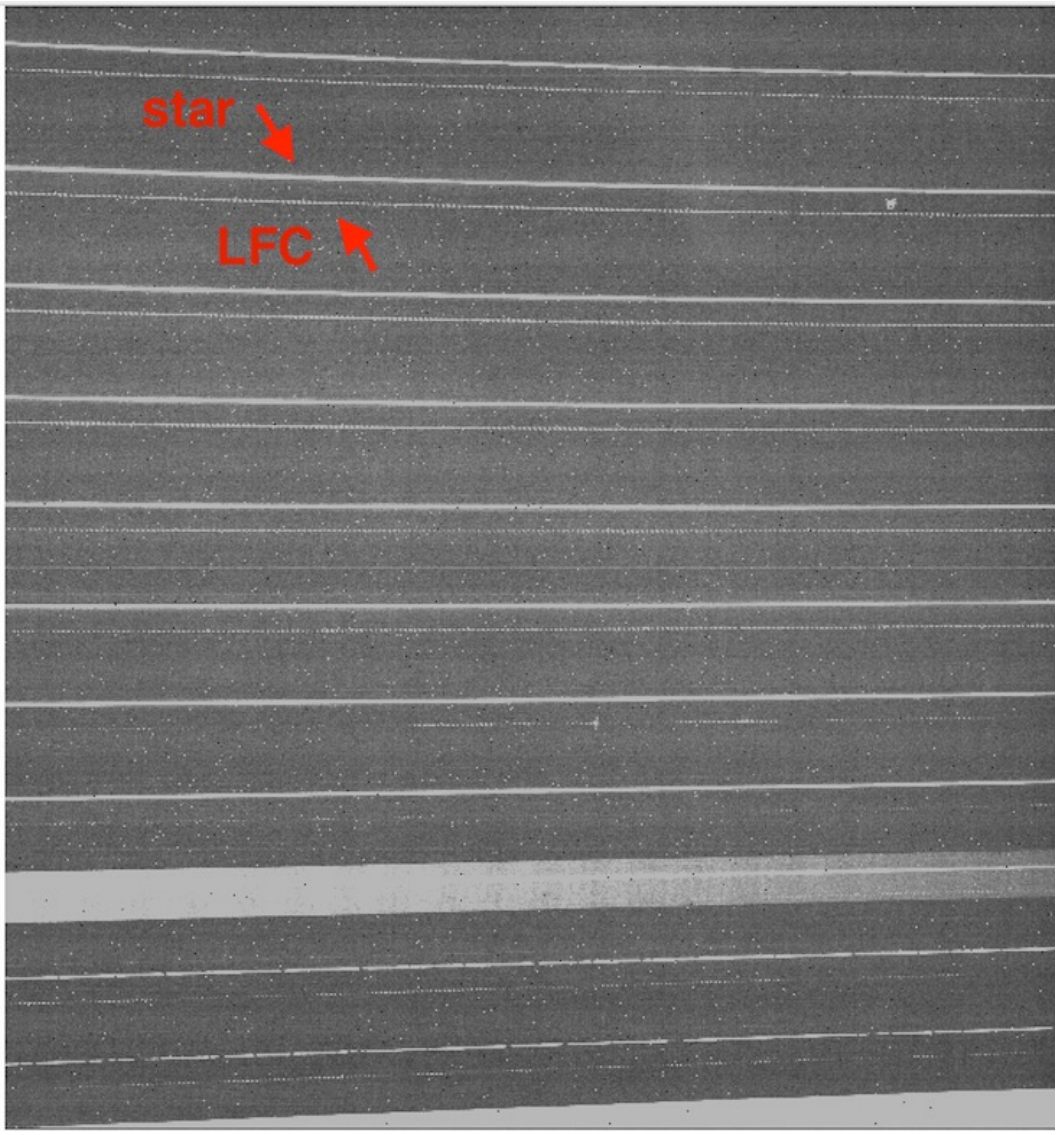

Figure 7.9: **Simultaneous exposure of LFC and star light.**

Appendix A

THE FOURIER TRANSFORM OF DIRAC COMB

In this section, we explain why the Fourier transform of Dirac comb distribution is itself. Dirac comb distribution was defined in Eq. (1.100), reads

$$\text{Ш}(x) = \sum_{n\in\mathbb{Z}} \delta(x-n).$$

And we want to show that the Fourier transform of $\text{Ш}(x)$ is itself, as summarized in Eq. (1.101), reads

$$\mathcal{F}\left[\text{Ш}(x)\right] = \text{Ш}(x).$$

A.1 Derivation of $\mathcal{F}\left[\text{Ш}(x)\right] = \text{Ш}(x)$

The equation in Eq. (1.101) can be derived by calculating the (inverse) Fourier series of $\text{Ш}(x)$. $\text{Ш}(x)$ is a distribution defined on $x \in \mathbb{R}$, with a period of 1, i.e.,

$$\text{Ш}(x) = \text{Ш}(x+n), \quad \forall n \in \mathbb{Z},\, x \in \mathbb{R}. \tag{A.1}$$

Thus, $\text{Ш}(x)$ can be decomposed into orthonormal basis functions:

$$h_m(x) = \mathrm{e}^{-i2\pi mx}, \quad m \in \mathbb{Z},\, x \in \mathbb{R}, \tag{A.2}$$

with the inner product:

$$\langle h_m, h_n\rangle = \int_a^b h_m(x) h_n^*(x)\,\mathrm{d}x = \delta_{m,n}, \quad \text{for } b-a=1. \tag{A.3}$$

This decomposition, or inverse Fourier series, of $\text{Ш}(x)$ is:

$$\text{Ш}(x) = \sum_{m\in\mathbb{Z}} C_m \mathrm{e}^{-i2\pi mx}, \quad x \in \mathbb{R}. \tag{A.4}$$

Calculating C_m by taking the inner product of $\text{Ш}(x)$ with $\mathrm{e}^{-i2\pi mx}$, we get:

$$C_m = \langle \text{Ш}(x), \mathrm{e}^{-i2\pi mx}\rangle = \int_a^b \text{Ш}(x)\mathrm{e}^{i2\pi mx}\,\mathrm{d}x = 1, \quad \text{for } b-a=1,\ a \notin \mathbb{Z}. \tag{A.5}$$

Therefore, $\text{Ш}(x) = \sum_{m\in\mathbb{Z}} \mathrm{e}^{-i2\pi mx}$. This verifies Eq. (1.101) by:

$$\text{Ш}(x) = \sum_{m\in\mathbb{Z}} \mathrm{e}^{-i2\pi mx} = \sum_{m\in\mathbb{Z}} \mathcal{F}\left[\delta(x-m)\right] = \mathcal{F}\left[\sum_{m\in\mathbb{Z}} \delta(x-m)\right] = \mathcal{F}\left[\text{Ш}(x)\right]. \tag{A.6}$$

In Eq. (A.6), we used $\mathcal{F}\left[\delta(x)\right] = 1$ and $\mathcal{F}\left[\delta(x-m)\right] = \mathrm{e}^{-i2\pi mx}$.

Appendix B

LINESHAPE OF THE OPTICAL RESONATOR COUPLED WITH WAVEGUIDE ETALON

B.1 Derivation of the lineshape

Three of the devices being tested in Chapter 2 (Si_3N_4, $Al_{0.2}Ga_{0.8}As$ and Ta_2O_5) feature integrated waveguides, so that light is coupled to the chip through the waveguide facets located at the side of the chips. Of these three devices, the facets of the $Al_{0.2}Ga_{0.8}As$ are angled, while the Si_3N_4 and Ta_2O_5 have flat facets, causing the light in the waveguide to be reflected at these endpoints. The reflections form a Fabry–Pérot (FP) cavity out of the on-chip waveguide, and the measured resonator transmission lineshapes appear with a modulated background. In the following we model this FP background in order to extract resonator properties accurately.

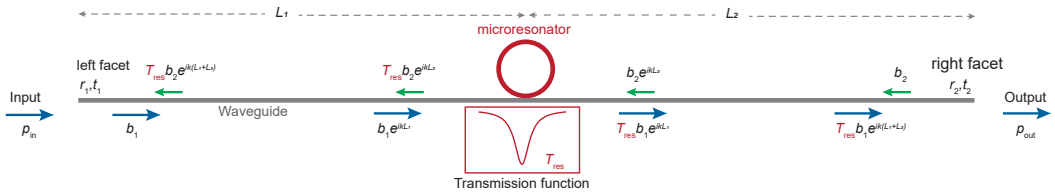

Figure B.1: **Schematic used for modelling transmission spectra with FP backgrounds.** The micro-resonator (red ring) is coupled to the bus waveguide (gray line). Quantities are defined in the text.

We denote b_1 (b_2) as the slowly-varying field just inside the input (output) waveguide facet propagating towards the resonator (Fig. B.1). At the output facet, the field propagating towards the facet reads $T_{\mathrm{res}}\mathrm{e}^{ik(L_1+L_2)}b_1$, where T_{res} is the linear transmission function of the resonator, k is the wavevector, and L_1 and L_2 are waveguide lengths from the resonator coupling point to the input and output facets, respectively. This expression assumes no loss on the waveguide, and the exponential factor accounts for the propagation phase. Similarly, at the input facet, the field propagating towards the facet reads $T_{\mathrm{res}}\mathrm{e}^{ik(L_1+L_2)}b_2$. Reflection at the facets cause the fields in the two directions to couple together as follows:

$$b_1 = r_1 T_{\mathrm{res}} b_2 \mathrm{e}^{ik(L_1+L_2)} + t_1 p_{\mathrm{in}}, \tag{B.1}$$

$$b_2 = r_2 T_{\mathrm{res}} b_1 \mathrm{e}^{ik(L_1+L_2)}, \tag{B.2}$$

where r_1 (r_2) and t_1 (t_2) are reflection and transmission coefficients, respectively, at the input (output) waveguide facet, and p_{in} is the input field at the waveguide facet. Solving the above equations gives

$$b_1 = \frac{t_1 p_{\text{in}}}{1 - r_1 r_2 T_{\text{res}}^2 \mathrm{e}^{2ikL_{\text{wg}}}}. \tag{B.3}$$

with $L_{\text{wg}} \equiv L_1 + L_2$. The output field from the waveguide p_{out} is

$$p_{\text{out}} = t_2 T_{\text{res}} b_1 \mathrm{e}^{ikL_{\text{wg}}}. \tag{B.4}$$

and the output power can be found as

$$P_{\text{out}} = |p_{\text{out}}|^2 = |t_1 t_2|^2 \frac{|T_{\text{res}}|^2}{|1 - r_1 r_2 T_{\text{res}}^2 \mathrm{e}^{2ikL_{\text{wg}}}|^2} |p_{\text{in}}|^2. \tag{B.5}$$

To see how this power transmission gives the FP background, we consider the case when the resonator is not on resonance, i.e., $T_{\text{res}} = 1$. The above equation simplifies to

$$P_{\text{out}} = \frac{|t_1 t_2|^2}{|1 - r_1 r_2 \mathrm{e}^{2ikL_{\text{wg}}}|^2} |p_{\text{in}}|^2. \tag{B.6}$$

For later convenience, the wavevector k is replaced with the cavity detuning of a certain resonance, $\Delta_{\text{res}} = \omega_{\text{c,res}} - \omega_p$, where $\omega_{\text{c,res}}$ is the resonance frequency and ω_p is the pump frequency. The exponential factor can then be written as,

$$\exp(2ikL_{\text{wg}}) = \exp\left[2i\frac{L_{\text{wg}}}{c}(\omega_{\text{c,res}} - \Delta_{\text{res}})\right] = \exp\left(-i\frac{\Delta_{\text{res}}}{\omega_{\text{FP}}} + i\phi\right) \tag{B.7}$$

where we have identified $\omega_{\text{FP}} = c/(2L_{\text{wg}})$ as the free spectral range of the FP cavity and $\phi = \omega_{\text{c,res}}/\omega_{\text{FP}}$ is a phase offset. Therefore, the power transmission reads

$$P_{\text{out}} = \frac{|t_1 t_2|^2}{|1 - r_1 r_2 \mathrm{e}^{-i\Delta_{\text{res}}/\omega_{\text{FP}} + i\phi}|^2} |p_{\text{in}}|^2. \tag{B.8}$$

From here, the total reflection $r = |r_1 r_2|$, total transmission $|t_1 t_2|$ and the phase offset ϕ can be fitted from the experiment data. We note that the phase of $r_1 r_2$ can be absorbed into ϕ and the fitting parameters can be restricted to be real.

Near the resonance frequency, the linear transmission T_{res} can be found from the coupled-mode equation and the input-output relations of the resonator:

$$\frac{\mathrm{d}a_{\text{res}}}{\mathrm{d}t} = -\left(\frac{\kappa_{\text{res}}}{2} + i\Delta_{\text{res}}\right) a_{\text{res}} + \sqrt{\kappa_{e,\text{res}}} a_{\text{in}}, \tag{B.9}$$

$$a_{\text{out}} = -\sqrt{\kappa_{e,\text{res}}} a_{\text{res}} + a_{\text{in}}, \tag{B.10}$$

where a_{res} is the field amplitude of the resonance, κ_{res} and $\kappa_{e,\mathrm{res}}$ are the intrinsic loss rate and external coupling rate of the resonance mode, respectively, a_{in} and a_{out} are the waveguide fields before and after the resonator, and Δ_{res} is the detuning introduced previously. At steady state ($\mathrm{d}a_{\mathrm{res}}/\mathrm{d}t = 0$) the transmission can be solved as

$$T_{\mathrm{res}} = \frac{a_{\mathrm{out}}}{a_{\mathrm{in}}} = 1 - \frac{\kappa_{e,\mathrm{res}}}{\kappa_{\mathrm{res}}/2 + i\Delta_{\mathrm{res}}}. \tag{B.11}$$

The overall power transmission now reads

$$P_{\mathrm{out}} = |t_1 t_2|^2 \frac{|T_{\mathrm{res}}|^2}{|1 - r_1 r_2 T_{\mathrm{res}}^2 \mathrm{e}^{-i\Delta_{\mathrm{res}}/\omega_{\mathrm{FP}} + i\phi}|^2} |p_{\mathrm{in}}|^2. \tag{B.12}$$

where T_{res} should be substituted with the previous equation. From here, κ_{res} and $\kappa_{e,\mathrm{res}}$ can be fitted using experimental data and parameters from the previous stage.

It is important to note that the lineshape is not a product of the FP background and the bare Lorentzian resonance $|T_{\mathrm{res}}|^2$. The appearance of T_{res} on the denominator of P_{out} creates interference between the two lineshapes, which leads to about 20% error for Q values for the current data unless the FP interference is taken into account. An example of a Ta_2O_5 resonance is shown in Fig. B.2.

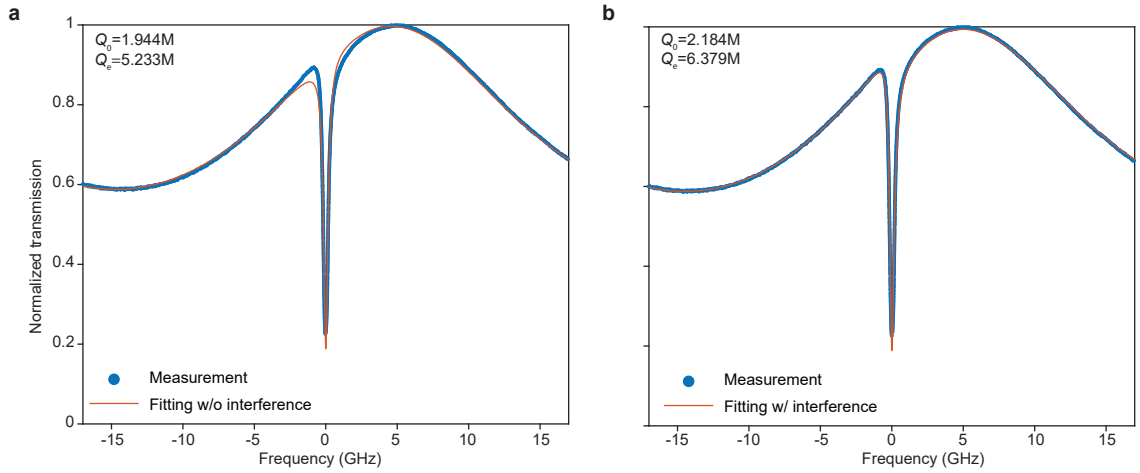

Figure B.2: Q **fitting with FP background.** **(a)** and **(b)** are the results of fitting the same resonance of a Ta_2O_5 resonator TE mode at 1559.4nm. **(a)** An overly simplified model of the FP background times the Lorentzian resonance is used here to fit the experiment data. A deviation between data and fitting can be observed around the resonance. **(b)** The improved model (Eq. (B.12) and Eq. (B.11)) is used to fit data and gives a more accurate fitting. Q_0 is the fitted intrinsic Q and Q_e is the fitted external (coupling) Q. The Q factors obtained in both cases have a difference about 20%, showing that it is essential to take the FP interference effect into account.

The above results do not apply to the case when the resonance undergoes nonlinear broadening, where T_{res} now depends on the pump power at the resonator. The analysis is further complicated by the fact that the transmitted power after the resonator will be reflected to affect the pumping power, and the backward-propagating light sees a different resonance in the resonator due to the difference between self- and cross-phase Kerr modulations. To get around these problems, we assume that at all frequencies, the pumping power for the resonator is the waveguide power with FP effects but without the cavity resonance, and we do not iterate further to consider the effect of reflected transmission on the pumping power. This is justified as the overall reflection r observed in the samples is relatively weak ($< 10\%$). In this case, starting from the coupled-mode equations with nonlinear effects,

$$\frac{\mathrm{d}a_{\text{res}}}{\mathrm{d}t} = -\left(\frac{\kappa_{\text{res}}}{2} + i(\Delta_{\text{res}} - (\alpha + g)\rho_{\text{res}})\right) a_{\text{res}} + \sqrt{\kappa_{e,\text{res}}}a_{\text{in}}, \tag{B.13}$$

where $\rho_{\text{res}} = |a_{\text{res}}|^2/V_{\text{eff}}$ is the resonance mode energy density, the transmission at steady state can be determined as

$$T_{\text{res}} = 1 - \frac{\kappa_{e,\text{res}}}{\kappa_{\text{res}}/2 + i(\Delta_{\text{res}} - (\alpha + g)\rho_{\text{res}})}. \tag{B.14}$$

The overall power transmission is approximated by substituting the above nonlinear T_{res} into Eq. (B.12), and is used to fit the sum measurement data. The fitting results of the sum of Kerr and thermal coefficient $\alpha + g$ are shown in Fig. 2.2(b).

Appendix C

MODEL FOR RATIO EXPERIMENT IN CHAPTER 2

C.1 Model for ratio experiment

Here we derive Eqs. (2.9), (2.10), and (2.11), which describe the response of the probe mode transmission when the power pumping the pump mode is modulated. The modulation can be broken down into three independent processes. The modulation of pumping power leads to the change of intracavity power in the pump mode, which leads to frequency shifts of the probe mode, which in turn leads to the transmission changes at a fixed frequency. The overall transfer function is the product of the three individual responses.

The dynamics of the pump mode reads

$$\frac{\mathrm{d}a_\mathrm{p}}{\mathrm{d}t} = -\frac{\kappa_\mathrm{p}}{2}a_\mathrm{p} + \sqrt{\kappa_{e,\mathrm{p}}}a_\mathrm{in,p}, \tag{C.1}$$

where a_p is the pump mode amplitude, κ_p and $\kappa_{e,\mathrm{p}}$ are the total loss rate and external coupling rate of the pump mode, respectively, $a_\mathrm{in,p}$ is the pump input amplitude, and the frequency detuning term has been removed because the pump laser is locked close to the mode resonance in the experiment. The steady-state solution reads

$$a_\mathrm{p}^{(0)} = \frac{2}{\kappa_\mathrm{p}}\sqrt{\kappa_{e,\mathrm{p}}}a_\mathrm{in,p}^{(0)}, \tag{C.2}$$

where $z^{(0)}$ is the steady-state value of variable z. Fourier transforming Eq. (C.1) gives

$$i\Omega\widetilde{a_\mathrm{p}} = -\frac{\kappa_\mathrm{p}}{2}\widetilde{a_\mathrm{p}} + \sqrt{\kappa_{e,\mathrm{p}}}\widetilde{a_\mathrm{in,p}}, \quad \widetilde{a_\mathrm{p}} = \frac{1}{\kappa_\mathrm{p}/2 + i\Omega}\sqrt{\kappa_{e,\mathrm{p}}}\widetilde{a_\mathrm{in,p}}, \tag{C.3}$$

where the AC component of z's Fourier transform is denoted as $\widetilde{z}$. Similarly

$$\widetilde{a_\mathrm{p}^*} = \frac{1}{\kappa_\mathrm{p}/2 + i\Omega}\sqrt{\kappa_{e,\mathrm{p}}}\widetilde{a_\mathrm{in,p}^*}. \tag{C.4}$$

We denote $I_\mathrm{p} = |a_\mathrm{p}|^2$ as the intracavity energy and $P_\mathrm{in} = |a_\mathrm{in,p}|^2$ the pumping power. For small-signal modulations, we have

$$\widetilde{I_\mathrm{p}} \approx (a_\mathrm{p}^{(0)})^*\widetilde{a_\mathrm{p}} + a_\mathrm{p}^{(0)}\widetilde{a_\mathrm{p}^*}, \quad \widetilde{P_\mathrm{in}} \approx (a_\mathrm{in,p}^{(0)})^*\widetilde{a_\mathrm{in,p}} + a_\mathrm{in,p}^{(0)}\widetilde{a_\mathrm{in,p}^*}. \tag{C.5}$$

After substituting $a_{\mathrm{p}}^{(0)}$ with $a_{\mathrm{in,p}}^{(0)}$ and using Eq. (C.3) and (C.4), we get

$$\frac{\widetilde{I_{\mathrm{p}}}(\Omega)}{\widetilde{P_{\mathrm{in}}}(\Omega)} = \frac{2\eta_{\mathrm{p}}}{i\Omega + \kappa_{\mathrm{p}}/2}, \tag{C.6}$$

where $\eta_{\mathrm{p}} = \kappa_{e,\mathrm{p}}/\kappa_{\mathrm{p}}$ is the coupling efficiency for the pump mode. We note that the modulation of I_{p} also shifts the frequency of the pump mode. However, since I_{p} is maximized at zero detuning, such detuning changes do not influence I_{p} up to first order, which justifies dropping the detuning term from the beginning.

The resonance shift of the probe mode δ_{b} can be written similarly as (2.1) in the main text and reads

$$\frac{\widetilde{\delta_{\mathrm{b}}}(\Omega)}{\widetilde{I_{\mathrm{p}}}(\Omega)} = -\frac{\alpha\tilde{r} + \gamma g}{V_{\mathrm{eff}}}. \tag{C.7}$$

Here $\widetilde{r}(\Omega)$ is the thermal response found in Eq. (1.65) through simulation (with $\widetilde{r}(\Omega = 0) = 1$). The modulation frequency range is much lower than the electronic response in materials, thus we do not associate a response function to g. An extra correction factor γ is added to g as the probe mode sees cross-phase modulation rather than the previous self-phase modulation. For $Al_{0.2}Ga_{0.8}As$ and Ta_2O_5 resonators, a nearby mode in the same mode family is used as the probe mode, and in these cases $\gamma = 2$. For Si_3N_4 resonators, another transverse mode with a different polarization is used to improve contrast between thermal and Kerr effects, and the γ factor is evaluated to be $\gamma = 0.67$.

Finally we calculate the transmission change of the probe mode $\widetilde{T_{\mathrm{p}}}$ with respect to $\widetilde{\delta_{\mathrm{b}}}$. The probe dynamics are given by

$$\frac{\mathrm{d}a_{\mathrm{b}}}{\mathrm{d}t} = -\left(\frac{\kappa_{\mathrm{b}}}{2} + i\Delta_{\mathrm{b}}\right) a_{\mathrm{b}} + \sqrt{\kappa_{e,\mathrm{b}}}a_{\mathrm{in,b}}, \tag{C.8}$$

where a_{b} is the probe mode amplitude, κ_{b} and $\kappa_{e,\mathrm{b}}$ are the total loss rate and external coupling rate of the probe mode, respectively, and $a_{\mathrm{in,b}}$ is the probe input amplitude. Its steady-state solution is

$$a_{\mathrm{b}}^{(0)} = \frac{\sqrt{\kappa_{e,\mathrm{b}}}a_{\mathrm{in,b}}}{\kappa_{\mathrm{b}}/2 + i\Delta_{\mathrm{b}}^{(0)}}, \tag{C.9}$$

with $\Delta_{\mathrm{b}}^{(0)}$ the steady-state detuning of the probe mode.

Fourier transforming Eq. (C.8) while expanding to first order of $\widetilde{\delta_{\mathrm{b}}}$ gives

$$i\Omega\widetilde{a_{\mathrm{b}}} = -(\frac{\kappa_{\mathrm{b}}}{2} + i\Delta_{\mathrm{b}})\widetilde{a_{\mathrm{b}}} - i\widetilde{\delta_{\mathrm{b}}}a_{\mathrm{b}}^{(0)}, \quad \widetilde{a_{\mathrm{b}}} = \frac{-ia_{\mathrm{b}}^{(0)}}{\kappa_{\mathrm{b}}/2 + i\Delta_{\mathrm{b}} + i\Omega}\widetilde{\delta_{\mathrm{b}}}, \tag{C.10}$$

and $\widetilde{a_{\mathrm{b}}^{*}}$ can be found similarly. It should be noted that input probe amplitude $a_{\mathrm{in,b}}$ is not modulated and $\widetilde{a_{\mathrm{in,b}}}$ does not appear in Eq. (C.10).

The transmitted power for the probe mode is found though the input-output relation:

$$T_{\mathrm{b}} = \left| a_{\mathrm{in,b}} - \sqrt{\kappa_{e,\mathrm{b}}} a_{\mathrm{b}} \right|^2 . \tag{C.11}$$

Because the probe input amplitude $a_{\mathrm{in,b}}$ is not modulated, $\widetilde{a_{\mathrm{in,b}}}$ does not show in the AC component of Eq. (C.11). Fourier transforming Eq. (C.11) while expanding to first order of $\widetilde{a_{\mathrm{b}}^{*}}$ gives

$$\widetilde{T_{\mathrm{b}}} = \left(a_{\mathrm{in,b}} - \sqrt{\kappa_{e,\mathrm{b}}} a_{\mathrm{b}}^{(0)} \right) \sqrt{\kappa_{e,\mathrm{b}}} \widetilde{a_{\mathrm{b}}^{*}} + \left[a_{\mathrm{in,b}}^{*} - \sqrt{\kappa_{e,\mathrm{b}}} \left(a_{\mathrm{b}}^{(0)} \right)^{*} \right] \sqrt{\kappa_{e,\mathrm{b}}} \widetilde{a_{\mathrm{b}}}. \tag{C.12}$$

Plugging in $a_{\mathrm{b}}^{(0)}$ (Eq. (C.9)) and $\widetilde{a_{\mathrm{b}}}$ (Eq. (C.10)) results in

$$\widetilde{T_{\mathrm{b}}} = \frac{i\kappa_{e,\mathrm{b}}}{(\kappa_{\mathrm{b}}/2)^2 + \left(\Delta_{\mathrm{b}}^{(0)}\right)^2} \left[\frac{\kappa_{\mathrm{b}}/2 - \kappa_{e,\mathrm{b}} + i\Delta_{\mathrm{b}}^{(0)}}{\kappa_{\mathrm{b}}/2 + i\Omega - i\Delta_{\mathrm{b}}^{(0)}} - \frac{\kappa_{\mathrm{b}}/2 - \kappa_{e,\mathrm{b}} - i\Delta_{\mathrm{b}}^{(0)}}{\kappa_{\mathrm{b}}/2 + i\Omega + i\Delta_{\mathrm{b}}^{(0)}} \right] \left| a_{\mathrm{in,b}} \right|^2 \widetilde{\delta_{\mathrm{b}}} \tag{C.13}$$

$$= -\frac{2\kappa_{e,\mathrm{b}}\Delta_{\mathrm{b}}^{(0)}}{(\kappa_{\mathrm{b}}/2)^2 + \left(\Delta_{\mathrm{b}}^{(0)}\right)^2} \frac{\kappa_{\mathrm{b}} - \kappa_{e,\mathrm{b}} + i\Omega}{(\kappa_{\mathrm{b}}/2 + i\Omega)^2 + \left(\Delta_{\mathrm{b}}^{(0)}\right)^2} \left| a_{\mathrm{in,b}} \right|^2 \widetilde{\delta_{\mathrm{b}}}. \tag{C.14}$$

The overall response function is the product of responses of the three processes,

$$\widetilde{\mathcal{R}}(\Omega) = \frac{\widetilde{T_{\mathrm{b}}}(\Omega)}{\widetilde{P_{\mathrm{in}}}(\Omega)} = \frac{\widetilde{T_{\mathrm{b}}}(\Omega)}{\widetilde{\delta_{\mathrm{b}}}(\Omega)} \frac{\widetilde{\delta_{\mathrm{b}}}(\Omega)}{\widetilde{I_{\mathrm{p}}}(\Omega)} \frac{\widetilde{I_{\mathrm{p}}}(\Omega)}{\widetilde{P_{\mathrm{in}}}(\Omega)}, \tag{C.15}$$

and corresponds to Eq. (2.11) in the main text. The last two factors (derived in Eq. (C.7) and (C.6)) correspond to Eq. (2.9) in the main text. The first factor (derived in Eq. (C.14)) corresponds to Eq. (2.10) in the main text.

Appendix D

DISCUSSION FOR EACH INDIVIDUAL MATERIAL IN CHAPTER 2

D.1 Measurement of SiO_2 microresonators

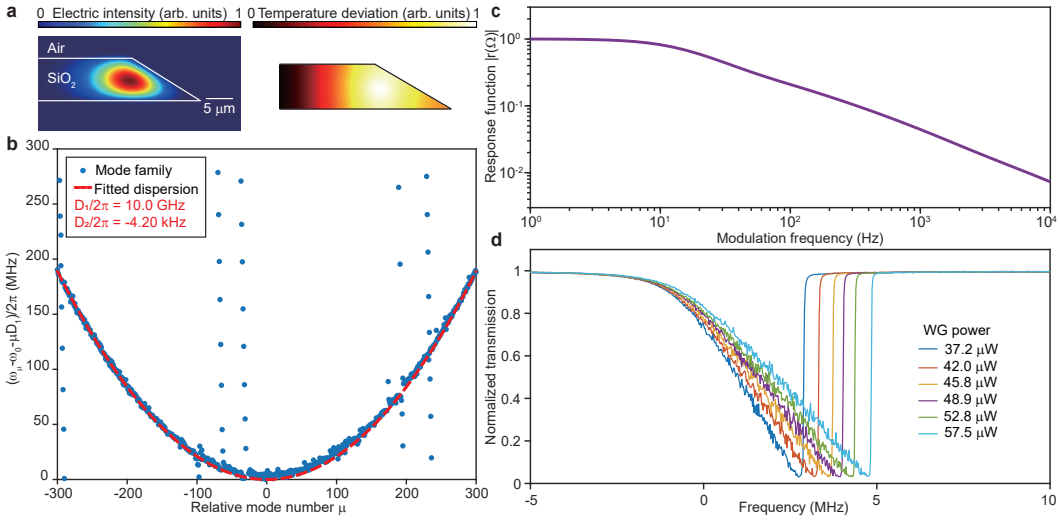

Figure D.1: **SiO_2 measurements.** **(a)** Mode profiles of the measured mode family (left) and equilibrium temperature distribution of the resonator upon heating due to optical absorption (right). The geometry of the resonator is: radius 3.24 mm, thickness 8 μm, wedge angle 27° and undercut 137.5 μm. **(b)** Measured dispersion spectrum of the experimental mode family. The dashed red line is the parabola fitting, and the dispersion parameters are fitted to be $D_1/2\pi = 10.0$ GHz and $D_2/2\pi = 4.20$ kHz. Relative mode number $\mu = 0$ corresponds to the wavelength of 1550 nm. **(c)** Simulated thermal diffusion responsivity $r(\Omega)$ versus modulation frequency $\Omega/2\pi$. **(d)** Representative normalized transmission spectra under different on-waveguide (WG) power. Intrinsic Q_0 and external (coupling) Q_e of this mode are 418.6 Million and 625.9 Million, respectively. This mode is at 1550nm.

The SiO_2 resonator is a disk with a wedge suspended in air, which supports a number of modes in each polarization. The fundamental TM mode (with the highest Q factor) is used for the measurements. The mode identification method is described elsewhere[1] and its profile is shown in Fig. D.1(a). To evaluate the mode temperature (as defined in Eq. (1.50)) change upon optical absorption, i.e., $\overline{\delta T}/P_{\text{abs}}$ in Eq. (2.2) in the main text, finite-element method simulation is performed (Fig. D.1(a)) using parameters in Section 2.8.6. The heating rate distribution is assumed

to be proportional to the electric field intensity. Here, $\overline{\delta T}/P_{\text{abs}}$ is evaluated to be 552 K·W^{-1}. Measured integrated mode dispersion $D_{\text{int}}/2\pi = (\omega_\mu - \omega_0 - \mu D_1)/2\pi$ of this mode family is shown in the Fig. D.1(b), along with a parabola fitting.

The simulated thermal diffusion responsivity $\tilde{r}(\Omega)$ (as defined in Eq. (1.65)) is plotted in Fig. D.1(c). The thermal relaxation bandwidth (3 dB) is <100 Hz, where the probe response is suppressed by the servo feedback locking loop with a bandwidth of 1kHz (see Fig. 2.3(b) and Fig. 2.3(c) in the main text). Measuring the low-frequency photothermal response requires a locking bandwidth smaller than 10 Hz, which is challenging. Thus the ratio experiment is not performed on the silica resonator. Also, due to the suspended nature of the silica structure, the optical absorption effect for the current resonator is typically 10^2 higher than Kerr nonlinear effect ($g \ll \alpha$)[2]. Therefore, it is reasonable to neglect the Kerr contribution in the sum experiment, and attribute all the resonance shift to material absorption ($\alpha + g \approx \alpha$).

Representative linewidth broadening curves at different waveguide pumping power are plotted in Fig. D.1(d) and exhibit the characteristic thermal 'triangle' features, as expected. Eq. (B.12) (in this case r=0) and Eq. (B.14) are used to fit the lineshape in Fig. D.1(d), and the thermal absorption coefficient α is extracted. As mentioned in the main text, the laser frequency must be tuned adiabatically to ensure thermal equilibrium at all times. This is checked by decreasing laser frequency scanning speed at constant power, while monitoring the transmission spectra, until the edge of the 'triangle' stops shifting to the red-detuned direction. Here the frequency scanning speed is set to 20 MHz s^{-1}, which is achieved by using a narrow-linewidth fiber laser.

This experiment is repeated using another SiO_2 resonator ($D_1/2\pi$ = 10 GHz) with different mode polarization. The TE and TM modes are measured to have absorption Q factors of 4148 ± 264 M and 4160 ± 250 M, respectively. These results show that polarization does not significantly affect the measured absorption Q factors of the SiO_2 device. We note that spatial mode identification is not performed in this repeated experiment, which affects the value of $\overline{\delta T}/P_{\text{abs}}$. For example, $\overline{\delta T}/P_{\text{abs}}$ is evaluated to be 554, 537, 522 K·W^{-1} for TE0, TE1, TE2 modes and 552, 535, 519 K·W^{-1} for TM0, TM1, TM2 modes, respectively. As a result, the error uncertainty in the absorption Q factors for this device is larger.

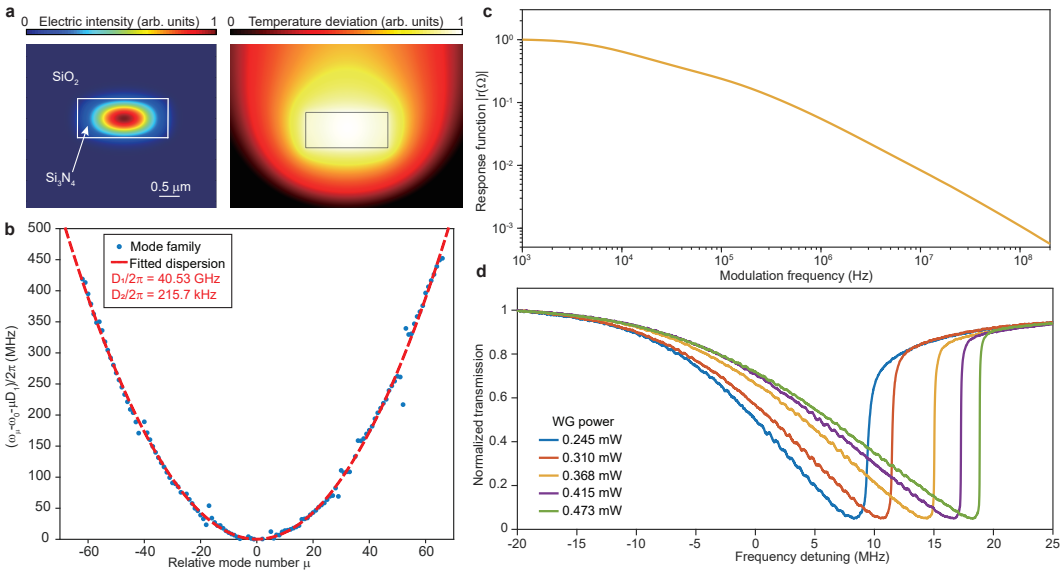

Figure D.2: **Si_3N_4 measurements. (a)** Mode profile of the measured mode family (left) and temperature distribution in the resonator when heated by optical absorption (right). The Si_3N_4 core is 2.2 μm $\times$ 0.95 μm and is cladded by 3.45 μm-thick silica. The resonator radius is 0.562 mm. **(b)** Measured dispersion spectrum of the measured mode family. The dashed red line is the parabola fitting with $D_1/2\pi = 40.53$ GHz and $D_2/2\pi = 215.7$ kHz. Relative mode number $\mu = 0$ corresponds to wavelength close to 1550 nm. **(c)** Simulated thermal diffusion response $\tilde{r}(\Omega)$ versus modulation frequency $\Omega/2\pi$. **(d)** Representative normalized transmission spectra under different on-waveguide (WG) power. Intrinsic Q_0 and external (coupling) Q_e of this mode are 29.0 Million and 52.1 Million, respectively. This mode is at 1544.1nm.

D.2 Measurement of Si_3N_4 microresonators

The cross-section of the integrated Si_3N_4 resonator consists of a rectangular Si_3N_4 core with silica cladding at all sides. The resonator supports two transverse modes (fundamental TE and TM modes) and the fundamental TE mode is used in sum measurement. The mode profile and temperature distribution upon optical absorption heating are shown in Fig. D.2(a). Here, $\overline{\delta T}/P_{\text{abs}}$ is evaluated to be 95.3 K·W^{-1}. The Dispersion spectrum is shown in Fig. D.2(b).

The thermal diffusion responsivity $\tilde{r}(\Omega)$ (as defined in Eq. (1.65)) of this resonator is plotted in Fig. D.2(c). As an aside, thermal and Kerr effects are comparable in Si_3N_4, and in the ratio experiment the contrast between the two plateaus is low. In order to increase the contrast, pump and probe modes are chosen as two mode families with different polarizations (i.e., fundamental TE mode as pump, fundamental TM mode as probe). The cross phase modulation factor γ in this case

is smaller than 2, which effectively suppresses the second (Kerr effect) plateau and increases the contrast between two plateaus. The cross phase modulation factor yields

$$\gamma = \frac{2\int n_o^2 n_2 \left[|\mathbf{F}_{\mathrm{TE}}|^2|\mathbf{F}_{\mathrm{TM}}|^2 + |\mathbf{F}_{\mathrm{TE}}\cdot\mathbf{F}_{\mathrm{TM}}^*|^2 + |\mathbf{F}_{\mathrm{TE}}\cdot\mathbf{F}_{\mathrm{TM}}|^2\right]\mathrm{d}V}{\int n_o^2 n_2 \left[2|\mathbf{F}_{\mathrm{TE}}|^4 + |\mathbf{F}_{\mathrm{TE}}\cdot\mathbf{F}_{\mathrm{TE}}|^2\right]\mathrm{d}V}\frac{(\overline{n_o n_g})_{\mathrm{TE}}}{(\overline{n_o n_g})_{\mathrm{TM}}} = 0.67. \tag{D.1}$$

In the sum experiment, the fundamental TE mode is tested at multiple wavelengths across the C-band. The result at 1544.1 nm under different pump power on waveguide is shown in Fig. D.2(d). A low scanning speed (12.7 GHz·s^{-1}) is used to ensure the resonator reaches thermal equilibrium.

The correction factor for heterogeneous mode distribution in Eqs. (1.43), (1.45), and (1.53) is calculated based on finite-element method simulation, with

$$\overline{n_2} = 0.996 n_{2,\mathrm{Si_3N_4}} + 0.004 n_{2,\mathrm{SiO_2}}, \tag{D.2}$$

$$\overline{n_o n_g} = 0.933 (n_o n_g)_{\mathrm{Si_3N_4}} + 0.067 (n_o n_g)_{\mathrm{SiO_2}}, \tag{D.3}$$

$$\overline{\kappa_{\mathrm{a}}} = 0.964 \kappa_{a,\mathrm{Si_3N_4}} + 0.036 \kappa_{a,\mathrm{SiO_2}}. \tag{D.4}$$

These correction factors are applied to extract material absorption rate $\overline{\kappa_{\mathrm{a}}}$ and nonlinearity $\overline{n_2}$. The n_o and n_g factors (at 1.55 μm) used for SiO_2 are $n_o = 1.44$, $n_g = 1.46$ (ref. [3]), for Si_3N_4 are $n_o = 2.00$, $n_g = 2.04$ (ref. [4]).

D.3 Measurement of $Al_{0.2}Ga_{0.8}As$ microresonators

The cross-section of the integrated $Al_{0.2}Ga_{0.8}As$ resonator consists of a rectangular $Al_{0.2}Ga_{0.8}As$ core with silica cladding at all sides. The cladding has protrusions on top of the resonator, as illustrated in Fig. D.3(a). The resonator supports two transverse modes (fundamental TE and TM modes) and the fundamental TE mode is used in both the sum and ratio measurements. The mode profile and equilibrium temperature distribution when heated by optical absorption from $Al_{0.2}Ga_{0.8}As$ core (i.e., bulk absorption) are shown in Fig. D.3(a). Here, $\overline{\delta T}/P_{\mathrm{abs}}$ is evaluated to be 90.7 K·W^{-1}. Dispersion spectrum of this mode family is shown in Fig. D.3(b) along with a parabola fitting with $D_1/2\pi = 17.93$ GHz and $D_2/2\pi = -19.58$ kHz.

We note that surface absorption may be prominent for aluminium gallium arsenide waveguides depending on fabrication details. This changes the distribution of absorbed heat for the waveguide cross-section. However, the $\overline{\delta T}/P_{\mathrm{abs}}$ coefficient from simulations differs by less than 1% even if the surface absorption is taken into

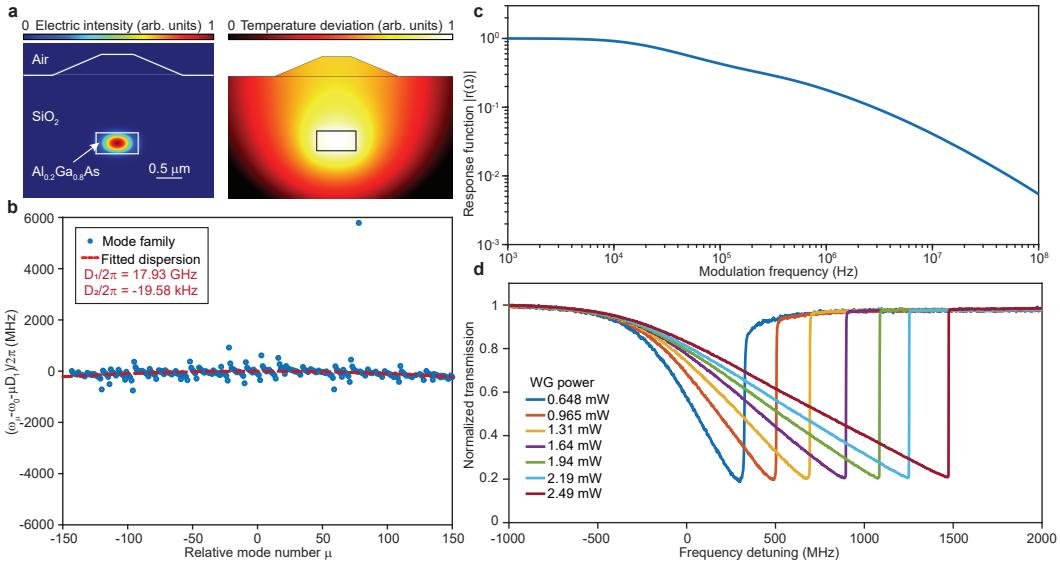

Figure D.3: **$Al_{0.2}Ga_{0.8}As$ measurements.** **(a)** Mode profile of the measured mode family (left) and temperature distribution in the resonator upon optical absorption heating (right). The core is 0.8 μm ×0.4 μm $Al_{0.2}Ga_{0.8}As$ and is cladded by 1.5μm-thick silica. The resonator radius is 0.719 mm. It is noted that the top surface is not flat. **(b)** Measured frequency dispersion of measured mode family. The dashed red line is parabola fitting with $D_1/2\pi = 17.93$ GHz and $D_2/2\pi = -19.58$ kHz. Relative mode number $\mu = 0$ corresponds to wavelength close to 1550 nm. **(c)** Simulated thermal diffusion responsivity $\tilde{r}(\Omega)$ versus modulation frequency Ω. **(d)** Representative normalized transmission spectra under different on-waveguide (WG) power. Intrinsic Q_0 and external (coupling) Q_e of this mode are 1.01 Million and 2.44 Million, respectively. This mode is at 1560.1nm.

account. This is because the spatially larger profile of the thermal distribution is not significantly affected by the exact location of the smaller modal heat source. The reported Q_{abs} here includes both bulk and surface contributions and, as noted in the main text, $Al_{0.2}Ga_{0.8}As$ resonators with Q factors higher than Q_{abs} have been reported elsewhere.

The thermal diffusion responsivity $\tilde{r}(\Omega)$ (as defined in Eq. (1.65)) of the resonator is simulated using the finite-element method technique and is shown in D.3(c). In the ratio experiment the pump and probe modes belong to the same fundamental TE mode. In this case the cross phase modulation factor $\gamma = 2$.

In the sum experiment the fundamental TE mode is tested at multiple wavelengths across the C-band. The result at 1560.1 nm under different on-waveguide pumping power is shown in Fig. D.3(d). A low scanning speed (783.9 GHz·s^{-1}) is used to ensure that the resonator reaches thermal equilibrium. As an aside, two-photon

absorption and harmonic generation will lead to a decrease in coupling efficiency as pump power increases [5]. Such effects are not significant in Fig. D.3, indicating that the processes are not prominent for the current samples.

The correction factor for heterogeneous mode distribution in Eqs. (1.43), (1.45), and (1.53) is calculated based on finite-element method,

$$\overline{n_2} = 0.997 n_{2,\mathrm{Al_{0.2}Ga_{0.8}As}} + 0.003 n_{2,\mathrm{SiO_2}}, \tag{D.5}$$

$$\overline{n_o n_g} = 0.892 (n_o n_g)_{\mathrm{Al_{0.2}Ga_{0.8}As}} + 0.108 (n_o n_g)_{\mathrm{SiO_2}}, \tag{D.6}$$

$$\overline{\kappa_\mathrm{a}} = 0.977 \kappa_{a,\mathrm{Al_{0.2}Ga_{0.8}As}} + 0.023 \kappa_{a,\mathrm{SiO_2}}. \tag{D.7}$$

These correction factors are applied to extract material absorption rate $\overline{\kappa_\mathrm{a}}$ and nonlinearity $\overline{n_2}$. The n_o and n_g factors (at 1.55 μm) used for $Al_{0.2}Ga_{0.8}As$ are $n_o = 3.28$, $n_g = 3.22$ (ref. [6]).

D.4 Measurement of Ta_2O_5 microresonators

The cross-section of the integrated Ta_2O_5 resonator consists of a rectangular Ta_2O_5 core on top of a silica substrate, and there's no cladding on the other sides of the resonator. The resonator supports two transverse modes (fundamental TE and TM) and the fundamental TE mode is used in both the sum and ratio measurements. The mode profile and equilibrium temperature distribution when heated by optical absorption are shown in Fig. D.4(a). Here, $\overline{\delta T}/P_\mathrm{abs}$ is evaluated to be 1085.1 $\mathrm{K{\cdot}W^{-1}}$ (using thermal conductivity 0.4 $\mathrm{W{\cdot}m^{-1}{\cdot}K^{-1}}$). Dispersion spectrum is shown in Fig. D.4(b). The red dashed line indicates a parabola fitting with $D_1/2\pi = 195.2$ GHz and $D_2/2\pi = -8.188$ kHz.

In this study, the thermal conductivity assumed in the calculation of Q_abs was taken from that reported for electron-beam deposited Ta_2O_5, which is 0.4 $\mathrm{W{\cdot}m^{-1}{\cdot}K^{-1}}$ (ref. [7]). Other reported values vary from 0.2 to 5 $\mathrm{W{\cdot}m^{-1}{\cdot}K^{-1}}$ (ref. [8–10]) as thermal conductivity is strongly dependent upon deposition process among other factors. As discussed in section IIC, larger thermal conductivity will lead to faster thermal diffusion and therefore a lower value for Q_abs inferred from the measurements (see also Fig. D.5). We also note that the measured value of Q_0 of the device places an upper bound on the total loss of the resonator. As absorption is only a component of the total resonator loss, Q_0 also therefore also sets a lower bound on Q_abs.

The thermal diffusion responsivity $\tilde{r}(\Omega)$ (as defined in Eq. (1.65)) of the resonator is simulated using the finite-element method technique and shown in D.4c. In the

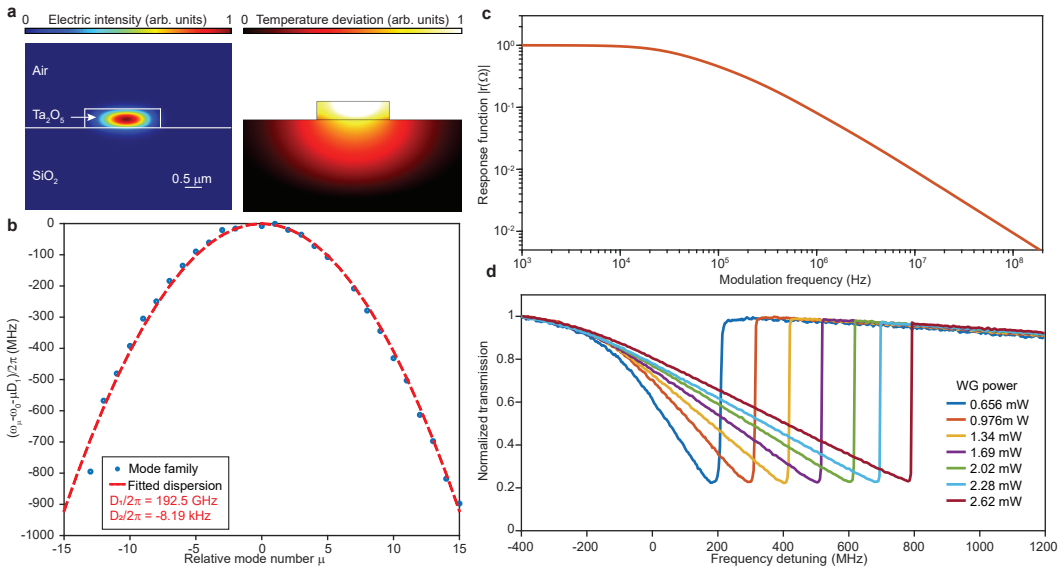

Figure D.4: **Ta_2O_5 measurements.** **(a)** Mode profile of the measured mode family (left) and equilibrium temperature distribution inside the resonator upon optical absorption heating (right). The resonator consists a 2.25 μm $\times$ 0.57 μm core (Ta_2O_5) and a silica substrate. The resonator radius is 0.1095mm. **(b)** Measured dispersion spectrum of the measured mode family. The dashed red line is parabola fit with $D_1/2\pi = 192.5$ GHz and $D_2/2\pi = -8.188$ MHz. Relative mode number $\mu = 0$ corresponds to wavelength close to 1550 nm. **(c)** Simulated temperature response $\tilde{r}(\Omega)$ versus modulation frequency $\Omega/2\pi$. **(d)** Representative normalized transmission spectra under different on-waveguide (WG) power. Intrinsic Q_0 and external (coupling) Q_e of this mode are 2.02 Million and 6.59 Million, respectively. This mode is around 1543.5nm.

ratio experiment the pump and probe modes belong to the same fundamental TE mode. In this case the cross phase modulation factor $\gamma = 2$.

In sum experiment the fundamental TE mode is tested at multiple wavelengths across the C-band. the result at 1543.5nm under different on-waveguide power is shown in Fig. D.4(d). A low scanning speed (1378 GHz$\cdot$s^{-1}) is used to ensure the thermal equilibrium.

The correction factor for heterogeneous mode distribution in Eqs. (1.43), (1.45), and (1.53) is calculated based on finite-element method,

$$\overline{n_2} = 0.989 n_{2,\mathrm{Ta_2O_5}} + 0.009 n_{2,\mathrm{SiO_2}} + 0.002 n_{2,\mathrm{Air}}, \tag{D.8}$$

$$\overline{n_o n_g} = 0.874 (n_o n_g)_{\mathrm{Ta_2O_5}} + 0.080 (n_o n_g)_{\mathrm{SiO_2}} + 0.046 (n_o n_g)_{\mathrm{Air}}, \tag{D.9}$$

$$\overline{\kappa_a} = 0.946 \kappa_{a,\mathrm{Ta_2O_5}} + 0.042 \kappa_{a,\mathrm{SiO_2}} + 0.012 \kappa_{a,\mathrm{Air}}. \tag{D.10}$$

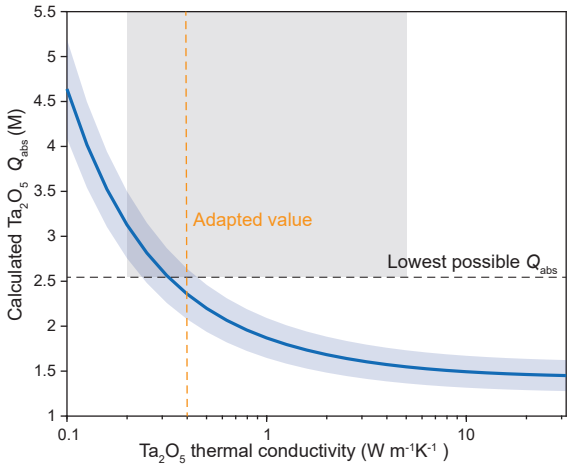

Figure D.5: **Calculated Q_{abs} of Ta_2O_5 versus thermal conductivity.** The calculated material limited Q_{abs} of Ta_2O_5 is plotted versus the thermal conductivity of Ta_2O_5 used in the FEM simulation. The light blue shading denotes the standard deviation from the measurements. The thermal conductivity value used in this study is marked with orange dashed line, while the reported range of values in the literature is shaded in gray. The lowest possible Q_{abs} as set by measured intrinsic Q factor is calculated from Eq. (D.10) and is also plotted as the black dashed line.

These correction factors are applied to extract material absorption rate $\overline{\kappa_{\text{a}}}$ and nonlinearity $\overline{n_2}$. The n_o and n_g factors (at 1.55 μm) used for Ta_2O_5 are $n_o = 2.06$, $n_g = 2.10$ (ref. [11]).

References

[1] Yi, X. *et al.* Single-mode dispersive waves and soliton microcomb dynamics. *Nat. Commun.* **8**, 14869 (2017).

[2] Rokhsari, H. & Vahala, K. J. Observation of Kerr nonlinearity in microcavities at room temperature. *Opt. Lett.* **30**, 427–429 (2005).

[3] Malitson, I. H. Interspecimen comparison of the refractive index of fused silica. *J. Opt. Soc. Am.* **55**, 1205–1209 (1965).

[4] Luke, K., Okawachi, Y., Lamont, M. R. E., Gaeta, A. L. & Lipson, M. Broadband mid-infrared frequency comb generation in a Si_3N_4 microresonator. *Opt. Lett.* **40**, 4823–4826 (2015).

[5] Parrain, D. *et al.* Origin of optical losses in gallium arsenide disk whispering gallery resonators. *Opt. Express* **23**, 19656–19672 (2015).

[6] Papatryfonos, K. *et al.* Refractive indices of MBE-grown $Al_xGa_{1-x}As$ ternary alloys in the transparent wavelength region. *AIP Adv.* **11**, 025327 (2021).

[7] Farsi, A., Siciliani de Cumis, M., Marino, F. & Marin, F. Photothermal and thermo-refractive effects in high reflectivity mirrors at room and cryogenic temperature. *J. Appl. Phys.* **111**, 043101 (2012).

[8] Wu, Z. L., Reichling, M., Hu, X.-Q., Balasubramanian, K. & Guenther, K. H. Absorption and thermal conductivity of oxide thin films measured by photothermal displacement and reflectance methods. *Appl. Opt.* **32**, 5660 (1993).

[9] Landon, C. D. *et al.* Thermal transport in tantalum oxide films for memristive applications. *Appl. Phys. Lett.* **107**, 023108 (2015).

[10] Grilli, M., Ristau, D., Dieckmann, M. & Willamowski, U. Thermal conductivity of E-beam coatings. *Appl. Phys. A* **71**, 71–76 (2000).

[11] Bright, T. J. *et al.* Infrared optical properties of amorphous and nanocrystalline Ta_2O_5 thin films. *J. Appl. Phys.* **114**, 083515 (2013).

Appendix E

OH ABSORPTION IN ON-CHIP HIGH-Q RESONATORS

This chapter is based on the following published paper:
Wu L., **Gao M.**, Liu J.-Y., Chen H.-J., Colburn K., Blauvelt H.A., and Vahala K., Hydroxyl ion absorption in on-chip high-Q resonators, *Opt. Lett.* 48, 3511-3514 (2023).
https://doi.org/10.1364/OL.492067

High-Q integrated resonators have become an essential component in nonlinear photonics. Most often, the guided light in these structures has a significant fractional overlap with silica (e.g., all-silica wedge resonators [1, 2] and silica-clad ultra-low-loss silicon nitride waveguides [3, 4]). It is therefore important to understand the loss limits imposed by the silica used in silicon photonic processing. Besides interface scattering loss, optical absorption from bound hydroxyl ions (Si-OH) can be a significant component of loss [5], especially since thermal silica is prepared using a process involving water. Bound hydroxyl ions produce a well-known fundamental absorption peak at 2720 nm [6] and the overtone at 1380 nm is used here to measure OH absorption loss in ultra-high-Q thermal-silica wedge microresonators. Further comparison to scattering loss is made over a wavelength range from 680 nm to 1550 nm. Also, using cavity-enhanced photo-thermal spectroscopy [5] near the 1380 nm band, the OH ion content level is estimated to be 2.4 ppm (weight). This value also agrees with Secondary Ion Mass Spectroscopy (SIMS) depth profiling performed on the resonator material. Outside of the 1380 nm band, scattering loss is confirmed by measurement and modeling to be the dominant loss mechanism in the samples tested.

Thermally-grown silica wedge whispering-gallery resonator devices were prepared as measurement samples, and featured 8 μm thermal oxide thickness with resonator diameter 6.5 mm (10 GHz free spectral range, FSR). The fabrication steps are detailed in reference [2]. The thermal silica was grown from float-zone (low background doping level) silicon wafers using the wet oxidation method. As a final step, the devices were annealed for 18-hours at 1000°C in N_2. The samples were stored and measured in a dry N_2 environment to minimize environmental impact on optical loss. Tapered fiber couplers [7, 8] were used to couple probe light to the resonator

samples.

A strong increase in loss near 1380 nm is apparent in all six samples, corresponding to the OH absorption band and reaching over 200 dB/km. This absorption quickly decreases for wavelengths above and below 1380 nm. The loss in other spectral regions is believed to be dominated by Rayleigh scattering. The wavelength dependence of this scattering within the resonator mode volume would scale approximately as λ^{-4}, and does not fit the data. Modeling of surface scattering is described in the Methods and provides better agreement with the wavelength dependence. This theoretical dependence is given by the purple curve (for the fundamental TE mode) where surface roughness variance (1.9 nm) and correlation length (350 nm) are assumed in the plot [9]. The origin of the increased loss at the shortest wavelengths measured is not known, but possibilities include absorption loss from metallic ion impurities and scattering from material density fluctuations. For example, SIMS data has shown that Chromium is a residual contaminant in our processing, and Cr^{3+} ions can contribute 1.6 dB/km/ppbw at 800 nm (peak at 625 nm) to absorption [10].

Material	1385 (dB/km)	1550 (dB/km)
thermal silica in this study	152	3.2
1 ppmw OH in silica [6]	62.7	
Wet fiber studied in [6]	48500	100
Fiber studied in [11]	1.172	0.045
low-OH fiber [12, 13]	0.05	0.02

Table E.1: Summary of absorption loss rates at both 1385 nm and 1550 nm from Fig. E.1 and taken from the literature. Note that ppmw is parts per million in weight (equivalently, μg/g).

Cavity-enhanced photothermal spectroscopy (CEPS) [5] was used to further study the OH absorption loss. This method measures the microresonator resonance thermal triangle formation induced by the thermo-optical effect [14] to determine mode volume absorption. Details on this method are provided in reference [5]. Fig. E.1 summarizes the wavelength dependence of the measured absorption loss in both the 1380 nm band and at 1550 nm. The measured absorption near 1380 nm follows reasonably well the OH overtone lineshape in silica as determined elsewhere [6] (blue curve superimposed in plot). To fit the magnitude of the lineshape function to the data, an OH content level of 2.4 ppm weight is used. Also, the data near 1550 nm indicates that by further reduction in scattering loss, the existing thermal silica can provide absorption limited Q factors as high as 8 billion. This value is 2×

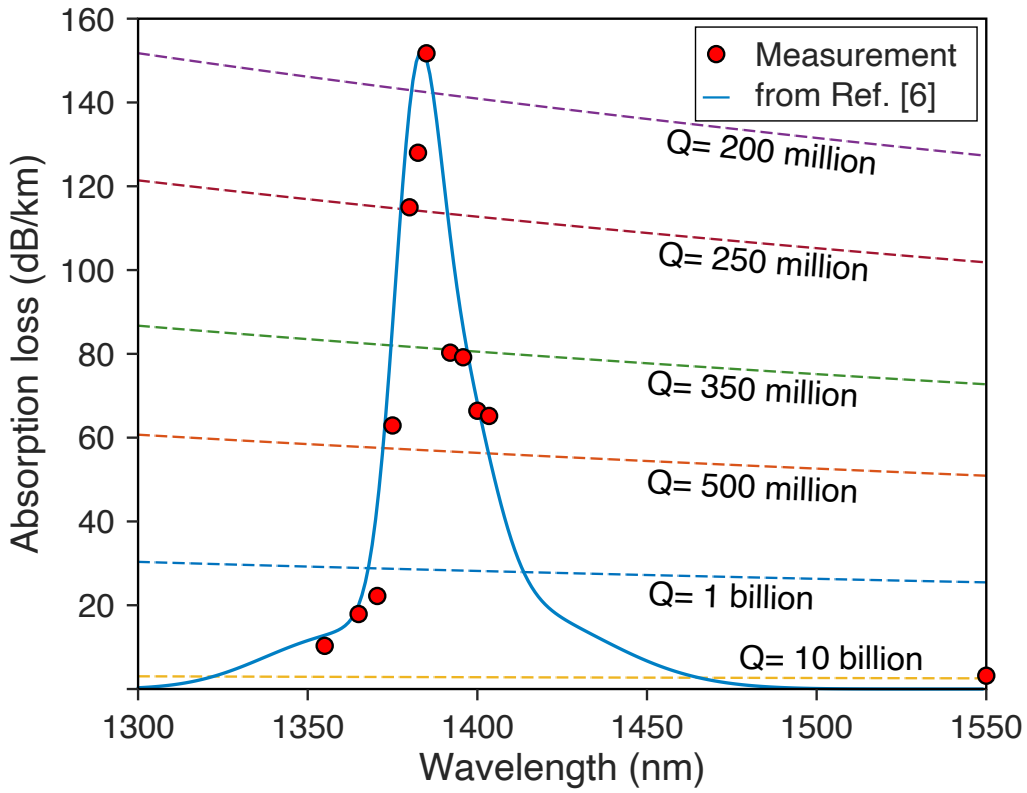

Figure E.1: **Absorption loss measurement results.** Absorption loss as measured by cavity-enhanced photothermal spectroscopy in the 1380 nm band. Red dots: data from sample device. Blue solid line: 2.4 ppm (weight) OH content level absorption lineshape based on reference (Humbach, *et. al. J. Non-Cryst. Solids* **203**, 19-26 (1996).).

larger than measured for wedge resonators in a previous study [5] and is attributed to application of an improved resist cleaning step. The absorption loss measurement results at 1385 nm and 1550 nm are summarized in Table E.1 and compared with values from the literature. The measured absorption ratio α(1385 nm)/α(1550 nm) in the current data is more consistent with the report in ref. [12]. The high OH concentration in ref. [6] could possibly account for this difference.

References

[1] Lee, H. *et al.* Chemically etched ultrahigh-Q wedge-resonator on a silicon chip. *Nat. Photon.* **6**, 369–373 (2012).

[2] Wu, L. *et al.* Greater than one billion Q factor for on-chip microresonators. *Opt. Lett.* **45**, 5129–5131 (2020).

[3] Jin, W. *et al.* Hertz-linewidth semiconductor lasers using CMOS-ready ultra-

high-Q microresonators. *Nat. Photon.* **15**, 346–353 (2021).

[4] Puckett, M. W. *et al.* 422 million intrinsic quality factor planar integrated all-waveguide resonator with sub-MHz linewidth. *Nat. Commun.* **12**, 934 (2021).

[5] Gao, M. *et al.* Probing material absorption and optical nonlinearity of integrated photonic materials. *Nat. Commun.* **13**, 3323 (2022).

[6] Humbach, O., Fabian, H., Grzesik, U., Haken, U. & Heitmann, W. Analysis of OH absorption bands in synthetic silica. *J. Non-Cryst. Solids* **203**, 19–26 (1996).

[7] Cai, M., Painter, O. & Vahala, K. J. Observation of critical coupling in a fiber taper to a silica-microsphere whispering-gallery mode system. *Phys. Rev. Lett.* **85**, 74–77 (2000).

[8] Spillane, S., Kippenberg, T., Painter, O. & Vahala, K. Ideality in a fiber-taper-coupled microresonator system for application to cavity quantum electrodynamics. *Phys. Rev. Lett.* **91**, 043902 (2003).

[9] Barwicz, T. & Haus, H. A. Three-dimensional analysis of scattering losses due to sidewall roughness in microphotonic waveguides. *J. Lightwave Technol.* **23**, 2719 (2005).

[10] Olshansky, R. Propagation in glass optical waveguides. *Rev. Mod. Phys.* **51**, 341–367 (1979).

[11] Thomas, G. A., Shraiman, B. I., Glodis, P. F. & Stephen, M. J. Towards the clarity limit in optical fibre. *Nature* **404**, 262–264 (2000).

[12] Li, T. *Optical Fiber Communications: Fiber Fabrication* (Academic Press, 1985).

[13] Keiser, G. *Optical Fiber Communications (4th edition)* (McGraw-Hill Education, 2010).

[14] Carmon, T., Yang, L. & Vahala, K. J. Dynamical thermal behavior and thermal self-stability of microcavities. *Opt. Express* **12**, 4742–4750 (2004).

Appendix F

THEORETICAL DISPERSION OF COUPLED 2- AND 3-RING RESONATORS

F.1 Eigenmodes of a two-ring coupled resonator

In this section we study the coupling between the two coupled rings and analyze the mode frequencies of the compound system. Eigenfrequencies of coupled resonators have traditionally been calculated from a coupled-mode perspective, where modal coupling are calculated as off-diagonal matrix elements. However, this approach becomes unfeasible in the current system as one longitudinal mode will couple to many modes from the opposite ring because mode number matching is not required. The dependence of coupling with respect to wavelength is also difficult to implement. To circumvent these problems, we instead use a transfer function formalism to determine the mode frequencies.

The resonator schematic is shown in Fig. F.1. L_A and L_B are the circumferences of the right and left ring, respectively, L_{co} is the length of the coupling region, c is the speed of light in vacuum, and $n_{wg}(\omega)$ is the effective phase index of the fundamental mode in the SiN waveguide at optical angular frequency ω. By defining a single index along the waveguide, we have neglected the geometric dispersions resulting from bending the waveguide. These have been shown to be small compared to the geometric dispersion induced by waveguide confinement. We now assume that light with a single frequency is propagating in the system. At the points opposite to the

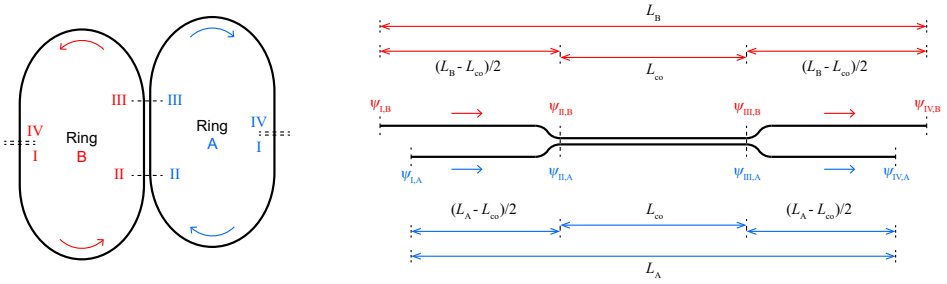

Figure F.1: **Schematic of the two-ring coupled resonator.** Left panel: Top view of the coupled resonator with key points marked. Right panel: Schematic of the resonator with straightened waveguides (not to scale). Segment lengths and field amplitudes have been marked.

coupling region, the field amplitude in each ring is denoted as $\psi_{\mathrm{I,A}}$ and $\psi_{\mathrm{I,B}}$. These amplitudes can be assembled into a vector as $\psi_{\mathrm{I}} = (\psi_{\mathrm{I,A}}, \psi_{\mathrm{I,B}})^{\mathbf{T}}$, where $^{\mathbf{T}}$ denotes the transpose of a vector or matrix. Similarly, the field just before the coupling part can be found as

$$\begin{pmatrix} \psi_{\mathrm{II,A}} \\ \psi_{\mathrm{II,B}} \end{pmatrix} = \begin{pmatrix} e^{in_{\mathrm{wg}}\omega(L_{\mathrm{A}}-L_{\mathrm{co}})/(2c)} & 0 \\ 0 & e^{in_{\mathrm{wg}}\omega(L_{\mathrm{B}}-L_{\mathrm{co}})/(2c)} \end{pmatrix} \begin{pmatrix} \psi_{\mathrm{I,A}} \\ \psi_{\mathrm{I,B}} \end{pmatrix}. \tag{F.1}$$

For the coupling section, we denote the coupling rate per unit length as g_{co}. The coupling depends on ω, and is assumed to be uniform along the coupling section (i.e., boundary effects from adiabatic bends are included in the effective coupling length). The field after the coupling section can be expressed with a matrix exponential:

$$\begin{pmatrix} \psi_{\mathrm{III,A}} \\ \psi_{\mathrm{III,B}} \end{pmatrix} = \exp\left[iL_{\mathrm{co}} \begin{pmatrix} n_{\mathrm{wg}}\omega/c & g_{\mathrm{co}} \\ g_{\mathrm{co}} & n_{\mathrm{wg}}\omega/c \end{pmatrix} \right] \begin{pmatrix} \psi_{\mathrm{II,A}} \\ \psi_{\mathrm{II,B}} \end{pmatrix}. \tag{F.2}$$

Finally, returning to the points opposite to the coupling region, the field reads

$$\begin{pmatrix} \psi_{\mathrm{IV,A}} \\ \psi_{\mathrm{IV,B}} \end{pmatrix} = \begin{pmatrix} e^{in_{\mathrm{wg}}\omega(L_{\mathrm{A}}-L_{\mathrm{co}})/(2c)} & 0 \\ 0 & e^{in_{\mathrm{wg}}\omega(L_{\mathrm{B}}-L_{\mathrm{co}})/(2c)} \end{pmatrix} \begin{pmatrix} \psi_{\mathrm{III,A}} \\ \psi_{\mathrm{III,B}} \end{pmatrix}. \tag{F.3}$$

For modes in the system, we require the state to reproduce itself after one round trip:

$$\psi_{\mathrm{IV}} = e^{i\Theta}\psi_{\mathrm{I}}. \tag{F.4}$$

This requires finding the eigenvalues of the roundtrip transfer matrix T, which is the product of the previous three transfer matrices:

$$\psi_{\mathrm{IV}} = T\psi_{\mathrm{I}}, \;\; T = e^{in_{\mathrm{wg}}\omega\overline{L}/c} \begin{pmatrix} e^{in_{\mathrm{wg}}\omega\Delta L/c}\cos(g_{\mathrm{co}}L_{\mathrm{co}}) & i\sin(g_{\mathrm{co}}L_{\mathrm{co}}) \\ i\sin(g_{\mathrm{co}}L_{\mathrm{co}}) & e^{-in_{\mathrm{wg}}\omega\Delta L/c}\cos(g_{\mathrm{co}}L_{\mathrm{co}}) \end{pmatrix}, \tag{F.5}$$

where $\overline{L} = (L_{\mathrm{A}} + L_{\mathrm{B}})/2$ and $\Delta L = (L_{\mathrm{B}} - L_{\mathrm{A}})/2$. Each one of the two eigenvalues defines a transverse mode family of the system. Furthermore, when the accumulated phase Θ equals an integer multiple of 2π, a longitudinal mode can be found at the corresponding frequency. Diagonalizing the T matrix gives

$$\Theta = n_{\mathrm{wg}}\omega\overline{L}/c \mp \arccos[\cos(g_{\mathrm{co}}L_{\mathrm{co}})\cos(n_{\mathrm{wg}}\omega\Delta L/c)]. \tag{F.6}$$

Now we define a mode number associated with the average length of the rings:

$$m \equiv \frac{n_{\mathrm{wg}}\omega\overline{L}}{2\pi c}. \tag{F.7}$$

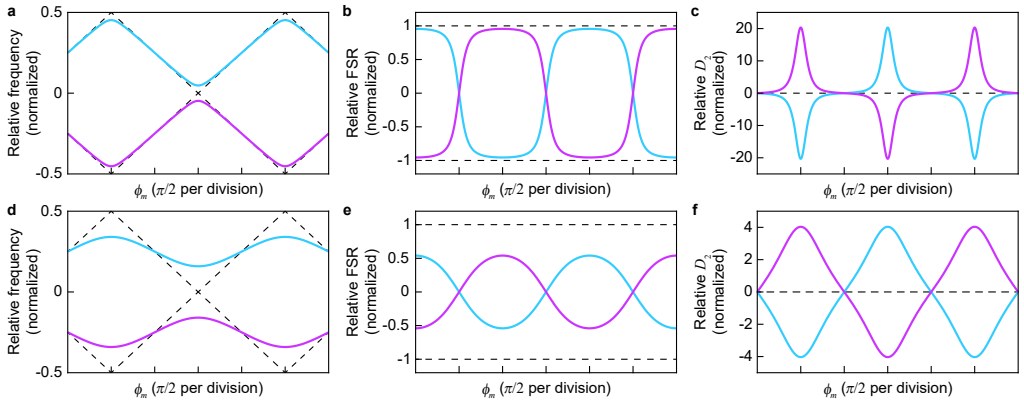

Figure F.2: **Eigenfrequency plots for the two-ring coupled resonator. (a,b,c)** Relative frequency (normalized to $D_{1,m}$), relative FSR (normalized to $\epsilon D_{1,m}$) and relative D_2 (normalized to $\epsilon^2 D_{1,m}$) plots for $g_{\mathrm{co}}L_{\mathrm{co}} = 0.3$. **(d,e,f)** Similar plots but with $g_{\mathrm{co}}L_{\mathrm{co}} = 1.0$. The horizontal axis is defined as $\phi_m = 2\pi\epsilon m$. Relative mode frequency, FSR and D_2 for individual rings before coupling have been superimposed (black dashed lines). The relative FSR is found by differentiating the relative frequency, and the relative D_2 is found by differentiating the relative FSR.

The relation can be inverted to give a solution of ω_m dependent on m. When m is an integer, ω_m would be the mode frequencies for a ring resonator with length $\overline{L}$. As $g_{\mathrm{co}} \ll \omega/c$ and $\Delta L \ll \overline{L}$, the phase contribution related to the coupling varies slowly compared to the $n_{\mathrm{wg}}\omega\overline{L}/c$ part. This allows us to approximate the coupled mode frequencies using ω_m, and the eigenfrequencies $\omega_{m,\pm}$ can be solved as:

$$\begin{aligned} 2\pi m &= n_{\mathrm{wg}}\omega_{m,\pm}\overline{L}/c \mp \arccos[\cos(g_{\mathrm{co}}L_{\mathrm{co}})\cos(n_{\mathrm{wg}}\omega_{m,\pm}\Delta L/c)] \\ &\approx n_{\mathrm{wg}}\omega_{m,\pm}\overline{L}/c \mp \arccos[\cos(g_{\mathrm{co}}L_{\mathrm{co}})\cos(n_{\mathrm{wg}}\omega_m\Delta L/c)], \end{aligned} \tag{F.8}$$

$$\begin{aligned} \omega_{m,\pm} &= \omega_m \pm \left[\frac{\overline{L}}{c}\frac{\partial(n_{\mathrm{wg}}\omega)}{\partial\omega}\right]^{-1}\Bigg|_{\omega=\omega_m} \times \arccos\left[\cos(g_{\mathrm{co}}L_{\mathrm{co}})\cos\left(2\pi\frac{\Delta L}{\overline{L}}m\right)\right] \\ &= \omega_m \pm \frac{D_{1,m}}{2\pi}\arccos\left[\cos(g_{\mathrm{co}}L_{\mathrm{co}})\cos\left(2\pi\epsilon m\right)\right], \end{aligned} \tag{F.9}$$

where $D_{1.m}$ is the local FSR that depends on ω_m and $\epsilon = \Delta L/\overline{L}$ is the length contrast of the rings. The result shows that the mode structure can be seen as splitting off from the length-averaged resonator modes, where the splitting gap is determined by g_{co} and modulated with respect to mode number with period ϵ^{-1}. Note that Eq. (3.2) in the main text is obtained by replacing the mode number m with the relative mode number μ in Eq. (F.9). Such a variable change is valid when μ is referenced to a frequency degeneracy of the rings.

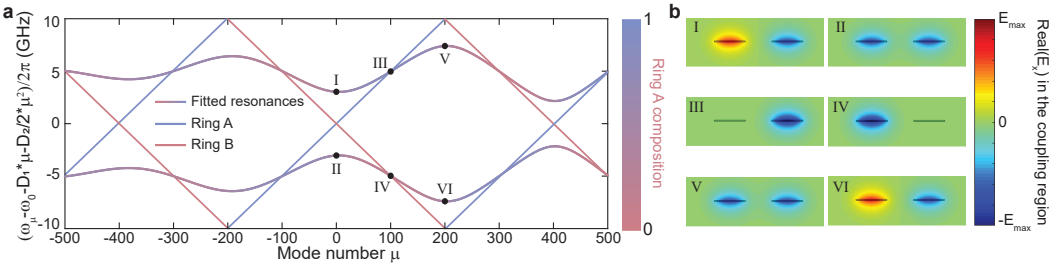

Figure F.3: **Illustration of mode hybridization in the coupling region. (a)** Fitted optical resonance frequency dispersion of the coupled resonator (solid curves) and fitted mode frequency dispersion of the single rings (red and blue lines) plotted versus relative mode number μ. These plots are the same as Fig. 3.3(b). **(b)** Cross-sectional view of simulated electric field amplitudes in the coupled region at mode numbers indicated in panel (a) by the black points. The right (left) waveguide belongs to ring A (B). At the crossing center (I, II, V and VI), two waveguides have the same field intensity and the opposite (same) phase for the anti-symmetric (symmetric) mode. When hybrid mode frequencies meet the single-ring resonances (III and IV), the electrical field at the coupled region is contributed by a single ring.

To gain insight into the model, Fig. F.2 plots mode frequency, FSR and the second-order dispersion parameter D_2 relative to ω_m for different values of g_{co} as predicted by Eq. (F.9). In these plots ω_m has been subtracted from the mode frequencies, and only the contributions associated with FSR difference of the two rings and the coupling are considered. The $D_{1,m}$ is also approximated as a constant. The FSRs of the transverse modes show a typical avoided crossing behavior as shown in Fig. F.2(b) and F.2(e). The FSR of one mode continuously transitions to the other mode at the avoided crossing, and similar to the coupling itself, this process is also periodic in the frequency domain. The calculated D_2 shows spikes at the avoided crossing center, and the positive spike can be used to counter the normal dispersion present in the averaged resonator dispersion. Smaller g_{co} leads to higher peak D_2 with smaller crossing bandwidth. To get a larger crossing bandwidth, g_{co} could be increased at the expense of lower D_2, but the maximum bandwidth is half the modulation period (i.e., the vernier FSR) as the effect of the neighboring crossings set in and shifts the D_2 in the opposite direction.

In addition to the mode frequency, the mode compositions can also be derived from the transfer matrix T. As the change of mode profile is large enough across the measured optical bandwidth, the mode compositions has an impact on soliton power distribution in the rings (as in Fig. 3.2 in the main text), and complements FSRs and dispersions when describing the dispersion characteristics. The eigenvectors of

T read,

$$\psi_{\mathrm{I}} \propto \left(\sqrt{\frac{\sin(\alpha+\phi_m)}{2\sin\alpha\cos\phi_m}},\ \mp\sqrt{\frac{\sin(\alpha-\phi_m)}{2\sin\alpha\cos\phi_m}} \right)^{\mathbf{T}},\ \phi_m = 2\pi\epsilon m,\ \alpha = \mp\arccos\left[\cos(g_{\mathrm{co}}L_{\mathrm{co}})\cos\phi_m\right]. \tag{F.10}$$

This gives the relative field intensities in the non-coupled regions of the rings for a particular mode, and is used to plot composition ratios in Fig. 3.3. Another point of interest is the center of the coupled region. Here the field can be found as

$$\begin{aligned}\psi_{\mathrm{co}} &\propto \begin{pmatrix} \cos(g_{\mathrm{co}}L_{\mathrm{co}}/2) & i\sin(g_{\mathrm{co}}L_{\mathrm{co}}/2) \\ i\sin(g_{\mathrm{co}}L_{\mathrm{co}}/2) & \cos(g_{\mathrm{co}}L_{\mathrm{co}}/2) \end{pmatrix} \begin{pmatrix} e^{i\phi_m/2} & 0 \\ 0 & e^{-i\phi_m/2} \end{pmatrix} \psi_{\mathrm{I}} \\ &\propto \left(\sqrt{\frac{\sin\alpha+\sin\phi_m}{2\sin\alpha}},\ \mp\sqrt{\frac{\sin\alpha-\sin\phi_m}{2\sin\alpha}} \right)^{\mathbf{T}}. \end{aligned} \tag{F.11}$$

There are some special cases of ϕ_m that lead to simplified field distributions and are demonstrated in Fig. F.3. For example, if ϕ_m/π is an integer (crossing centers), the modes become purely symmetrical and anti-symmetrical:

$$\psi_{\mathrm{I}} \propto (\sqrt{1/2}, \mp\sqrt{1/2})^{\mathbf{T}},\ \ \psi_{\mathrm{co}} \propto (\sqrt{1/2}, \mp\sqrt{1/2})^{\mathbf{T}}. \tag{F.12}$$

Points I, II, V, and VI in Fig. F.3(b) belong to these cases. Points II and V are symmetric modes formed by the two rings, with equal mode intensities and the same phase. On the other hand, points I and VI are anti-symmetric modes, with equal mode intensities but opposite phase. These results happen to agree with coupled-mode calculations when only the pair of degenerate longitudinal modes from each ring are considered. However, while the energy is equally distributed in the two rings in the same way as the reduced coupled-mode theory predicted, other longitudinal modes still participate in the coupling because the wavevector in the coupled region differs from that in the uncoupled region. On the other hand, if ϕ_m/π is a half-integer (halfway between crossing centers), then at the center of coupling position the field is entirely within a single ring:

$$\psi_{\mathrm{I}} \propto (\cos(g_{\mathrm{co}}L_{\mathrm{co}}/2), \sin(g_{\mathrm{co}}L_{\mathrm{co}}/2))^{\mathbf{T}},\ \ \psi_{\mathrm{co}} \propto (1,0)^{\mathbf{T}},\ \ \text{or} \tag{F.13}$$

$$\psi_{\mathrm{I}} \propto (\sin(g_{\mathrm{co}}L_{\mathrm{co}}/2), -\cos(g_{\mathrm{co}}L_{\mathrm{co}}/2))^{\mathbf{T}},\ \ \psi_{\mathrm{co}} \propto (0,-1)^{\mathbf{T}}. \tag{F.14}$$

Points III and IV in Fig. F.3(b) belong to these cases.

An interesting feature of the field distribution is that, for a single continuous branch, the field compositions exchange parity at the next degeneracy point, and the anti-symmetric mode now becomes the symmetric mode (from point I to V) and vice

versa (from point II to VI). The change of parity shows that the modes repeat themselves every two vernier periods (every two degeneracy points) instead of one, in agreement with Eq. (F.9). While the parity exchange is obvious after plotting the dispersion (Fig. F.3(a)), it can also be understood from a mode number argument. We consider the total phase accumulated in ring A for a specific mode divided by 2π, which should be an integer and denoted as m_{A}. This is the "mode number" for ring A for the specific mode. Similarly m_{B} could be defined. These two numbers equal to the respective mode numbers of the closest uncoupled modes, which can be seen by adiabatically turning of the coupling. For a single vernier period, the total mode number changes by an odd number. However, going to the next longitudinal mode by changing the frequency alone changes both m_{A} and m_{B} by one. The only way to induce a separate mode number change is to create a zero in the field amplitude somewhere in the respective ring, which is indeed the case for points III and IV shown in Fig. F.3(b). Considering that the individual mode numbers are about equally distributed around the averaged-length mode number m (e.g., $|(m_{\mathrm{B}} - m) - (m - m_{\mathrm{A}})| \leq 1$), the extra increment of m_{B} and decrement of m_{A} should have taken place alternatively between the vernier periods, indicating the mode branch switches mode compositions for each vernier period.

F.2 Eigenmodes of a three-ring coupled resonator

In this section we study the mode frequencies of the three-ring coupled resonator. Although the derivation is similar to that of the two-ring resonator, we will highlight some features of the coupled system that are not obvious in the two-ring case. The result can also be readily generalized to multi-ring arrangements.

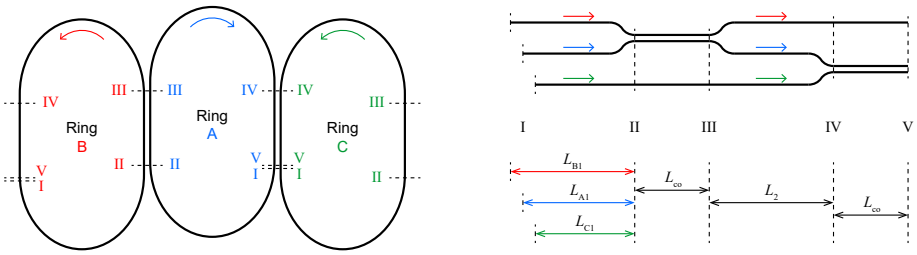

Figure F.4: **Schematic of the three-ring coupled resonator.** Left panel: Top view of the coupled resonator with key points marked. Right panel: Schematic of the resonator with straightened waveguides (not to scale). Segment lengths have been marked.

The schematic for the three-ring coupled resonator is shown in Fig. F.4 along with definitions of segment lengths. Unlike the two-ring case, there is no explicit symmetry to take advantage of, and the segmentation method is chosen to reduce calculation complexity. We can assemble the field amplitudes from ring C, A, and B, in that order, into a vector and find the transfer matrix for each section:

$$\psi_{\mathrm{II}} = \exp\left[in_{\mathrm{wg}}\omega/c \begin{pmatrix} L_{\mathrm{C1}} & 0 & 0 \\ 0 & L_{\mathrm{A1}} & 0 \\ 0 & 0 & L_{\mathrm{B1}} \end{pmatrix}\right]\psi_{\mathrm{I}}, \tag{F.15}$$

$$\psi_{\mathrm{III}} = \exp\left[iL_{\mathrm{co}} \begin{pmatrix} n_{\mathrm{wg}}\omega/c & 0 & 0 \\ 0 & n_{\mathrm{wg}}\omega/c & g_{\mathrm{co}} \\ 0 & g_{\mathrm{co}} & n_{\mathrm{wg}}\omega/c \end{pmatrix}\right]\psi_{\mathrm{II}}, \tag{F.16}$$

$$\psi_{\mathrm{IV}} = \exp\left[in_{\mathrm{wg}}\omega/c \begin{pmatrix} L_2 & 0 & 0 \\ 0 & L_2 & 0 \\ 0 & 0 & L_2 \end{pmatrix}\right]\psi_{\mathrm{III}}, \tag{F.17}$$

$$\psi_{\mathrm{V}} = \exp\left[iL_{\mathrm{co}} \begin{pmatrix} n_{\mathrm{wg}}\omega/c & g_{\mathrm{co}} & 0 \\ g_{\mathrm{co}} & n_{\mathrm{wg}}\omega/c & 0 \\ 0 & 0 & n_{\mathrm{wg}}\omega/c \end{pmatrix}\right]\psi_{\mathrm{IV}}. \tag{F.18}$$

The overall round-trip transfer matrix is the product of the previous four matrices and reads

$$T = \begin{pmatrix} e^{in_{\mathrm{wg}}\omega L_{\mathrm{C}}/c}\cos(g_{\mathrm{co}}L_{\mathrm{co}}) & ie^{in_{\mathrm{wg}}\omega L_{\mathrm{A}}/c}\cos(g_{\mathrm{co}}L_{\mathrm{co}})\sin(g_{\mathrm{co}}L_{\mathrm{co}}) & -e^{in_{\mathrm{wg}}\omega L_{\mathrm{B}}/c}\sin^2(g_{\mathrm{co}}L_{\mathrm{co}}) \\ ie^{in_{\mathrm{wg}}\omega L_{\mathrm{C}}/c}\sin(g_{\mathrm{co}}L_{\mathrm{co}}) & e^{in_{\mathrm{wg}}\omega L_{\mathrm{A}}/c}\cos^2(g_{\mathrm{co}}L_{\mathrm{co}}) & ie^{in_{\mathrm{wg}}\omega L_{\mathrm{B}}/c}\cos(g_{\mathrm{co}}L_{\mathrm{co}})\sin(g_{\mathrm{co}}L_{\mathrm{co}}) \\ 0 & ie^{in_{\mathrm{wg}}\omega L_{\mathrm{A}}/c}\sin(g_{\mathrm{co}}L_{\mathrm{co}}) & e^{in_{\mathrm{wg}}\omega L_{\mathrm{B}}/c}\cos(g_{\mathrm{co}}L_{\mathrm{co}}) \end{pmatrix}, \tag{F.19}$$

where we defined the total length of ring C, $L_{\mathrm{C}} = L_{\mathrm{C1}} + L_2 + 2L_{\mathrm{co}}$, and L_{A} and L_{B} are defined similarly. Note that the dependence on individual segment lengths L_{C1}, L_{A1}, L_{B1}, and L_2 have disappeared from T, indicating that the relative position of the couplers on ring A does not matter for eigenfrequency calculations. This is because propagating the same distance for all three components provides only a global phase for the state, which can be moved past the coupler. Mathematically,

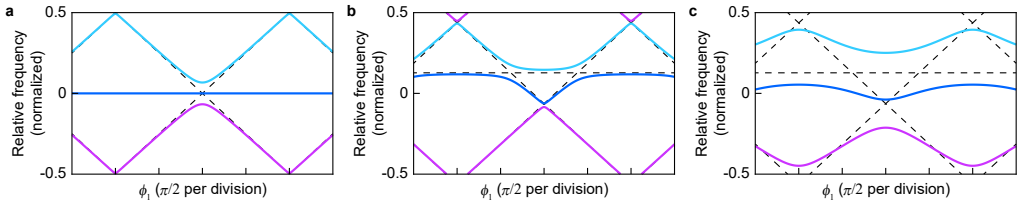

Figure F.5: **Eigenfrequency plots for the three-ring coupled resonator, showing relative frequency (normalized to $D_{1,m}$) versus ϕ_1.** Parameters are **(a)** $g_{co}L_{co} = 0.3$ and $\phi_2 = 0$; **(b)** $g_{co}L_{co} = 0.3$ and $\phi_2 = 0.4$; **(c)** $g_{co}L_{co} = 1.0$ and $\phi_2 = 0.4$.

the coupling matrix commutes with the propagation matrix, which is proportional to the identity matrix for identical ring cross sections:

$$\left[L_{co} \begin{pmatrix} n_{wg}\omega/c & 0 & 0 \\ 0 & n_{wg}\omega/c & g_{co} \\ 0 & g_{co} & n_{wg}\omega/c \end{pmatrix}, \; n_{wg}\omega/c \begin{pmatrix} L_2 & 0 & 0 \\ 0 & L_2 & 0 \\ 0 & 0 & L_2 \end{pmatrix} \right] = 0. \tag{F.20}$$

For the coupler itself, the propagating part (diagonal elements) also commute with the pure coupling part (off-diagonal elements), although different couplers do not commute. Therefore, the system is equivalent to propagating along the entire length of individual rings, followed by two point couplers with the same coupling ratios as the original couplers. This argument works for all coupled resonators with identical ring cross-sections coupled in a chain or tree topology, and provides a degree of freedom for placing the rings in the design phase.

Following the two-ring analysis, we define an averaged length for the resonators and its associated mode number:

$$\overline{L} \equiv \frac{L_C + L_A + L_B}{3}, \quad m \equiv \frac{n_{wg}\omega\overline{L}}{2\pi c}. \tag{F.21}$$

We will also need to define two length differences. For the current design, we have $L_C + L_B \approx 2L_A$, and the following contrast definitions become convenient:

$$\epsilon_1 = \frac{L_B - L_C}{2\overline{L}}, \quad \epsilon_2 = \frac{L_C + L_B - 2L_A}{6\overline{L}}. \tag{F.22}$$

With these notations, T can be written as

$$T = e^{2\pi m i}$$

$$\begin{pmatrix} e^{i(-\phi_1+\phi_2)}\cos(g_{co}L_{co}) & ie^{-2i\phi_2}\cos(g_{co}L_{co})\sin(g_{co}L_{co}) & -e^{i(\phi_1+\phi_2)}\sin^2(g_{co}L_{co}) \\ ie^{i(-\phi_1+\phi_2)}\sin(g_{co}L_{co}) & e^{-2i\phi_2}\cos^2(g_{co}L_{co}) & ie^{i(\phi_1+\phi_2)}\cos(g_{co}L_{co})\sin(g_{co}L_{co}) \\ 0 & ie^{-2i\phi_2}\sin(g_{co}L_{co}) & e^{i(\phi_1+\phi_2)}\cos(g_{co}L_{co}) \end{pmatrix}, \tag{F.23}$$

with $\phi_1 = 2\pi\epsilon_1 m$ and $\phi_2 = 2\pi\epsilon_2 m$. For the current design, $\epsilon_1 \approx 3 \times 10^{-3}$ and $\epsilon_2 \approx 1.5 \times 10^{-6}$, which ensures a slowly-varying phase contributed by the coupling. The eigenfrequencies are given by

$$\omega = \omega_m - \frac{D_{1,m}}{2\pi}\theta, \tag{F.24}$$

where $e^{i\theta}$ is given by the roots to the cubic characteristic equation:

$$\begin{aligned} &x^3 - (e^{-2i\phi_2}\cos(g_{\mathrm{co}}L_{\mathrm{co}}) + 2e^{i\phi_2}\cos(\phi_1))\cos(g_{\mathrm{co}}L_{\mathrm{co}})x^2 \\ &+ (e^{2i\phi_2}\cos(g_{\mathrm{co}}L_{\mathrm{co}}) + 2e^{-i\phi_2}\cos(\phi_1))\cos(g_{\mathrm{co}}L_{\mathrm{co}})x - 1 = 0, \quad x \equiv e^{i\theta}. \end{aligned} \tag{F.25}$$

The unitary nature of T ensures that all three roots for x lie on the complex unit circle.

As $\epsilon_2 \ll \epsilon_1$ for the current design, ϕ_2 varies much more slowly compared to ϕ_1 and we will take ϕ_2 to be a constant to simplify the discussions below. Fig. F.5 plots the relative frequencies for some parameter combinations. In the case of $\phi_2 = 0$ (Fig. F.5(a)), the mode frequencies of ring A coincides with the averaged frequency, and the mode frequencies of ring A and B are symmetrically distributed around the averaged frequency. As a result, the coupled frequency spectrum resembles that of the two-ring resonator. A key difference here is that the two gaps opened have different widths. For crossings at integer $\phi_1/(2\pi)$ locations, ring A participates in the coupling, and the total gap is approximately $2\sqrt{2}g_{\mathrm{co}}L_{\mathrm{co}} \times D_{1,m}/(2\pi)$ for small $g_{\mathrm{co}}L_{\mathrm{co}}$. For the other crossings at half-integer $\phi_1/(2\pi)$ locations, the mode from ring A is half an FSR away from ring C and B, and the coupling becomes indirect. Here the gap width is approximately $(g_{\mathrm{co}}L_{\mathrm{co}})^2 \times D_{1,m}/(2\pi)$ for small $g_{\mathrm{co}}L_{\mathrm{co}}$, which is second order in the coupling strength. A nonzero $\phi_2 = 0$ breaks the frequency-domain symmetry and leads to additional avoided crossings (Fig. F.5(b)). For stronger coupling strengths, the bandwidths of the crossings expand and merge with the other crossings (Fig. F.5(c)) similar to the two-ring case. Here the frequency dispersion become smoother and have less overall coupling-contributed dispersion.

Figure F.6(a) shows the measured dispersion data for the three-ring resonator. The topmost branch is used for soliton generation and is also shown in Fig. 3.1(e). Fitting the averaged frequency (not plotted) gives an averaged FSR of 19.9711 GHz and a second-order dispersion parameter of 282.7 kHz, consistent with the two-ring results. After subtracting the averaged frequency, Fig. F.6(b) shows the relative frequency with a similar structure of Fig. F.5(c). Using the exponential decaying coupling model as described in the methods ($g_{\mathrm{co}} = g_{\mathrm{co},0}\exp(-\mu/\mu_g)$), the fitted

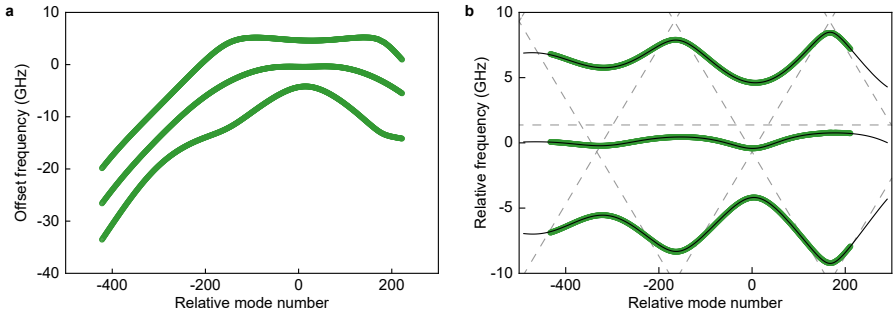

Figure F.6: **Dispersion of the coupled three-ring resonator. (a)** Measured dispersion for the three-ring resonator. The topmost branch is also shown in Fig. 3.1(e) in the main text. **(b)** Mode frequencies relative to the averaged frequencies (circles). Solid curves show the fitted result using the three-ring model, and are in excellent agreement with the data. Dashed lines indicate frequencies of the individual rings before coupling.

result for the relative frequencies also shows good agreement with the measured data. The fitted parameters are $g_{\mathrm{co},0}L_{\mathrm{co}} = 0.985$, $\mu_g = 1175$ and $\phi_2 = 0.216$.

Appendix G

CODE TO PLOT UP-TO-DATE FIG. 7.1

G.1 Python code to plot the up-to-date number of exoplanets found using different methods

```
import xml.etree.ElementTree as ET, urllib.request, gzip, io,
    numpy as np, matplotlib.pyplot as plt
from collections import Counter

url = "https://github.com/OpenExoplanetCatalogue/oec_gzip/raw/
    master/systems.xml.gz"
oec = ET.parse(gzip.GzipFile(fileobj=io.BytesIO(urllib.request.
    urlopen(url).read())))

# Extract discovery years and methods
years_methods = Counter((int(planet.findtext("discoveryyear")),
    planet.findtext("discoverymethod"))
     for planet in oec.findall(".//planet")
     if planet.findtext("discoveryyear"))

years = range(1995, max(years_methods)[0] + 1)

# Get the set of discovery methods
methods = set(method for year, method in years_methods)
# plot 'RV' the first, 'transit' the last
methods = list(methods)
methods.remove('RV')
methods.remove('transit')
methods = ['RV']+methods+['transit']

# Create a list of all counts
counts = np.array([[years_methods[(year, method)] for method in
    methods] for year in years])

# Use more contrasting colors
colors = plt.cm.tab20(np.linspace(0, 1, len(methods)))

# Create a stacked bar plot
for i, method in enumerate(methods):
    plt.bar(years, counts[:, i], bottom=np.sum(counts[:, :i], axis
```

```
    =1), color=colors[i], label=method)

# Add labels and legend
plt.xlabel("Year")
plt.ylabel("Number of planets discovered")
plt.ylim(0, 200)
plt.legend()
plt.show()
```

Listing G.1: Python code to plot the number of exoplanets found using different methods with up-to-date information from Open Exoplanet Catalogue database.

INDEX